SCHOOL OF
CIVIL ENGINEERING

INDIANA
DEPARTMENT OF TRANSPORTATION

JOINT HIGHWAY RESEARCH PROJECT

FHWA/IN/JHRP-96/17
Final Report

TESTING OF MULTI-SPAN BRIDGES WITH FULL-SPAN PRECAST PRESTRESSED CONCRETE PANELS (PHASE 1)

Robert J. Peterman
Julio A. Ramirez

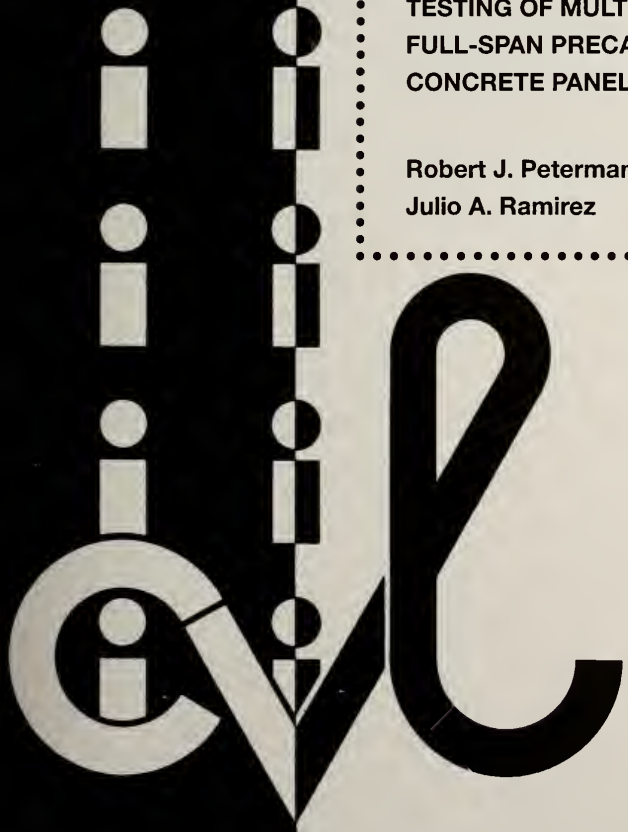

PURDUE UNIVERSITY

Final Report

TESTING OF MULTI-SPAN BRIDGES WITH FULL-SPAN PRECAST PRESTRESSED CONCRETE PANELS (PHASE 1)

Robert J. Peterman
Julio A Ramirez

Purdue University

Joint Highway Research Project

Project Number: HPR-2097
File Number: 7-4-34

Conducted in Cooperation with the

Indiana Department of Transportation

and

Federal Highway Administration

The contents of this report reflect the views of the authors who are responsible for the facts and the accuracy of the data presented herein. The contents do not necessarily reflect the views or policies of the Federal Highway Administration and the Indiana Department of Transportation. This report does not constitute a standard, specification, or regulation.

Purdue University
West Lafayette, IN 47907
May 30, 1997

Digitized by the Internet Archive
in 2011 with funding from
LYRASIS members and Sloan Foundation; Indiana Department of Transportation

http://www.archive.org/details/testingofmultisp00pete

ACKNOWLEDGMENTS

Appreciation is expressed to the Indiana Department of Transportation (INDOT) and the Federal Highway Administration (FHWA) for providing funding for this research. Specifically, INDOT personnel Tony Zander, Hasmukh Patel, Tom Seeman and FHWA personnel Larry O'Donnell were key resource persons within these organizations.

TECHNICAL REPORT STANDARD TITLE PAGE

1. Report No.	2. Government Accession No.	3. Recipient's Catalog No.
FHWA/IN/JHRP-96/17		

4. Title and Subtitle	5. Report Date
Testing of Multi-Span Bridges with Full-Span Precast Prestressed Concrete Panels (Phase 1)	May, 1997
	6. Performing Organization Code

7. Author(s)	8. Performing Organization Report No.
Robert J. Peterman and Julio A. Ramirez	FHWA/IN/JHRP-96/17

9. Performing Organization Name and Address	10. Work Unit No.
Joint Highway Research Project Civil Engineering Building Purdue University West Lafayette, Indiana 47907-1284	
	11. Contract or Grant No. HPR-2097

12. Sponsoring Agency Name and Address	13. Type of Report and Period Covered
Indiana Department of Transportation State Office Building 100 North Senate Avenue Indianapolis, IN 46204	Final Report
	14. Sponsoring Agency Code

15. Supplementary Notes

16. Abstract

The purpose of this study was to assess the behavior and durability of multi-span bridges constructed with full-span prestressed concrete form panels. The use of full-span prestressed concrete form panels for bridges with spans of 40 ft. or less is an economical method of construction due to the reduction of on-site formwork and labor required by alternate cast-in-place systems. In this research, a pair of two-span bridges utilizing full-span prestressed concrete form panels were fabricated and tested in the Karl H. Kettelhut Structural Engineering Laboratory at Purdue University. Time-dependent effects were monitored during the cast-in-place (CIP) concrete cure period of each bridge.

At the conclusion of this period, each bridge was subjected to 5 million cycles of repeated service loading prior to a final loading to failure. In addition, one of the test bridges and five smaller composite specimens were exposed to a 15% sodium chloride solution followed by 3 days of drying at a minimum of 100° F. The durability of these bridges was then assessed by determining the potential for the build-up of chlorides at the boundary of the prestressed panels and CIP topping, and the resistance of the reinforcement to corrosion induced by chlorides.

This study found that the PCA and CTL methods considerably overestimated the negative moments due to the restraint of time-dependent deformations in the laboratory test bridges. The negative restraint moments could be more accurately determined using a new method proposed in this report. The proposed method includes the effect of cracking of the CIP concrete at interior piers.

This study also showed that adequate long-term performance could be achieved with bridges constructed using full-span precast prestressed concrete panels. The 5 million cycles of repeated service loading did not reduce the continuity between adjacent spans. Durability cycling revealed that an accumulation of chlorides at the boundary of the CIP topping and prestressed panels would not lead to a diminished load-carrying capacity of the structure. Severe corrosion occurred at the positive moment connection in the diaphragm of the test bridge. The connection detail should be modified before this construction method is implemented in the field.

17. Key Words	18. Distribution Statement
concrete, deck panels, bridge decks, load testing, durability, precast, prestressed, time dependent effects	No restrictions. This document is available to the public through the National Technical Information Service, Virginia, 22161

19. Security Classif. (of this report)	20. Security Classif. (of this page)	21. No. of Pages	22. Price
Unclassified	Unclassified	343	

Form DOT F 1700.7 (8-69)

TABLE OF CONTENTS

Page

LIST OF TABLES v

LIST OF FIGURES vii

CHAPTER 1 INTRODUCTION 1

1.1 Background Information 1
1.2 Objective 2
1.3 Scope 3

CHAPTER 2 LITERATURE REVIEW 4

2.1 Introduction 4
2.2 Previous Studies 4
2.2.1 Hays, Cox, and Obranic (1980) 4
2.2.2 Buckner and Turner (1981) 7
2.3 Practices by Other DOT's 9
2.4 Summary of Related Research 9

CHAPTER 3 EXPERIMENTAL PROGRAM 12

3.1 Test Set-up 12
3.2 Test Specimens 12
3.2.1 Fabrication 13
3.2.2 Fabrication of Composite Test Bridges 14
3.3 Loading 15
3.4 Durability Cycling and Testing 16
3.4.1 Chloride Ion Powder Samples 17
3.4.2 Corrosion of Reinforcement in Concrete 18
3.4.3 The Role of Chlorides in Reinforcement Corrosion 19
3.4.4 Half-Cell Potentials 19
3.4.5 Measured Corrosion Current 22
3.4.6 AC-Resistance 23
3.4.7 Condition of Epoxy-Coated Reinforcement 23

3.4.8 Rapid Determination of Chloride Permeability of Concrete 24
3.4.9 Additional Durability Specimens 25
3.5 Instrumentation 28
3.5.1 Strain Measurements with Electrical Resistance Gages 28
3.5.2 End Reactions 30
3.5.3 Deflections 31
3.5.4 Differential Deflection Measurements 32
3.5.5 Strand Slip Gages 32
3.5.6 Crack Width Measurements 32
3.5.7 Strain Measurements With a Whittemore Gage 33
3.5.8 End Rotation Measurements 33
3.5.9 Impact-Echo 34
3.6 Material Properties 35
3.6.1 Prestressed Concrete 36
3.6.2 Cast-In-Place Concrete for Bridge #1 37
3.6.3 Cast-In-Place Concrete for Bridge #2 37
3.6.4 Cast-In-Place Concrete for Small Durability Specimens 39
3.6.5 Mild Steel Reinforcement 40
3.6.6 Prestressed Reinforcement 40
3.7 Summary of Experimental Procedures 41

CHAPTER 4 TIME DEPENDENT EFFECTS 79

4.1 Introduction 79
4.2 PCA Method 80
4.3 CTL Method 82
4.4 Experimental Determination of Restraint Moments 85
4.4.1 Restraint Moments in Bridge #1 85
4.4.2 Restraint Moments in Bridge #2 87
4.5 Comparison of Experimental Restraint Moments with Predicted Results 88
4.5.1 Modified PCA Method 91
4.6 Displacement Measurements During the Cure Period of Bridge #2 96
4.7 Whittemore Gage Measurements During the Cure Period of Bridge #2 97
4.8 Summary of Time-Dependent Effects 98

CHAPTER 5 RESPONSE TO SUPERIMPOSED LOADING 132

5.1 Introduction 132
5.2 Initial Loadings of Bridge #1 132
5.2.1 Continuity Moments 133
5.2.2 Midspan Deflections 134
5.2.3 Strain Measurements 136
5.3 Initial Loadings of Bridge #2 137

5.3.1 Continuity Moments 138
5.3.2 Midspan Deflections 140
5.3.3 Strain Measurements 141
5.4 Summary of Initial Loadings 143
5.5 Overview of Cyclic Loading 144
5.6 Cyclic Loading of Bridge #1 145
5.7 Cyclic Loading of Bridge #2 148
5.8 Summary of Cyclic Loadings 149
5.9 Overview of Failure Loadings 149
5.10 Calculation of Failure Loads 150
5.11 Failure Loading of Bridge #1 152
5.12 Failure Loading of Bridge #2 155
5.13 Moment Redistribution 159
5.13.1 Moment Redistribution in Bridge #1 160
5.13.2 Moment Redistribution in Bridge #2 161
5.13.3 Moment Redistribution Summary 161
5.14 Summary of Failure Loadings 162

CHAPTER 6 DURABILITY EVALUATION 238

6.1 Introduction 238
6.2 Durability Assessment of Bridge #1 238
6.2.1 Chloride Ion Powder Samples Taken From Bridge #1 239
6.2.2 Summary of Chloride Ion Powder Samples 244
6.2.3 Comparison of Chloride Data With Data From Bridges in Service 244
6.2.4 Summary of Comparisons With Other Bridges 250
6.2.5 Concrete Permeability 251
6.2.6 Results From Impact-Echo Testing 252
6.2.7 Measured Corrosion Current in Bridge #1 253
6.2.8 Half-Cell Potentials (Bridge #1) 255
6.2.9 AC-Resistance 258
6.2.10 Visual Inspection of Reinforcement 259
6.2.11 Summary of Corrosion Assessment of Bridge #1 260
6.3 Durability Assessment of 3 ft x ft Specimens 261
6.3.1 Chloride Ion Powder Samples 261
6.3.2 Summary of Chloride Ion Powder Samples 263
6.3.3 Measured Corrosion Currents 263
6.3.4 Half-Cell Potentials 265
6.3.5 Visual Inspection of Rebars 265
6.3.6 Summary of Corrosion Assessment of Durability Specimens 266
6.3.7 Comparison of Durability Specimens With Bridge #1 267

CHAPTER 7 SUMMARY,CONCLUSIONS, AND RECOMMENDATIONS 327
7.1 Summary of Results 327
7.1.1 Introduction 327
7.1.2 Restraint Moments 328
7.1.3 Response to Superimposed Loading 329
7.1.3.1 Initial Loading 329
7.1.3.2 Cyclic Loading 330
7.1.3.3 Failure Loading 330
7.1.4 Durability 331
7.1.4.1 Chloride Penetration in Bridge #1 331
7.1.4.2 Chloride Penetration in the 3 ft x 3 ft Durability Specimens 332
7.1.4.3 Reinforcement Corrosion in Bridge #1 333
7.1.4.4 Reinforcement Corrosion in 3 ft x 3 ft Durability Specimens 334
7.2 Conclusions 334
7.3 Implementation 337
7.4 Suggestions for Phase 2 339

LIST OF REFERENCES 342

LIST OF TABLES

Table		Page
3.1	Specimen Details	43
3.2	Prestressed Concrete Properties (Bridge #1)	43
3.3	Prestressed Concrete Properties (Bridge #2)	44
3.4	Cast-in-Place Concrete Properties (Bridge #1)	45
3.5	Cast-in-Place Concrete Properties (Bridge #2)	46
4.1	End Reactions and Restraint Moments During the CIP Concrete Cure Period (Bridge #1)	99
4.2	End Reactions and Restraint Moments During the CIP Concrete Cure Period (Bridge #2)	100
5.1	Nominal Moment Capacities and Estimated Failure Loads of Bridge #1	163
5.2	Nominal Moment Capacities and Estimated Failure Loads of Bridge #2	163
5.3	Crack Widths at Diaphragm During Failure Loading of Bridge #1	164
5.4	Strand Slip at West End During Failure Loading of Bridge #1	165
5.5	Strand Slip at East End During Failure Loading of Bridge #1	165
5.6	Crack Widths at Diaphragm During Failure Loading of Bridge #2	166
6.1	Chloride Ion Concentrations After 12 Weeks of Exposure Cycling (Bridge #1)	269
6.2	Chloride Ion Concentrations After 24 Weeks of Exposure Cycling (Bridge #1)	270
6.3	Chloride Ion Concentrations After 36 Weeks of Exposure Cycling (Bridge #1)	271

Table Page

6.4 Chloride Ion Concentrations After 48 Weeks of Exposure Cycling (Bridge #1) 272

6.5 Random Sampling of Base Chlorides in the CIP Concrete of Bridge #1 273

6.6 Estimated Time Represented by Southern Exposure Cycling (By Linear Extrapolation).....274

6.7 Chloride Ion Concentrations in Durability Specimens After 12 Weeks of Exposure 275

6.8 Chloride Ion Concentrations in Durability Specimens After 24 Weeks of Exposure 276

LIST OF FIGURES

Figure Page

2.1 Detail Proposed by Hays, Cox and Obranic 11

3.1 Laboratory Test Setup 47

3.2 Detail at Diaphragm 1 48

3.3 Cross-Section of Test Specimen 49

3.4 Mild Steel Reinforcement in Prestressed Panels 50

3.5 Transverse Reinforcement in Cast-In-Place Topping 51

3.6 Raked Finish Being Applied to the Prestressed Panels 52

3.7 Epoxy-Coated Reinforcement in CIP Topping 53

3.8 Raked Finish Applied to CIP Topping at Center Pier 53

3.9 15% Sodium Chloride Solution Being Pumped Onto Bridge #1 54

3.10 The Ponded Region of Bridge #1 54

3.11 Bridge #1 During the Drying Phase of the Exposure Cycling 55

3.12 The Half-Cell Potential Measurement 56

3.13 Location of Weekly Half-Cell Potential Measurements 57

3.14 Electrically Interconnected Reinforcement in the CIP Topping of Bridge #1 58

3.15 Measured Corrosion Current 59

3.16 Uncoated Reinforcement in Bottom Panels of 3 ft x ft Durability Specimens 60

3.17 Initial Pre-Formed Crack in 3 ft x 3 ft Durability Specimens 61

Figure Page

3.18 Typical Damage to Epoxy Coating at Ribbed Locations of Bars 61

3.19 Damaged Areas of Epoxy-Coated Bars in 3 ft x 3 ft Durability Specimens 62

3.20 Location of Epoxy-Coating Defects in the 3 ft x 3 ft Durability Specimens 63

3.21 3 ft x 3 ft Durability Specimens with Electrical Switches Used to Isolate Bars 64

3.22 The Location of Weekly Half-Cell Measurements on 3 ft x 3 ft Specimens 64

3.23 Location of Strain Gages on Prestressed Strand in Precast Panels 65

3.24 Location of Strain Gages on Bottom Surface of Precast Panels 66

3.25 Location of Strain Gages on Longitudinal Reinforcement in CIP Topping (Bridge #1) 67

3.26 Location of Strain Gages on Longitudinal Reinforcement in CIP Topping (Bridge #2) 68

3.27 Location of Strain Gages on Transverse Reinforcement in CIP Topping 69

3.28 Location of Strain Gages on Top Surface of CIP Concrete 70

3.29 Spreader Beam on Two Load Cells at Panel Ends 71

3.30 LVDTs Used to Measure Deflections at Midspan 71

3.31 Differential Deflection Measurements Using an Electronic Dial Gage 72

3.32 Dial Gages Used to Measure Strand Slip at End 72

3.33 Measuring Crack Widths with an Optical Measuring Scale 73

3.34 Whittemore Points at the Center Pier of Bridge #2 73

3.35 Dial Gages Used to Determine End Rotations of Bridge #2 74

3.36 Impact-Echo Testing of Bridge #1 74

3.37 Shrinkage Data from Cast-In-Place Concrete Used in Bridge #2 75

Figure Page

3.38 Typical Stress-Strain Curve of #4 Bars Used in this Study....76

3.39 Typical Stress-Strain Curve of #6 Bars Used in this Study....77

3.40 Stress-Strain Curves of Prestressed Steel (Obtained Using Strain Gages on Individual Wires of a 7-Wire Strand)....78

4.1 Deformation Due to Differential Shrinkage in Simple-Span Composite Construction....101

4.2 Deformation Due to Differential Shrinkage in a Composite, Two-Span Continuous Bridge....102

4.3 Calculation of Restrain Moment Due to Uniform Applied Moment....103

4.4 Relationship of Restraint Moments to Measured Changes in End Reactions....104

4.5 End Reactions During the CIP Concrete Cure Period of Bridge #1....105

4.6 Cracking During the CIP Concrete Cure Period of Bridge #1 (Plan View)....106

4.7 Cracking During the CIP Concrete Cure Period of Bridge #1 (Elevations)....107

4.8 End Reactions During the CIP Concrete Cure Period of Bridge #2....108

4.9 CIP Concrete Temperature During the Cure Period (Bridge #2)....109

4.10 Cracking During the CIP Concrete Cure Period of Bridge #2....110

4.11 Cracking During the CIP Concrete Cure Period of Bridge #2 (Elevations)....111

4.12 Curve Fit Through Shrinkage Beam Data from the CIP Concrete Used in Bridge #2....112

4.13 Air Temperature During the CIP Concrete Cure Period of Bridge #1....113

4.14 Relative Humidity During the CIP Concrete Cure Period of Bridge #1....114

4.15 Air Temperature During the CIP Concrete Cure Period of Bridge #2....115

4.16 Relative Humidity During the CIP Concrete Cure Period of Bridge #2....116

Figure Page

4.17 Experimentally Determined Restraint Moments and Values Calculated Using PCA and CTL Methods (Bridge #1) 117

4.18 Experimentally Determined Restraint Moments and Values Calculated Using PCA and CTL Methods (Bridge #2) 118

4.19 Derivation of Shrinkage Reduction Factor 119

4.20 Experimentally Determined Restraint Moments and Values Calculated Using Modified PCA Method (Bridge #1) 120

4.21 Experimentally Determined Restraint Moments and Values Calculated Using Modified PCA Method (Bridge #2) 121

4.22 Typical Moment-Curvature Relationship of a Reinforced Concrete Beam 122

4.23 Experimental Restraint Moments and Modified PCA Method Assuming No Change After Cracking (Bridge #1) 123

4.24 Experimental Restraint Moments and Modified PCA Method Assuming No Change After Cracking (Bridge #2) 124

4.25 Midspan Deflections During CIP Concrete Cure Period (Bridge #2) 125

4.26 Displacement Profiles During CIP Concrete Cure Period (Bridge #2) 126

4.27 Location of Whittemore Points At Center Pier (Bridge #2) 127

4.28 Mean Whittemore Strains During CIP Concrete Cure Period of Bridge #2 (North Face) 128

4.29 Mean Whittemore Strains During the CIP Concrete Cure Period of Bridge #2 (South Face) 129

4.30 Mean Strain Distributions During CIP Concrete Cure Period of Bridge #2 (North Face) 130

4.31 Mean Strain Distributions During CIP Concrete Cure Period of Bridge #2 (South Face) 131

5.1 Cracks Occurring During the Initial Loading of Bridge #1 (Plan View) 167

Figure Page

5.2 Cracks Occurring During the Initial Loading of Bridge #1 (Elevations at Pier) 168

5.3 Continuity Moments During the Initial Loading of Bridge #1 169

5.4 Change in Continuity Moments During the Initial Loading of Bridge #1 170

5.5 Models Used to Calculate Moments and Deflections Due to Superimposed Loading 171

5.6 Changes in Continuity Moments During Second Loading of Bridge #1 172

5.7 Midspan Deflections During the Initial Loading of Bridge #1 (East Span) 173

5.8 Midspan Deflections During the Initial Loading of Bridge #2 (West Span) 174

5.9 Comparison of Measured Deflections with Values Calculated Using Analytical Models (Bridge #1) 175

5.10 Illustration of Method Used to Calculate Deflections Occurring Simultaneously with Decreasing Restraint Moments 176

5.11 Incremental Deflections During the Second Loading of Bridge #1 177

5.12 Incremental Strains in Rebar Gages Located Near the Crack Which Opened at 13 Kips (Bridge #1) 178

5.13 Incremental Strains in Rebar Gages Located Near the Crack Which Opened at 19.9 Kips (Bridge #1) 179

5.14 Cracks Occurring During the Initial Loading of Bridge #2 (Plan View) 180

5.15 Cracks Occurring During the Initial Loading of Bridge #2 (Elevations at Pier) 181

5.16 Continuity Moments During the Initial Loading of Bridge #2 182

5.17 Change in Continuity Moments During the Initial Loading of Bridge #2 183

5.18 Change in Continuity Moments During the Second Loading of Bridge #2 184

5.19 Midspan Deflections During the Initial Loading of Bridge #2 (East Span) 185

5.20 Midspan Deflections During the Initial Loading of Bridge #2 (West Span) 186

Figure Page

5.21 Comparison of Measured Deflections with Values Calculated Using Analytical Models (Bridge #2) 187

5.22 Incremental Deflections During the Second Loading of Bridge #2 188

5.23 Incremental Strains in Rebar Gages Located at the Center of the Pier (Bridge #2) 189

5.24 Strains Measured During the Initial Loading of Bridge #2 Using a Whittemore Gage 190

5.25 Load Versus Deflection Curves During the Cyclic Loading of Bridge #1 (East Span) 191

5.26 Load Versus Deflection Curves During the Cyclic Loading of Bridge #1 (West Span) 192

5.27 Comparison of Instantaneous Deflections During the Cyclic Loading of Bridge #1 (East Span) 193

5.28 Comparison of Instantaneous Deflections During the Cyclic Loading of Bridge #1 (West Span) 194

5.29 Continuity Moments at East Side of Pier During the Cyclic Loading of Bridge #1 195

5.30 Continuity Moments at West Side of Pier During the Cyclic Loading of Bridge #1 196

5.31 Load Versus Deflection Curves During the Cyclic Loading of Bridge #2 (East Span) 197

5.32 Load Versus Deflection Curves During the Cyclic Loading of Bridge #2 (West Span) 198

5.33 Comparison of Instantaneous Deflections During the Cyclic Loading of Bridge #2 (East Span) 199

5.34 Comparison of Instantaneous Deflections During the Cyclic Loading of Bridge #2 (West Span) 200

Figure Page

5.35 Continuity Moments at East Side of Pier During the Cyclic Loading of Bridge #2 201

5.36 Continuity Moments at West Side of Pier During the Cyclic Loading of Bridge #2 202

5.37 Calculation of Failure Loads By Virtual Work 203

5.38 Calculation of AASHTO Moment at Prestressed Section (Bridge #1) 204

5.39 Calculation of AASHTO Moment at Prestressed Section (Bridge #2) 205

5.40 Calculation of AASHTO Moment at Pier (Bridge #1) 206

5.41 Calculation of AASHTO Moment at Pier (Bridge #2) 207

5.42 Moment-Curvature Relationship of Composite Precast Section (Bridge #1) 208

5.43 Moment-Curvature Relationship of Composite Precast Section (Bridge #2) 209

5.44 Moment-Curvature Relationship of Section at Pier (Bridge #1) 210

5.45 Moment-Curvature Relationship of Section at Pier (Bridge #2) 211

5.46 Calculation of Cracking Moment at Prestressed Section (Bridge #1) 212

5.47 Midspan Deflections During the Failure Loading of Bridge #1 (East Span) 213

5.48 Midspan Deflections During the Failure Loading of Bridge #1 (West Span) 214

5.49 Failure of Bridge #1 at the Loading Point in the West Span 215

5.50 Cracks Occurring During the Failure Loading of Bridge #1 (Plan View) 216

5.51 Cracks During the Failure Loading of Bridge #1 (Elevations at Pier) 217

5.52 Cracks During the Failure Loading of Bridge #1 (East Span Elevations) 218

5.53 Cracks During the Failure Loading of Bridge #1 (West Span Elevations) 219

5.54 Calculation of Cracking Moment at Prestressed Section (Bridge #2) 220

Figure Page

5.55 Incremental Strains in Concrete Surface Gages on Bottom of Precast Panels (Bridge #2 - East Span) 221

5.56 Incremental Strains in Concrete Surface Gages on Bottom of Precast Panels (Bridge #2 - West Span) 222

5.57 Incremental Strains in Concrete Surface Gages at Interface (Bridge #2) 223

5.58 Cracks Occurring During the Failure Loading of Bridge #2 (Plan View) 224

5.59 Cracks During the Failure Loading of Bridge #2 (Elevations at Pier) 225

5.60 Cracks During the Failure Loading of Bridge #2 (East Span Elevations) 226

5.61 Cracks During the Failure Loading of Bridge #2 (West Span Elevations) 227

5.62 Midspan Deflections During the Failure Loading of Bridge #2 (East Span) 228

5.63 Midspan Deflections During the Failure Loading of Bridge #2 (West Span) 229

5.64 End Rotations During the Failure Loading of Bridge #2 230

5.65 Comparison of Midspan Deflections with Values Estimated From End Rotations 231

5.66 Failure of Bridge #2 Occurred at the Edge of the Loading Plate 232

5.67 Calculation of Failure Load of Bridge #2 By Virtual Work 233

5.68 Comparison of Negative Moments at Pier with Elastic Moments (Bridge #1) 234

5.69 Comparison of Positive Moments at Loading Point with Elastic Moments (Bridge #1) 235

5.70 Comparison of Negative Moments at Pier with Elastic Moments (Bridge #2) 236

5.71 Comparison of Positive Moments at Loading Point with Elastic Moments (Bridge #2) 237

6.1 Location of Powder Samples Taken After 12 Weeks of Exposure (Bridge #1) 277

6.2 Location of Powder Samples Taken After 24 Weeks of Exposure (Bridge #1) 278

Figure Page

6.3 Location of Powder Samples Taken After 36 Weeks of Exposure (Bridge #1) 279

6.4 Location of Powder Samples Taken After 48 Weeks of Exposure (Bridge #1) 280

6.5 Chloride Concentrations Near Transverse Cracks After 36 Weeks of Exposure 281

6.6 Additional Data From Powder Samples Taken Near Transverse Cracks After 36 Weeks of Exposure (Bridge #1) 282

6.7 Chloride Concentrations Near Transverse Cracks After 48 Weeks of Exposure (Bridge #1) 283

6.8 Additional Data from Powder Samples Taken Near Transverse Cracks After 48 Weeks of Exposure (Bridge #1) 284

6.9 Comparison of Chlorides in Bridge #1 With Data from S.R. 912 Near Gary, IN ...285

6.10 Comparison of Chlorides in Bridge #1 With Data from U.S. 31 in South Bend, IN 286

6.11 Comparison of Chlorides in Bridge #1 With Data from S.R. 7 in Jennings County, IN 287

6.12 Comparison of Chlorides in Bridge #1 With Data from I-70 Over White River in Indianapolis, IN 288

6.13 Comparison of Chlorides in Bridge #1 With Data from I-70 Over Warman Ave. in Indianapolis, IN 289

6.14 Comparison of Chlorides in Bridge #1 With Data from S.R. 29 in Carroll County, IN 290

6.15 Chloride Concentrations for Bridges on S.R. 912, U.S. 31, and S.R. 7 291

6.16 Chloride Concentrations for I-70 Over White River and I-70 Over Warman Avenue 292

6.17 Chloride Concentrations for Bridges on S.R. 29 and S.R. 144 293

6.18 37-Year-Old Bridge on S.R. 144 Near Mooresville, IN 294

6.19 Field Data Collected from S.R. 144 Near Mooresville, IN 295

Figure Page

6.20 Comparison of Chlorides in Bridge #1 With Data from S.R. 144 Near Mooresville, IN 296

6.21 Chloride Concentrations Calculated Using Fick's Diffusion Equation 297

6.22 Results from Rapid Chloride Ion Permeability Testing 298

6.23 Amplitude Spectrums from Impact-Echo Testing of Bridge #1 299

6.24 Corrosion Currents Within the Ponded Region of Bridge #1 300

6.25 Corrosion Currents Outside of the Ponded Region of Bridge #1 301

6.26 Average Chloride Concentrations Taken After 12, 24, 36, and 48 Weeks of Exposure 302

6.27 Variation of Corrosion Currents During the Weekly Exposure Cycle 303

6.28 Half-Cell Potentials Measured Inside of the Ponded Region of Bridge #1 304

6.29 Half-Cell Potentials Measured Outside of the Ponded Region of Bridge #1 305

6.30 Comparison of Measured Half-Cell Potentials of Bridge #1 306

6.31 Equi-potential Contour Map of the Ponded Region of Bridge #1 After 7 Weeks of Exposure 307

6.32 Equi-potential Contour Map of the Ponded Region of Bridge #1 After 48 Weeks of Exposure 308

6.33 AC-Resistances Measured During the 48 Weeks of Exposure Cycling (Bridge #1) 309

6.34 Longitudinal Splitting of Epoxy-Coating Due to Corrosion (A) 310

6.35 Longitudinal Splitting of Epoxy-Coating Due to Corrosion (B) 310

6.36 Corrosion of Epoxy-Coated Bar at Rib Locations 311

6.37 Severe Corrosion and Pitting of Prestressing Strand in Diaphragm 312

6.38 Location of Powder Samples Taken After 12 Weeks (Durability Specimens) 313

Figure Page

6.39 Chloride Concentrations at Holes Located Away from Crack After 12 Weeks of Exposure (Durability Specimens) 314

6.40 Chloride Concentrations at Holes Located Near the Crack After 12 Weeks of Exposure (Durability Specimens) 315

6.41 Location of Powder Samples Taken after 24 Weeks (Durability Specimens) 316

6.42 Chloride Concentrations at Holes Located Away from Crack after 24 Weeks of Exposure (Durability Specimens) 317

6.43 Chloride Concentrations at Holes Located Near the Crack after 24 Weeks of Exposure (Durability Specimens) 318

6.44 Measured Corrosion Currents of Undamaged Epoxy-Coated Bars 319

6.45 Measured Corrosion Currents of Epoxy-Coated Bars With 1/2 % Defects 320

6.46 Measured Corrosion Currents of Epoxy-Coated Bars With 1 % Defects 321

6.47 Measured Corrosion Currents of Epoxy-Coated Bars With 2 % Defects 322

6.48 Measured Corrosion Currents of Epoxy-Coated Bars With 4 % Defects 323

6.49 Measured Corrosion Currents of Epoxy-Coated Bars With 8 % Defects 324

6.50 Measured Corrosion Currents of Black Bars 325

6.51 Severe Pitting of Black Bar After 24 Weeks of Exposure (Specimen C) 326

7.1 Alternate Pier Details 341

CHAPTER 1 - INTRODUCTION

1.1 Background Information

In bridge construction, the reduction of on-site concrete formwork often leads to savings in the total structure cost. For multi-span bridges with 40 ft (12 m) spans or less, the most economical structure is often a continuous reinforced concrete slab without girders.

One alternative to this structure utilizes full-span, precast prestressed concrete panels. These panels, which span adjacent piers, are placed side by side and serve as stay-in-place formwork for a composite cast-in-place (CIP) concrete topping. The full-span, simply-supported panels support their own weight, the weight of the composite topping, and construction loads. The panels act compositely with the CIP topping, and the panel reinforcement serves as the positive moment reinforcement for superimposed loads applied after the topping has hardened. Mild steel reinforcement is placed in the CIP topping over the piers to provide for negative moment in the continuous structure.

The Florida Department of Transportation was a pioneer in the use of full-span form panels in the 1970's. Unfortunately, very regular cracking was observed in the first bridges built with this approach [1]. Longitudinal cracks in the CIP deck were observed over almost every panel joint and usually extended for the full length of the bridge. In

addition, transverse cracking was observed at the negative moment region over the piers. This cracking was attributed to differential shrinkage between the precast panels and CIP topping, as well as traffic loading.

1.2 Objective

In order to eliminate falsework expense and reduce forming costs, the Indiana Department of Transportation (INDOT) would like to use full-span, prestressed concrete panels for many bridges that need replacement. However, INDOT decided that before implementing this system more widely, further research was needed to investigate its behavior when exposed to repeated service loading and severe environments.

INDOT was also concerned about the effects from possible chloride accumulation at the interface between the 5000-6000 psi (34-41 MPa) prestressed concrete panels and the 4000 psi (28 MPa) CIP topping. Chlorides, which are introduced to the bridge deck through the application of de-icing salts, can quickly migrate to the interface through cracks in the CIP topping. It was suspected that a significant accumulation of chlorides at this region could weaken the bond between the two layers of concrete and cause delamination.

The main objective of this study, therefore, was to evaluate the behavior and durability of bridges constructed with full-span, prestressed concrete panels when exposed to repeated loadings and severe bridge deck environments. Behavior of these bridges was assessed by:

(1) Quantifying the flexural stresses at continuous supports due to the restraint of time-dependent effects.

(2) Determining the effects of repeated loading on the continuity at interior piers.

(3) Evaluating the ultimate strength of bridges constructed with full-span, prestressed concrete panels.

Durability of these structures was evaluated by:

(1) Determining the potential for accumulation of chlorides at the interface of the prestressed panels and CIP topping.

(2) Evaluating the resistance of bridges constructed with full-span, prestressed concrete panels to chloride-induced reinforcement corrosion.

1.3 Scope

This study experimentally evaluated the performance of two full-scale specimens in order to model the performance of short-span bridges constructed with full-span prestressed concrete panels subjected to repeated loads and severe environments. The work is presented in the subsequent chapters of this document. Chapter 2 contains a summary of previous research related to this study. A detailed description of the test program is given in chapter 3. Chapter 4 contains the results from the evaluation of time-dependent effects. Chapters 5 and 6 discuss the results from structural testing and durability testing, respectively. Chapter 7 summarizes the results of this study and contains recommendations for implementation of these results and for additional research.

CHAPTER 2 - LITERATURE REVIEW

2.1 Introduction

This chapter describes the previous research pertaining to the use of full-span prestressed concrete form panels for short-span bridges. In addition, the results of a survey of current practices by other state DOTs pertaining to the use of full-span prestressed concrete form panels is presented.

2.2 Previous Studies

2.2.1 Hays, Cox, and Obranic (1980)

Hays, Cox, and Obranic [1] performed extensive numerical and experimental studies on the static behavior of full-span bridges constructed with concrete form panels. These studies included field investigations and testing of existing bridges that had been in service up to 3 years, as well as the testing of half-scale laboratory specimens.

The field investigation portion of this research involved the coring and surface mapping of 9 bridges constructed with full-span form panels. These inspections revealed a consistent pattern of cracking in all bridge decks observed. The cracking included longitudinal "reflective cracking," found over nearly every panel joint, which ran the full length of the panels, as well as transverse cracking at the negative moment regions. While

there appeared to be a correlation between the amount of traffic loading and cracking, one bridge, which was inspected before being opened to traffic loading, already had longitudinal and transverse cracking. Even though pattern cracking was found at all bridges, there were no additional maintenance expenses associated with these decks.

Field corings at panel joints indicated that the longitudinal cracks were directly over the panel joints for bridges using flat panels, and slightly offset from the panel joints for bridges using ribbed panels. It was concluded that the widths of these cracks were small enough to allow shear transfer to take place across the cracks. Corings at the piers revealed that the ends of the precast panels were not well bonded to the CIP topping. This was believed to be due to the smooth surface of the panel ends, and aggravated by the lack of positive moment reinforcement at the pier.

Finite element studies were performed to determine the magnitude of stresses introduced by the shrinkage of the CIP concrete and restraint of shrinkage by the prestressed panels. These studies showed that the stresses developed due to shrinkage alone were large enough to cause the observed longitudinal cracking above the precast panel joints.

Laboratory tests were made on three two-span specimens, each consisting of four form panels (two per span) and loaded eccentrically at midspan. The span length and precast panel dimensions were approximately 1/2 scale. The major variables in the test were the percentages of steel used in the prestressed panels and CIP topping, and the shape of the panel cross-sections (rectangular or inverted T-shaped slabs). The surfaces

of the form panels were given a broom finish. In one specimen, a cold-joint in the CIP topping was created above the precast panel joint to simulate a longitudinal crack.

In spite of the loading eccentricity, which the authors believed to be more severe than in actual bridges, all three laboratory specimens developed strengths in excess of that predicted by limit analysis considering full width of the specimens at sections of positive and negative moment. Also, good ductility was exhibited by all specimens, and no problems were observed with the bond of the panels to the CIP topping.

Field testing was also performed on an eight-span, form-panel bridge, in which load was applied to the bridge by a hydraulic jack pressing against a truck frame. Deflection profiles from this field test showed that load was indeed transferred across the longitudinal panel joints. Differential deflections across a longitudinal joint were in all cases less than 6 percent of the total joint deflection under a loading equal to 1 1/2 times the design service wheel load including impact. The load versus deflection curves also showed an increase of stiffness with an increase in load. This was attributed to the observed cracking at the interface of the panel ends and the CIP topping over the pier.

Based on the field observations, corings, laboratory testing and numerical analyses, the authors made the following conclusions and recommendations:

- Excellent bond between the precast panels and CIP topping can be achieved by applying a broom finish to the panels and by wetting the panels prior to placing the CIP topping. A minimum amount of horizontal shear reinforcement could be specified to protect against possible contamination of the panel surface (oil spills, dirt, etc.).

- The AASHTO effective width formula for a one-way slab ($E = 4 + 0.06S \leq 7.0$ ft.), where "E" is the effective width in feet and "S" is the span length in feet, is adequate for determining the design longitudinal moments due to live load.
- A minimum panel width of 4 feet should be used. Although panels with smaller widths and designed using the effective width formula would have adequate ultimate strength, such panels might be highly overstressed under moderate overload.
- A minimum transverse reinforcement of #4 bars @ 12 inches in the CIP slab and a minimum CIP slab thickness of 4 1/2 inches are adequate to provide load transfer between adjacent panels. However, for improved resistance to longitudinal cracking above panel joints, the authors recommended the detail shown in figure 2.1.
- An improved detail over piers and at end abutments is needed. This should include either shear keys in the panel ends or provision for direct bearing of the panels on the CIP concrete at the supports. In addition, positive moment reinforcement at the piers should be used to reduce separation of the CIP concrete from the panel ends.

2.2.2 Buckner and Turner (1981)

Buckner and Turner [2] investigated the effects of repeated loading on the serviceability and strength of composite panel-form bridge decks. Six single span, simply-supported composite specimens were fabricated and tested. Each specimen had an overall thickness of 13 inches and utilized 3 prestressed form panels. The variables tested in this study were the depths of the prestressed panels and CIP topping, the geometry of the panels (flat or beveled edges), and the amount of transverse reinforcement. The top

surface and beveled edges of the panels were raked transversely with metal tines to depths of approximately 1/8 inch. All lifting loops in the panels were cut off prior to casting the CIP topping to eliminate all mechanical shear connections between the panels and CIP topping.

Each specimen was subjected to 2 million cycles of loading, applied at midspan, before a final monotonic loading to failure. An upper load level of 41.6 kips represented a HS20-44 design axle load of 32 kips with a 1.3 impact factor. A lower load level of 3 kips was used to prevent separation between the actuator and loading beams. Intermediate static tests were performed after every 500,000 cycles of loading. For all six specimens, the experimentally determined failure moment exceeded the computed moment capacity.

The authors made the following conclusions based on the results from these tests:

- The composite deck can withstand 2 million cycles of design load without significant loss of serviceability or strength.
- Adequate composite action is obtained by roughening the interface surfaces of the precast panels and by water-blasting this surface immediately prior to placing the topping slab.
- Adequate serviceability and strength can be obtained using flat precast panels rather than more expensive beveled-edge panels.
- There is no indication that thickness of the topping slab relative to the total thickness affects the fatigue strength of the composite deck up to 2 million cycles.
- For HS20-44 live loads, adequate shear transfer is provided by a 5-inch topping slab reinforced transversely with #4 grade 60 rebars spaced 12 inches on center. This shear

transfer is available even when a longitudinal crack exists in the topping slab over the panel.

2.3 Practices by Other DOTs

Federal Highway Administration (FHWA) Regional Bridge Engineers were contacted and asked about current practices pertaining to full-span prestressed concrete form panels. None of the regional engineers contacted was aware of state DOTs that still used full-span composite panels. Bridge Engineers in Regions 3 (DE, DC, MD, PA, VA, WV), 4 (AL, FL, GA, KY, MS, NC, SC, TN), 6 (AR, LA, OK, NM, TX), and 10 (AK, ID, OR, WA) said that full-span, full-depth precast panels were being used for short-span bridges. These panels typically have keyways along the longitudinal edges which are filled with grout after the panels are placed side-by-side. Shear transfer between adjacent panels is then ensured by transverse post-tensioning after the grout has cured. Regions 4 and 10 use both solid panels and voided (or hollowcore) slabs.

2.4 Summary of Related Research

Previous research pertaining to short span bridges constructed with full-span precast prestressed panels has shown that stresses due to shrinkage of the CIP concrete are sufficient to cause longitudinal and transverse cracking of the decks. The effect of these cracks on durability, after long-term exposure of the decks to severe environments, was uncertain. Previous research included monotonic loadings of two-span bridges, and cyclic loadings of single span specimens. The current investigation extends this research

to determine the performance of multi-span bridges, utilizing full-span precast prestressed panels, when exposed to cyclic loading and extreme environmental conditions. Chapter 3 describes the experimental program in detail.

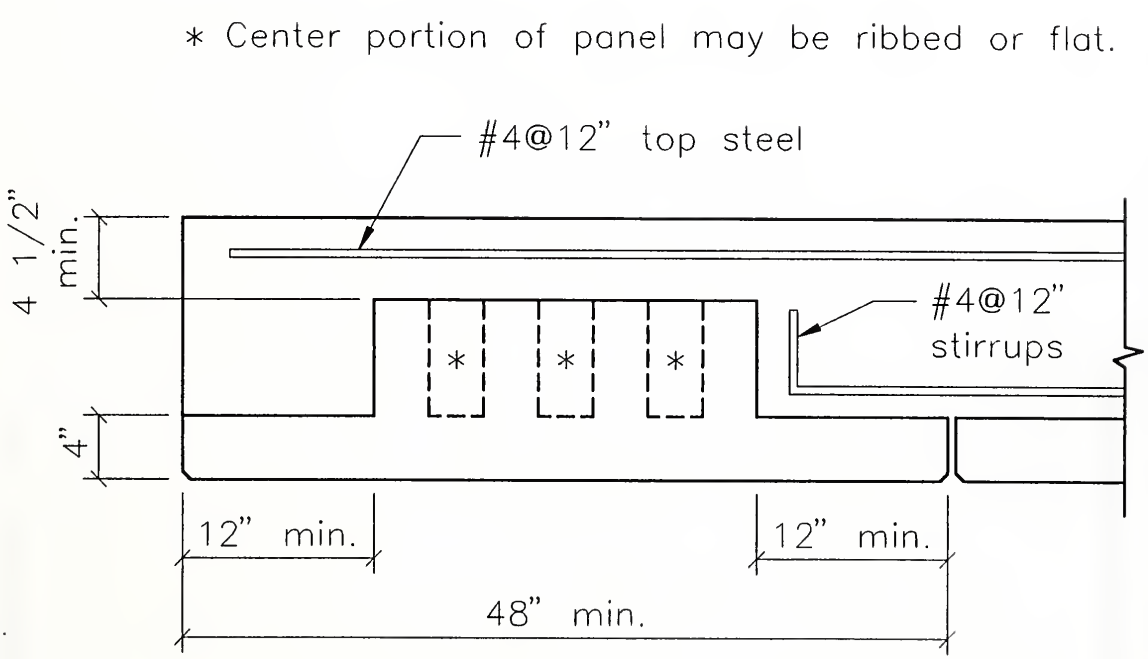

Figure 2.1 Detail Proposed by Hays, Cox, and Obranic [1]

CHAPTER 3 - EXPERIMENTAL PROGRAM

3.1 Test Setup

To evaluate the behavior in regard to durability and strength of bridges constructed with full-span, prestressed concrete panels, two bridges, each with two spans, were fabricated and tested in the Karl H. Kettelhut Structural Laboratory at Purdue University. Each span of a bridge consisted of two prestressed concrete form panels measuring 21 ft long, 4 ft wide, and 6-in thick (6.4 m x 1.2 m x 150 mm), topped with a 6 inch (150 mm) thick composite CIP slab. Figure 3.1 shows the geometric characteristics of the test setup. Continuity between precast panels in adjacent spans was achieved by extending the strands out of the panel ends and anchoring them in a diaphragm cast at the time of the CIP slab (see Figure 3.2). Composite action between the precast concrete form panels and CIP topping was attained by applying a rake finish on the top surface of the form panels.

3.2 Test Specimens

Table 3.1 shows the differences in reinforcement of the two test bridges. The prestressed panels in Bridge #1 contained (8) - 1/2" special uncoated low-relaxation strands, while the panels in Bridge #2 contained four such strands. Each strand had an area of 0.167 in^2 (108 mm^2) and a minimum ultimate stress of 270 ksi (1860 MPa). This

corresponds to a reinforcement ratio, ρ_p, of 0.0027 for Bridge #1 and 0.0014 for Bridge #2. The higher ratio represents an average value which could be expected in this type of structure, while the lower ratio is based on a practical minimum number of strands per panel. For both bridges, the reinforcement in the CIP topping over the pier was approximately equal to the minimum amount of 200/fy. Bridge #1 contained (16) - #4 bars at the pier with a reinforcement ratio, ρ, equal to 0.0036. Bridge #2 had (6) - #6 bars at the pier with $\rho = 0.0030$. Longitudinal bars were also placed in the CIP topping elsewhere for shrinkage and temperature control. These consisted of #4 bars at 16-inch spacings. Figure 3.3 shows a cross-sectional view of the test bridges. In addition to the longitudinal steel, transverse mild steel was used in both the prestressed panels and CIP topping. #4 bars at 18-inch spacings were used in the prestressed panels for shrinkage and temperature control (see Figure 3.4). #4 epoxy-coated bars at 12-inch spacings were used in the CIP slab as recommended by Buckner and Turner [2] (see Figure 3.5).

3.2.1 Fabrication of Precast Slabs

The prestressed panels for this study were cast at Hydro Conduit Corporation's prestressed concrete plant in Lafayette, IN. The four panels for each bridge were cast simultaneously in one prestressing bed, separated by wooden header blocks. The panels were given a raked finish using a rake with tines at one inch on center. The depth of the rake depressions was approximately 1/4 inch (see Figure 3.6). Each panel also had (4) - #4 bent bars extending out of the surface at lifting locations. These provided the only mechanical shear connections between the precast panels and CIP concrete slab in the

composite structure. The four prestressed panels for bridge #1 were cast on 10/26/93, while the panels for Bridge #2 were cast on 10/18/94.

3.2.2 Fabrication of Composite Test Bridges

After the panels were allowed to cure they were shipped to the Karl H. Kettelhut Structures Laboratory at Purdue University. The panels were then moved onto the simulated bridge piers in the laboratory and placed on supports consisting of plates and rollers. The supports at the center pier modeled pin connections, while the supports at discontinuous ends represented roller connections. Formwork was then built to contain the wet CIP concrete topping. The formwork was anchored to the panels using Hilti Quickcon Anchors. The top of the formwork was set at an elevation which provided for a minimum topping thickness of 6 inches. Because of camber of the panels, the topping was 6 inches thick at midspan and thicker near the piers. Epoxy-coated bars were then placed on top of stainless steel bar chairs which sat on the surface of the panels (see Figure 3.7). The epoxy-coated bars had a clear cover of at least 2 1/2 inches as specified by AASHTO [3] (2" + 1/2" wearing surface). Before the topping was cast, the surfaces of the panels were cleaned using a high-pressure air hose. Approximately 15 minutes before the topping was cast, the surfaces of the panels were sprayed with a water hose and all standing water was dissipated using an air hose. This was done to prevent wicking of moisture from the fresh concrete. Because of the location of the test setup, the CIP concrete had to be pumped. Placement of this concrete took about 1 1/2 hours for each bridge. The top surface of the concrete was given a smooth finish in order to facilitate the

detection of cracks. However, the region over the center pier of Bridge #1 was given a raked finish similar to that specified by INDOT for all new bridges (see Figure 3.8). This is the area which was later subjected to durability exposure cycling. The CIP slab for Bridge #1 was cast on 3/28/94; the slab for bridge #2 was cast on 12/11/95.

3.3 Loading

After the CIP topping had cured for 50 days (Bridge #1) and 44 days (Bridge #2), each bridge was subjected to 5 million cycles of service loading by two hydraulic actuators (one per span). The actuators were located at a distance of 8'-3" (2.51 m) from the center of the middle pier and were centered over the precast panel joints. This location was close to the loading point which produced the maximum negative moment over the center pier. Load was applied to the deck through 1/2" thick neoprene bearing pads measuring 10" x 13" in area, simulating a tire footprint as in the study by Buckner and Turner [1]. The loads were applied at a frequency of 1 1/2 Hz. and produced a maximum stress of 44 ksi in the reinforcement over the center pier with a stress range of 18 ksi. These stresses are slightly larger than the AASHTO maximum design service loads and are believed to represent the extreme case of repeated overloads. The load ranges were from 4500 lbs. to 20,800 lbs. for Bridge #1 and from 6900 lbs. to 20,000 lbs. for Bridge #2. These loads were estimated from moment-curvature relationships computed for the composite structure and were verified by strain gage measurements. In order to take measurements, static loadings were performed prior to, and periodically throughout, the 5 million cycles of loading. A detailed description of these measurements is given in section 3.5.

After the 5 million loading cycles had been applied, the bridge was loaded to failure using the same hydraulic actuators. For this part of the research, the load in each span was applied to the deck surface through a 24" x 24" bearing pad to prevent a punching-shear failure at the loading point. Measurements were taken at even load increments through the point of failure.

3.4 Durability Cycling and Testing

In addition to the loadings above, a portion of Bridge #1 was subjected to 48 weeks of southern exposure cycling. This weekly cycle consisted of 4 days of exposure to a 15% sodium chloride solution followed by 3 days of drying at a minimum of 100° F (38° C). The area subjected was the negative moment region over the center support. This portion of concrete decks typically has transverse cracking at the surface and is believed to be the most critical to long-term performance. This was also the area of the bridge deck given a raked finish as described in section 3.2.2. The exposure cycling of Bridge #1 began after 2 million cycles of service loading had been applied to ensure that crack patterns had been fully established.

To contain the sodium chloride solution, a 2 1/2" high barrier was constructed on the surface of the bridge deck using plastic angles, wood, and silicone caulk. The barriers were secured to the deck by stainless steel Quickcon anchors. The sodium chloride solution was mixed in a specially designed 55-gallon (208-liter) plastic barrel with an attached motor and stainless steel paddle. The solution was then pumped on and off the bridge on the appropriate days (see Figures 3.9 and 3.10).

After the sodium chloride solution was pumped from the deck, any remaining solution was removed with a vacuum cleaner. Then, the surface was cleaned by two successive rinses of tap water that filled the pond above the previous level of the sodium chloride solution. Following the removal of the tap water by pumping, the deck surface was again vacuumed and allowed to dry. Heat was then applied to the deck surface to raise the concrete temperature above 100° F (38° C). This was done using halogen lamps. An aluminum grid containing (32) - 500-watt quartz halogen lights was suspended above the deck from a crane. During the drying phase of the exposure cycle, the grid was lowered to within 4 ft (1.2 m) of the deck and supplied near-uniform heat to the bridge (see Figure 3.11).

The purpose of the exposure cycling was to determine the potential for chloride accumulation at the interface and to evaluate the resistance to reinforcement corrosion. The potential for chloride accumulation was evaluated primarily by extracting powder samples from the bridge and testing for chloride ion content. The resistance to reinforcement corrosion was assessed by taking weekly measurements during the drying phase of the cycle. These measurements included half-cell potentials, AC-resistance, and corrosion currents.

3.4.1 Chloride Ion Powder Samples

Chloride ion powder samples were extracted from Bridge #1 after every 12 weeks of ponding. This process consisted of drilling into the bridge deck with a hammer drill and collecting the concrete powder at 1/2" increments. The holes were drilled at least 7 inches

(180 mm) deep, extending past the interface and into the prestressed panels. The concrete powder was taken to INDOT's Materials and Testing Facility in Indianapolis, IN, where it was tested for total chloride ion content using the AASHTO Standard Test T 260 procedure.

3.4.2 Corrosion of Reinforcement in Concrete

Reinforcing steel corrodes in concrete by the formation of electrochemical cells, called galvanic cells. Galvanic cells can be formed in many ways, but to be operative, all require the presence of (1) an electrolyte (a solution containing dissolved ions which conduct electricity); and (2) two electrodes (electrically connected metal surfaces which have different electrical potentials with respect to the electrolyte in contact with them).

In reinforced concrete, the electrode is supplied by pore water and the differences in electrical potential are set up by temperature differentials or by variations in the concentrations of moisture, oxygen, or dissolved ions at the surface of the bars [4]. Corrosion begins as a current flow is established between the two electrodes. The electrode at which metal tends to go into solution as positively charged ions, simultaneously developing a corresponding negative charge, is called the anode. The principal chemical reaction at the anode may be written:

$$\underset{\text{(iron)}}{Fe} \rightarrow \underset{\substack{\text{iron ions} \\ \text{in solution}}}{Fe^{++}} + \underset{\text{two electrons}}{2e^{-}}$$

The iron ions then react with water and oxygen to form rust. The electrolyte to which the electrons from the anode flow, and at which other various chemical reactions involving

oxygen occur, is called the cathode. Electron current flows from the anode to the cathode through the electrical interconnection between the two, and then back to the anode through the electrolyte (as charged ions) to complete the circuit.

3.4.3 The Role of Chlorides in Reinforcement Corrosion

Concrete will normally provide a natural protective barrier against the corrosion of reinforcing steel. Its high alkalinity (pH $\approx$ 13.5 to 13.8) quickly causes the formation of a film of ferric oxide on the surface of the steel which acts as a barrier against corrosion [5]. Laboratory studies have indicated that steel will remain passive in alkaline solutions having a pH in excess of 11.5 [6]. The presence of chloride ions in high concentrations, however, can reduce or destroy this protective mechanism offered by the concrete and enable the steel to corrode. The concentration of chloride ions required to initiate corrosion of the reinforcing steel is often called the "threshold value." The threshold value was determined in research carried out by the FHWA [7, 8] to be 0.2% by weight of the cement content of the concrete. For a typical bridge deck concrete (6 1/2 bags of cement per cubic yard or 363 kg/m^3), the threshold value is 1.2 lb/yd^3 (0.73 kg/m^3) [6].

3.4.4 Half-Cell Potentials

As described earlier, corrosion proceeds as current flows between two electrodes having different electrical potentials. This difference, or voltage, between the anode and

cathode may be measured using a voltmeter. However, the difference in measured voltage between the two unstable electrodes (or half cells*) is not meaningful because the electrical activity will change as the electrolyte changes. Therefore, to compare readings on a standard scale over a period of time, a standard reference half cell that remains at a constant electrical potential must be used [9].

The reference electrode most commonly used to measure the electrical activity of steel in concrete is the copper-copper sulfate half cell. It consists of a copper rod suspended in a saturated copper sulfate solution contained in a plastic tube with a porous end plug. The copper rod is stable in the solution and its potential remains constant regardless of changing conditions. Therefore, the copper rod represents a half cell of constant electrical potential (-0.316 V at 72° F (22.2° C) as referenced to the hydrogen electrode).

The electrical potential of reinforcing steel embedded in concrete is compared to that of the copper rod by connecting the two metals. This is done by making a positive connection to the top mat of reinforcing steel and by providing a moisture connection through the concrete between the copper rod and the reinforcing steel at the point where the potential value is determined [9]. A voltmeter is then placed in the circuit to measure the potential difference (see Figure 3.12). The potentials for uncoated bars are interpreted according to the following empirical guidelines [10]:

* Each electrode is sometimes referred to as a "half cell" since it is 1/2 of the galvanic cell.

- If potentials over an area are more positive than -0.20 V, there is a greater than 90% probability that no reinforcing steel corrosion is occurring in that area.

- If potentials over an area are in the range of -0.20 V to -0.35 V, corrosion activity of reinforcing steel in that area is uncertain.

- If potentials over an area are more negative than -0.35 V, there is a greater than 90% probability that reinforcing steel corrosion is occurring in that area.

Half-cell measurements on Bridge #1 were taken both inside and outside the ponded area throughout the 48 weeks of exposure cycling. A 3 ft x 3 ft grid was established within the ponded area and grid points were marked on the surface of the bridge where the weekly measurements were taken. Figure 3.13 shows the location of these points. Half-cell measurements were also taken at intermediate points periodically throughout the test. These readings were used to create Equi-potential contour maps (contour maps with lines connecting points of equal potential). Equi-potential contour maps are used to identify areas of relative corrosion activity.

In order to take half-cell potentials for Bridge #1, electrical connections were made to the epoxy-coated reinforcement prior to casting the composite topping. This consisted of removing the epoxy coating at selected areas of the bars and connecting wires to the exposed steel using hose clamps.

The half-cell survey is sensitive to continuity, and it is desirable that all reinforcement within a given equi-potential map be electrically continuous. Theoretically, when epoxy-coated reinforcing steel is used, every bar is electrically isolated. However, some tests on existing structures with epoxy-coated rebar show continuity between 40% to 80% of the bars [11]. For Bridge #1, electrical interconnection between several epoxy-coated bars was ensured by removing the epoxy coating at the points of intersection and securing the connection with plastic cable ties. There were 3 sets of 4 interconnected bars which formed rectangular areas (see Figure 3.14). These interconnected "grids" were then used to measure half-cell potentials in their corresponding vicinities.

3.4.5 Measured Corrosion Current

Macrocell corrosion currents between the epoxy-coated bars in the CIP slab and the uncoated steel in the prestressed panels were monitored weekly during the exposure cycling. This was done by measuring the voltage drop across a 100Ω resistor placed between wires connected to the epoxy-coated steel and wires connected to the uncoated rebar and strands in the panels. Figure 3.15 illustrates this procedure. The wires connected to the epoxy-coated bars were the same as those used to take the half-cell potential readings. Wire connections to the panel reinforcement were secured with hose clamps prior to casting the panels. Voltage drops across the resistors were measured at the end of the drying phase of the weekly cycle. Corrosion currents were then calculated

by Ohm's Law. With the voltmeter "common" connected to the panel reinforcement, negative voltages correspond to positive galvanic current (that is, the epoxy-coated bars are anodes) [12].

3.4.6 AC-Resistance

The electrical resistance between the epoxy-coated bars in the topping and the uncoated reinforcement in the panels was also measured using an AC-resistance meter. This was also done weekly using the same wires utilized in the corrosion current measurements. These "mat-to-mat" resistance readings were used to gain additional insight into the corrosion measurements. Initial resistance measurements give a good indication about the amount of defects (holidays) in the epoxy coating at the start of the test. Changes in the resistance are then attributed to either changes in the concrete resistivity or additional defects in the epoxy coating.

3.4.7 Condition of Epoxy-Coated Reinforcement

The original condition of the epoxy-coated bars in Bridge #1 was evaluated by checking (10) - 15 ft (4.57 m) long bars for holidays after they arrived at the structures laboratory. These bars had an average of 1.4 holidays per foot with a maximum of 3.1 holidays per foot. These numbers are believed to be reasonable since current AASHTO

Specifications permit up to 2 holidays per foot by the manufacturer (prior to shipping and handling) [13].

After exposure cycling and loading to failure, the epoxy-coated rebars in Bridge #1 were examined for evidence of corrosion. The bridge area inspected included the ponded region at the diaphragm, where half-cell potentials indicated most severe corrosion. Reinforcing steel was extracted from the deck using a small air hammer after saw cuts were made between adjacent longitudinal bars.

3.4.8 Rapid Determination of Chloride Permeability of Concrete

Another test was conducted relating to determine chloride permeability of the concrete using the AASHTO Standard Test T 277 [14]. This procedure involves monitoring the electrical current passing through a 2-inch (51 mm) thick slice of a 4-inch (102 mm) diameter concrete core over a period of six hours, during which 60 volts DC are applied across its length. During the test, the original top surface of the concrete is maintained in a 3% sodium chloride solution and chloride ions in solution are forced to migrate through the concrete by the applied voltage. The current is recorded every 30 minutes during the 6-hour test and plotted as a function of time. The area under the curve is the total charge passed through the concrete, in coulombs, and has been correlated with permeability results from 90-day ponding tests [15].

Several 4-inch (102 mm) diameter cores were extracted from both test bridges to evaluate the permeability of the in-place concrete. This information was particularly valuable for Bridge #1 with respect to the concern about chloride accumulation at the interface resulting from a less permeable prestressed concrete. Also, for Bridge #2, a new low-shrinkage concrete mix was used for the CIP topping and resulting permeabilities were of interest.

3.4.9 Additional Durability Specimens

In addition to the durability testing of Bridge #1, five 3 ft x 3 ft (0.91 m x 0.91 m) composite durability specimens were fabricated and tested. The bottom panels for these specimens were 6 inches (152 mm) thick and were cast in the same prestressing bed and at the same time as the panels for Bridge #2. Uncoated mild reinforcing steel and strands were used in the bottom panels (see Figure 3.16). The top CIP concrete was also 6 inches (152 mm) thick and consisted of a "Class C" concrete mix as per INDOT designation. The CIP concrete was given a raked finish similar to that used in the ponded region of Bridge #1.

The CIP portions, which contained epoxy-coated reinforcement having a 1-inch (25 mm) clear cover, were cast with an initial "crack" extending through the entire topping thickness (see Figure 3.17). These cracks were formed using a piece of corrugated cardboard with corrugations aligned to allow liquid penetration in the vertical

direction. These specimens, after being subjected to weekly exposure cycling, gave additional data about the potential for chloride accumulation at the interface.

Another aspect of these smaller durability specimens is that they contained epoxy-coated reinforcing bars with varying numbers of defects. Each specimen had #4 bars with 0.5%, 1%, 2%, 4%, and 8% damage as well as an uncoated bar and a bar "as delivered" and used in Bridge #1. Percent damage was based on 3/8-inch (9.5 mm) wide defects. The perimeter of a #4 bar is 1.57 inches (40 mm). With a 36-inch (0.91 m) length of bar embedded in the concrete, the total embedded surface area of a bar is then 56.5 in^2 (365 cm^2). Therefore, a bar with 0.5% damage will have 0.28 in^2 (1.82 cm^2) of damage. This is approximately equal to a 3/4 in x 3/8 in (19 mm x 9.5 mm) wide defect. These appropriate areas were marked on the bars, and the epoxy coating was removed using a Dremel hand-held rotary tool with a sanding attachment. It is important to note that only the epoxy coating at ribbed locations within the marked areas was removed in order to reflect typical damage which would occur in the field by dragging or mishandling bars (see Figure 3.18). Therefore, "percent damage" as described herein is always much larger than the actual percentage of steel area exposed.

Figure 3.19 shows the sizes and locations of damaged areas of the epoxy-coated bars contained in each of the five specimens. The maximum length of defect was held to 1 1/2 inches (38 mm). Therefore, bars with higher percentages of damage have multiple areas of defects located on all sides of the bars. The areas shown in Figure 3.19 are

believed to be the only locations on these epoxy-coated bars which contain damage. Prior to damaging the coating, all bars were given two extra coats of 3M brand epoxy touch-up paint to ensure against additional defects. Figure 3.20 shows the relative bar positions as well as the locations of the defects with respect to the pre-formed crack.

These specimens are being used to gain additional understanding about the potential for chloride accumulation, as well as the importance of epoxy-coating defect sizes on the long-term corrosion resistance of the bars. Therefore, it is anticipated that testing of these specimens will continue long after the conclusion of this study. The CIP composite topping of these specimens was cast on 4/28/95 and weekly exposure cycling began on 9/14/95. Chloride ion powder samples were taken after every 12 weeks of exposure. Half-cell potentials, macrocell corrosion currents, and AC-resistance readings were taken weekly during the drying phase of the cycling. These specimens contained a series of electrical switches which allowed each bar in the topping to be electrically isolated from all other bars to monitor the response of that particular bar (see Figure 3.21). Electrical connections to the reinforcement in these specimens was made by attaching wires to the portion of the bars which extended out of the concrete. Connections to the prestressing strands were made using hose clamps. Connections to the bars in the topping were made by drilling and tapping a hole in each bar. Stainless steel screws were then used to secure the wires to the bars. Figure 3.22 shows the measurement grid used when recording weekly half-cell potentials, which were measured

with respect to the uncoated (black) bar, the "as delivered" bar, and the bar with 8% defects.

3.5 Instrumentation

Throughout this study, numerous measurements of the response of the two test bridges when subjected to structural loading were recorded. A full description of these measurements, and the instrumentation and procedures used to obtain them are included in this section.

3.5.1 Strain Measurements with Electrical Resistance Gages

Electrical resistance strain gages were used to measure strains in concrete and steel in both bridge specimens. All strain gages used in this study were manufactured by Micro-Measurements (a division of Measurements Group, Inc.). Strains in the prestressed strands were measured using EA-06-062DN-350 type gages, having a gage length of 1/16 inch (1.6 mm). Strain gages were installed on a single wire of the 7-wire prestressed strand. Twelve strain gages were installed on the strands in each prestressed panel. The locations were the same for each test bridge and are shown in Figure 3.23. Strain gages were installed on the strands after they were stressed to 5000 pounds (22.24 kN). Following the installation of strain gages, the strands were pulled to 33,820 pounds (150.43 kN) and the concrete was cast. In addition to the strain gages on the strands, two

gages (type EA-06-20CBW-120) were installed on the top surface of each prestressed panel at midspan after the concrete had cured for 3 days, but prior to stripping the forms and transfer of prestress. Small areas of the top surface were given a smooth finish to accommodate the installation of these gages, which had a gage length of 2 inches (51 mm). Additional surface gages were installed on the underside of the precast panels after they were moved to Purdue University and placed on the simulated bridge piers, but prior to casting the composite topping. The locations of these bottom surface gages are shown in Figure 3.24.

Strain gages were also installed on the epoxy-coated reinforcing in the CIP topping. To do this, the ribs of the bars at the location of the gages were removed by sanding with a 1-inch (25 mm) wide air-powered belt sander. Load tests on bars with and without these sanded areas revealed that the reduction of the bar area due to sanding was minimal (the average tensile capacity of the sanded bars was more than 99% of the original tensile capacity for both the #4 and #6 bars). Strain gages (type CEA-06-125UN-350) with a gage length of 1/8 inch (3.2 mm) were placed on negative moment reinforcement at the center support, as well as on the longitudinal shrinkage and temperature reinforcement at midspan. Figures 3.25 and 3.26 show the locations of these strain gages in Bridge #1 and Bridge #2, respectively. Strain gages of the same type were also installed on the transverse #4 bars over the panel joint near the actuator. The locations of these gages for both bridges is shown in Figure 3.27. Surface strain gages

were also installed near midspan on CIP concrete prior to beginning the cyclic loading. Their locations are shown in Figure 3.28.

All electrical resistance strain gages were installed using adhesives and protective coatings manufactured by Micro Measurements. M-Bond 200 adhesive was used to apply all strain gages. Prior to applying the surface gages, a thin layer of M-Bond AE-10 epoxy was spread on the concrete to fill all pores. After soldering wires to the gages, special protective coatings were applied to prevent moisture and mechanical damage. Moisture barriers consisted of applications of Micro-crystalline wax and M-Coat J. A final wrap of duct tape was used to prevent any mechanical damage as the concrete was poured.

3.5.2 End Reactions

The discontinuous end reactions of each bridge were monitored throughout the testing using load cells. Two load cells were placed at each end (one per panel) underneath a spreader beam assembly (see Figure 3.29). The load cells were used to determine the internal moments of the two-span, statically-indeterminate structure. Load cell readings were monitored throughout the cure period of the CIP top slab to study the combined effects of creep and shrinkage. Load cell readings were also recorded during the cyclic loading phase of the project, as well as during the final loading to failure. During these loadings, the reactions at the center pier due to the applied load were

calculated by subtracting the additional end reaction in each span from the total applied load in that span.

3.5.3 Deflections

For Bridge #1, deflections of the composite structure were measured using six LVDT's, three located at the midpoint of each span. These LVDT's were placed at the two edges of the bridge and at center of the bridge over the panel joint (see Figure 3.30). Deflection measurements were taken during the cyclic loading period and during the final monotonic loading to failure.

For Bridge #2, deflections of the prestressed panels because of the weight of the topping were measured using both LVDT's and dial gages. LVDT's were placed below the center of each prestressed panel and recordings were taken prior to casting the composite slab. Dial gages were also placed at 2 ½-ft (0.76 m) spacings along the south face of each span and used to measure deflections due to the weight of the topping. In addition, the LVDT's and dial gages were monitored throughout the entire cure period of the topping. The dial gages were also used to record deflections during the cyclic loadings and during the failure loading. Midspan deflections were measured for Bridge #2 during both the cyclic load phase and final loading phase as done for Bridge #1. Deflections of Bridge #2 at the point load were also measured using LVDT's during the final loading to failure.

3.5.4 Differential Deflection Measurements

Differential deflections between the two prestressed panels were measured for each bridge during the final loading to failure. These measurements were taken using an electronic dial gage secured to the bottom of one panel, which measured the change in distance to the bottom of the adjacent panel (see Figure 3.31).

3.5.5 Strand Slip Gages

Prestressing strand slip was measured at the discontinuous ends of the bridge by attaching dial gages to the strands which extended out of the panels (see Figure 3.32). The dial gages were monitored throughout the cyclic loading and as the bridge was loaded to failure.

3.5.6 Crack Width Measurements

The width of cracks at the surface of the concrete in the negative moment region were recorded during the cyclic loading phase and during the failure loading. Crack widths were measured using both an optical measuring scale (see Figure 3.33) with a resolution of .001 inch (.025 mm) and a crack comparator.

3.5.7 Strain Measurements With a Whittemore Gage

Strains in the concrete at the center pier of Bridge #2 were also measured using a Whittemore Strain Gage having a gage length of 10 inches (254 mm). Special stainless steel pieces with small bored holes were fastened to the concrete using a rapid-set epoxy. These pieces were secured in horizontal rows of four points, spaced at roughly 10-inch intervals (see Figure 3.34). The locations of the points were the following: On the top surface of the CIP concrete; at the level of the epoxy-coated steel; 1 inch above the interface; 1 inch below the interface; at the level of the prestressing steel. The Whittemore points were attached after the 96 hours of moist curing of the CIP slab.

Initial readings were taken after all points had been secured. Additional readings were then taken at regular intervals throughout the cure period, during the cyclic loading of the bridge, and during the final loading to failure. The Whittemore gage had a precision of 0.0001 inches.

3.5.8 End Rotation Measurements

End rotations of Bridge #2 were determined during the failure loading. This was accomplished by welding a steel bar to the bearing plate at each end of the bridge and measuring the deflection of each bar at distances of 15 inches on both sides of the center of bearing (see Figure 3.35). The end rotation (in radians) was then determined by dividing the total deflection (downward deflection on one side plus upward deflection on the other side) by 30 inches.

3.5.9 Impact-Echo

Impact-echo tests were performed on Bridge #1 after the 5 million cycles of load and 48 weeks of exposure cycling. Impact-echo is a non-destructive test procedure which relies on the interpretation of surface displacements caused by resonating compression waves (P-waves). A stress pulse is introduced into the concrete by mechanical impact at the surface. Its waves propagate into the structure and are reflected by internal flaws or interfaces and by external boundaries. The waves are then reflected at the free surface and propagate back into the structure to be reflected again at interfaces and boundaries. A transient resonance condition is established by the reflection of the waves between the surface and internal defects or external boundaries. A displacement transducer located at the surface of the concrete monitors the arrival of the reflected waves.

The frequency of the wave arrivals is determined by transforming the recorded time-domain signal into the frequency domain using the fast Fourier transform technique [16]. Dominant frequencies show up as peaks in the resulting amplitude spectrum. For a solid plate, one large amplitude peak exists at a frequency, f, corresponding to reflections between the top surface and bottom surface (or defect if one exists). If the P-wave speed, C_p, is known, then the depth, d, to an internal defect or bottom surface can be calculated as:

$$d = \frac{C_p}{2f} \tag{3.1}$$

For Bridge #1, the P-wave speed was calculated by taking readings (determining wave arrival frequencies) outside the ponded area at several areas having a known thickness. These readings showed the wave speed to vary between 12,500 to 13,100 ft per second (3800 to 4000 m/s). Areas of delaminations within the ponded region could be detected by monitoring the wave arrival frequencies. An increase in the dominant frequency indicates P-waves are being reflected at a depth less than the through-thickness (i.e. at an internal void or delamination). With the wave speed known, the depth of the delamination could then be calculated. Figure 3.36 shows impact-echo tests being performed on Bridge #1. The impact-echo tests were performed by Dr. Randall W. Poston of Whitlock, Dalrymple, Poston & Associates, Inc. Impact-echo tests were performed at various places within the ponded region prior to the final loading, at loads of 55, 100, and 120 kips, and after failure.

3.6 Material Properties

The physical properties of the concrete and steel reinforcement used in this study were tested and documented. This section contains the results from these tests, as well as the concrete mix designs used.

3.6.1 Prestressed Concrete

The concrete used in the prestressed panels of both bridges was batched at the prestressed plant. The mix design used was the standard (6.9 bag) mix used for other bridge beams poured at that plant and had the following batch weights per cubic yard:

Type III Cement	649 lbs
Sand	1415 lbs
Gravel	1655 lbs
Water	208 lbs
Mighty 150 superplasticizer	65 oz
Daravair air entraining admixture ...	10 oz
Daratard retarder	15 oz

The concrete for the panels used in Bridge #1 was batched on 10/26/93 and had had a 4-inch (100 mm) slump and a 6.2% air content. The temperature at the time the concrete was poured was 64° F (18° C). After the panels were poured they were covered with heavy canvas tarps and allowed to cure for 3 days. Numerous 6-inch diameter by 12-inch long cylinders were cast along with 6 in. x 6 in. x 24 in. beams to determine the concrete's compressive strength and modulus of rupture at various ages throughout the study. These properties are shown in Table 3.2. The prestress force was transferred to the panels on 11/2/93 by cutting the strands with a torch. The average concrete cylinder strength at the time of transfer was 5470 psi (37.7 MPa).

The concrete for the panels in Bridge #2 was batched on 10/18/94 and had a 6-inch (150 mm) slump and a 6.2% air content. Properties of this concrete are listed in Table 3.3. The prestress force was transferred to the panels on 10/25/93 by cutting the

strands with a torch. The average concrete cylinder strength at the time of transfer was 4700 psi (32.4 MPa).

3.6.2 Cast-In-Place Concrete for Bridge #1

The concrete used in the CIP portion of Bridge #1 was a "Class A" (6 bag) mix per INDOT designation. The concrete was supplied by IMI Materials and was batched at their plant on South River Road in West Lafayette, IN. Batch weights per cubic yard of this mix are listed below.

Type I Cement	564 lbs
Sand	1340 lbs
#8 Limestone	1800 lbs
Water	192 lbs
Microair air entraining admixture ...	6 oz
Pozzolith retarder	11 oz

The CIP concrete for bridge #1 was cast on 3/28/94. The concrete arrived at the Purdue structures lab at 1:20 PM and had a slump of 2 1/2 inches (65 mm). The placing and finishing of the concrete was completed by 3:00 PM. After the concrete had taken set it was covered with 6 mil visqueen and allowed to cure for 3 days. Table 3.4 lists the properties of this concrete at various ages throughout the study.

3.6.3 Cast-In-Place Concrete for Bridge #2

The concrete used in the CIP portion of Bridge #2 was a "modified Class C" (7 bag) mix per INDOT designation and was poured on 12/11/95. This was a mix specially

designed to minimize shrinkage of the concrete, and thus reduce early cracking. Batch weights for this mix (based on a 1 cubic yard yield) are listed below.

Type I Cement	501 lbs
Class A Fly Ash	158 lb
#23 Natural Sand.....	1006 lbs (SSD)
#8 Crushed Limestone	1872 lbs (SSD)
Water (@134° F)	265 lbs
Air entraining admixture	13 oz
Type F Chemical Admixture	118 oz

The mix had the following characteristics which theoretically help reduce shrinkage:

1. Low cement content. The cement content of this mix was reduced by 24% from the Standard Class C structural concrete mix by the addition of fly ash.
2. High coarse aggregate content (65%, by weight of the total aggregate).
3. High-quality, angular, crushed limestone with a low absorption (0.91%).
4. Low water/cementitious ratio (0.402).

Fly ash was used to reduce the cement content and to increase the slump for improved workability and pumping characteristics of the concrete. The concrete was placed over a period of 1 1/4 hours. Air contents taken near the start and end of this time were 8.8% and 8.3%, respectively. Corresponding slumps measured 4 1/2 inches and 4 1/4 inches. Relative yields were 1.048 and 1.040. The above batch weights have been corrected for over yielding. Table 3.5 lists the structural properties of this concrete at various ages.

The casting and surface finishing was completed at approximately 4:00 PM. However, because the surface did not set for some time, the concrete was not covered with wet burlap and plastic until after 10:00 PM. The topping was allowed to cure for 4 days before the forms were stripped. During the cure, the plastic was uncovered and the burlap was saturated daily with a garden hose.

Additional beams were cast to help estimate the amount of shrinkage in the actual bridge. These measured 6 in x 6 in x 30 in, and after curing they were placed on visqueen to reduce friction and allow for unrestrained shrinkage. Stainless steel "Whittemore points" were then attached to 3 sides of each beam and regular shrinkage readings were taken over a period of several months. The resulting shrinkage data for these beams is shown in Figure 3.37.

3.6.4 Cast-In-Place Concrete for Small Durability Specimens

The CIP concrete for the 3 ft x 3 ft durability specimens was supplied by IMI Materials and cast on 4/28/95. This concrete was a "Class C" (7 bag) mix per INDOT designation and had the following batch weights per cubic yard.

Type I Cement	658 lbs
Sand	1222 lbs
#8 Gravel	1850 lbs
Water	209 lbs
Microair air entraining admixture ...	10 oz
Pozzolith retarder	13 oz

The concrete had a 2 3/4" (70 mm) slump and an air content of 4.75 %. The surface was given a raked finish similar to the ponded area of Bridge #1. After initial set of the concrete, the specimens were covered with plastic and allowed to cure for three days. This concrete had a 28-day strength of 6110 psi.

3.6.5 Mild Steel Reinforcement

The epoxy-coated reinforcement used in both test bridges was supplied by Midwest Pipe Company in Schererville, IN, where the epoxy coating was applied. The steel bars were produced by Birmingham Steel Corporation in Bourbonnais, IL. Numerous tensile tests were run on both the #4 bars and #6 bars. Stress-strain curves of these bars are shown in Figures 3.38 and 3.39, respectively.

Figure 3.38 shows a typical stress-strain relationship of the #4 epoxy-coated bars. These bars did not have a notable yield plateau and began strain-hardening almost immediately after the yield strain was reached. Figure 3.39, on the other hand, shows the well defined yield plateau of the #6 epoxy-coated bars used in this study. These bars did not begin strain-hardening until nearly twice the yield strain had been reached.

3.6.6 Prestressed Reinforcement

The prestressing steel used in this study was 1/2" Special low-relaxation Grade 270 strand. The steel was manufactured by Florida Wire and Cable, Inc. in Jacksonville,

FL. The mill report listed the following properties:

Area	0.167 in^2	(107.7 mm^2)
Breaking Load	46,818 lbs	(208,245 N)
Load @ 1% Extension	43,579 lbs	(193,840 N)
Modulus of Elasticity	28,500 ksi	(196,508 MPa)
Ultimate Elongation	5.21%	(5.21 %)
Elongation @ 33,750 lbs ...	0.00709 in/in	(.00709 m/m)

Strands were tested in the laboratory by installing strain gages on individual wires as was done for the two bridge specimens. Unfortunately, the strands failed prematurely at the grips which held them in the testing machine. Partial stress vs. strain curves for the strand are shown in Figure 3.40. The strains in Figure 3.40 are the strains in the individual wires of the 7-wire strand and not the longitudinal strain of the strand.

3.7 Summary of Experimental Procedures

This experimental program consisted of testing two composite bridges, utilizing precast prestressed concrete panels, in the laboratory. The bridges were exposed to 5 million cycles of service load prior to the final monotonic failure loading. Possible degradation of these bridges due to repeated loading was assessed by monitoring end reactions, deflections, and strains. The long-term performance of this type of structure was also determined by subjecting one bridge to 48 weeks of durability cycling, consisting of exposure to salt water and heat lamps. During this time, half-cell potentials, corrosion currents, and AC-resistances were measured weekly. The influence of time-dependent

effects (creep and shrinkage) on moments at the piers was assessed by monitoring end reactions during the CIP concrete cure period. The results from these tests are included in the subsequent chapters. Chapter 4 covers the findings pertaining to time-dependent effects.

Table 3.1 Specimen Details

Specimen	Prestressed Steel Prestress Ratio (ρ_p)	Mild Steel Reinforcement Ratio (ρ)
Bridge #1	0.0027	0.0036
Bridge #2	0.0014	0.0030

Table 3.2 Prestressed Concrete Properties (Bridge #1)

Date	Age (days)	Batch #	Average Cylinder Strength (psi)	Modulus of Rupture (psi)
11/2/93	7	1	5430	-------
11/2/93	7	2	5730	-------
11/9/93	14	1	4750	-------
11/16/93	21	1	7250	-------
11/23/93	28	1	7440	-------
11/26/93	31	1	7620	-------
5/23/94	209	1	7140	-------
5/23/94	209	2	6720	-------
7/6/95	618	1	7030	-------
8/1/95	644	1	6940	820
8/1/95	644	2	6370	-------

Unit weights of this concrete were 141.7 pcf for Batch #1 and 142.4 pcf for Batch #2.

Table 3.3 Prestressed Concrete Properties (Bridge #2)

Date	Age (days)	Batch #	Average Cylinder Strength (psi)	Modulus of Rupture (psi)	Modulus of Elasticity (ksi)
10/25/94	7	1	4560	-------	-------
10/25/94	7	2	6690	-------	-------
11/2/94	15	1	7350	-------	-------
11/2/94	15	2	7760	-------	-------
11/8/94	21	1	8020	-------	-------
11/8/94	21	2	9090	-------	-------
11/15/94	28	1	7750	-------	-------
11/15/94	28	2	8560	-------	-------
1/27/96*	464	1	8170	840	-------
1/27/96*	464	2	7900	900	-------
3/28/96	527	1	7440	840	-------
3/28/96	527	2	8460	920	-------
4/1/96	531	1	7920	-------	4330
4/1/96	531	2	9090	-------	4960

*These cylinders and flexure beams were tested between 1/25/96 and 1/29/96.

Unit weights of this concrete were 144.1 pcf for Batch #1 and 145.7 pcf for Batch #2.

Table 3.4 Cast-In-Place Concrete Properties (Bridge #1)

Date	Age (days)	Average Cylinder Strength (psi)	Modulus of Rupture (psi)
3/29/94	1	2410	-------
3/31/94	3	3020	-------
4/4/94	7	4240	-------
4/11/94	14	5590	560
4/18/94	21	5850	-------
4/25/94	28	6150	-------
5/23/94	56	6160	-------
7/6/95	465	6100	-------
8/1/95	491	6290	850

The unit weight of this concrete was 146.7 pcf.

Table 3.5 Cast-In-Place Concrete Properties (Bridge #2)

Date	Age (days)	Average Cylinder Strength (psi)	Modulus of Rupture (psi)	Modulus of Elasticity (ksi)
12/12/95	1	2200	-------	-------
12/14/95	3	3440	-------	-------
12/17/95	6	-------	540	-------
12/18/95	7	4990	-------	-------
12/25/95	14	5660	610	-------
1/1/96	21	5380	-------	-------
1/8/96	28	6300	-------	-------
1/25/96	45	6250	690	-------
2/26/96	77	5760	-------	4050
3/28/96	108	5610	-------	-------
3/29/96	109	-------	690	-------
4/22/96	133	5730	-------	3430

The unit weight of this concrete was 144.0 pcf.

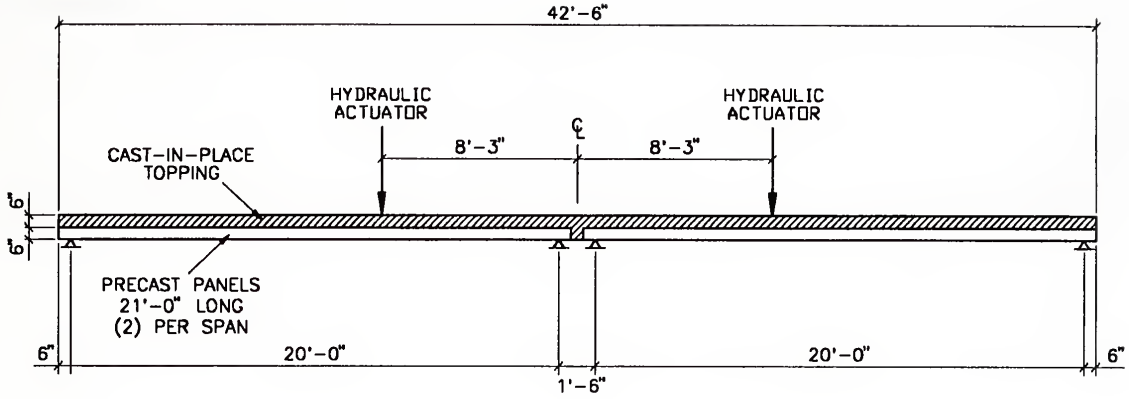

Figure 3.1 Laboratory Test Setup

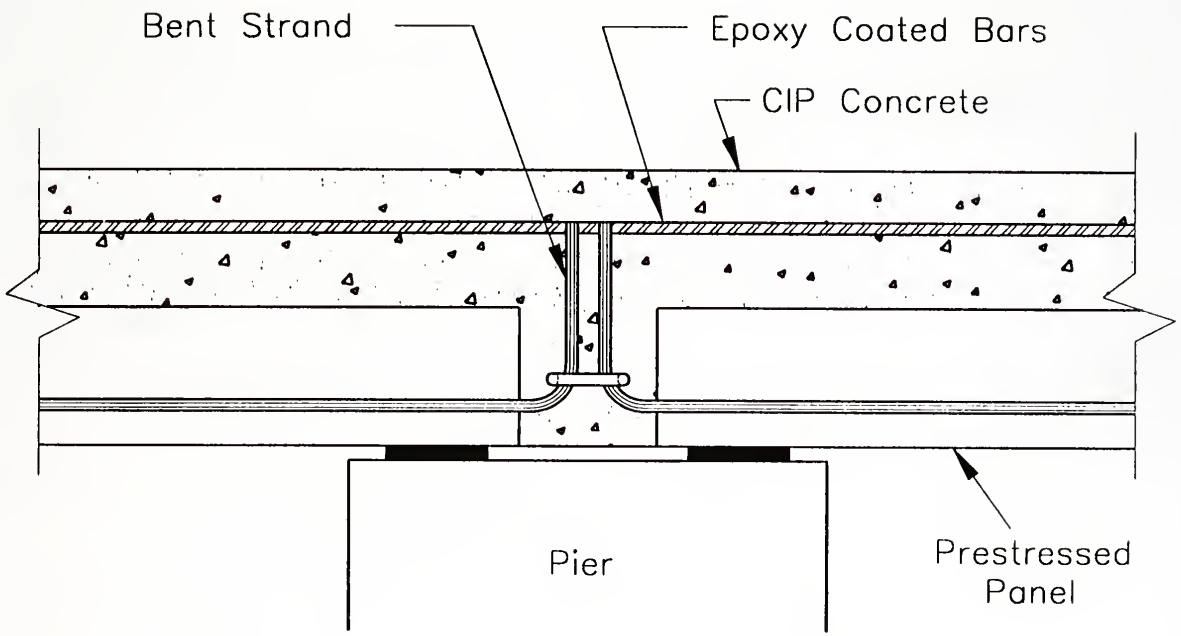

Figure 3.2 Detail at Diaphragm

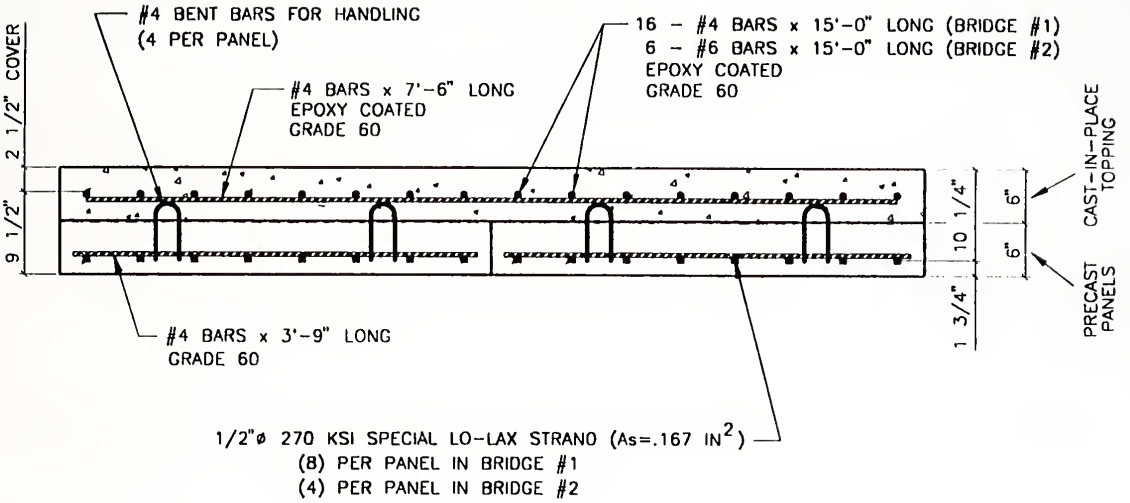

Figure 3.3 Cross-Section of Test Specimen

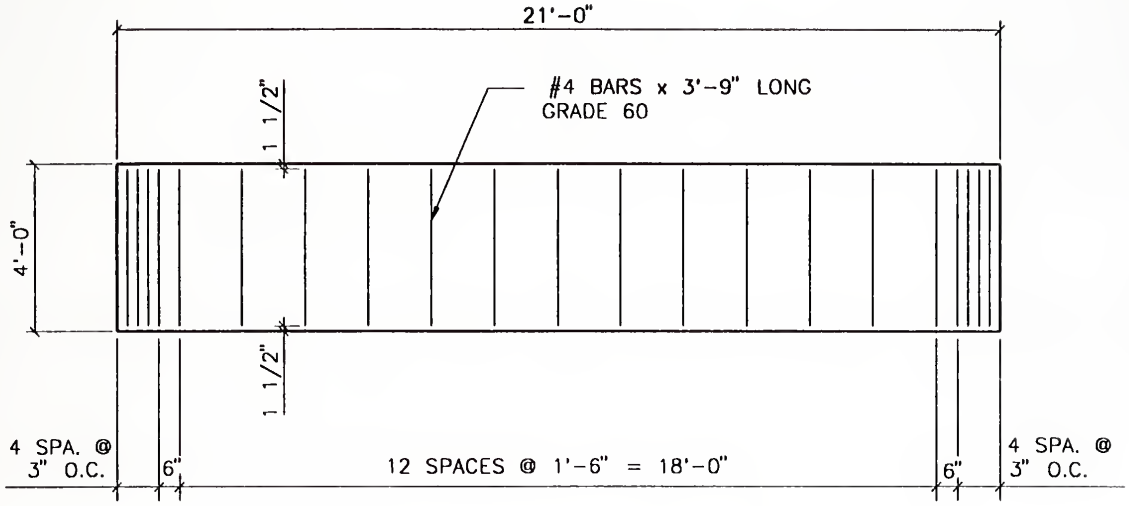

Figure 3.4 Mild Steel Reinforcement in Prestressed Panels

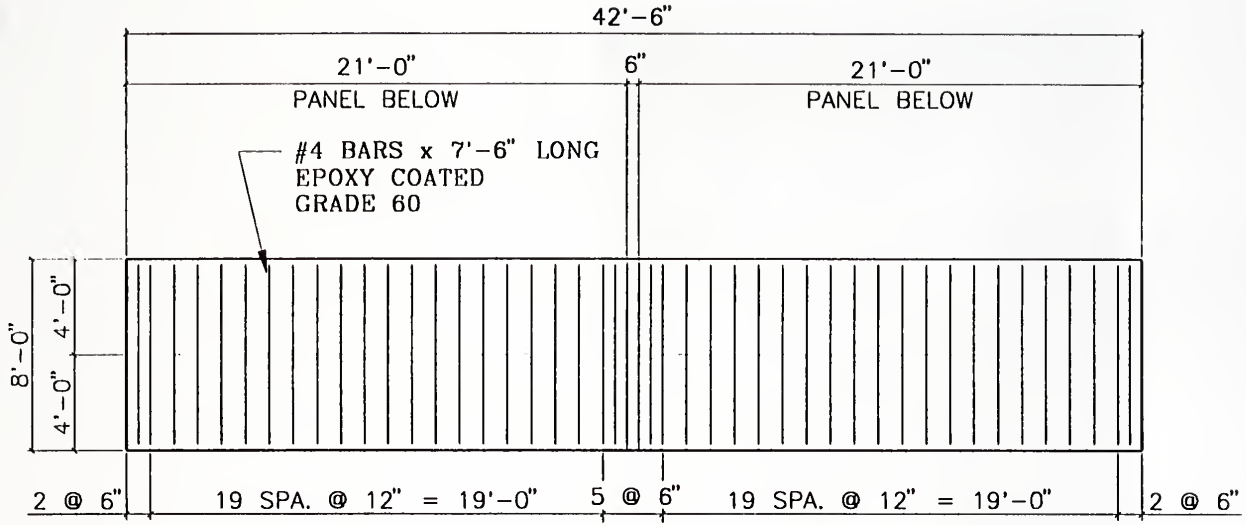

Figure 3.5 Transverse Reinforcement in Cast-In-Place Topping

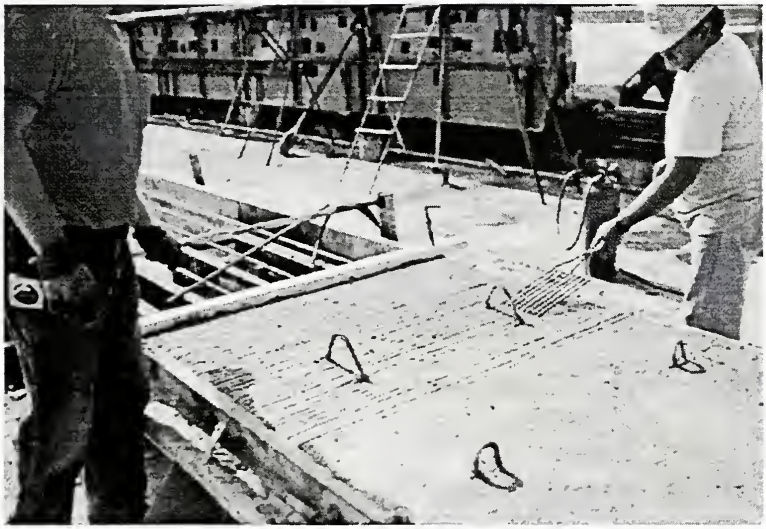

Figure 3.6 Raked Finish Being Applied to the Prestressed Panels

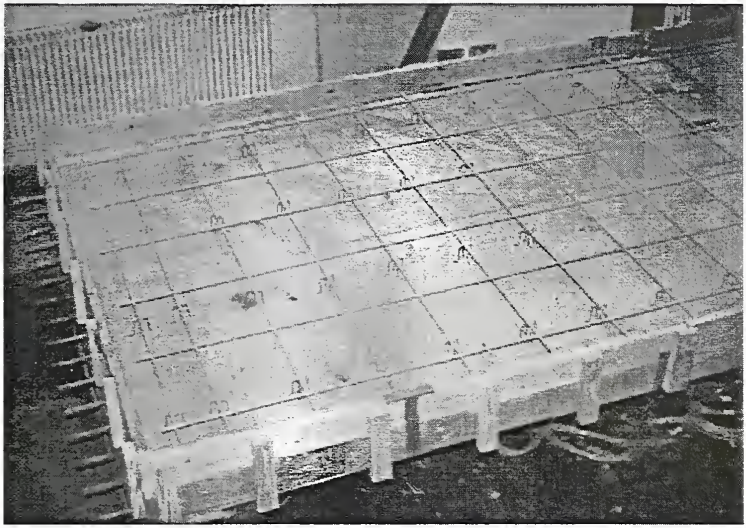

Figure 3.7 Epoxy-Coated Reinforcement in CIP Topping

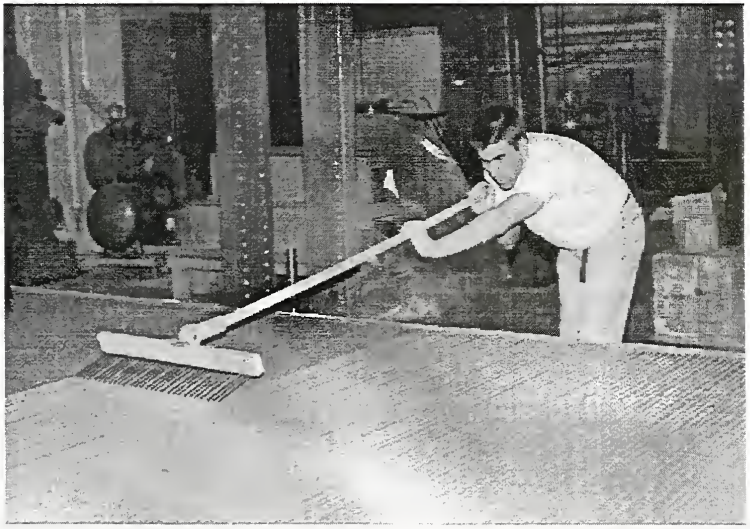

Figure 3.8 Raked Finish Applied to CIP Topping at Center Pier

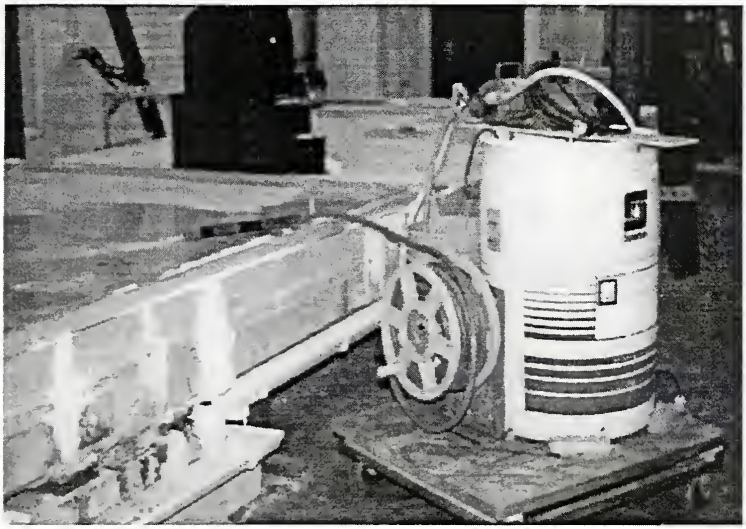

Figure 3.9 15% Sodium Chloride Solution Being Pumped Onto Bridge #1

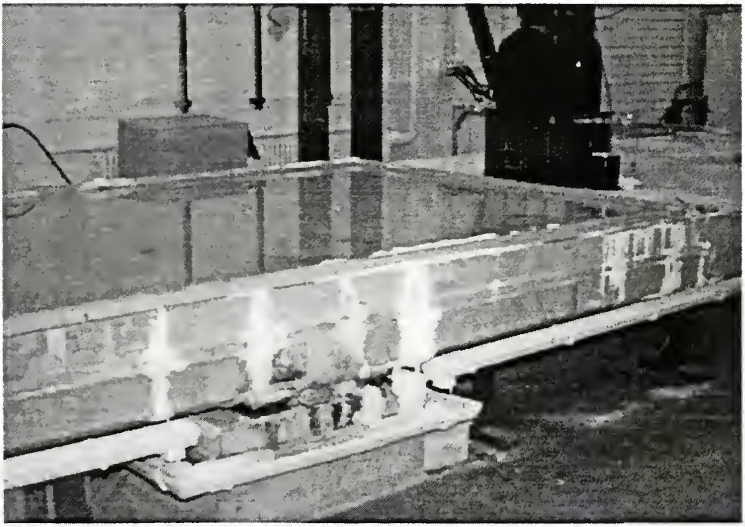

Figure 3.10 The Ponded Region of Bridge #1

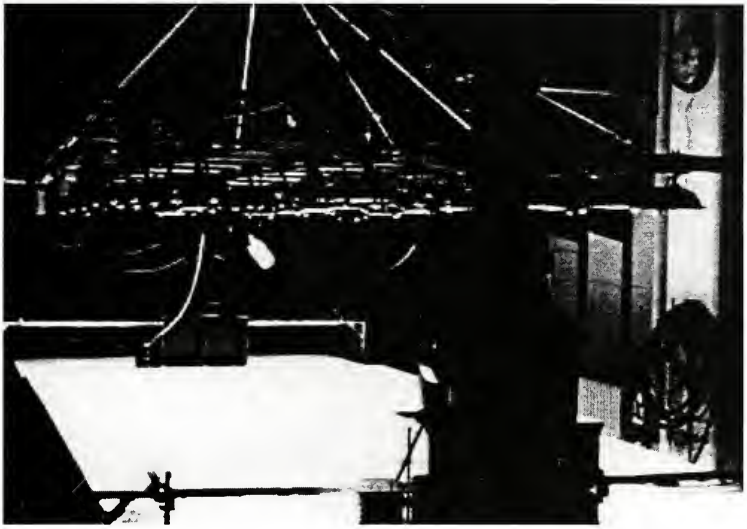

Figure 3.11 Bridge #1 During the Drying Phase of the Exposure Cycling

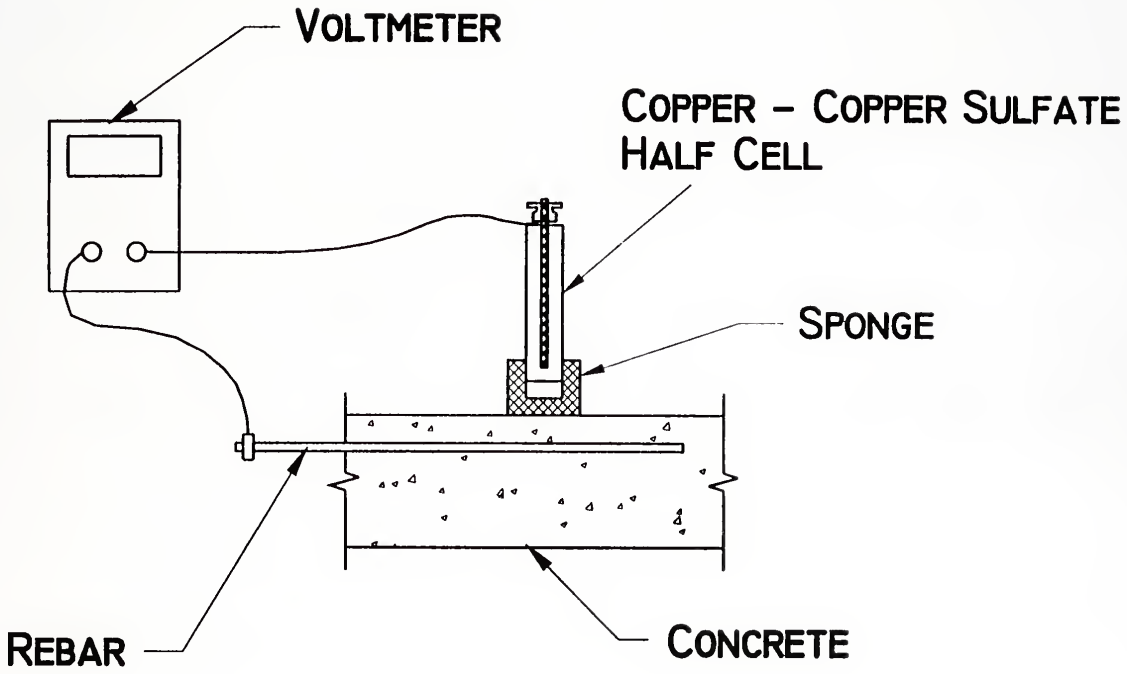

Figure 3.12 The Half-Cell Potential Measurement

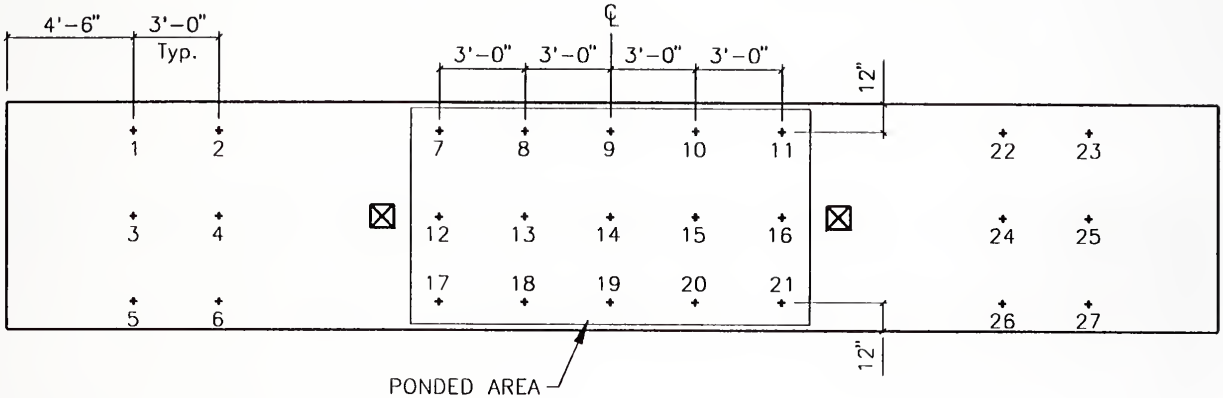

Figure 3.13 Location of Weekly Half-Cell Potential Measurements

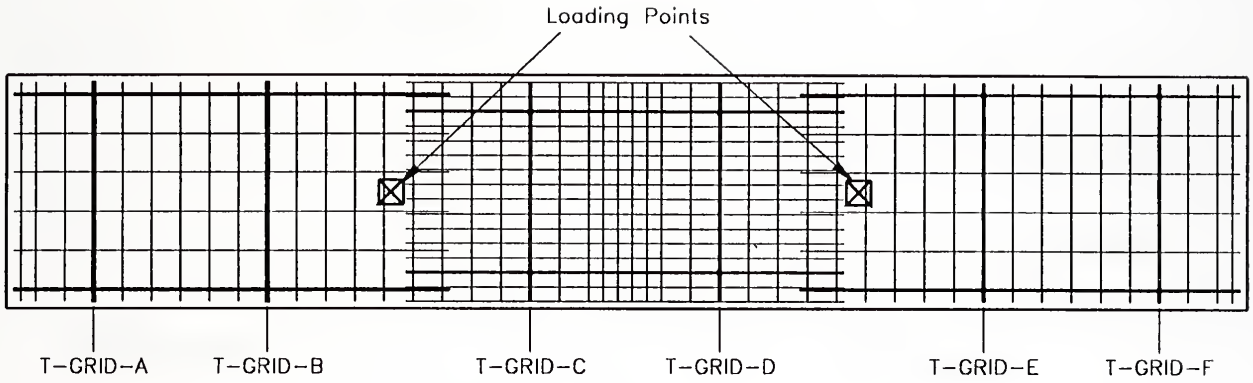

NOTE: HEAVY LINES INDICATE ELECTRICALLY INTERCONNECTED REBARS

Figure 3.14 Electrically Interconnected Reinforcement in the CIP Topping of Bridge #1

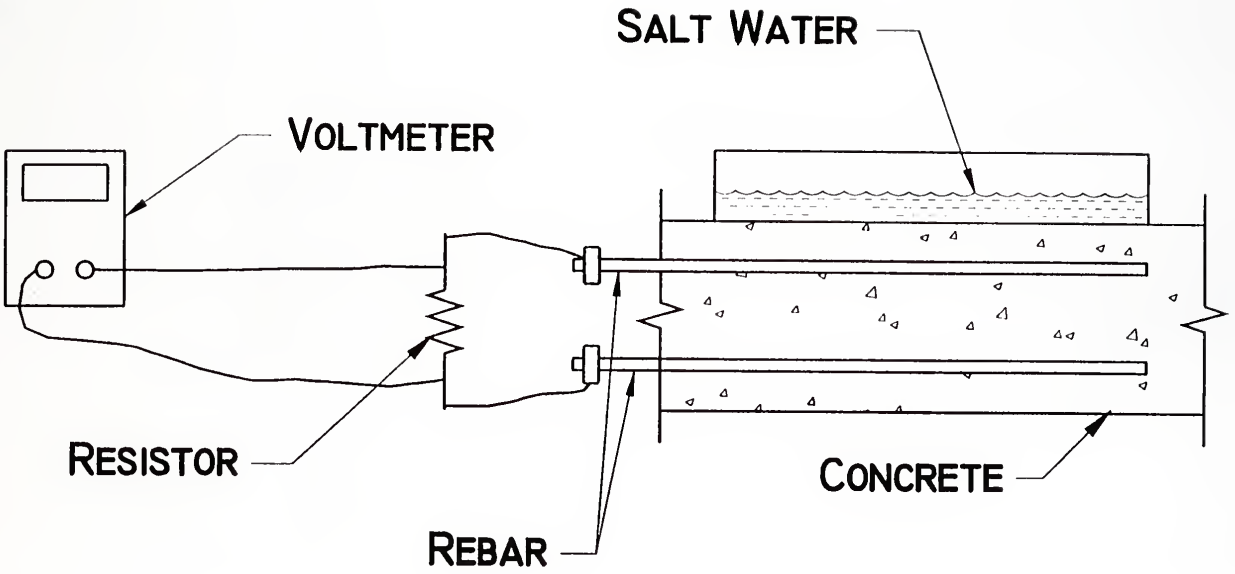

Figure 3.15 Measured Corrosion Current

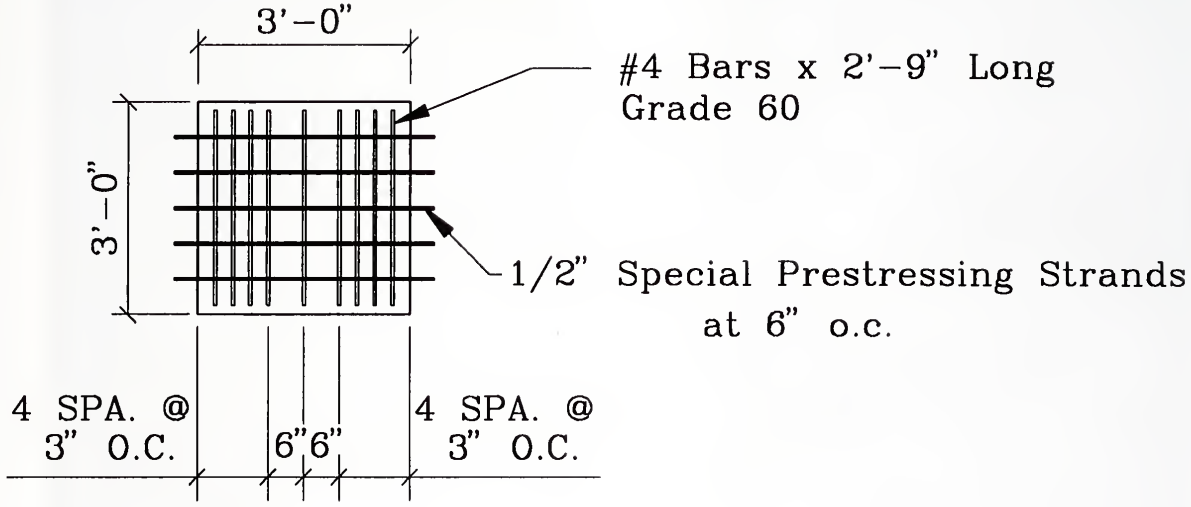

Figure 3.16 Uncoated Reinforcement in Bottom Panels of 3 ft x 3 ft Durability Specimens

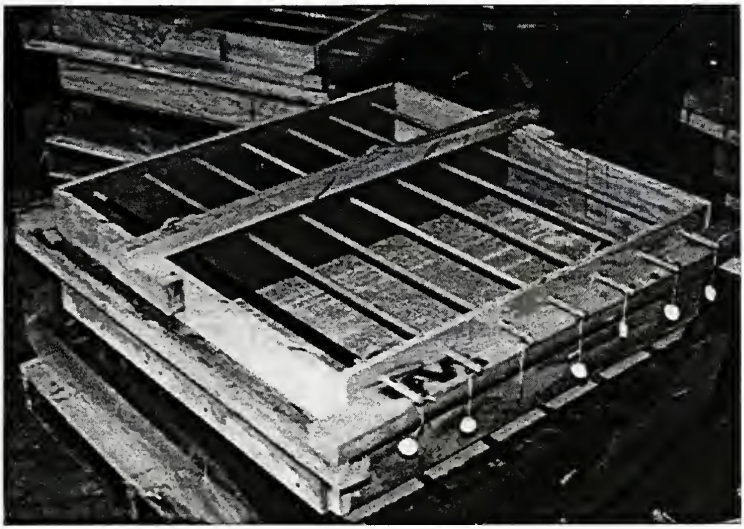

Figure 3.17 Initial Pre-Formed Crack in 3 ft x 3 ft Durability Specimens

Figure 3.18 Typical Damage to Epoxy Coating at Ribbed Locations of Bars

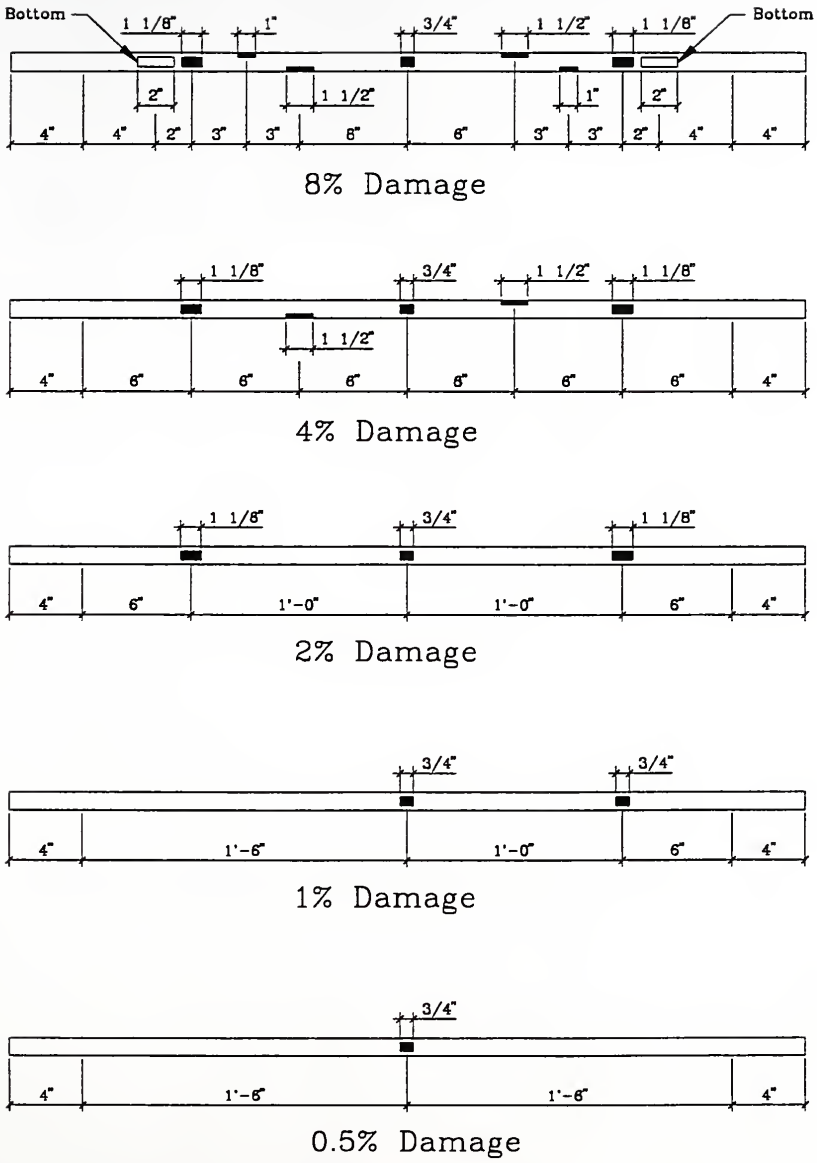

Figure 3.19 Damaged Areas of Epoxy Coated Bars in 3 ft x 3 ft Durability Specimens

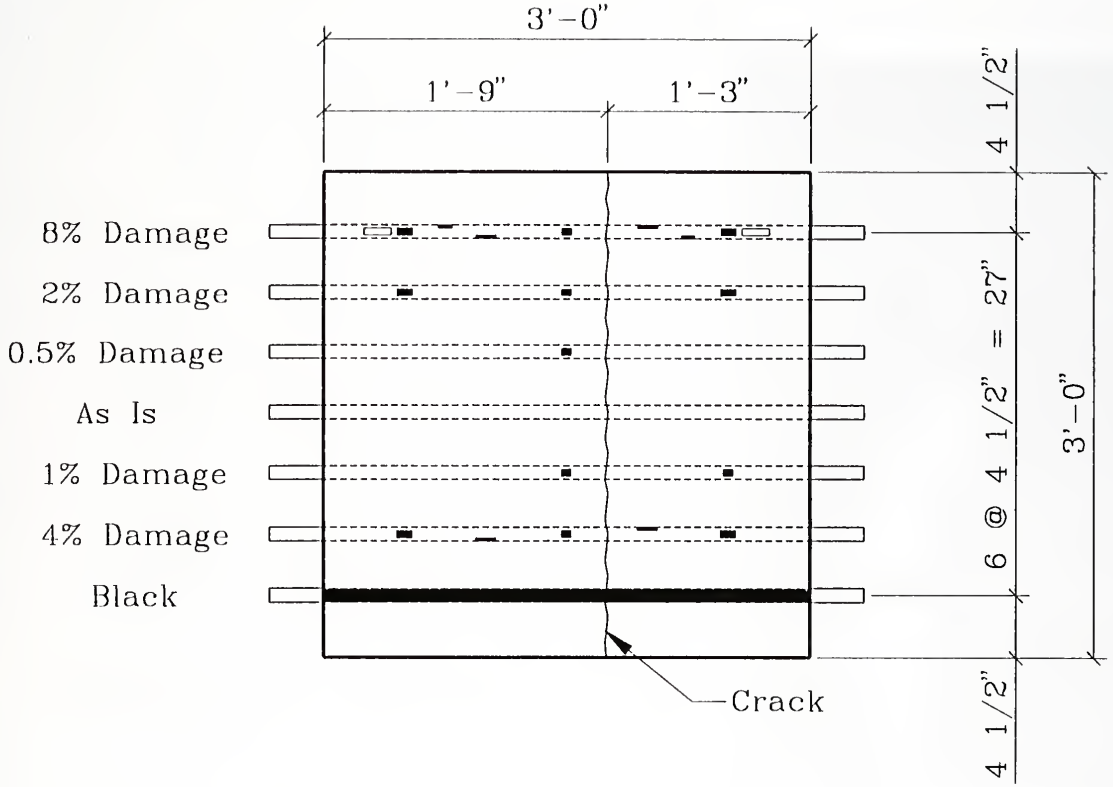

Figure 3.20 Location of Epoxy Coating Defects in the 3 ft x 3 ft Durability Specimens

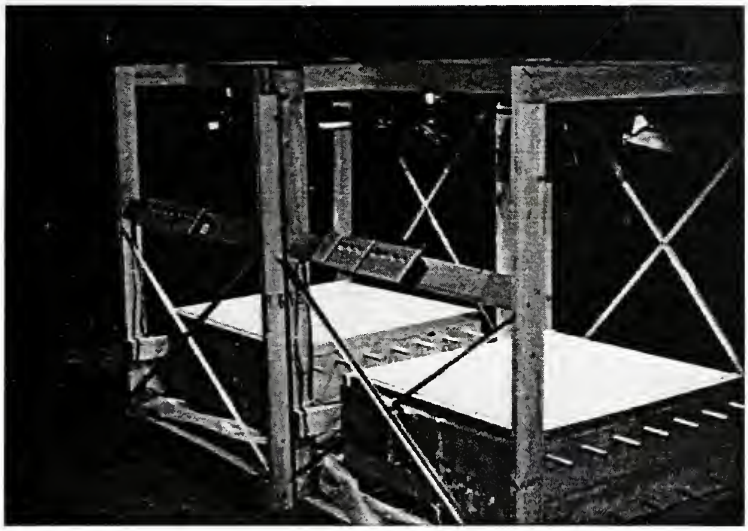

Figure 3.21 3 ft x 3 ft Durability Specimens with Electrical Switches Used to Isolate Bars

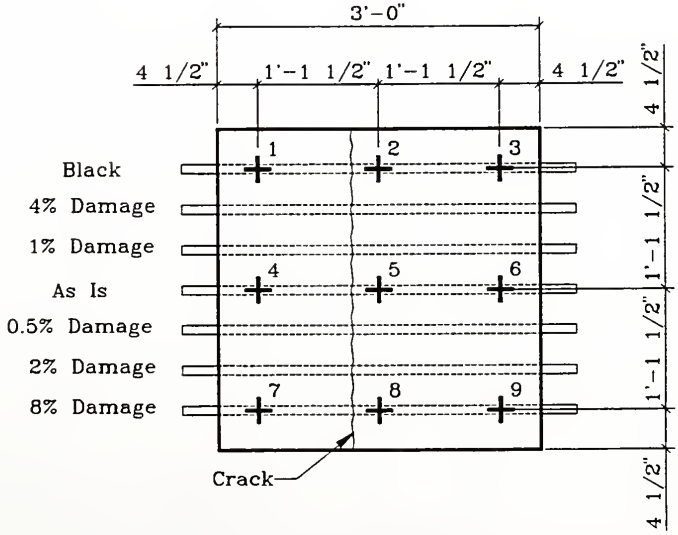

Figure 3.22 The Location of Weekly Half-Cell Measurements on 3 ft x 3 ft Specimens

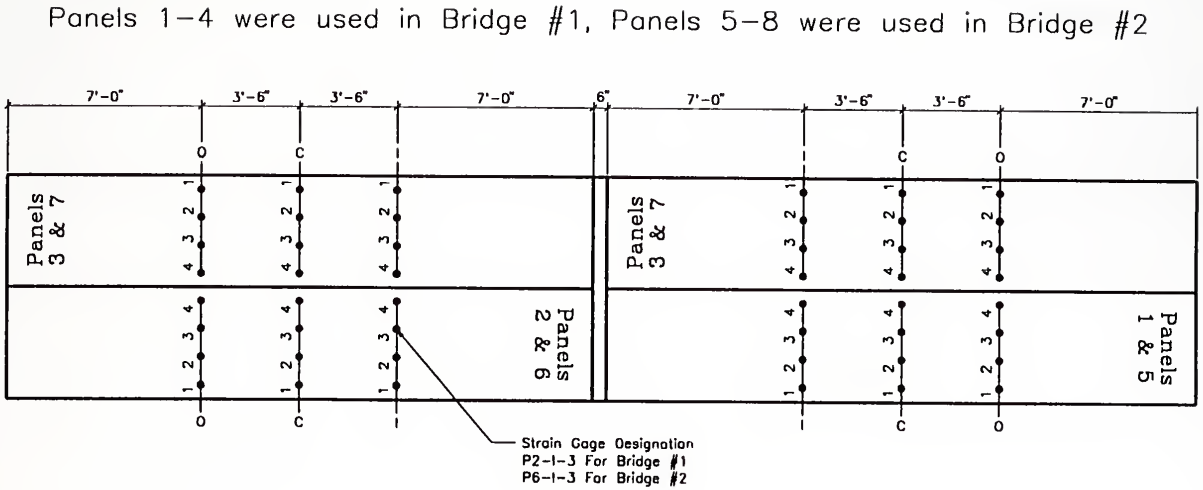

Figure 3.23 Location of Strain Gages on Prestressed Strand in Precast Panels

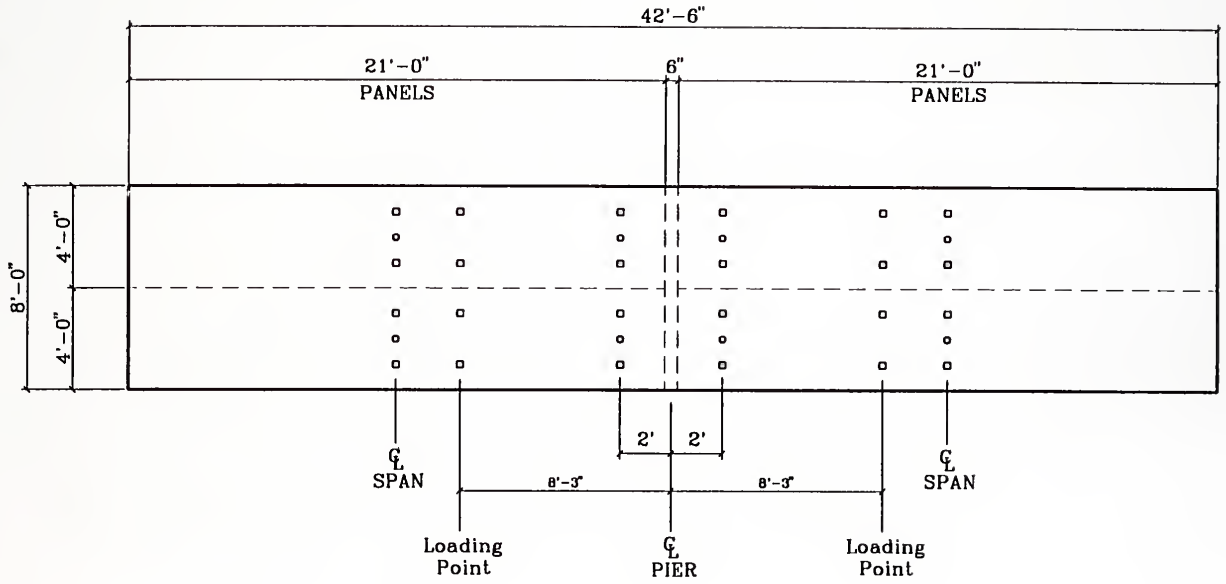

O = Location of Gages in Bridge #1

□ = Location of Gages in Bridge #2

Figure 3.24 Location of Strain Gages on Bottom Surface of Precast Panels

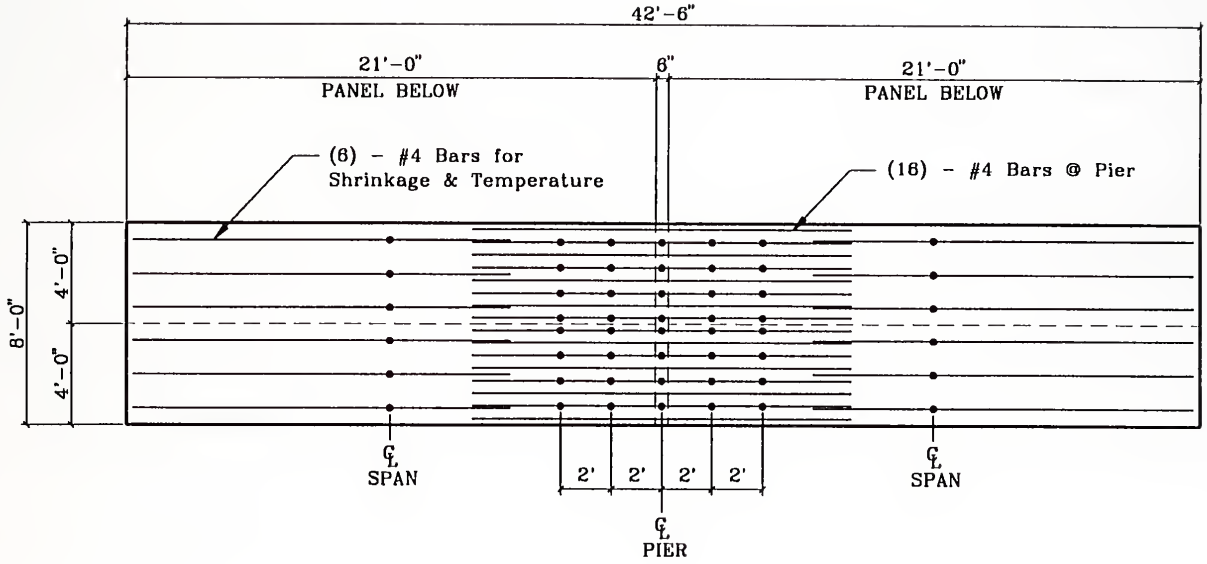

Figure 3.25 Location of Strain Gages on Longitudinal Reinforcement in CIP Topping (Bridge #1)

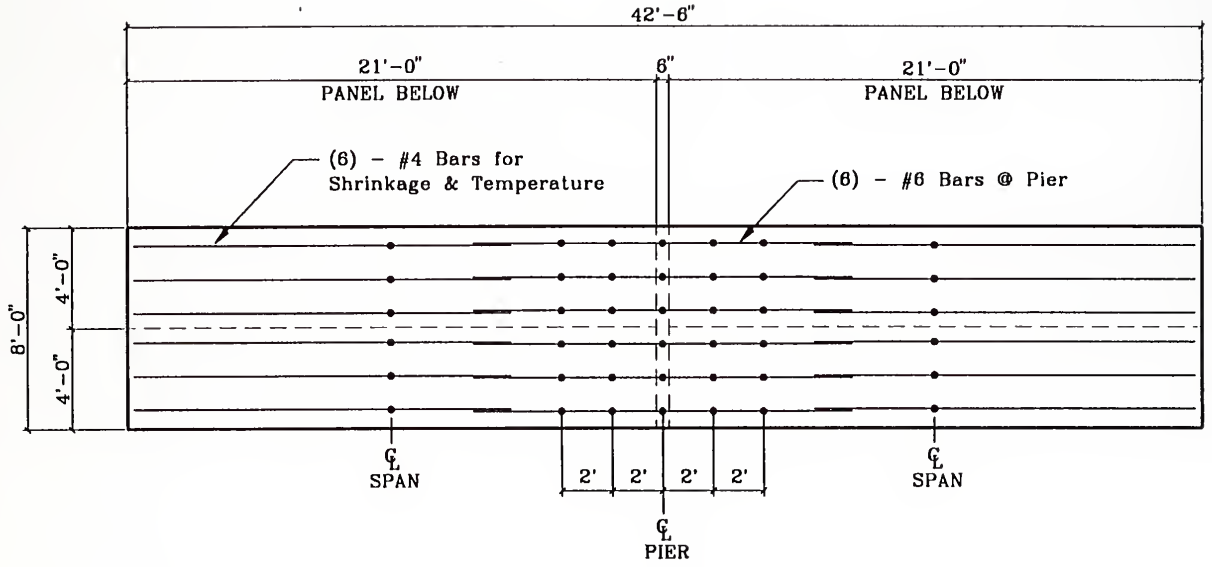

Figure 3.26 Location of Strain Gages on Longitudinal Reinforcement in CIP Topping (Bridge #2)

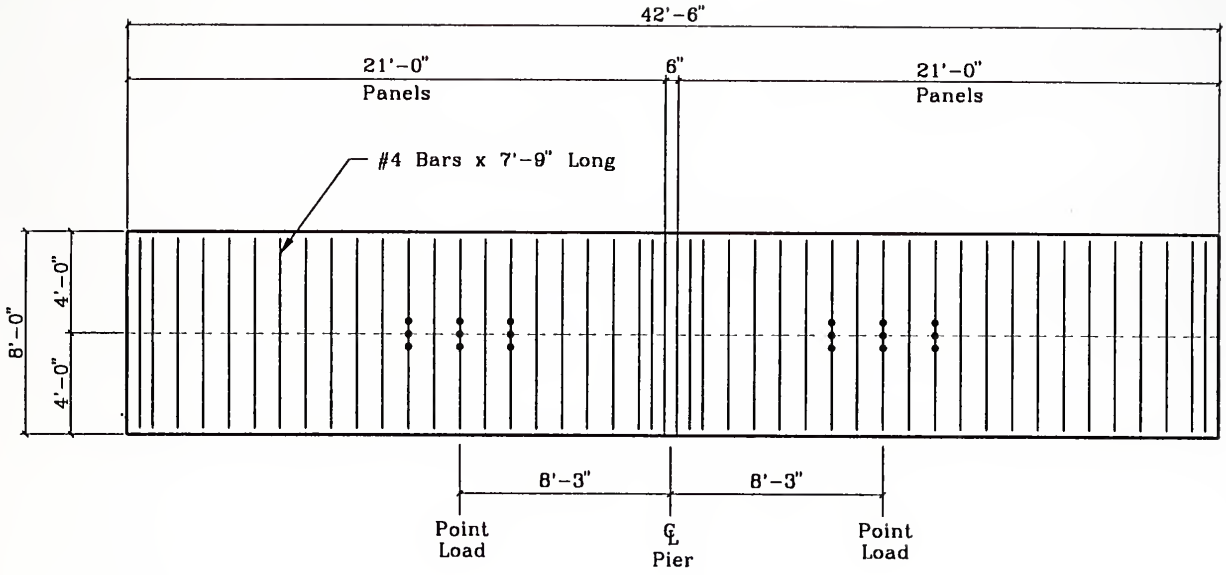

Figure 3.27 Location of Strain Gages on Transverse Reinforcement in CIP Topping

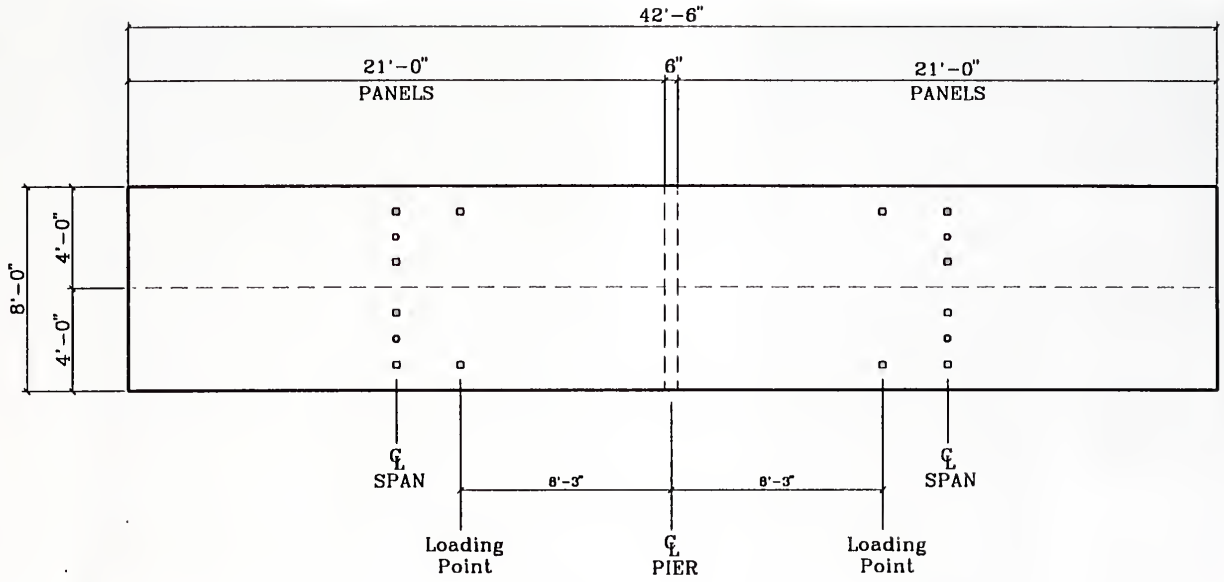

O = Location of Gages in Bridge #1

□ = Location of Gages in Bridge #2

Figure 3.28 Location of Strain Gages on Top Surface of CIP Concrete

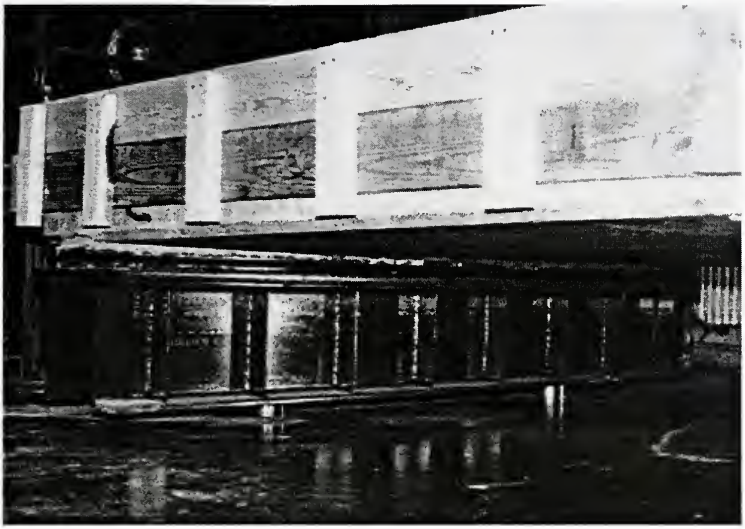

Figure 3.29 Spreader Beam on Two Load Cells at Panel Ends

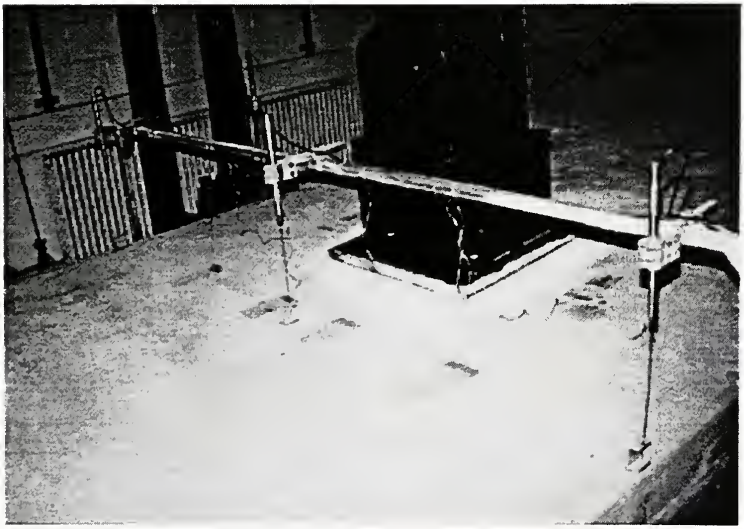

Figure 3.30 LVDTs Used to Measure Deflections at Midspan

Figure 3.31 Differential Deflection Measurements Using an Electronic Dial Gage

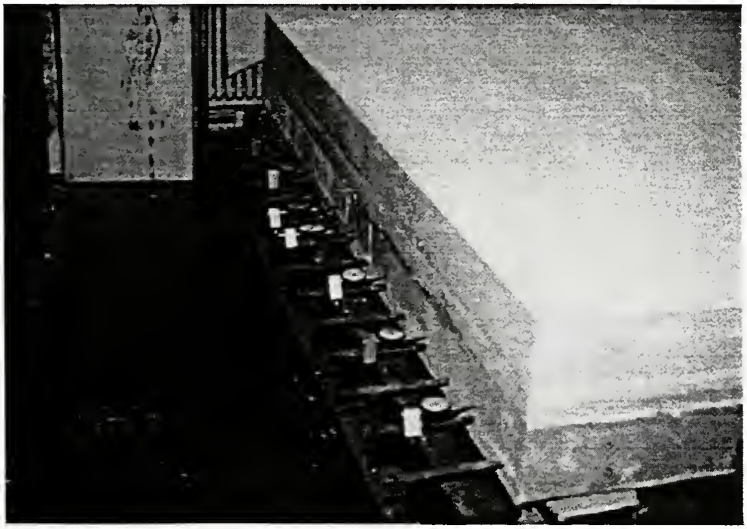

Figure 3.32 Dial Gages Used to Measure Strand Slip at End

Figure 3.33 Measuring Crack Widths with an Optical Measuring Scale

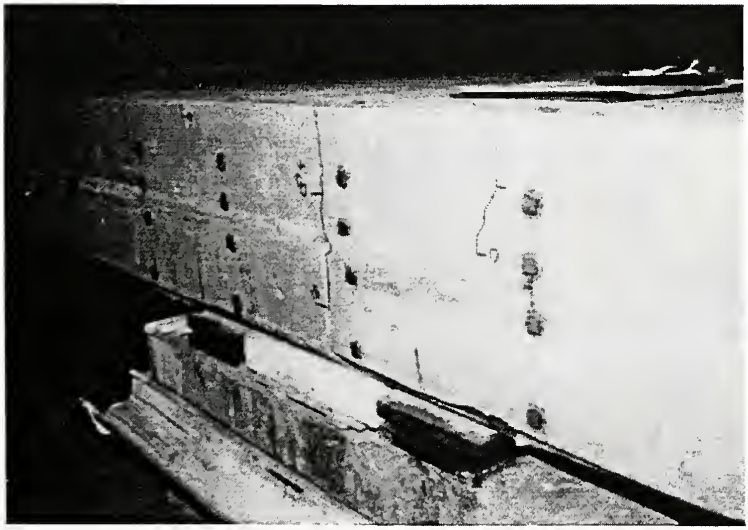

Figure 3.34 Whittemore Points at the Center Pier of Bridge #2

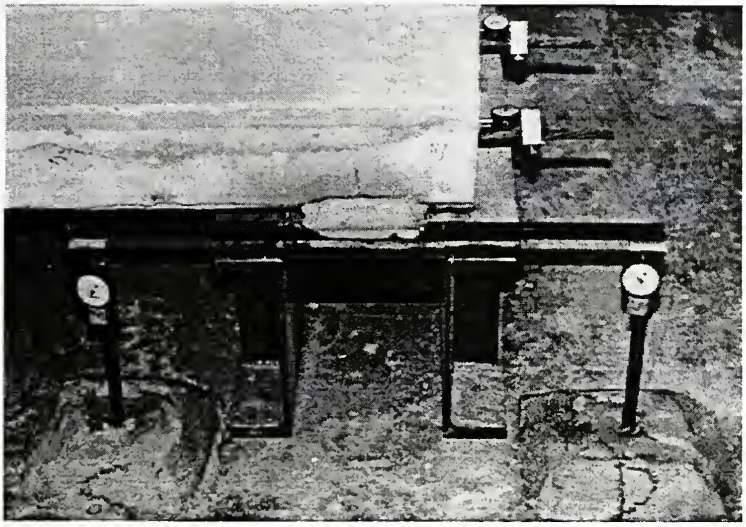

Figure 3.35 Dial Gages Used to Determine End Rotations of Bridge #2

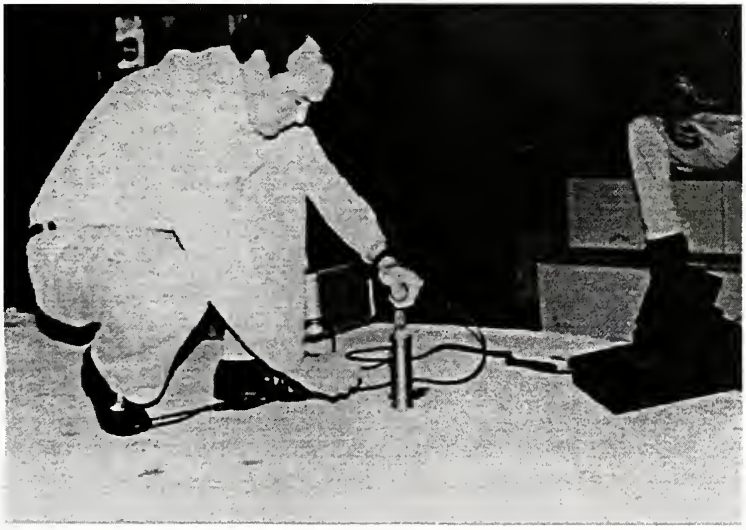

Figure 3.36 Impact-Echo Testing of Bridge #1

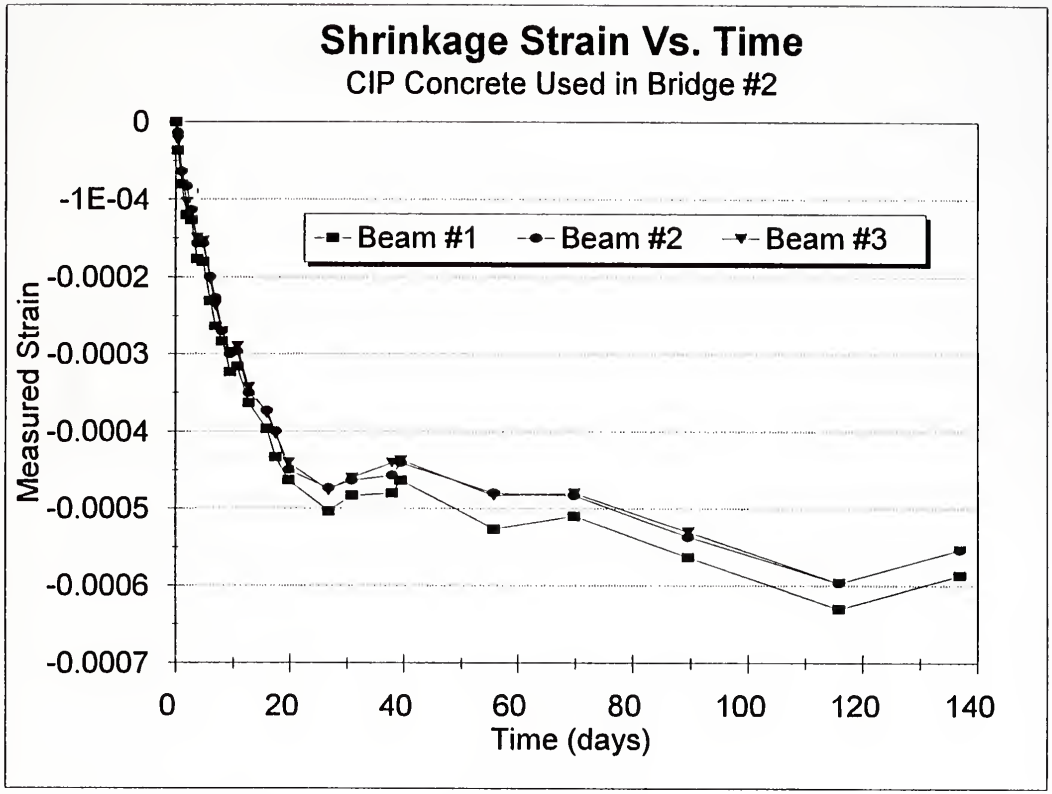

Figure 3.37 Shrinkage Data From Cast-In-Place Concrete Used in Bridge #2

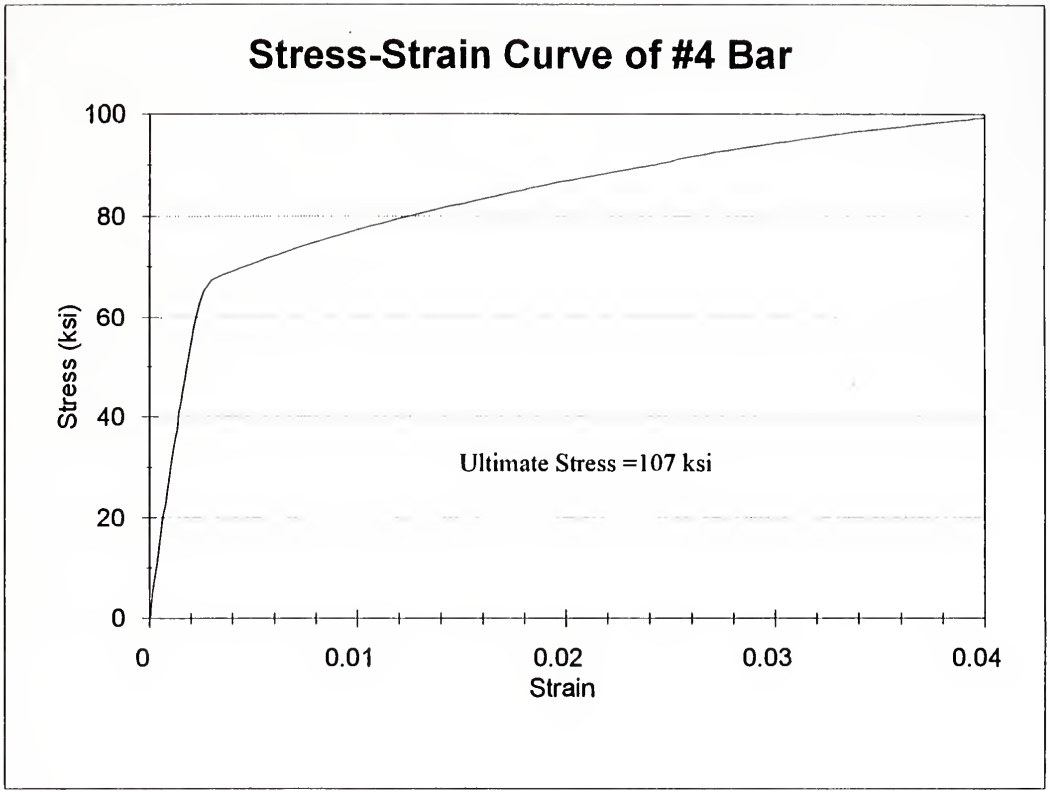

Figure 3.38 Typical Stress-Strain Curve of #4 Bars Used in This Study

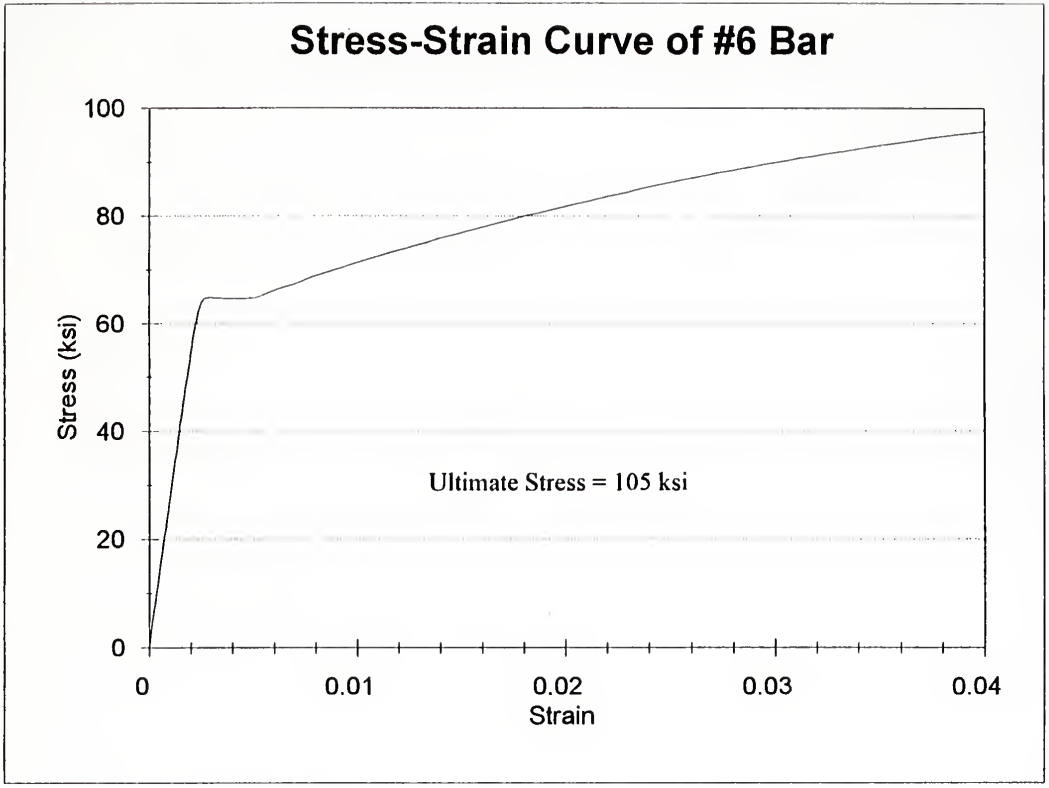

Figure 3.39 Typical Stress-Strain Curve of #6 Bars Used in This Study

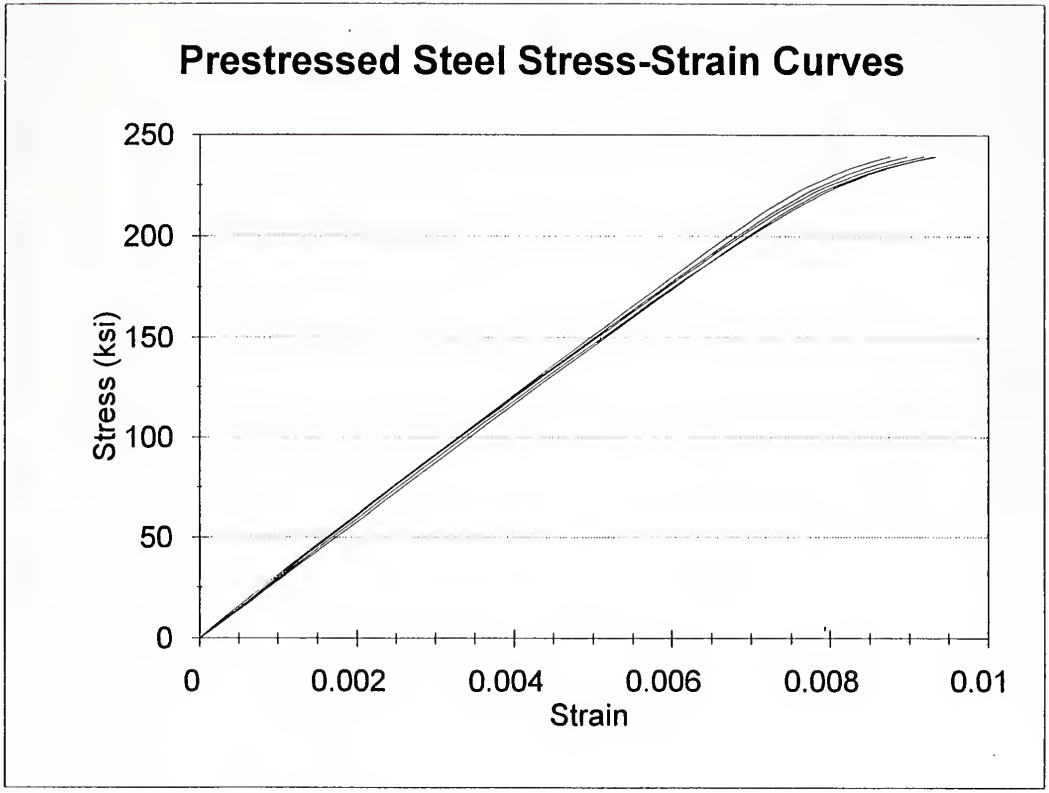

Figure 3.40 Stress-Strain Curves of Prestressed Steel (Obtained Using Strain Gages on Individual Wires of a 7-Wire Strand)

CHAPTER 4 - TIME-DEPENDENT EFFECTS

4.1 Introduction

In composite construction using precast sections, the precast members are often cast several months before they are installed in the field. Consequently, most of the concrete drying shrinkage in these members will have occurred before the composite CIP concrete is cast. As the fresh CIP concrete cures, its shrinkage will then be partially restrained by the precast members to which it has been bonded. For simple-span construction where member ends are free to rotate, this restraining force will cause the composite section to deform as indicated in Figure 4.1. However, in the case of continuous construction, the continuous ends are not allowed to rotate and a negative restraint moment is produced. The corresponding deformed shape of a two-span bridge, neglecting gravity effects, is shown in Figure 4.2. For an actual two-span bridge, the result is a decrease in the reactions at the discontinuous ends and an increase in the reactions at the center pier.

Concrete drying shrinkage is to a large extent a reversible phenomenon. If concrete is saturated with water after it has shrunk, it will expand to almost its original volume. Therefore, alternating drying and wetting conditions will cause alternating

volume changes of the concrete. This phenomenon is partly responsible for fluctuating deflections of concrete structures exposed to seasonal changes each year [17].

The effect of creep due to prestressing will usually have the opposite effect as that due to differential shrinkage between the precast panels and CIP topping. For prestressed concrete bridge members, the center of the prestress force usually lies below the neutral axis of the section. This eccentricity of force causes the members to bow upwards (commonly referred to as camber) and will produce rotations at the member ends. This camber will generally increase with time due to creep of the concrete under the sustained, eccentric prestressing force. When these members are made continuous in the field, additional end rotations due to creep are restrained and positive moments result at the interior piers.

Also, for continuous construction using precast concrete members, forces resulting from the restraint of creep deformations due to gravity loads acting on the precast members will be in the same direction as the forces which would be produced if the same loads had been applied after the structure was made continuous [18]. Thus, the restraint of creep deformations due the weight of the precast panels and CIP topping will produce negative moments at interior piers.

4.2 PCA Method

The Portland Cement Association (PCA) conducted experimental and analytical research to determine the long-term effects of creep and shrinkage at the continuous support of a two-span composite bridge (see Mattock [18]). This investigation was later

extended by Freyermuth [19], who proposed a procedure for the design of continuity connections between adjacent precast prestressed girders in multi-span bridges. As suggested by both Mattock and Freyermuth, the uniform differential shrinkage moment in a composite concrete section at any time is given by:

$$M_s = \varepsilon_s E_d A_d \left(e_c + \frac{h}{2} \right) \tag{4.1}$$

where

ε_s = differential shrinkage strain (assumed uniform over the thickness of the slab)

E_d = modulus of elasticity of CIP concrete

A_d = cross-sectional area of CIP slab

h = CIP slab thickness

e_c = distance between top of precast member and centroid of composite section.

The restraint moment at the center support of a two-span continuous bridge is then calculated as:

$$M_r = \left(\frac{3}{2} M_p - M_d \right) \left(1 - e^{-\phi} \right) - \frac{3}{2} M_s \left(\frac{1 - e^{-\phi}}{\phi} \right) \tag{4.2}$$

where

M_p = moment caused by the prestressing force about the centroid of the composite member

M_d = the mid-span moment due to dead load

e = the base of the Naperian Logarithms (2.7183)

ϕ = ratio of creep strain to elastic strain at the time of interest.

Equation 4.2 shows that the total restraint moment at the pier is equal to the sum of the three components of shrinkage, dead load creep, and creep due to prestress. In this equation, the shrinkage moment and the moment caused by the eccentric prestressing force are each multiplied by the factor (3/2). This is the multiplier used to obtain the moment at the center support of a two-span continuous beam due to an applied uniform moment and is derived in Figure 4.3. The moment due to dead load, on the other hand, only has a multiplier of 1. This is because the moment at the center support of a two-span beam with uniform loading in both spans is equal to the midspan moment of a uniformly loaded simply supported beam of equal span length. The restraint components due to dead load and prestressing are then multiplied times the factor $(1-e^{-\phi})$, which is equal to zero when ϕ is zero and increases with increasing values of ϕ. The component due to differential shrinkage is multiplied by the factor $(1-e^{-\phi})/\phi$, which is equal to one when ϕ is zero and decreases with increasing values of ϕ.

Mattock concluded that the deformations due to creep and differential shrinkage did not influence the ultimate load-carrying capacity of the continuous girders considered in the study, and that the influence of creep and shrinkage is restricted to deformations and the possibility of cracking at the service load level.

4.3 CTL Method

Another method for the analysis of precast prestressed beams made continuous was developed by Oesterle, Glikin, and Larson [20] at the Construction Technology Laboratory (CTL). This method takes into account the stiffness and length of connection

at the continuous supports. Also, the equation used to calculate moments due to shrinkage accounts for restraining action by the precast members and by the steel reinforcement in the CIP slab. The computer program BRIDGERM was developed at CTL to calculate time- dependent restraint moments for multi-span bridges using precast prestressed members.

The analysis in BRIDGERM is conducted by superimposing incremental restraint moments over a series of time intervals. For each time step, the three components of the restraint moment (differential shrinkage, creep due to dead load, and creep due to prestress) are calculated using the rate of creep method. The rate of creep method assumes that the rate of creep $d\varepsilon_c/dt$ is known and that the creep after time T is given by:

$$\text{creep} = \int_0^T \frac{d\varepsilon_c}{dt} dt \tag{4.3}$$

The calculated increment of restraint moment is then added to the sum at the preceding time step to determine the restraint moment at the end of an interval. Different time-dependent functions for creep and shrinkage of both the prestressed concrete members and CIP slab were used.

BRIDGERM uses the following equation to calculate the incremental moment due to differential shrinkage:

$$\Delta M_{si} = \Delta\varepsilon_{si} E_{di} A_d \left(e_c + \frac{h}{2} \right) \left(\frac{1}{1 + \frac{E_p A_p}{E_{di} A_d}} \right) \tag{4.4}$$

where

$\Delta\varepsilon_{si}$ = $[\varepsilon_{sdi}-\varepsilon_{sd(i-1)}]-[\varepsilon_{spi}-\varepsilon_{sp(i-1)}]$

ε_{sdi} = shrinkage strain in CIP slab at time t_i (modified for the effect of restraint by the steel reinforcement using the formula suggested by Dischinger [21])

ε_{spi} = shrinkage strain in prestressed member at time t_i

E_p = modulus of elasticity of the prestressed member

A_p = cross-sectional area of the prestressed member

E_{di} = modulus of elasticity of CIP concrete at time t_i

A_d = cross-sectional area of CIP slab

h = CIP slab thickness

e_c = distance between top of precast member and centroid of composite section.

The first part of Equation 4.4 is similar to that used in the PCA method, with modification for use in a time-step calculation procedure. The second part of this equation is a reduction factor that accounts for the restraining effect that the prestressed member has on the shrinkage of the CIP slab. This reduction factor was not used in the PCA method. Restraint moments due to differential shrinkage, dead load creep, and prestress creep are then calculated using the PCA approach (Equation 4.2), with appropriate modifications for a time-step implementation. For the calculation of restraint moments due to prestress-induced creep, the prestress force is adjusted at each time step to account for losses due to shrinkage, creep, and relaxation. This is done by estimating the prestress loss occurring during each time step using the procedure recommended by the PCI Committee on

Prestress Losses [24]. The stress in the prestressed strand at the end of each time step is then equal to the stress at the beginning of the time step minus the losses occurring during that interval.

4.4 Experimental Determination of Restraint Moments

The reactions at the discontinuous ends of each test bridge were monitored throughout the cure period (50 days for Bridge #1 and 44 days for Bridge #2). For a two-span bridge with simply supported ends, the restraint moment at the center pier is equal to the change in end reaction times the span length (20 ft. for the test bridges). This is illustrated in Figure 4.4. End reactions were monitored approximately daily for Bridge #1 and at 1/2-hour intervals for Bridge #2. Values of the end reactions for Bridge #1 and Bridge #2 during the cure periods are listed in Tables 4.1 and 4.2, respectively. These values are also graphed in Figures 4.5 and 4.8, respectively.

4.4.1 Restraint Moments in Bridge #1

Figure 4.5 shows that the end reactions in Bridge #1 decreased rapidly during the first few days and then stabilized. This decrease corresponds to a negative restraint moment at the interior support, indicating that differential shrinkage and creep due to dead load are the dominant time-dependent effects occurring during this period. This figure also shows a slight increase in the reaction between days one and three. This is believed to have been caused by the curing procedure used.

After the CIP concrete had set (day zero), the entire bridge was covered with visqueen. The visqueen extended to the floor and created a condition which allowed the underside of the panels to be warmed due to the heat of hydration of the CIP topping. This did not represent actual field conditions, however, where the panel bottoms would be exposed to the environment. After one day, the bottom of the visqueen was adjusted to allow air flow beneath the panels, better representing conditions in the field. The increase in the end reactions between days one and three is believed to be due to a thermal bowing effect, where the panels tend to camber upward due to the cooling of the underside. This bowing, and corresponding end rotations, is resisted by the continuity connection at the center pier, creating a positive restraint moment and a corresponding increase in end reaction.

Figure 4.5 shows two other large changes in end reactions (between days 13 and 14, and between days 18 and 20). These changes correspond to observed cracking in the CIP concrete deck. On day 14 of the cure period a transverse crack was observed which extended completely across the bridge. The crack was located at the west support point of the center pier. From Table 4.1, the west restraint moment at day 13 was 94 kip-ft. This corresponded to a top fiber stress of 490 psi (3.4 MPa) based on gross section properties. Two flexure beams, made from the CIP concrete used in Bridge #1, were tested on day 14 and had moduli of rupture of 520 psi (3.6 MPa) and 600 psi (4.1 MPa). A second transverse crack occurred near the east support point of the center pier and was noticed after day 20 of the cure period. The large change in the east end reaction shown in Figure 4.5 corresponds to this crack. It is evident that the observed cracks were

flexural cracks due to the negative restraint moments at the center support. The cracking reduced the stiffness at the center pier and the restraint moments decreased. The locations of the two cracks are shown in Figures 4.6 and 4.7.

4.4.2 Restraint Moments in Bridge #2

Figures 4.8 shows that Bridge #2 behaved similarly to Bridge #1, with the exception of the response during the first day. Figure 4.8 shows a rapid increase in the end reaction during the first 10 hours after casting. The initial increase is believed to be due to a temperature differential between the CIP topping and the precast panels.

The temperature of the CIP concrete in Bridge #2, which is plotted in Figure 4.9, was measured during the cure period by placing a temperature probe in the wet concrete. The concrete temperature at the time of placement was about 60° F (16° C) and increased to 84° F (29° C) within 18 hours due to the surrounding air temperature and hydration of the cement. This was likely larger than the temperature at the bottom of the panels, causing a thermal bowing which was resisted by a positive restraint moment and increased end reactions. This restraint moment was relieved as the increase in the CIP concrete temperature slowed, and the resulting differential decreased.

A similar increase in end reactions may also have occurred in Bridge #1, but would not have been detected from daily readings. During the cure period of Bridge #2, end reactions were recorded every half hour during the first week and hourly for the remainder of the testing. This allowed for the detection of the initial increase. If readings had been

taken only once per day during the cure period of Bridge #2, as was done for Bridge #1, the initial increase in end reactions would not have been observed.

After the initial increase, the end reactions decreased until day 5 and then stabilized. The first crack, which extended transversely across the entire bridge near the east support point of the center pier, was noticed on day 6. Another crack was observed at the west support at the center pier the following day. Two additional transverse cracks, each located about one foot away from the first two cracks, were noticed on day 13. These, and other cracks occurring during the cure period of Bridge #2, are shown in Figures 4.10 and 4.11.

The negative restraint moment at the west support point of the center pier, prior to cracking on day 5, was 73 kip-ft. This corresponded to a top fiber stress of 380 psi (2.6 MPa) based on gross section properties. Two flexure beams, made from the CIP concrete used in Bridge #2, were tested on day 6 and had moduli of rupture of 510 psi (3.5 MPa) and 570 psi (3.9 MPa). These numbers suggest that the cracks were likely caused by the combined effects of concrete drying shrinkage and flexure.

4.5 Comparison of Experimental Restraint Moments with Predicted Results

Restraint moments for each bridge were calculated using both the PCA method and the CTL method (with the program BRIDGERM). These methods are dependent on the ultimate shrinkage and creep coefficients of the concrete and on the relationship of shrinkage and creep with time. The time-dependent relationships of shrinkage and creep have been studied by many researchers, and various models of these relationships, with

varying degrees of complexity, have been proposed. The studies have revealed the difficulty in accurately predicting these relationships, as there is considerable scatter in data pertaining to identical concrete mixes. For this reason, it was believed that a simple model of these relationships would suffice.

One of the simplest expressions was used by Corley and Sozen [22] and assumes the time-dependent relationships for creep and shrinkage are the same. For periods of less than 2 years, the proportion "R" of the total time-dependent effect occurring at time t (in days) is obtained from the expression:

$$R = 0.13 \ln (t + 1). \tag{4.5}$$

This model was used in the following calculations for the relationships of shrinkage and creep with time. Shrinkage strains for the CIP concrete used in Bridge #2 were measured using a Whittemore gage. These measurements were made on three small beams cast at the time of the CIP topping, and the results are shown in Figure 3.37. A curve was fit through the mean values for these beams using the above expression and a strong correlation was found (see Figure 4.12). This relationship assumes a shrinkage strain at 2 years of 0.00082 and was used in the PCA method of analysis . The ultimate shrinkage strain of the precast concrete was assumed to be 0.00060. Program BRIDGERM uses different time-dependent relationships for shrinkage and creep as recommended by ACI Committee 209 [23]. In this BRIDGERM program, an ultimate shrinkage strain of 0.00090 was used for the CIP concrete in both bridges. In both analyses, the ultimate creep coefficients for Bridge #1 and Bridge #2 were assumed to be 2.1 and 2.3,

respectively. These values were estimated from relationships recommended in reference [23] based on temperature and relative humidity.

Air temperature and relative humidity near the center of each bridge were monitored during the cure period. For Bridge #2, monitoring began at the conclusion of the moist cure (after 4 days). Figures 4.13 and 4.14 show the air temperature and relative humidity, respectively, during the cure period of Bridge #1. The average temperature during this time was 77° F (25° C) and the average relative humidity was 34%. Figures 4.15 and 4.16 show the corresponding data for Bridge #2. The average temperature during the cure period of Bridge #2 (after moist curing) was 76° F (24° C) and the average relative humidity was 14%. These average values of temperature and relative humidity were used to calculate the ultimate creep coefficients.

Values of the prestress force at the time of continuity connection were estimated using the "Recommendations for Estimating Prestress Losses" prepared by the PCI committee on Prestress Losses [24]. The estimated strand stresses were 177 ksi (13% losses) for Bridge #1 and 181 ksi (11% losses) for Bridge #2 just prior to casting the top slab. These stresses increased due to the weight of the CIP concrete and were estimated at 179 ksi and 183 ksi, respectively, immediately after the topping was cast. These values were then used in the calculation of restraint moments due to prestress-induced creep.

Figures 4.17 and 4.18 plot the observed restraint moments with those predicted by the PCA and CTL methods for Bridge #1 and Bridge #2, respectively. The figures show that both methods considerably over-estimate the negative restraint moment. For each bridge, the PCA estimated moment is higher than the CTL moment. This is because the

PCA method calculates the shrinkage moment based on differential "unrestrained" shrinkage values, while the CTL method considers the restraining effects of the precast members and the steel in the CIP topping. Neither method, however, considers the effect of cracking in the calculation of restraint moments. These methods were developed from studies of continuous bridges using pretressed girders, in which the CIP slab thickness is only a small fraction of the composite depth. For bridges using full-span precast panels, however, the slab thickness is a significant percentage of the composite depth (50% for the two bridges tested). Therefore, cracking that occurs in the CIP slab at the piers of these bridges greatly reduces the stiffness of the section and the corresponding restraining moments. Oesterle, et al. [20] recommend that the design negative restraint moment be limited to 125% of the calculated cracking moment in the case where BRIDGERM-calculated negative restraint moments become excessive.

4.5.1 Modified PCA Method

The author has developed a modified form of the PCA method, which accounts for the length and stiffness of the diaphragm (due to cracking) as well as the restraint of CIP concrete shrinkage by the precast panels and reinforcement in the CIP topping. This method estimates the differential shrinkage moment using Equation 4.1, multiplied by the following factors to account for restraint by the precast member and reinforcement in the CIP slab.

$$\left(\frac{1}{1+\frac{E_pA_p}{E_dA_d}}\right)\left(\frac{1}{1+\frac{E_sA_s}{E_dA_d}}\right)$$

E_p and A_p are the modulus of elasticity and area of the prestressed panels. E_s and A_s are the modulus of elasticity and area of the steel reinforcement in the CIP deck. E_d and A_d are the modulus of elasticity and area of the CIP deck at the time of interest. The derivation of these restraint factors is shown in Figure 4.19.

This method also considers the length of the continuity connection and the effects of cracking by modifying Equation 4.2 as follows.

$$M_r = \left(\frac{3}{2}\alpha M_p - \alpha M_d\right)\left(1-e^{-\phi}\right) - \frac{3}{2}\alpha M_s\left(\frac{1-e^{-\phi}}{\phi}\right) \tag{4.6}$$

where

$$\alpha = \frac{\frac{2I_d}{L_d}}{\frac{2I_d}{L_d}+\frac{3I_m}{L_m}} \tag{4.7}$$

and

I_d = moment of inertia of the diaphragm region (area between support points at the center pier)

L_d = length of the diaphragm region

I_m = moment of inertia of the main spans

L_m = length of the main spans.

α is a coefficient which accounts for the relative stiffnesses of the diaphragm region and main spans. All other variables are the same as in Equation 4.2. The PCA method, which assumes a knife-edged support at the center pier and a constant member

stiffness, uses a value of α equal to one. For a two-span bridge having 20-ft. spans, a distance between center bearing points of 1.5 ft., and a constant EI (see Figure 3.1), the value of α is 0.90. This is the value used for the two test bridges prior to cracking.

The effect of cracking is modeled by checking the restraint moment obtained using Equation 4.5 with the calculated cracking moment at that section for each time of interest. Once the calculated restraint moment exceeds the cracking moment, the restraint moments are re-calculated using a new value of α which accounts for the reduced stiffness at the cracked section (diaphragm region). Once cracking occurs, all subsequent calculations are based on the new value of α.

The value of α used after cracking was based on a two-span bridge with a stiffness Ig within the main spans and Icr-top between the center supports (Ig is the moment of inertia of the gross section; Icr-top is the moment of inertia based on a crack depth equal to the thickness of the CIP topping). The section between the center supports was assumed to be cracked to a depth equal to the topping thickness since most cracking during the cure phases extended through the full depth of the CIP slab and then stopped. For Bridge #1, Icr-top was equal to 0.15 Ig and the corresponding value of α was 0.57. For Bridge #2, Icr-top was equal to 0.19 Ig and α was 0.63. The moduli of rupture used in the calculations were 7.5 and 6 times the square root of the CIP concrete compressive strength (f'c) for Bridge #1 and Bridge #2, respectively.

Figures 4.20 and 4.21 plot the observed restraint moments with those predicted using this modified PCA approach for Bridge #1 and Bridge #2, respectively. Figure 4.20 shows a good correlation between estimated and observed restraint moments for Bridge

#1, in both magnitude and anticipated time of cracking. The modified PCA method predicted initial cracking on day 16, while actual cracking was observed on day 14. This method overestimated the change in moment associated with cracking, however, by a factor of nearly two.

Figure 4.21 demonstrates a strong correlation, up to the point of cracking, between the actual test data for Bridge #2 and the response calculated using the modified PCA method. The modified PCA method predicted a considerable decrease in negative moment due to cracking, and predicted that negative moments would increase with time after the initial reduction due to cracking. However, neither of these behaviors was observed for Bridge #2. Instead, negative moment increased steadily until cracking then remained essentially constant during the rest of the cure period. The corresponding CIP concrete shrinkage beams showed that the top concrete continued to shrink at an approximately steady rate until about day 20 of the cure period (see Figure 3.37).

This phenomenon can be explained by considering the typical moment-curvature relationship of reinforced concrete beams as shown in Figure 4.22. Initially, the member responds to shrinkage-induced curvatures based on the stiffness of the gross section plus the transformed area of reinforcement. After cracking, however, there is a transition between the initial stiffness and that based on the cracked, transformed section. During this transition region, the response of the member to increasing curvature will depend on an incremental stiffness which is less than that of the cracked, transformed section and can approach zero. Thus, after cracking and before yielding of the reinforcement, increases in member curvature may not be coupled with significant increases in moment.

A distinctive characteristic of Bridge #2 is the number of cracks which occurred during the cure period. This is best seen by comparing the cracking of Bridge #2 with that of Bridge #1 (see Figures 4.6 and 4.10). Bridge #1 had essentially two transverse cracks occur during the CIP concrete cure period, while Bridge #2 had about eight transverse cracks occur during approximately the same time interval. These additional cracks, which opened throughout the cure period, decreased the stiffness of the negative moment region and may also explain why restraint moments in Bridge #2 were nearly constant after initial cracking.

The increased cracking which occurred in the CIP topping of Bridge #2 was probably the result of concrete drying shrinkage. The "modified Class C" concrete used for the topping exhibited substantially more shrinkage than expected. While the water content of 265 pounds per cubic yard and the extremely high dosage of Type F chemical admixture were necessary to provide a pumpable mix, the presence of these constituents may have served to offset the other mix characteristics aimed at reducing shrinkage [48]. Figure 4.16 shows that the CIP concrete in Bridge #2 was exposed to relative humidities between 10 and 20 percent after the initial wet curing. These low humidities would also increase the amount of concrete drying shrinkage and accelerate its occurrence.

It is important to note that for both bridges tested, the maximum negative restraint moments during the cure period occurred prior to cracking. This suggests that the presence of cracking stops the growth of the restraint moments due to differential shrinkage. Therefore, bridges which crack at an earlier age (such as Bridge #2) will have lower restraining moments than bridges that crack at a later age (such as Bridge #1).

Figures 4.23 and 4.24 show the results of the modified PCA method, with restraint moments held constant after cracking, for Bridges #1 and #2, respectively. This assumption results in a reasonable model of the behavior exhibited by both bridges.

4.6 Displacement Measurements During the Cure Period of Bridge #2

Midspan deflections of each prestressed panel were monitored for Bridge #2 during the cure period using LVDT's and are plotted in Figure 4.25. Deflections sharply decreased during the first 12 hours after casting, and then began increasing. This supports the assumption of a thermal bowing effect in which the panels bow upward due to a temperature gradient and the corresponding deflections decrease. Deflections remained somewhat constant between days 2 and 5, and then increased after day 5 (when cracking first occurred).

In addition to midspan deflections, displacements were also measured along the south edge of Bridge #2 during the cure period using dial gages spaced at 2'-6" (0.76 m) on center. Displacements at several time intervals are graphed in Figure 4.26. These also show increasing deflections (negative displacements) with time. This is due to both dead load creep and differential shrinkage. After cracking of the CIP concrete, the negative restraint moment did not increase. This means that additional differential shrinkage was not restrained by additional moments at the pier and resulted in an increase in deflection in a similar manner to that shown in Figure 4.1.

4.7 Whittemore Gage Measurements During the Cure Period of Bridge #2

Throughout the cure period of Bridge #2, mean strains were measured using a Whittemore Gage, having a gage length of 10 inches. The readings were taken on both faces of the bridge at the center pier. Figure 4.27 shows the locations where readings were taken. The points were secured to the face of the bridge immediately after the moist curing ended (after 96 hours). The points were located on the top surface, at the level of the #6 bars in the CIP topping, 1 inch above and below the interface, and at the level of the prestressed steel.

The three 10-inch gage readings at each depth were then averaged to determine the mean strains occurring over a 30-inch gage length at that level. Figures 4.28 and 4.29 show these mean strains plotted versus time throughout the cure period on the north and south faces, respectively. Mean strains on the north side are considerably higher than the corresponding strains on the south side. This is because of the cracking in that region. One of the transverse cracks fell within the Whittemore points on the north side of the bridge but outside of these points on the south side. These figures show that the strains at each level grew with time. This occurred without an increase in the restraint moment at the pier, and it is consistent with the explanation given in section 4.5.1. These figures also indicate that the neutral axis during this period was located in the precast portion of the bridge. This is expected since the CIP topping was still young, having a modulus of elasticity less than that of the prestressed panels.

These strains were plotted about the depth of the bridge to give the mean strain distributions acting at the pier at various times. These strain distributions are shown in

Figures 4.30 and 4.31. In these figures, the actual mean strains have been represented by straight lines determined from linear regression analyses. These strain distributions clearly show that curvatures at the pier continued to increase throughout the entire cure period.

4.8 Summary of Time-Dependent Effects

The modified PCA method is more accurate than the PCA and CTL approaches in estimating the magnitude of the restraint moments for both test bridges. The failure of the PCA method to account for restraint of shrinkage due to the precast elements and steel reinforcement leads to an overestimation of early shrinkage moments. Also, neither model accounts for cracking, which reduces the magnitude of the restraint moments and the rate at which additional restraint moments develop. While the modified PCA method improved the estimation of the restraint moment magnitudes, it overestimated the change in moments due to cracking and the ability of the moments to increase after cracking. For both specimens tested, negative restraint moments due to differential shrinkage and creep due to dead load were largest prior to cracking. A reasonable model of the specimen behavior was obtained using the modified PCA method before cracking, and then assuming moments due to differential shrinkage remain unchanged after cracking.

Table 4.1 End Reactions and Restraint Moments During the CIP Concrete Cure Period (Bridge #1)

Time Since Cast (Days)	West Reaction (Kips)	East Reaction (Kips)	Change in West Reaction (Kips)	Change in East Reaction (Kips)	West Restraint Moment (Kip-Ft)	East Restraint Moment (Kip-Ft)
(Before Cast)	6.30	6.16				
0.00	12.96	12.72	0.00	0.00	0.0	0.0
1.07	10.73	10.48	-2.23	-2.23	-44.6	-44.7
2.07	11.14	10.99	-1.82	-1.72	-36.5	-34.5
3.07	11.27	11.06	-1.70	-1.66	-34.0	-33.1
3.72	10.33	10.06	-2.63	-2.66	-52.6	-53.2
4.07	10.10	9.85	-2.86	-2.86	-57.2	-57.3
5.15	9.54	9.25	-3.42	-3.47	-68.5	-69.3
6.05	9.29	8.98	-3.67	-3.74	-73.5	-74.7
7.08	9.28	8.79	-3.68	-3.93	-73.7	-78.5
8.05	9.16	8.68	-3.80	-4.03	-76.0	-80.7
9.02	9.07	8.61	-3.89	-4.11	-77.8	-82.2
10.06	8.95	8.57	-4.02	-4.15	-80.3	-82.9
11.08	8.89	8.55	-4.07	-4.17	-81.5	-83.4
13.14	8.25	7.84	-4.71	-4.88	-94.2	-97.5
14.06	9.29	8.35	-3.67	-4.37	-73.5	-87.3
16.08	9.26	8.29	-3.71	-4.43	-74.1	-88.6
18.06	8.86	7.98	-4.10	-4.74	-82.0	-94.8
20.06	9.30	9.09	-3.66	-3.62	-73.2	-72.5
23.07	9.29	9.06	-3.67	-3.66	-73.5	-73.2
24.10	9.23	9.06	-3.73	-3.66	-74.6	-73.2
28.05	8.83	8.64	-4.13	-4.07	-82.6	-81.5
31.98	8.58	8.35	-4.38	-4.36	-87.6	-87.3
36.06	8.77	8.52	-4.19	-4.20	-83.8	-84.0
42.06	8.50	8.22	-4.46	-4.50	-89.3	-90.0
44.03	8.84	8.53	-4.12	-4.19	-82.4	-83.8
49.97	8.95	8.39	-4.02	-4.32	-80.4	-86.5

Table 4.2 End Reactions and Restraint Moments During the CIP Concrete Cure Period (Bridge #2)

Time Since Cast (Days)	West Reaction (Kips)	East Reaction (Kips)	Change in West Reaction (Kips)	Change in East Reaction (Kips)	West Restraint Moment (Kip-Ft)	East Restraint Moment (Kip-Ft)
(Before Cast)	6.62	6.34				
0.00	12.36	12.15	0.00	0.00	0.0	0.0
1.00	11.28	11.29	-1.07	-0.86	-21.5	-17.1
1.98	10.13	10.16	-2.23	-2.00	-44.5	-39.9
3.10	10.01	10.06	-2.35	-2.09	-46.9	-41.9
3.69	10.09	10.12	-2.27	-2.03	-45.3	-40.6
4.22	9.58	9.60	-2.77	-2.55	-55.5	-51.1
4.87	8.99	8.97	-3.37	-3.19	-67.4	-63.7
5.24	8.84	8.78	-3.52	-3.37	-70.3	-67.4
6.16	8.91	9.01	-3.45	-3.14	-68.9	-62.8
6.95	9.15	8.98	-3.21	-3.17	-64.1	-63.4
7.96	9.13	8.89	-3.23	-3.26	-64.6	-65.3
9.01	9.26	8.90	-3.10	-3.25	-62.0	-64.9
10.31	9.19	8.82	-3.17	-3.33	-63.4	-66.5
11.20	9.18	8.86	-3.18	-3.29	-63.6	-65.8
12.41	9.22	9.02	-3.14	-3.13	-62.8	-62.5
13.75	9.21	8.99	-3.15	-3.16	-63.0	-63.3
15.04	9.27	8.97	-3.09	-3.18	-61.8	-63.6
16.16	9.29	9.01	-3.07	-3.14	-61.4	-62.9
17.03	9.31	9.00	-3.05	-3.15	-61.0	-63.1
17.84	9.30	8.98	-3.05	-3.17	-61.1	-63.5
20.19	9.25	8.89	-3.11	-3.26	-62.1	-65.2
24.01	9.36	8.99	-2.99	-3.16	-59.9	-63.2
31.08	9.37	8.99	-2.99	-3.16	-59.8	-63.1
34.92	9.29	8.93	-3.07	-3.22	-61.4	-64.4
38.77	9.12	8.79	-3.24	-3.36	-64.7	-67.2
43.70	9.30	8.91	-3.06	-3.24	-61.1	-64.8

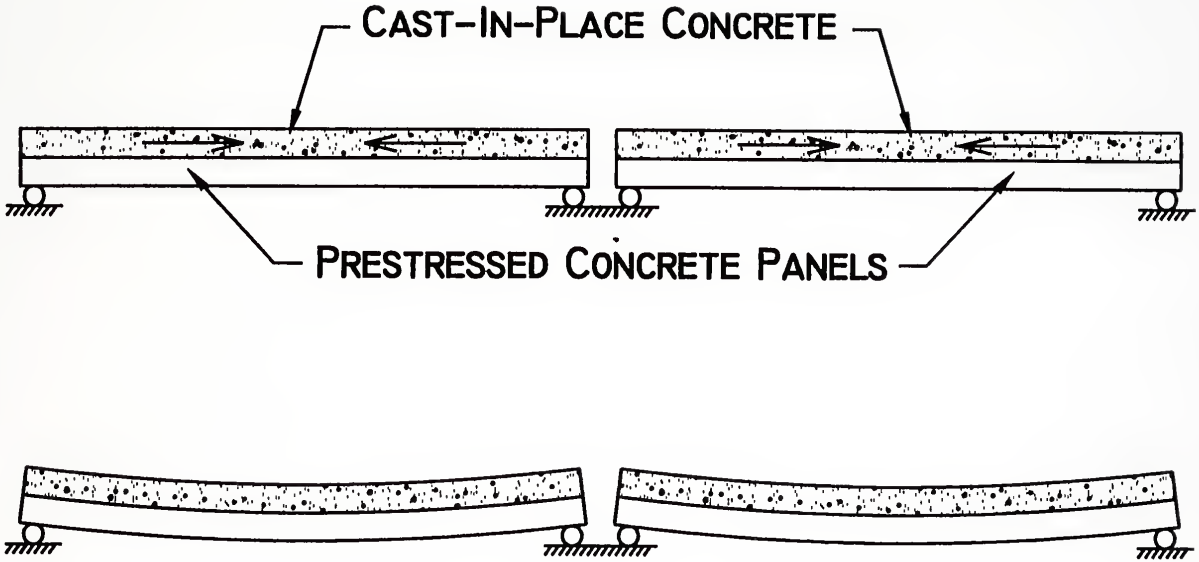

Figure 4.1 Deformation Due to Differential Shrinkage in Simple-Span Composite Construction

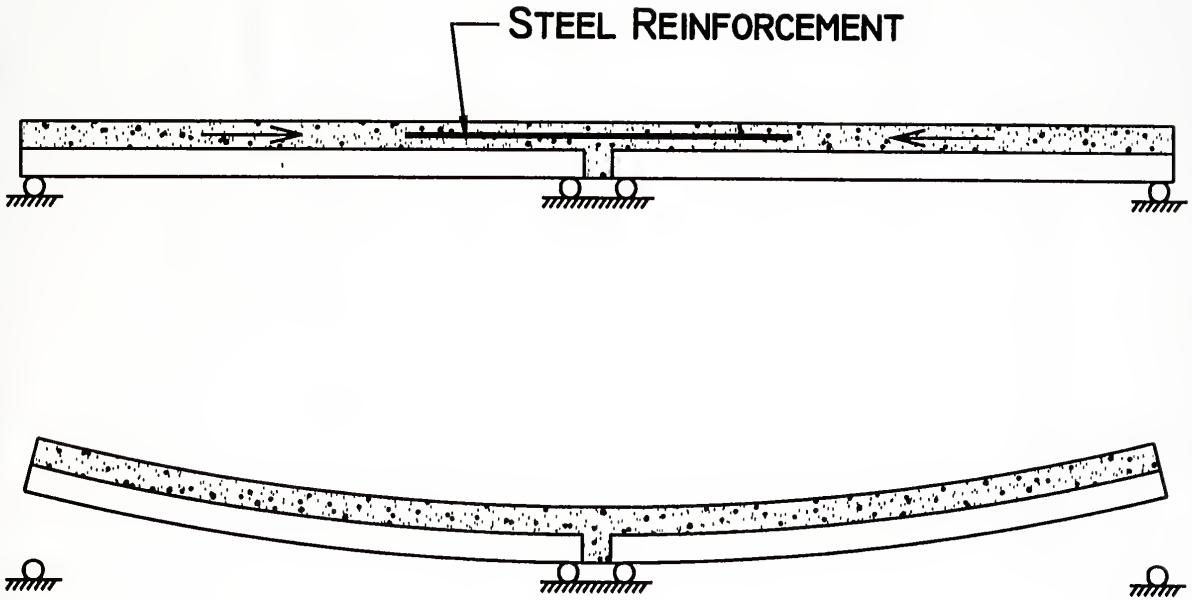

Figure 4.2 Deformation Due to Differential Shrinkage in a Composite, Two-Span Continuous Bridge

The restraint moments at the center pier of a two-span bridge due to a uniform moment can be found using the principle of superposition,

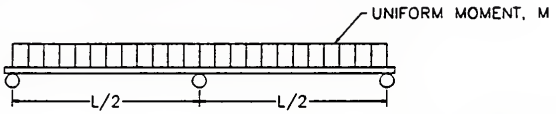

1. Remove center support.

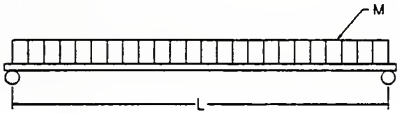

$$\phi = \frac{M}{EI}$$

$$\Delta = \frac{\phi L^2}{8} = \frac{ML^2}{8EI}$$

2. Determine applied force to return deflection to zero.

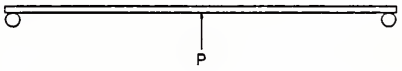

$$\Delta = \frac{PL^3}{48EI} = \frac{ML^2}{8EI}$$

$$P = \frac{6M}{L}$$

Thus, the corresponding end reactions are each

$$\frac{P}{2} = \frac{3M}{L}$$

The restraint moment, M_R is then

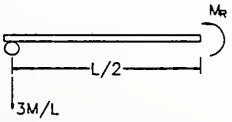

$$M_R = \frac{3M}{L}\left(\frac{L}{2}\right) = -\frac{3}{2}M$$

Figure 4.3 Calculation of Restraint Moment Due to Uniform Applied Moment

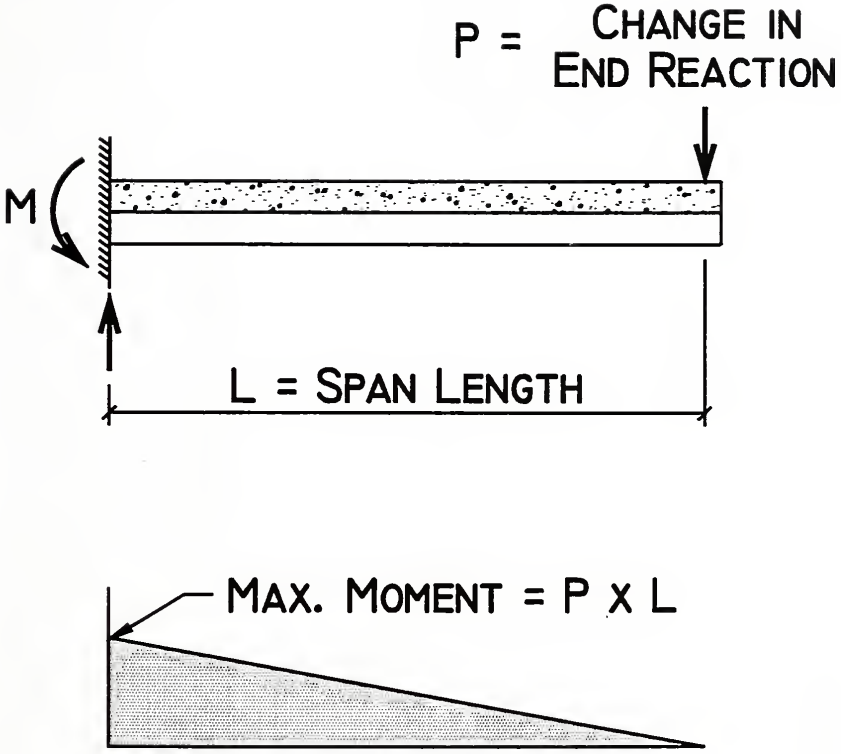

Figure 4.4 Relationship of Restraint Moments to Measured Changes in End Reactions

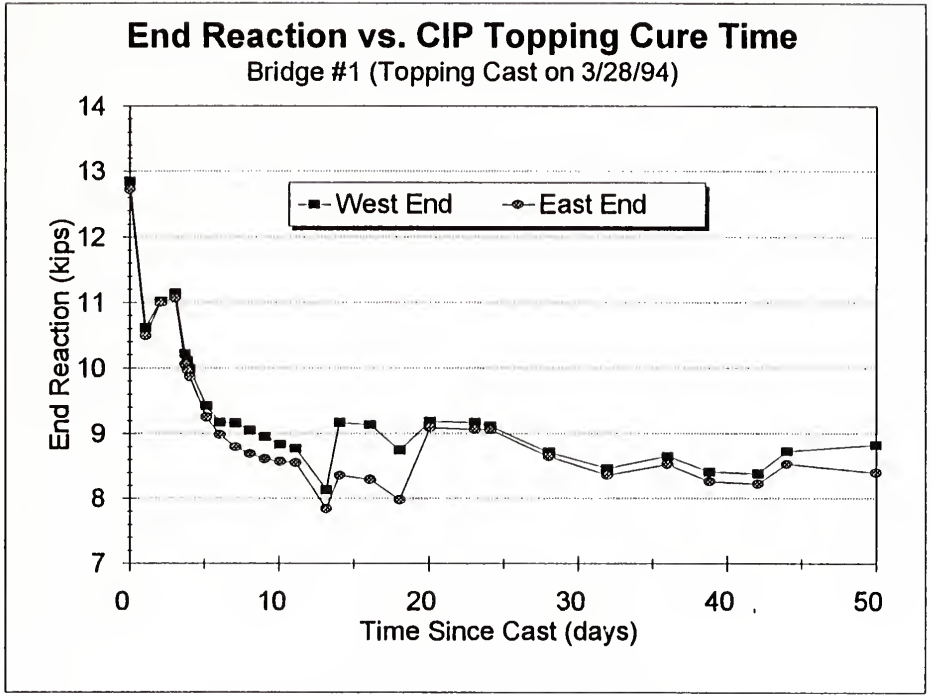

Figure 4.5 End Reactions During the CIP Concrete Cure Period of Bridge #1

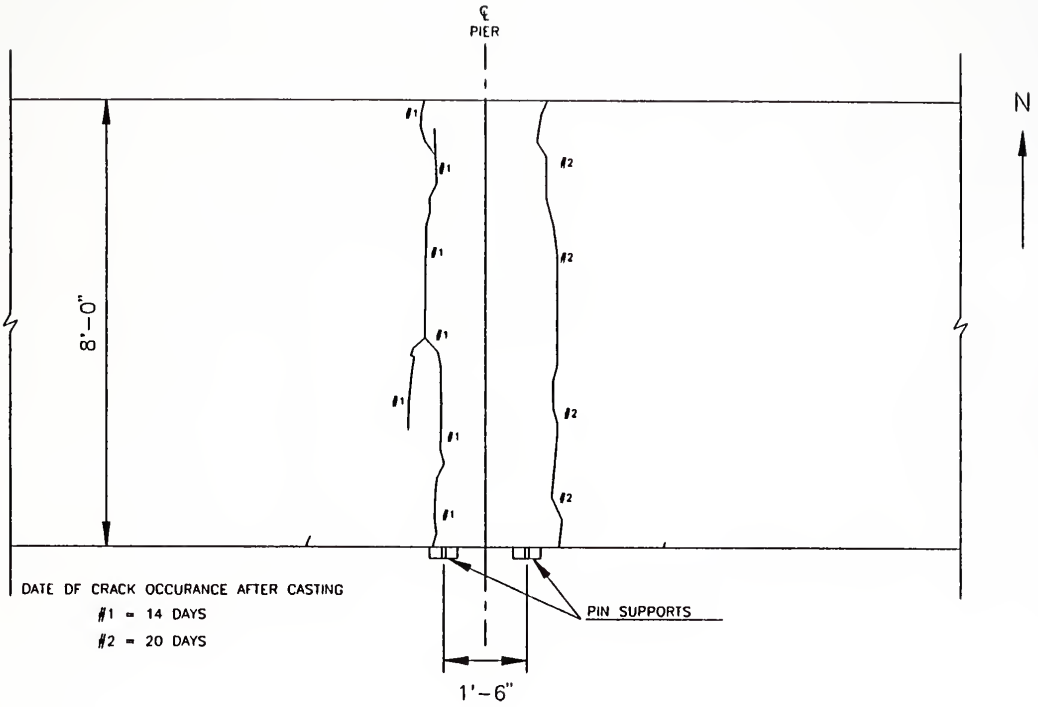

Figure 4.6 Cracking During the CIP Concrete Cure Period of Bridge #1 (Plan View)

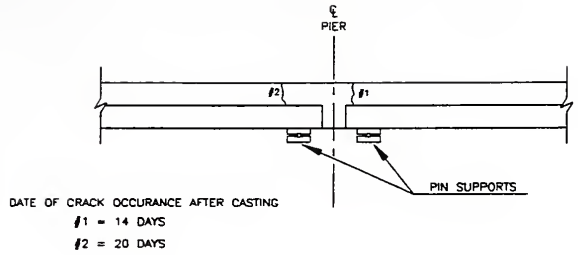

NORTH ELEVATION

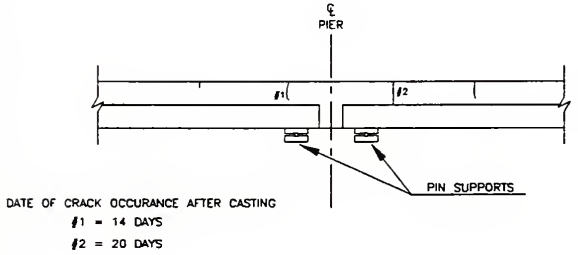

SOUTH ELEVATION

Figure 4.7 Cracking During the CIP Concrete Cure Period of Bridge #1 (Elevations)

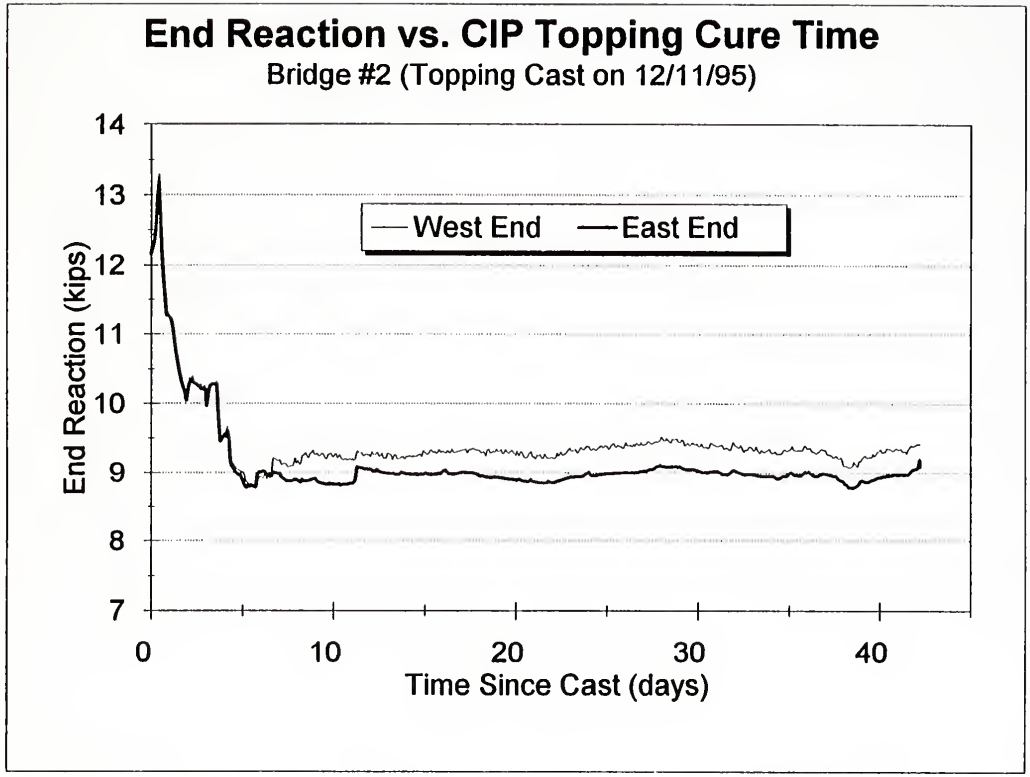

Figure 4.8 End Reactions During the CIP Concrete Cure Period of Bridge #2

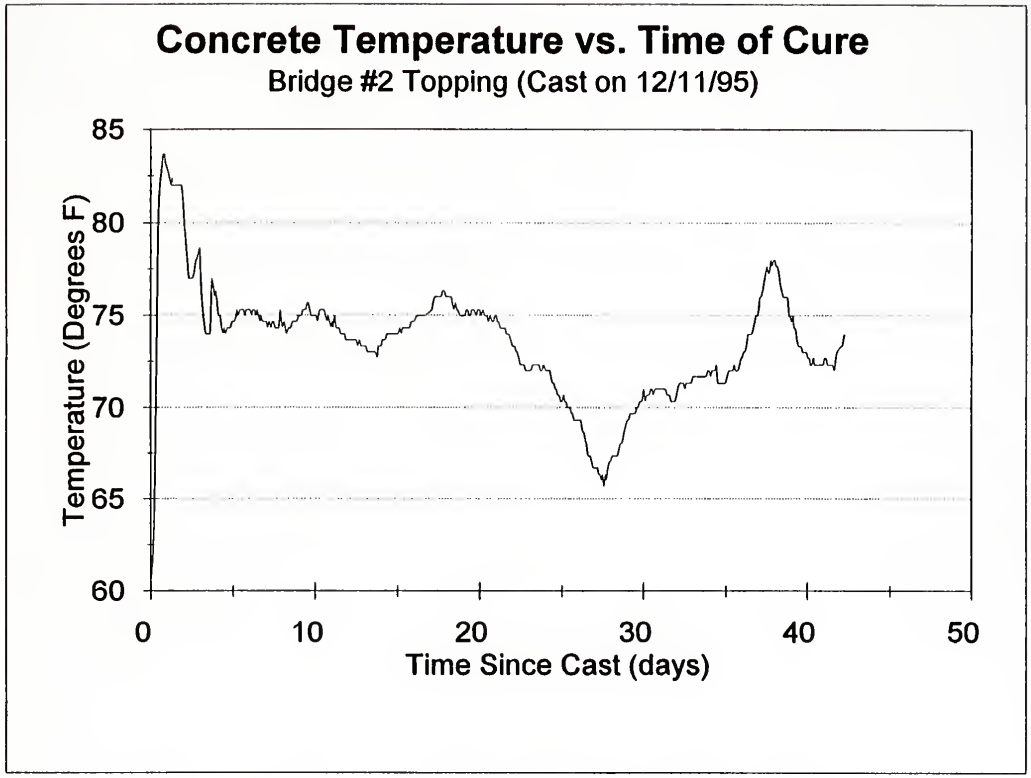

Figure 4.9 CIP Concrete Temperature During the Cure Period (Bridge #2)

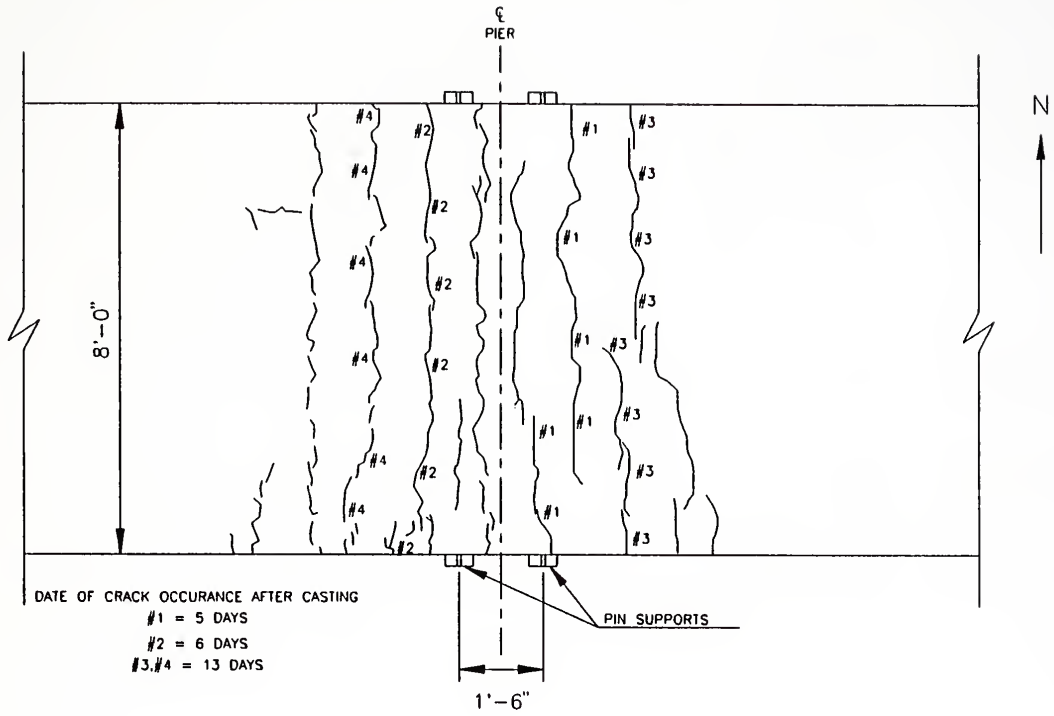

Figure 4.10 Cracking During the CIP Concrete Cure Period of Bridge #2

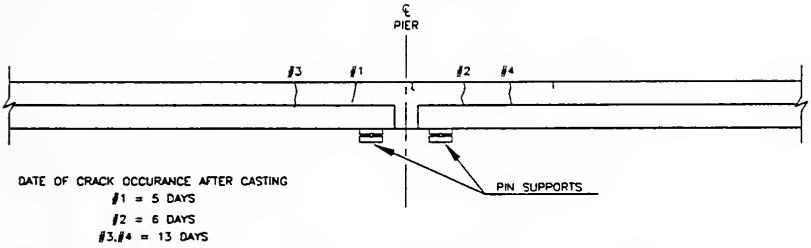

NORTH ELEVATION

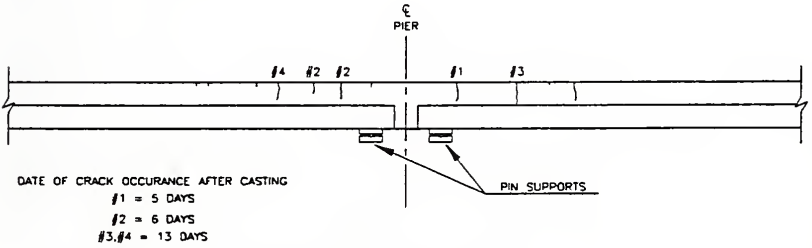

SOUTH ELEVATION

Figure 4.11 Cracking During the CIP Concrete Cure Period of Bridge #2 (Elevations)

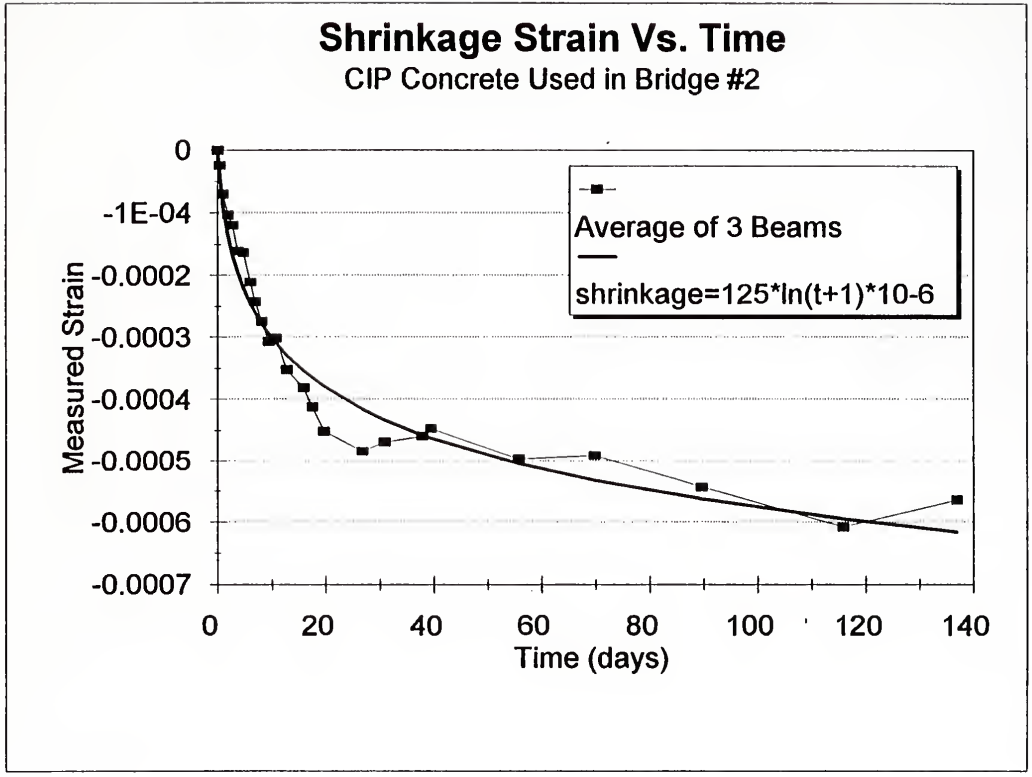

Figure 4.12 Curve Fit Through Shrinkage Beam Data from the CIP Concrete Used in Bridge #2

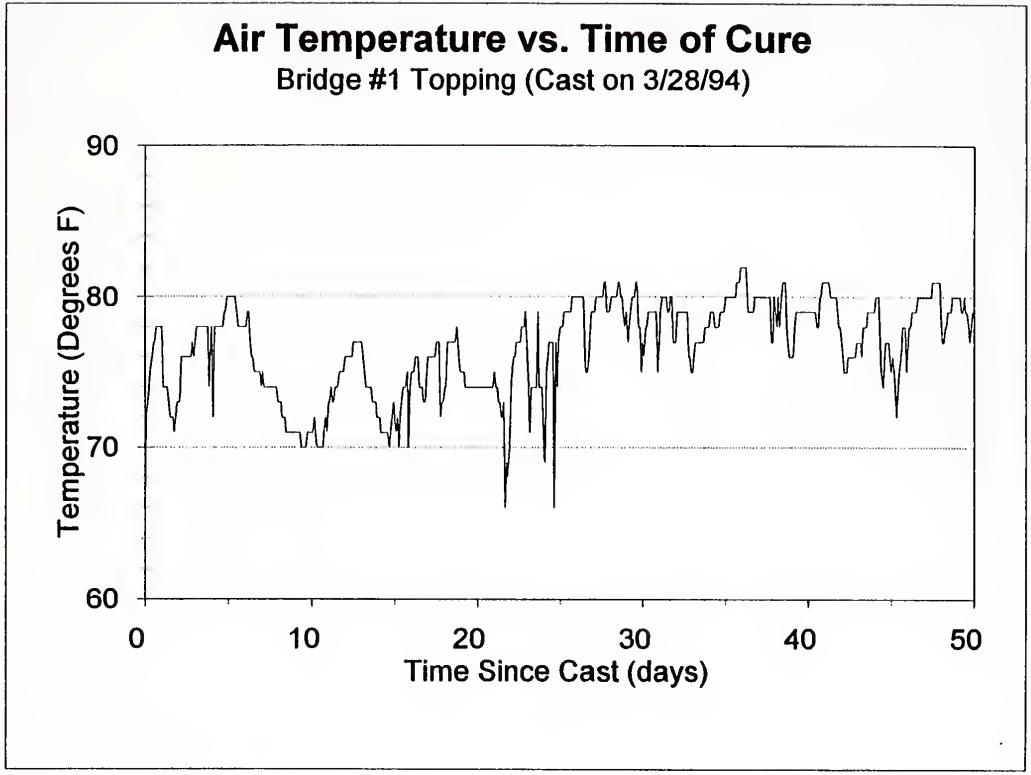

Figure 4.13 Air Temperature During the CIP Concrete Cure Period of Bridge #1

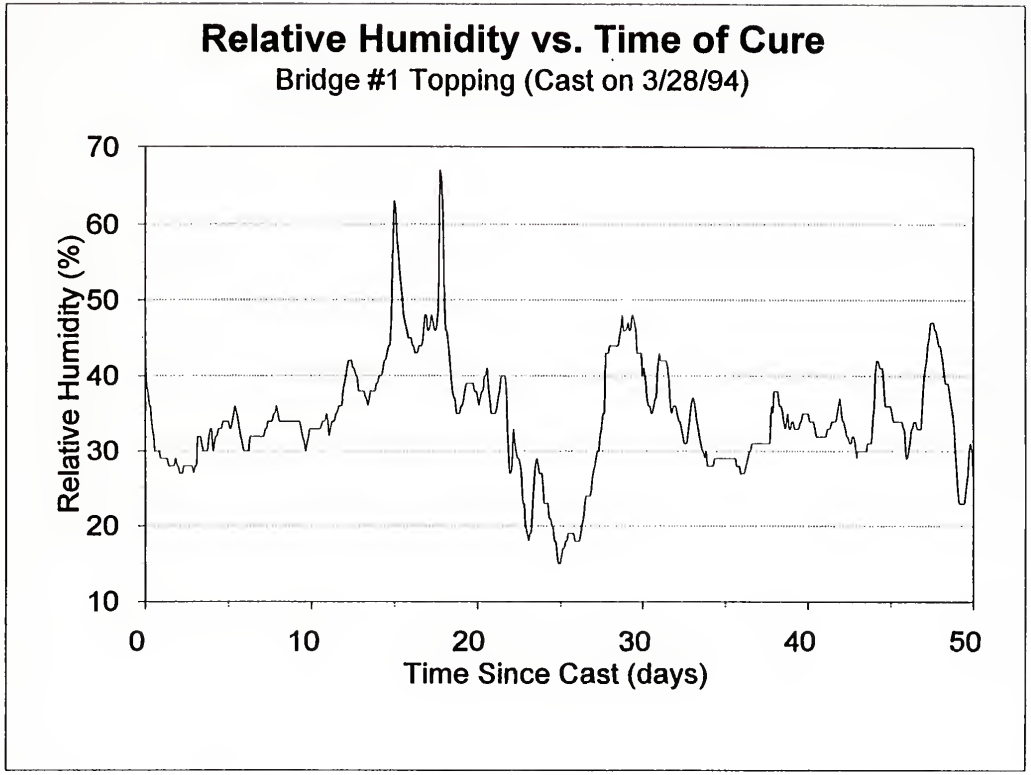

Figure 4.14 Relative Humidity During the CIP Concrete Cure Period of Bridge #1

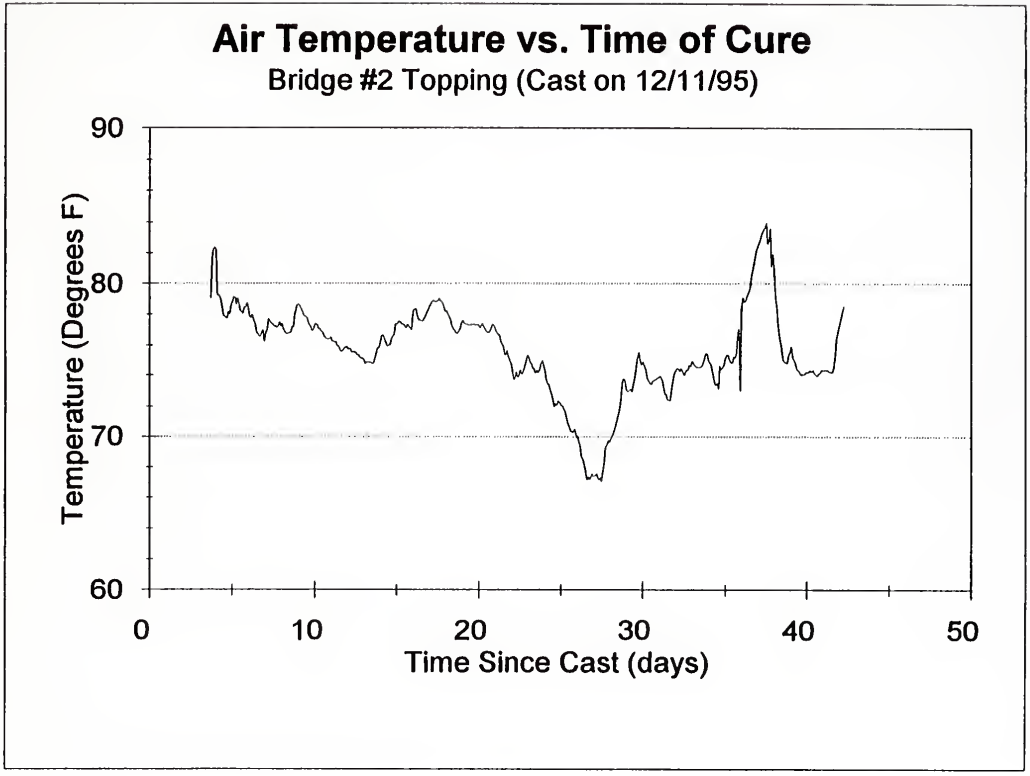

Figure 4.15 Air Temperature During the CIP Concrete Cure Period of Bridge #2

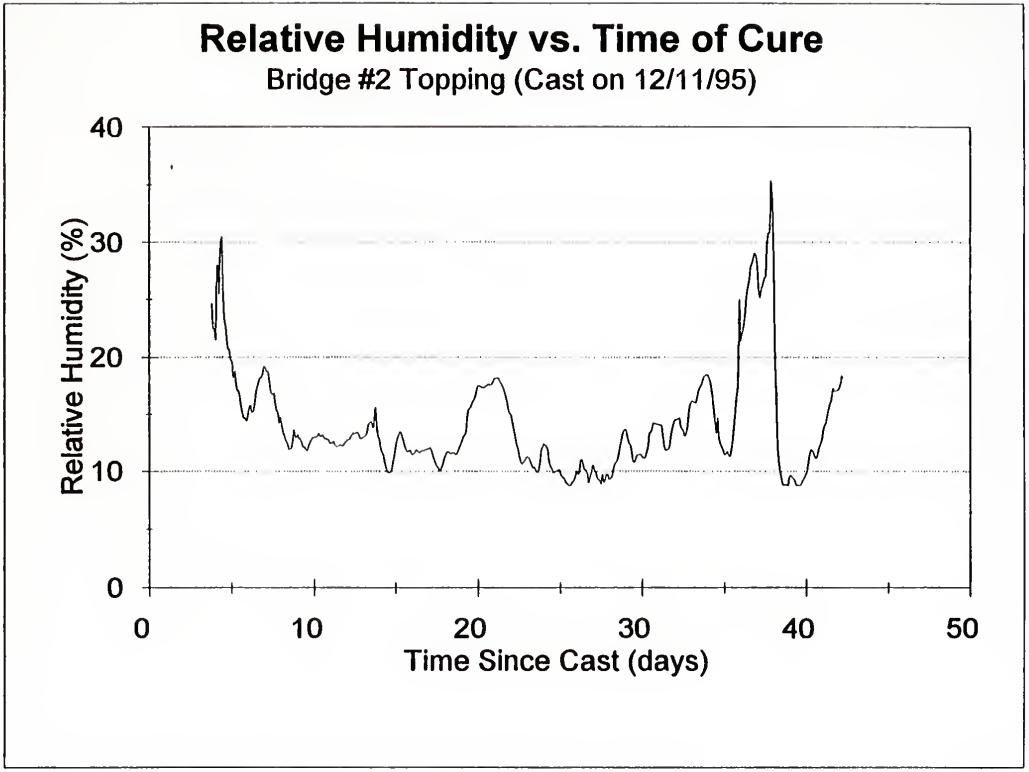

Figure 4.16 Relative Humidity During the CIP Concrete Cure Period of Bridge #2

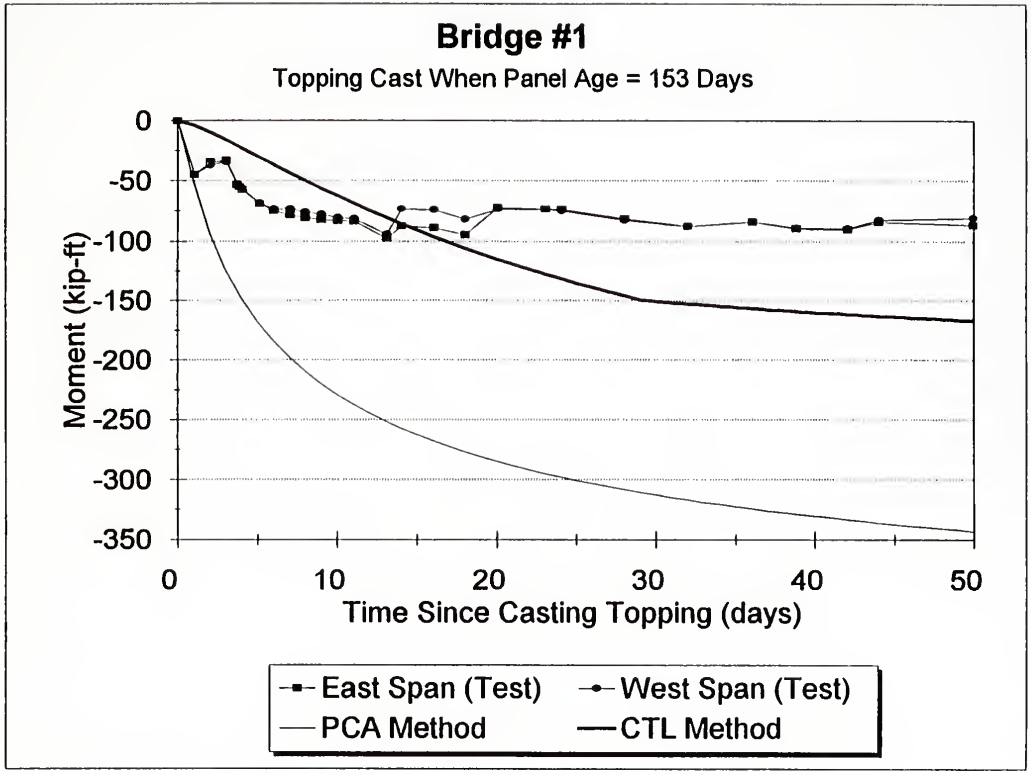

Figure 4.17 Experimentally Determined Restraint Moments and Values Calculated Using PCA and CTL Methods (Bridge #1)

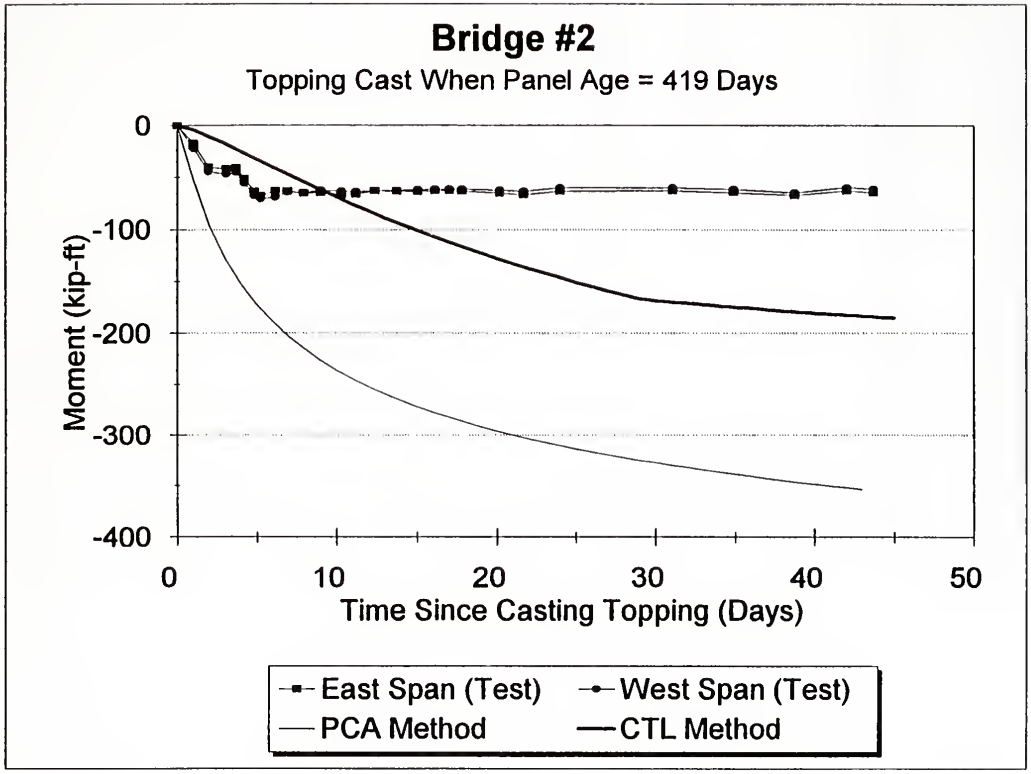

Figure 4.18 Experimentally Determined Restraint Moments and Values Calculated Using PCA and CTL Methods (Bridge #2)

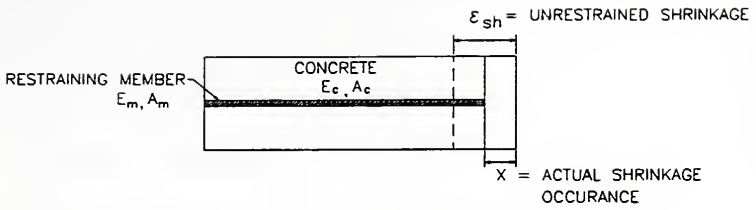

The stresses in the restraining material and the concrete are

$$f_m = \varepsilon_m E_m = xE_m \tag{1}$$

$$f_c = (\varepsilon_{sh} - x)E_c \tag{2}$$

By equilibrium of forces

$$f_c A_c = f_m A_m \tag{3}$$

which can be rewritten

$$f_c = \frac{f_m A_m}{A_c} \tag{4}$$

Substitution of Equations (4) and (1) into Equation (2) gives

$$\frac{(xE_m)A_m}{A_c} = (\varepsilon_{sh} - x)E_c \tag{5}$$

$$x\left(\frac{E_m A_m}{E_c A_c}\right) - \varepsilon_{sh} + x = 0 \tag{6}$$

$$x\left(1 + \frac{E_m A_m}{E_c A_c}\right) - \varepsilon_{sh} = 0 \tag{7}$$

$$x = \frac{\varepsilon_{sh}}{1 + \frac{E_m A_m}{E_c A_c}} = \left(\frac{1}{1 + \frac{E_m A_m}{E_c A_c}}\right)\varepsilon_{sh} \tag{8}$$

Figure 4.19 Derivation of Shrinkage Reduction Factor

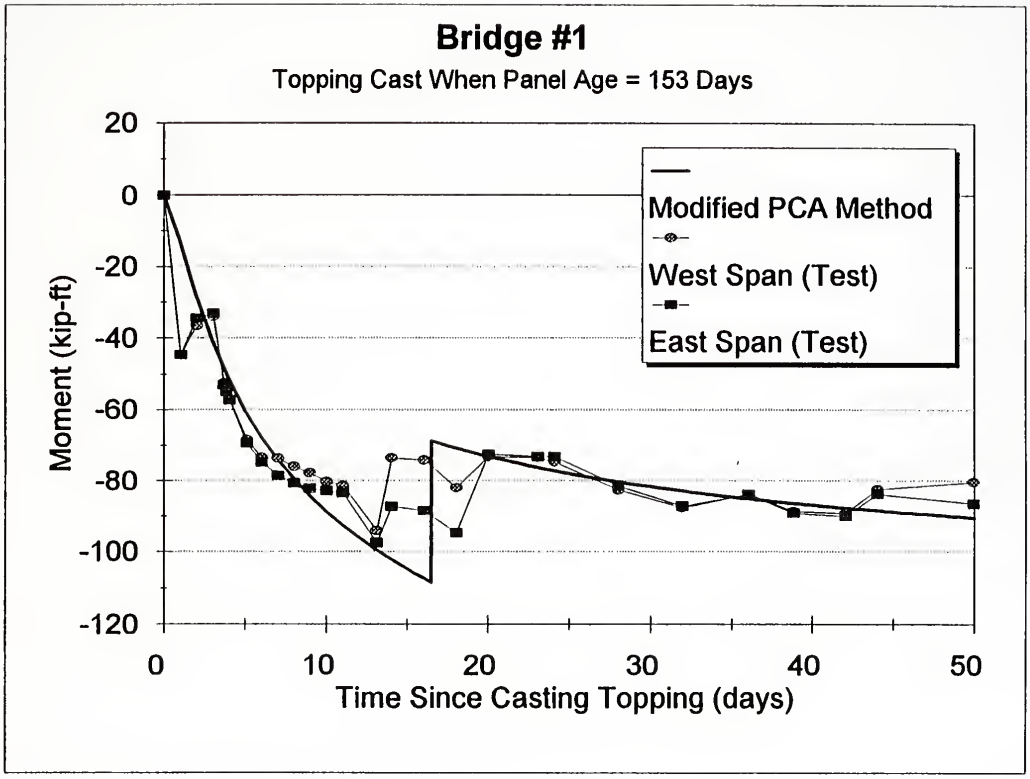

Figure 4.20 Experimentally Determined Restraint Moments and Values Calculated Using Modified PCA Method (Bridge #1)

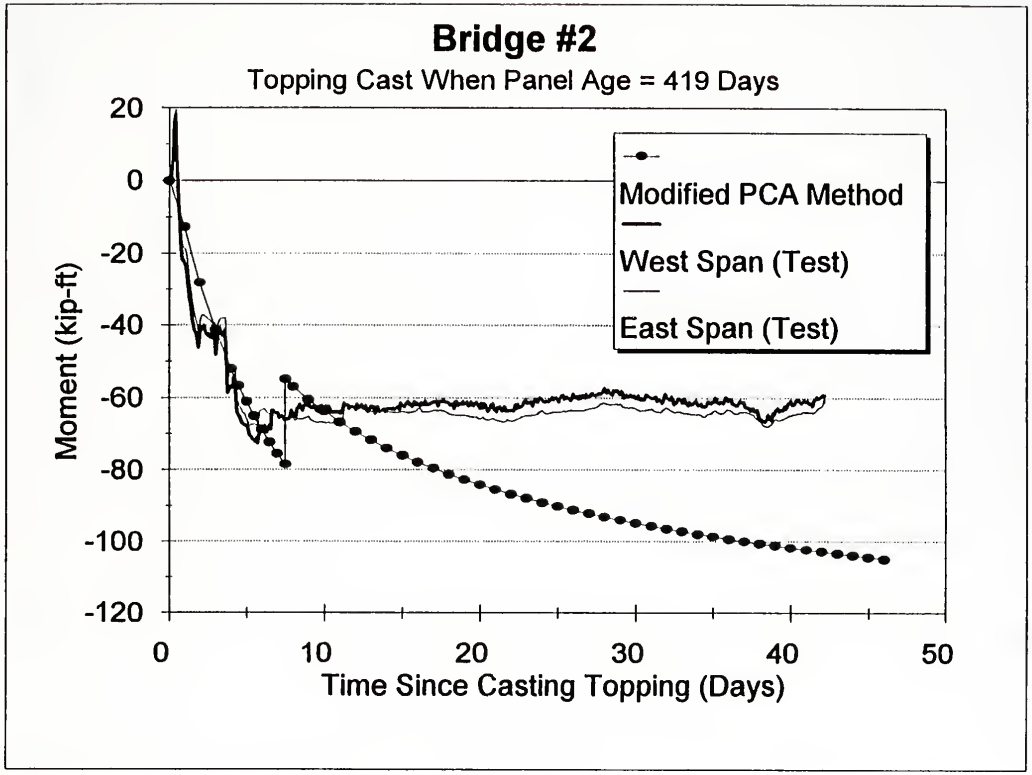

Figure 4.21 Experimentally Determined Restraint Moments and Values Calculated Using Modified PCA Method (Bridge #2)

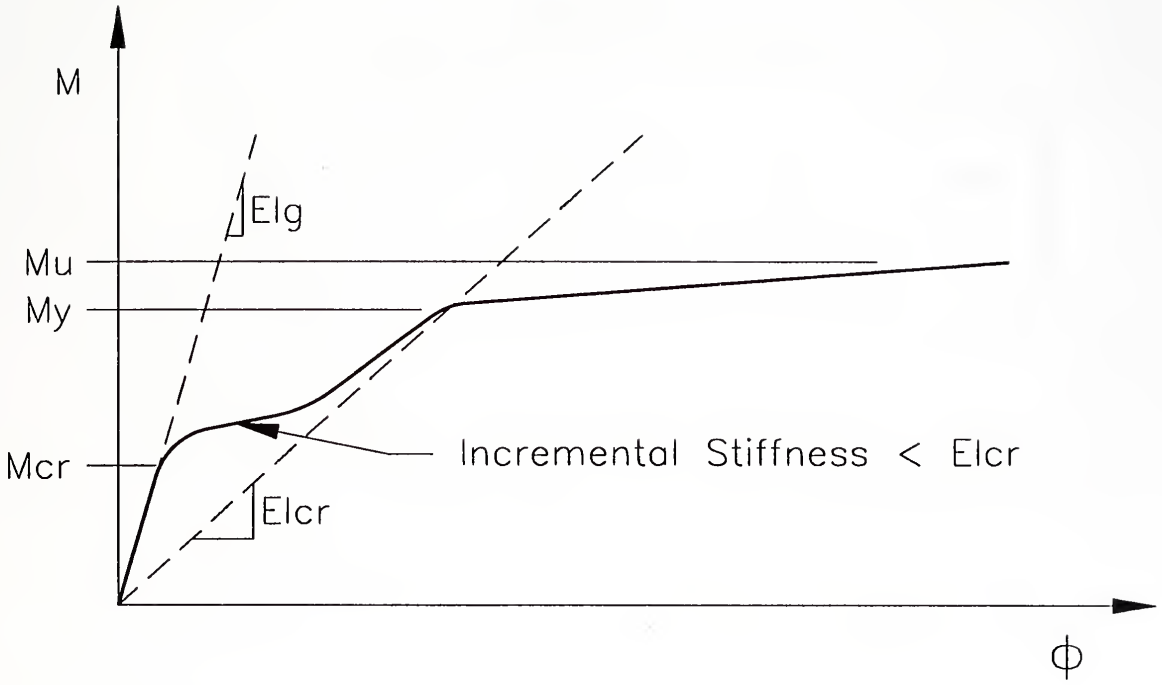

Figure 4.22 Typical Moment-Curvature Relationship of a Reinforced Concrete Beam

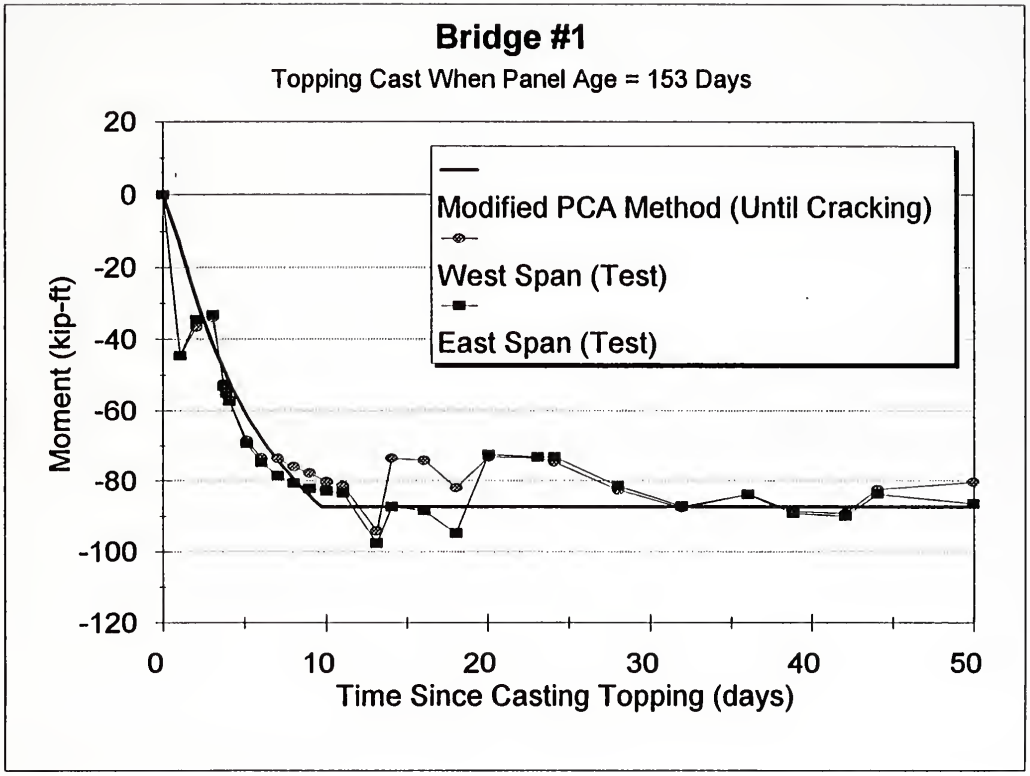

Figure 4.23 Experimental Restraint Moments and Modified PCA Method Assuming No Change After Cracking (Bridge #1)

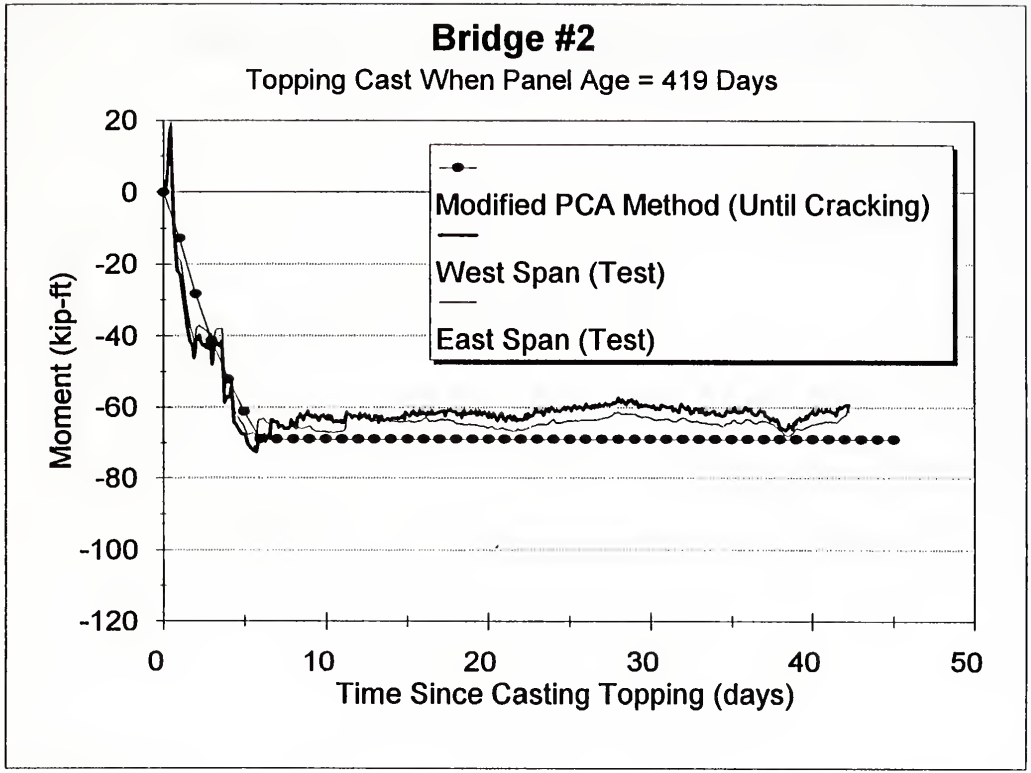

Figure 4.24 Experimental Restraint Moments and Modified PCA Method Assuming No Change After Cracking (Bridge #2)

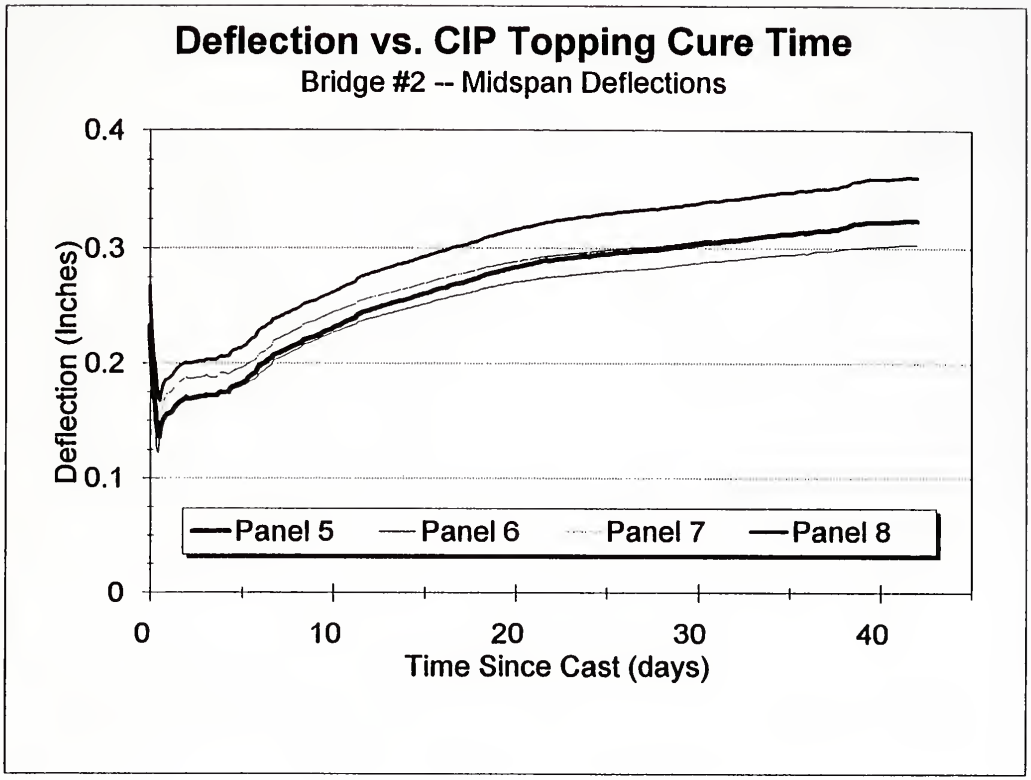

Figure 4.25 Midspan Deflections During CIP Concrete Cure Period (Bridge #2)

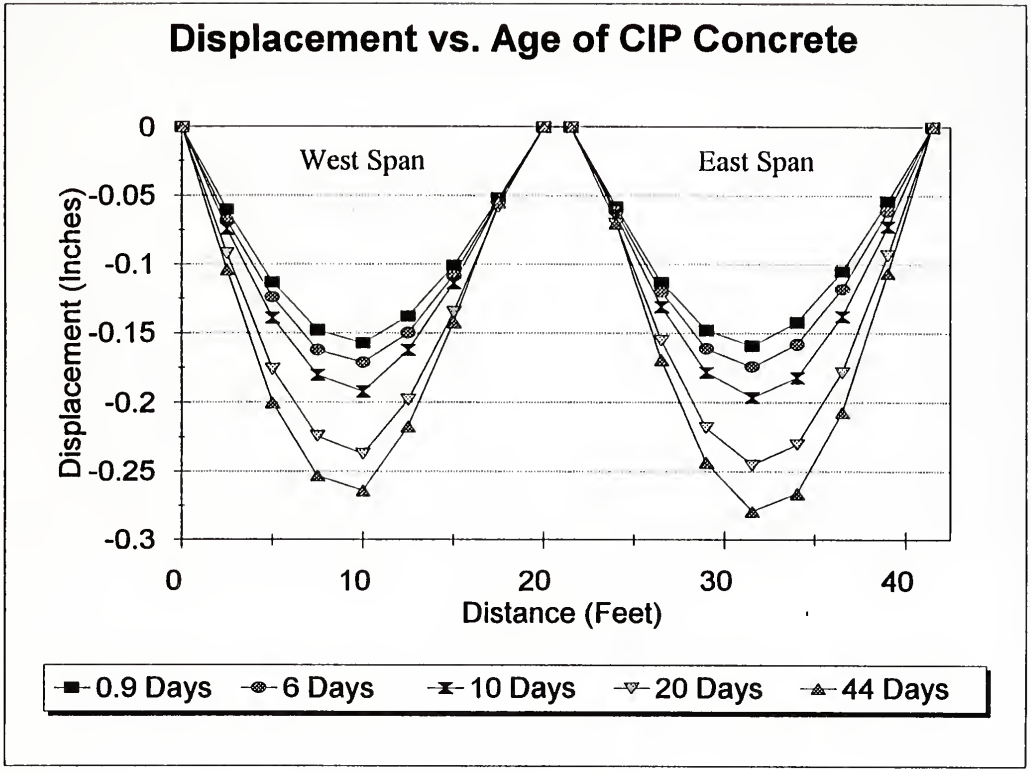

Figure 4.26 Displacement Profiles During CIP Concrete Cure Period (Bridge #2)

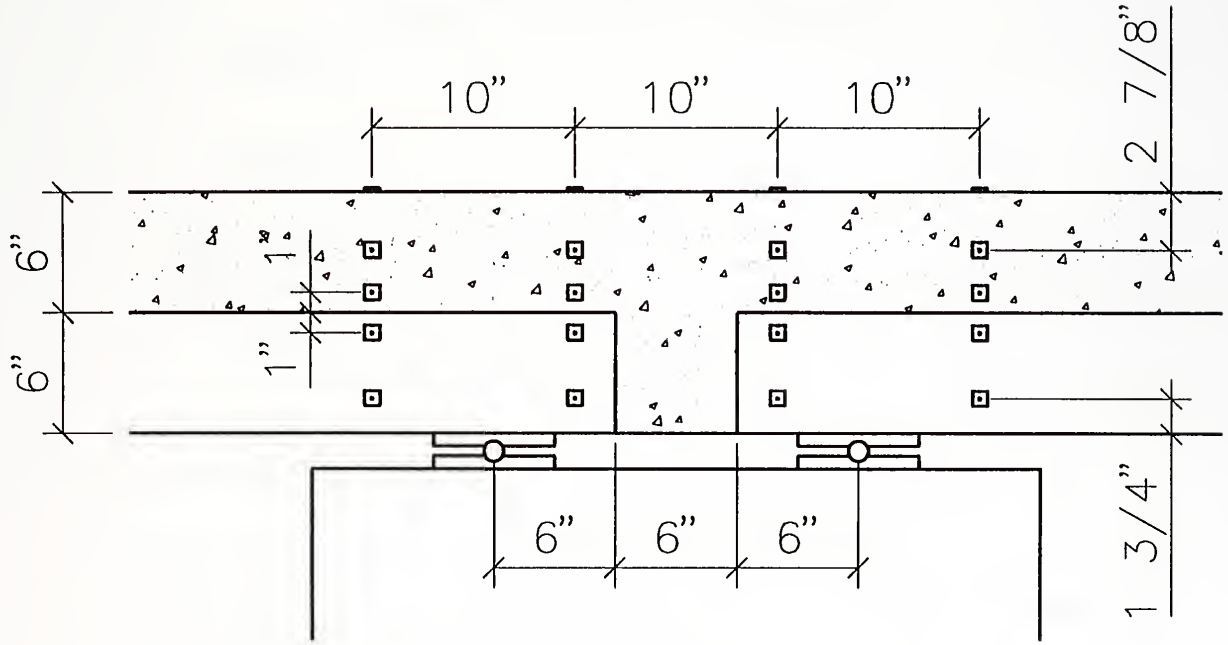

Figure 4.27 Location of Whittemore Points At Center Pier (Bridge #2)

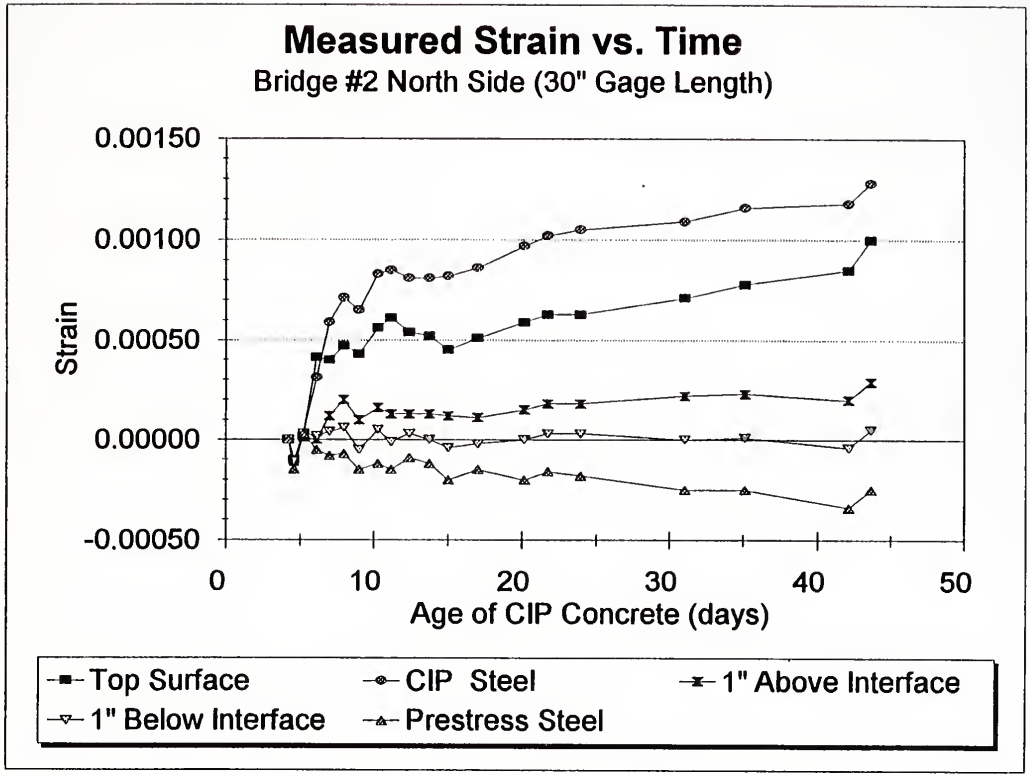

Figure 4.28 Mean Whittemore Strains During CIP Concrete Cure Period of Bridge #2 (North Face)

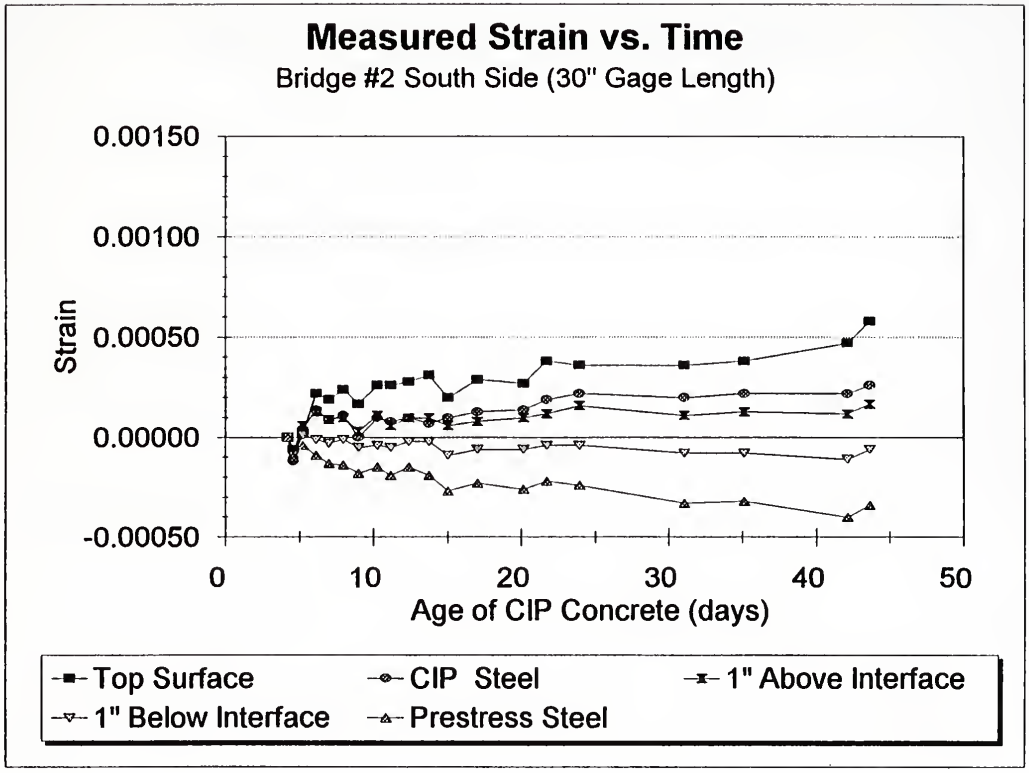

Figure 4.29 Mean Whittemore Strains During CIP Concrete Cure Period of Bridge #2 (South Face)

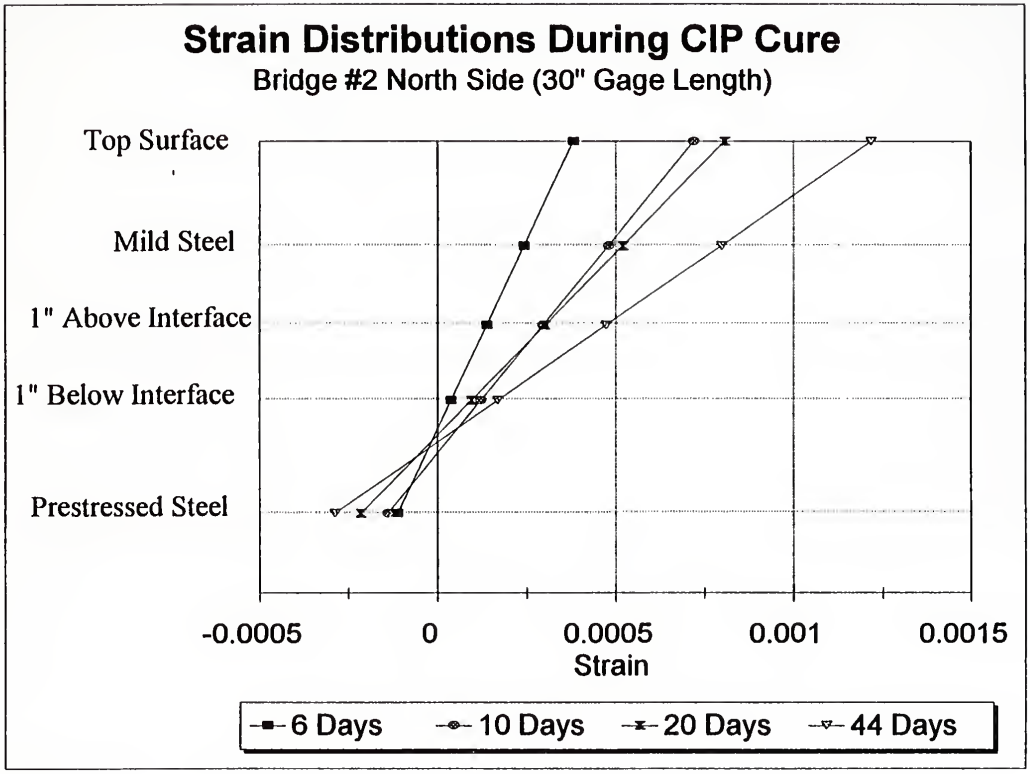

Figure 4.30 Mean Strain Distributions During CIP Concrete Cure Period of Bridge #2 (North Face)

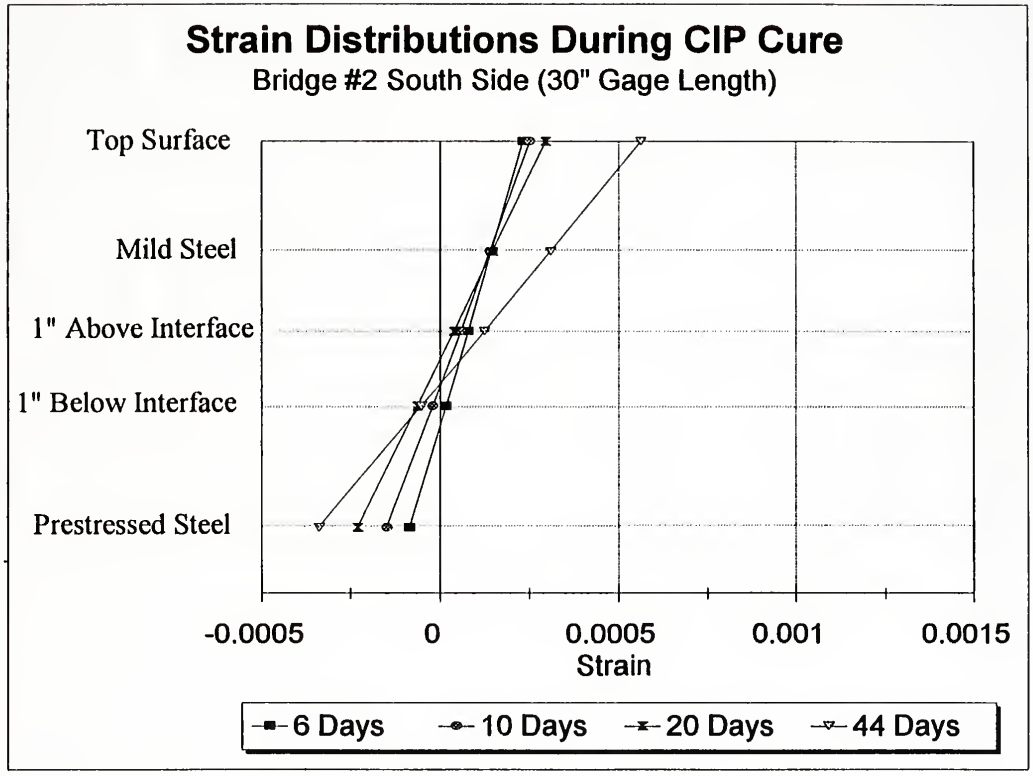

Figure 4.31 Mean Strain Distributions During CIP Concrete Cure Period of Bridge #2 (South Face)

CHAPTER 5 - RESPONSE TO SUPERIMPOSED LOADING

5.1 Introduction

At the conclusion of the cure period, each test bridge was subjected to 5 million cycles of superimposed service loading by two hydraulic actuators (one per span), followed by a monotonic loading to failure. Prior to beginning the cyclic loading, the bridges were loaded statically several times and measurements were taken in order to determine the upper and lower load levels to be used during the cyclic phase. The behavior of each bridge during these loadings is reported in section 5.2.

5.2 Initial Loadings of Bridge #1

Bridge #1 was initially loaded to 20 kips per span on 5/17/94, after 50 days of curing. Measurements of applied load, end reactions, strains, and midspan deflections were recorded at one-kip increments during the loading and unloading stages. Two large transverse cracks in the CIP topping, in addition to those observed during the cure period, occurred during this first loading. The first crack occurred at a load of 13 kips and was located on the south side of the deck, just west of the center pier. The second crack, occurring at about 19.9 kips, was located at the diaphragm and extending across the entire width of the bridge. These two cracks are shown in Figures 5.1 and 5.2, along with the cracks which occurred previously during the cure period.

5.2.1 Continuity Moments

The continuity moments (restraint moments at the center pier) were determined, by statics, from the values of the discontinuous end reactions and the applied load in each span. The values of the continuity moments during the initial loading of Bridge #1 are shown in Figure 5.3. The initial moments were -87 kip-ft and -80 kip-ft at the east and west sides of the center pier, respectively. Figure 5.3 shows that the magnitude of the continuity moments increased with increasing load until cracking. As a result of cracking at 13 kips, the continuity moments went from -118 kip-ft to -113 kip-ft on the east side of the pier and from -112 kip-ft to -104 kip-ft on the west side of the pier. These moments again increased with increasing load until cracking at 19.9 kips. This cracking reduced the moment magnitudes from -122 kip-ft and -113 kip-ft on the east and west sides of the pier at 19 kips of applied load to -90 kip-ft and -94 kip-ft on the east and west sides of the pier at 20 kips of applied load. After unloading, the restraint moments were -43 kip-ft on both sides of the pier. Thus, the initial loading (and resulting cracking) of the bridge reduced the moments due to the restraint of time-dependent deformations by roughly 50%.

Figure 5.4 shows the change in continuity moments during the initial loading for Bridge #1 compared with the values predicted by the models used in the PCA method, the CTL method, and the modified PCA method. The PCA method assumes a knife-edged support at interior piers and a constant member stiffness. The CTL method also assumes a constant member stiffness, but accounts for the length of the diaphragm. The modified PCA method accounts for both the length of the diaphragm and the reduced stiffness of the diaphragm due to cracking. These three models are illustrated in Figure 5.5. For

superimposed loading, the CTL method is identical to the modified PCA method with a diaphragm stiffness equal to that of the main spans.

Figure 5.4 shows that the increase in continuity moments during the first loading, and before cracking, falls between the values predicted by the CTL method, having a constant member stiffness, and the modified PCA method with the moment of inertia of the diaphragm equal to the cracked transformed moment of inertia (Icr). After cracking, however, the actual continuity moments are well below the moments predicted by all three methods. This is because the additional cracking releases part of the restraint moment which was previously carried by the concrete in tension. The result is an apparent diaphragm stiffness which is less than Icr.

Figure 5.6 shows the changes in continuity moment during the second loading of Bridge #1. The figure shows that these continuity moments can be predicted by using the modified PCA method with a diaphragm stiffness between Icr and Icr-top, where Icr-top is the moment of inertia of the section calculated assuming a crack depth equal to the depth of the CIP topping. This is because there were no additional cracks which opened since the first loading. All subsequent loadings prior to the cyclic loading period produced similar continuity moments.

5.2.2 Midspan Deflections

Midspan deflections of Bridge #1 were measured at the center of the bridge (over the panel joint), and at each edge. Figures 5.7 and 5.8 show the measured deflections in the east and west spans, respectively, for the initial loading of Bridge #1. These figures

show that deflections increased at a near constant rate until cracking. Deflections increases slightly due to the crack at 13 kips and considerably due to the crack which opened up at 19.9 kips. These figures also indicate that the deflections due to the 20 kip applied load were essentially the same across the width of the bridge. In these figures, the northwest, southwest, northeast, and southeast LVDTs were at the edge of the bridge and the east and west LVDTs were located at the center of the bridge. These uniform deflections indicated the entire width of the slab is effective in resisting the applied load. Figures 5.7 and 5.8 also show that the deflections associated with cracking remained in the structure after unloading. This permanent deformation was about 0.03 inches for the west span and about 0.025 inches for the east span.

Figure 5.9 shows a comparison of the measured displacements due to the initial loading with those predicted by the models previously discussed. As expected, the PCA and CTL methods, which use gross section properties, underestimated the actual deflections as the load increased and more cracking occurred. The proposed modified PCA method, which uses a reduced stiffness at the diaphragm region, was better at predicting the deflections but still underestimated the deflection at maximum load. This is because the restraint moment at the pier decreased with cracking. In section 5.2.1 it was noted that the magnitude of the restraint moments decreased from 87 kip-ft and 80 kip-ft at the east and west faces of the pier to 43 kip-ft at both faces during the initial loading. For deflection calculations, this is equivalent to applying positive moments at the center pier of 44 kip-ft and 37 kip-ft at the east and west sides, respectively. Figure 5.10 illustrates this principle. Using the modified PCA method, with a fully cracked section at

the diaphragm and the addition of the positive moments shown in figure 5.10, the calculated midspan deflections at 20 kips of applied load are 0.076 inches and 0.075 inches for the east and west spans, respectively. This agrees well with the corresponding measured deflections of 0.078 and 0.070 inches.

Figure 5.11 shows the incremental deflections corresponding to the second loading of Bridge #1. For this loading, and all other loadings prior to cycling, the measured deflections fell between those predicted by the CTL method and the modified PCA method with a stiffness corresponding to a crack depth equal to the CIP topping thickness.

5.2.3 Strain Measurements

In addition to the location of cracks which occurred during the first loading of Bridge #1, Figure 5.1 shows the location of the strain gages on the longitudinal steel reinforcement in the topping with respect to these cracks. The incremental strains recorded at three of these gages, located near the crack which opened at 13 kips, are shown in Figure 5.12. These gages show that the strain in the steel reinforcement at these locations increased linearly until about 10 kips. Between 10 and 13 kips the reinforcement strain increased at a at a faster rate with increasing load. At 13 kips there was a sudden increase in steel strain because of the transfer of concrete tensile forces to the reinforcement. The increase is about 300 microstrain, which represents a change in stress of about 8.7 ksi. This value is considerably less than the change estimated using elastic theory for a fully cracked section (42 ksi). This is because the section was not "fully cracked," as the crack did not extend across the full width of the bridge. Also, the gages

were located several inches from the crack. Therefore, at the gage locations, the concrete was carrying a portion of the tensile force. After cracking, the strains increased at a faster rate until cracking at 19.9 kips. The crack which opened at the diaphragm reduced the continuity moment at the pier, and the corresponding reinforcement stresses (and strains) decreased. Upon unloading, the strains in the reinforcement decrease linearly with load.

Figure 5.13 shows the change in strains at gages located near the crack which occurred at 19.9 kips. This figure shows that strains increased with load in a near linear manner until cracking, then greatly increased as tensile forces were transferred from the concrete to the steel. The incremental strain in the steel prior to cracking was about 50 microstrain, corresponding to a steel stress of 1.5 ksi. After cracking, strains were approximately 950 microstrain, indicating a steel stress of 27.5 ksi. The calculated reinforcement stress at the measured continuity moment, using elastic theory and a fully cracked section, was 38.5 ksi. Again, the gages were several inches away from the crack so the full calculated steel tension was not realized at these locations. Also, the strains shown in Figure 5.13 are incremental strains due to the applied load. Initial steel strains associated with the development of the restraint moment during the cure period are not reflected in this graph.

5.3 Initial Loadings of Bridge #2

Bridge #2 was initially loaded to 20 kips per span on 1/24/96, after 44 days of curing. Measurements of applied load, end reactions, strains, and midspan deflections were recorded at one-kip increments during the loading and unloading processes. In

addition, Whittemore gage readings were taken at two-kip increments during the loading stage, and three times during the unloading period. Only one new crack was observed during this initial loading. This crack, which occurred at a load of 8 kips, was located at the east side of the diaphragm region on the south side of the deck. The depths of this new crack and one existing crack at the pier increased to about 9 inches as the load increased to 20 kips. The cracking corresponding to this initial loading is shown in Figures 5.14 and 5.15.

5.3.1 Continuity Moments

The continuity moments during the initial loading of Bridge #2, which were determined in a similar manner as for Bridge #1, are shown in Figure 5.16. The initial moments were -61 kip-ft at the west side of the pier and -64 kip-ft on the east side of the pier. These moments increased in magnitude with applied load until additional cracking at 8 kips. Prior to this cracking, the continuity moments were 74 kip-ft and 75 kip-ft at the east and west sides of the center pier, respectively. These moments decreased to 67 kip-ft and 66 kip-ft because of the cracking. The moment magnitudes then became larger as the load was increased to 20 kips. During this additional loading, the rate of moment increase on the west side of the pier was greater than for the moment on the east side, as the newly formed crack was at the east side of the diaphragm. At 20 kips, the moments at the east and west sides of the pier were -89 kip-ft and -83 kip-ft, respectively. After unloading, the restraint moments were -44 kip-ft on both sides of the pier. This was essentially the same value as the moments in Bridge #1 after the initial loading to 20 kips (see Figure 5.3).

Thus, while Bridge #1 had initial restraint moments that were about 30 percent higher that those for Bridge #2, the superimposed loading served to "equalize" the two structures in terms of remaining continuity moments at service load.

Figure 5.17 shows the change in continuity moments during the initial loading of Bridge #2, along with the values predicted using the PCA, CTL, and modified PCA methods. As with Bridge #1, all three methods overestimate the increase in moments because the restraint moments are released by additional cracking. Initially, the change in continuity moments falls between the values predicted by the CTL method and the modified PCA method (assuming a fully cracked diaphragm region). At about 4 kips of applied load there is a decrease in the continuity moments (towards the values predicted by the modified PCA method). Since there were no observed cracks with this loading, this was believed to be caused by an increase in the depth of existing cracks. Between 4 kips and 8 kips, the observed increase in continuity moments is represented by the line corresponding to the modified PCA method. The cracking at 8 kips of applied load further reduces the continuity moments, with the largest change occurring at the east side of the pier (the side closest to the crack).

The change in continuity moments during the second loading of Bridge #2 are shown in Figure 5.18. During this loading, and all other loadings prior to cycling, the change in continuity moments is basically linear with applied load. The increase in moments at the west side of the pier is best represented by the modified PCA method, with a diaphragm stiffness based on a crack depth equal to the CIP topping thickness. The

increase in moments at the east side of the pier due to applied load, however, can be better represented by the modified PCA method assuming a fully cracked diaphragm.

5.3.2 Midspan Deflections

Figures 5.19 and 5.20 show the measured deflections in the east and west spans, respectively, for the initial loading of Bridge #2. These figures show a gradual increase in deflections in each span throughout the loading with the exception of the sudden change at an applied load of 8 kips, due to the additional cracking. The total midspan deflection at 20 kips of loading was about 0.09 inches for both spans. After unloading, a deformation of about 0.03 inches remained in each span. These figures show that the deflections were essentially constant across the width of the structure in the both spans, as was noted for Bridge #1.

Figure 5.21 compares the measured deflections with the values predicted using the PCA, CTL, and Modified PCA methods. This figure shows that all models underestimated the displacement at 20 kips of applied load. The modified PCA method, with a fully cracked diaphragm, did a good job at predicting the displacements prior to cracking at 8 kips. After cracking, the measured displacement response is essentially parallel to the line representing this method. As noted in section 5.2.2, a decrease in restraint moments at the pier has the same effect on displacements as applying a positive moment of equal value. For Bridge #2, the initial restraint moments of -64 kip-ft and -61 kip-ft at the east and west sides of the pier were reduced in magnitude to -44 kip-ft after the first loading. Using the modified PCA method, with a fully cracked diaphragm and

applied positive moments of 20 and 17 kip-ft at the east and west sides of the pier, the calculated deflections are 0.070 and 0.069 inches for the east and west spans, respectively. This is still less than the measured displacements of 0.089 and 0.086 inches. However, these values reflect the time dependent deformations caused by sustaining the load while Whittemore measurements were taken. These appear as horizontal segments in the measured deflection curves at every two kips of load. The totals of these incremental deflections due to sustained load, not including the values at 8 kips associated with cracking, are 0.016 inches for both spans. By subtracting out these values, the instantaneous deflections due to the applied load are calculated as 0.073 inches for the east span and 0.070 inches for the west span. These values agree well with the deflections of 0.070 and 0.069 inches, calculated using the modified PCA method with a fully cracked diaphragm and applied moments equal to the decreased restraint moments.

Figure 5.22 shows the incremental deflections due to the second loading of Bridge #2. These measured displacements are essentially the same as those predicted by the modified PCA method with a fully cracked diaphragm. Slight deviations from the predicted values occur at 5, 10, and 15 kips of load due to time-dependent deflections associated with Whittemore gage readings.

5.3.3 Strain Measurements

Figure 5.23 shows the change in strains at gages located on the longitudinal reinforcement at the center of the pier. The position of these gages with respect to transverse cracks is shown in Figure 5.14. All the gages in Figure 5.23 indicate a large

increase in strain was associated with the crack that occurred at 8 kips of load. This crack, which occurred at the south side of the bridge, was the extension of an existing crack located on the north side (see Figure 5.14). Thus, there was an earlier increase in strains at the gages located at the north side of the bridge, prior to the extension of the crack to the full width. This can be seen from Figure 5.23, where gages T-Long-5C and T-Long-6C show large increases in strain after only 3 kips of applied load. Gages T-Long-1C and T-Long-2C show larger increases in strain at 8 kips of applied load, when the crack extended to the full width.

The strain measurements shown in Figure 5.23 indicate an average incremental strain at 20 kips of about 1000 microstrain, corresponding to a steel stress of 29 ksi. The stress in the steel reinforcement at this load (which produced continuity moments of -89 and -83 kip-ft at the east and west sides of the pier) was calculated to be about 44 ksi assuming a fully cracked section. The measured incremental strains indicated a lower stress at the gages locations because the gages were not located directly at the cracks, and because the incremental values do not include the strains associated with to the initial restraint moments.

Figure 5.24 shows the mean strains (occurring over a 30 inch gage length) determined from Whittemore strain gage readings at the level of the mild steel reinforcement. The Whittemore readings correlate well with the data in Figure 5.23, obtained from electrical resistance strain gages. Figure 5.24 shows that the rate of strain increase was greater at the north side of the pier between applied loads of 2 and 6 kips, as the existing cracks widened. The crack, which opened at 8 kips, then caused a large

increase in strain at the south face of the pier. After cracking, strains increases at essentially the same rate until the maximum load of 20 kips was reached. At this load, the mean strains were approximately 0.0016 (1600 microstrain) at both sides of the pier. This strain corresponds to a steel stress of 46 ksi. Since the Whittemore gage measures the strain occurring at the face of the concrete, it is not necessarily equal to the average strain in the reinforcement, which was located at a distance of 8 inches from the surface in this case. Therefore, the average strain in the steel reinforcement is believed to have been lower than 46 ksi since the crack widths which contributed to the Whittemore readings would have been smaller at the surface of the reinforcement. Also, the Whittemore gage readings include slip between the steel reinforcement and the concrete and therefore overestimate the average strain in the reinforcement.

5.4 Summary of Initial Loadings

The restraint moments (induced by creep and shrinkage) decreased during the initial loading of each bridge due to additional transverse cracking at the pier. There was a 49% decrease in the restraint moments for Bridge #1, which had higher initial restraint moments and fewer initial cracks than Bridge #2, and a 30% decrease for Bridge #2. Because of cracking, the PCA, CTL, and modified PCA methods overestimated the increase in continuity moments for each bridge during this initial loading. For subsequent loadings which did not produce additional cracking, the modified PCA method (which assumed a diaphragm stiffness based on a section having a crack depth equal to the thickness of the CIP topping) gave a reasonable estimate of the change in continuity

moments. Both the PCA and CTL methods, which are based on gross section properties, considerably overestimated the additional continuity moments.

Similarly, due to the additional cracking and corresponding decrease in restraint moments, all three methods underestimated the midspan deflections caused by the initial loadings of each bridge. Values equal to these observed deflections could be obtained using the modified PCA method, assuming a fully cracked diaphragm region, with applied positive moments at the pier that were equal in magnitude to the measured decrease in restraint moments. Midspan deflections due to subsequent loadings could be reasonably estimated by using the modified PCA method, assuming a fully cracked diaphragm.

5.5 Overview of Cyclic Loading

Each bridge was subjected to 5 million cycles of service loading in order to evaluate the effects of repeated loading on the degree of continuity at interior piers. Any "softening" at the pier locations would be manifested in larger deflections and end reactions for a given load. The load levels used for the cyclic loading of each bridge were chosen so that the maximum stress in the longitudinal steel over the pier ranged from approximately 26 ksi to 44 ksi. The value of 26 ksi was believed to be an conservative estimate of the service load stress at cracked sections of lightly reinforced members due to dead loads. The upper limit of 44 ksi corresponded to a stress range of 18 ksi, which is equal to 120% of the maximum allowable design reinforcement stress range designated by AASHTO section 5.5.3.2.1 [3]. This stress range was believed to represent a worst case scenario of repeated loadings in excess of the design service load.

The moments corresponding to steel stresses of 26 and 44 ksi were determined for each bridge by elastic analysis using the following assumptions:

- Plane sections remain plane
- Full bond exists between the concrete and the steel reinforcement
- The concrete carries tension until strains reach the cracking strain and then carries no tension. The cracking strain assumed was 0.00014 (based of a modulus of rupture of 650 psi and an elastic modulus of 4500 ksi).

Using these assumptions, the magnitudes of the lower and upper cycling moments were determined to be 65 kip-ft and 104 kip-ft for Bridge #1, and 56 kip-ft and 87 kip-ft for Bridge #2. Each bridge was loaded several times after the initial loading, and end reactions monitored, to determine the applied loads that would produce negative moments at the pier with these magnitudes. These loads were then used as the upper and lower cycling limits for the entire 5 million cycles. For Bridge #1 the cyclic loading was from 4.5 kips to 20.8 kips. For Bridge #2 the cyclic loading was from 6.9 kips to 20.0 kips. The cyclic loading was applied at a frequency of 1.5 Hz for both bridges.

5.6 Cyclic Loading of Bridge #1

The cyclic loading of Bridge #1 began on 5/25/94. On 6/11/94, after 2 million cycles of load had been applied, the loading was halted and the bridge was subjected to 48 weeks of southern exposure cycling as part of the durability phase of this study. This weekly cycling consisted of 4 days of exposure to a salt water solution, followed by a 3 day drying period. The exposure cycling is described in Section 3.4 and the experimental

results are given in Chapter 6. At the conclusion of the exposure cycling an additional 3 million cycles of load, of the same magnitude as the first 2 million cycles, were applied. This loading began on 6/17/95 and concluded on 7/19/95. Measurements of end reactions and midspan deflections were taken during static loadings prior to cycling, and periodically throughout the 5 million loading cycles.

Figure 5.25 and 5.26 show the measured load vs. midspan deflection curves of Bridge #1 throughout the 5 million cycles of load for the east and west spans, respectively. In these figures, zero deflection corresponds to the position at the beginning of the cyclic loading. These figures each show two distinct sets of curves, each having a different slope. The first group of curves, which have zero-load deflections between 0.00 and 0.03 inches, correspond to the first 2 million cycles of loading. Although the zero-load deflection values during these 2 million cycles increased as more cycles of load were applied, the slopes of these curves remained the same. This increase was believed due to creep under sustained loading and not due to a decrease in continuity between adjacent spans, since a decrease in continuity would also reduce the slope of these curves. For this bridge, there was a sustained load of 4.5 kips (the lower load limit) during the cycling. The second group of curves, which have zero-load deflections in excess of 0.04 inches, corresponds to the 3 million cycles of loading which were applied after the conclusion of the exposure cycling. These curves have a higher slope than the first set of curves, indicating an increase in the stiffness of the structure. These curves are also grouped closer together than the curves corresponding to the first 2 million cycles, as creep effects were not as prominent for the older concrete.

The difference in the load-deflection relationship before and after the durability testing can be more clearly seen in Figures 5.27 and 5.28, where the deflections during the same static loadings have been normalized at the zero-load point. This normalization eliminates the time-dependent deformations and allows for direct comparison of instantaneous deflections due to the applied load. These figures clearly indicate that the stiffness of the bridge, and thus the continuity at the pier, remained essentially unchanged as a result of the cyclic loading. However, there was a significant increase in the stiffness of the bridge during the durability cycling, as indicated by the two distinct sets of load-deflection curves. This change in stiffness was significant, reducing midspan deflections by approximately 40% in the east span, and occurred during the first weeks of exposure cycling. A static loading after 4 weeks of exposure cycling showed that this change in stiffness had already occurred. The change in stiffness in the structure can be understood by examining the restraint moments at the pier throughout the cyclic loading. These moments are shown for the east and west spans in Figures 5.29 and 5.30, respectively. These figures show that the restraint moments (moments at zero applied load), which were negative throughout the first 2 million cycles of applied load, became positive restraint moments prior to the additional 3 million cycles of load (which were applied after the conclusion of the exposure cycling). Positive restraint moments would have a tendency to close the cracks which had been open under the negative restraint moments, thereby increasing the stiffness at the pier section.

The writers believes the change in restraint moments, which was observed after only 4 weeks of exposure cycling, was caused by the reversal of shrinkage due to re-

wetting of the CIP concrete. In section 4.1 it was explained that shrinkage is a reversible phenomenon, and that if concrete is saturated with water after it has experienced shrinkage, it will expand to almost its original volume. The weekly exposure cycle consisted of saturating the concrete with salt water for 4 consecutive days. If shrinkage of the CIP concrete had been the only time-dependent effect occurring during the CIP concrete cure period, then expansion of this concrete due to re-wetting would only serve to decrease the magnitude of the negative restraint moments. However, during this cure period, the length of the precast panels was also reduced by shrinkage of the precast concrete and by creep due to prestress. Thus, an attempt to restore the CIP concrete to its original volume (and length) would create positive restraint moments at the pier, consistent with the observed phenomenon.

5.7 Cyclic Loading of Bridge #2

The cyclic loading of Bridge #2 began on 1/30/96 and concluded on 3/13/96. Figures 5.31 and 5.32 show the load vs. midspan deflection curves of Bridge #2 throughout the 5 million cycles of load for the east and west spans, respectively. As with Bridge #1, the zero-load deflections increased with time, presumably due to creep under the sustained minimum load (6.9 kips in this case).

Figures 5.33 and 5.34 show the these same load-deflection curves after the elimination of time-dependent deflections. These figures clearly illustrate that the load-deflection relationship remained essentially constant throughout the 5 million loading cycles, and that deterioration of the continuity between spans did not occur. Figures 5.35

and 5.36 show the relationship of the continuity moments with applied load for the east and west spans, respectively during the cyclic loading. These figures indicate that the flexural stiffness at the pier, as indicated by the slope of the continuity moment versus applied load relationship, remained unchanged throughout the 5 million cycles of load.

5.8 Summary of Cyclic Loadings

Each bridge was subjected to 5 million cycles of service loading in order to evaluate the effect of repeated loading on the degree of continuity at interior piers. The testing showed that there was no appreciable change in the continuity between adjacent spans due to the repeated loadings, in which the calculated maximum reinforcement stress range exceeded the AASHTO allowable design stress range by 20 percent. Continuity between adjacent spans was evaluated by monitoring the instantaneous midspan deflections and discontinuous end reactions during static loadings which were conducted periodically throughout the 5 million cycles.

5.9 Overview of Failure Loadings

Each bridge was loaded to failure after the completion of the cyclic loading to determine its ultimate load-carrying capacity. The failure loading was applied by the same two hydraulic actuators used during the cyclic loading portions of this study. Prior to the final loading, a 26" x 26" Steel Plate was placed under each hydraulic actuator. Load was then applied to the bridge through 24" x 24" Bearing Pads which were placed between the concrete deck and the steel plates. This increased bearing area was used to prevent a

punching-shear failure at the point of loading. During the failure loading of each bridge, discontinuous end reactions, deflections, strains, strand slip, and differential panel deflections were recorded. The results of these loadings are discussed in the subsequent sections of this chapter.

5.10 Calculation of Failure Loads

The flexural capacities of the test bridges were calculated using the principle of virtual work, assuming full redistribution of elastic moments is possible. A collapse mechanism was presumed in which "hinges" form at the point of loading and at the pier location. The moments at these hinges were set equal to the nominal flexural strength of the section. The flexural failure load was then calculated by equating the internal work and external work corresponding to a virtual displacement of one unit at the applied load. This procedure is shown in Figure 5.37. Using this method, the failure loads of the test bridges were determined from the following expression:

$$P = 0.133M_1 + 0.213M_2 - 10w \qquad (5.1)$$

in which

P = applied load at failure

M_1 = nominal moment capacity at the pier

M_2 = nominal moment capacity of the composite prestressed section

w = uniform load due to the self weight of the precast panels and CIP topping.

The nominal moment capacities were calculated using the AASHTO code equations and by strain compatibility. The calculations using the AASHTO procedure are

shown in Figures 5.38 through 5.41. Strain compatibility calculations were performed using a computer program that was developed by the writers to calculate moment-curvature relationships of reinforced concrete sections. This program allowed for the stress-strain curves of the mild steel reinforcement, as determined from actual tension tests in the laboratory, to be used. These stress-strain relationships are shown in Chapter 3 (Figures 3.38 and 3.39). A modified Ramberg-Osgood equation was used to represent the stress-strain relationship of the prestressed steel as suggested by Collins and Mitchell [25]. A linear stress-strain relationship was assumed for the concrete at stresses below 0.5 f'c. At higher stresses, the stress-strain relationship of the concrete was represented by a simple parabolic expression recommended by Collins and Mitchell. Using this program, the nominal moment capacity was assumed to be the moment corresponding to a maximum concrete compressive strain of 0.004. The moment-curvature relationships generated for each bridge, and the corresponding nominal moment capacities, are shown in Figures 5.42 through 5.45. The assumed concrete compressive strength was 6.2 ksi for each bridge. The modulus of rupture used for the precast concrete was 820 psi for Bridge #1 and 875 psi for Bridge #2. For the composite prestressed sections, zero curvature corresponds to a moment of 60 kip-ft. This is the calculated dead load moment due to the weight of the precast panels and CIP topping.

Tables 5.1 and 5.2 list the calculated nominal moment capacities obtained from both the AASHTO equations and strain-compatibility, as well as the corresponding failure loads calculated using Equation 5.1 for Bridges #1 and #2, respectively. The uniform dead load due to self weight was 1.2 kips per foot for both bridges. Both tables show that

the calculated negative moment capacities, using the AASHTO equations are considerably less than those calculated using the strain compatibility method. This is mostly due to the strain hardening of the mild steel reinforcement. The AASHTO calculations consider the maximum reinforcement stress to be equal to the specified minimum yield stress, while the strain compatibility approach uses the actual stress-strain curve of the material. In addition, the positive moment capacities at the composite precast sections, determined from the strain compatibility calculations, are also higher than those from the AASHTO equations. This is primarily because the strain compatibility calculations included the shrinkage and temperature steel in the CIP topping, and because of the assumed higher concrete compressive strain at failure (0.004 versus 0.003, the basis for the AASHTO equations). Therefore, the calculated flexural failure loads for each bridge are highest when using the nominal moments obtained from strain compatibility.

The shear stresses at the center pier of each bridge, corresponding to the calculated flexural failure loads, were less than the allowable design shear stresses. Shear stresses at the center pier corresponding to the calculated flexural failure loads were 125 psi and 83 psi for Bridge #1 and Bridge #2, respectively. The allowable design shear stress of $2\sqrt{f'c}$ was approximately 150 psi for each bridge. Therefore, a flexural failure was expected for both test bridges.

5.11 Failure Loading of Bridge #1

Bridge #1 was loaded to failure on 8/2/95. During this final loading, the applied actuator force was increased in increments of 5 kips, and measurements were recorded at

each load level. Since the negative moment region had been cracked during the cure period and previous loadings, the load-deflection relationship was approximately linear until cracking occurred in the positive moment region. Observed flexural cracking of the prestressed panels in the positive moment region occurred at a load of about 99 kips for the east span and 104 kips for the west span. These loads corresponded to positive moments of 420 and 430 kip-ft, respectively, as determined from measurements of applied load and discontinuous end reactions. The moments are considerably higher than the calculated cracking moment for the section of 330 kip-ft. This calculation assumed a modulus of rupture of 820 psi, an estimated prestressing steel stress of 174 ksi, and gross section properties (see Figure 5.46). Since visual observation of cracking was limited to the sides of the 8-foot-wide bridge, it is possible that cracks may have occurred near mid-width of the bridge at lower loads but remained undetected. After cracking, midspan deflections and crack widths increased substantially with increasing load until failure (see Figures 5.47 and 5.48). These figures show that deflections in each span were nearly 3 inches prior to reaching the failure load, and that the deflections across the width of the bridge were essentially the same. The ultimate load of Bridge #1 was 140 kips, and was sustained for several minutes prior to flexural failure at the loading point in the west span. Spalling of the top concrete occurred gradually, as flexural cracks continued to grow and rotations increased. Sudden compression failure of the top concrete occurred after flexural cracks propagated horizontally below the compression chord (see Figure 5.49). Concrete crushing (evidenced by spalling) was also observed at the positive moment region in the east span at this loading but did not lead to collapse, as the test was

terminated after failure of the west span. The cracking which occurred during the final loading is shown in Figures 5.50 through 5.53. Crack widths measured at the diaphragm during this loading are shown in Table 5.3. The actual failure load of 140 kips was essentially the same as the value determined by virtual work (139 kips), using the nominal moment capacities obtained by strain compatibility. The failure load was approximately 13 percent larger than the estimated value of 124 kips, obtained using the AASHTO nominal moment capacities.

Tables 5.4 and 5.5 show the measured strand slip during the failure loading of Bridge #1 at the east and west ends, respectively. These tables show that considerable strand slip occurred prior to failure, especially at the west end. Strands #8 and #9, which were located at the center of the bridge and nearest to the applied load, had slips in excess of 1/4 inch at the west end. Strand slip was measured at the discontinuous ends, which were located more than 12 ft from the point of maximum positive moment. Slip began at a load of approximately 130 kips which corresponded to calculated maximum strand stress of 250 ksi and an average bond stress of only 185 psi. This strand slip did not prevent the section from reaching the design capacity, however, as the experimental moments (calculated from values of end reactions and applied load) exceeded the AASHTO design moment by nearly 4%. The maximum experimental moments were calculated to be 567 kip-ft in each span, while the AASHTO design moment was 547 kip-ft.

Differential deflections between the two precast panels in each span were also measured using electronic dial gages mounted on the underside of the bridge, below the actuators. These readings showed that differential displacements began at a load of 115

kips, and reached 0.013 inches for the west span, and 0.022 inches for the east span at 135 kips of applied load. These values are believed to have been due to transverse bending in the panels, and not due to separation between the panels and CIP topping since the full composite design moment capacity was attained.

5.12 Failure Loading of Bridge #2

Bridge #2 was loaded to failure on 3/26/96. During this final loading, the applied actuator force was increased in one-kip increments, and measurements of applied load, end reactions, deflections, and strains were recorded at each load level. Since the negative moment region had many transverse cracks prior to this loading, no additional cracks were observed at the pier until the bridge was near failure and considerable yielding of the reinforcement had taken place. Positive moment cracking was not observed until 60 kips of load had been applied in each span. The positive moments corresponding to this load were calculated (from values of end reactions and applied load) as 251 kip-ft and 247 kip-ft in the east and west spans, respectively. These moments are considerably larger than the estimated cracking load of 170 kip-ft, based of a modulus of rupture of 875 psi and a strand stress of 182 ksi. This calculation is shown in Figure 5.54.

Electrical resistance strain gages, however, which were attached to the concrete on the underside of the precast panels at midspan, indicated that cracking of the concrete occurred at a much lower load. Figures 5.55 and 5.56 show the incremental strains occurring, during the final loading, at concrete surface gages located on the bottom of the precast panels at midspan. Figure 5.55 shows that tensile strains increased in the concrete

with increasing load in the east span until a load level between 30 and 40 kips was reached, after which the incremental strains decreased. This behavior is evidence that transverse cracking occurred near the gage locations, thereby decreasing the strain in the concrete as the strain in the prestressed steel increased. Figure 5.56 suggests that cracking occurred as early as 27 kips in the west span. The positive moments corresponding to 30 kips of applied load were determined to be 137 kip-ft for the east span and 137 kip-ft for the west span. More evidence for this cracking can be seen in Figure 5.57, which shows the incremental strains at surface gages located on the top of the precast panels (the interface between the precast panels and the CIP topping) at midspan. This figure shows that incremental strains were approximately zero below 30 kips, since the neutral axis for the uncracked section was near mid-depth of the section. After cracking, however, the neutral axis was in the CIP concrete and tensile strains occurred at the gage level.

The failure load for Bridge #2 was 85 kips. This load was sustained for approximately ten minutes before collapse of the west span occurred due to flexure. Flexural failure occurred in the positive moment region, at the loading point in the west span. Spalling of the top concrete occurred gradually, initiating near the point of loading and moving towards the sides of the bridge. This spalling served to increase the curvature at the section and increase the stress in the steel. Collapse of the west span occurred when the strands fractured. After the west span failed, the load in the east span was maintained at 85 kips. Failure occurred in this span in a similar manner about 20 minutes later. Cracking which occurred during the failure loading of Bridge #2 is shown in Figures 5.58

through 5.61. Crack widths measured at the diaphragm during this loading are shown in Table 5.6.

Figures 5.62 and 5.63 show the deflections corresponding to the failure loading of Bridge #2 in the east and west spans, respectively, up to an applied load of 84 kips. The figures show that deflections increased linearly until cracking of precast panels occurred at about 30 kips. After cracking, the load-deflection relationship has a rapidly changing slope, as deflections increased at an accelerated rate with increasing load. This change in slope occurred as the compressed concrete area decreased and the reinforcement stress increased. After about 70 kips, the load-deflection curves have a very low slope, presumably due to yielding of the prestressing steel. The positive moments at 70 kips of applied load were approximately 290 kip-ft which would correspond to a stress in the prestressed steel of 250 ksi, calculated using the strain compatibility method described in section 5.10.

Figure 5.64 shows the rotations which were measured at the discontinuous ends of the bridge using two dial gages, spaced 30 inches apart, during the failure loading of Bridge #2 (see Figure 3.35). As expected, this graph has the same shape as the load-deflection relationship. A good approximation of the midspan deflections due to the applied load can be made by multiplying the end rotations (in radians) times one-half of the span length (120 inches). This is illustrated in Figure 5.65 for the west span.

The failure load of 85 kips was higher than the values predicted by Equation 5.1 using the nominal moment capacities obtained from both the AASHTO equations and strain compatibility. These values were 66 kips and 81 kips, respectively. Failure in both

spans occurred at the edge of the loading plate closest to midspan, as the plate acted to confine the concrete and prevent failure under the point load (see Figure 5.66). This resulted in a slightly higher failure load, since the failure mechanism was located away from the point of maximum moment. This increased failure capacity can also be estimated using the principle of virtual work as shown in Figure 5.67. The resulting expression for the failure load is:

$$P = 0.133M_1 + 0.232M_2 - 1.1333w \qquad (5.2)$$

where P, M_1, M_2, and w are the same as for Equation 5.1. The failure capacities calculated from Equation 5.2 are 69 kip using the AASHTO moments and 85 kips using the moments from strain compatibility.

Strand slip and differential deflections between panels were also measured during the failure loading of Bridge #2. Unlike Bridge #1, only minimal strand slip occurred during the final loading of Bridge #2. The maximum recorded strand slip was 0.005 inches. Displacement measurements between the adjacent panels showed that differential deflections began at a load of 74 kips, and increased until failure. The recorded differential displacements at 84 kips of load were 0.027 inches in each span. These values are believed to have been due to transverse bending of the panels and not due to separation between the precast panels and CIP concrete topping since the design nominal moment capacity, based on a fully composite section, was attained. The maximum positive moment, as determined from applied load and end reaction values, was 338 kip-ft. This exceeded the AASHTO nominal moment capacity of 290 kip-ft, as well as the moment calculated using strain compatibility of 312 kip-ft.

5.13 Moment Redistribution

When considering strength limit states, the AASHTO LRFD Bridge Design Specifications [3] allows the design engineer to decrease the negative moments determined by elastic theory at interior supports of continuous reinforced concrete beams, provided that positive moments are "adjusted to account for the changes in negative moments so as to maintain equilibrium of load and force effects." This is discussed in AASHTO section 5.7.3.5, and the redistribution of moments is limited to the following percentage:

$$20\left(1-2.36\frac{c}{d_e}\right) \tag{5.3}$$

where

c = the distance from the extreme compression fiber to the neutral axis

d_e = the depth to the centroid of the reinforcement tensile force, measured from the extreme compression fiber.

Redistribution of moments occurs due to changes in the relative stiffnesses of the sections at the pier and main spans. These changes are the result of both cracking of the concrete and yielding of the steel reinforcement. Redistribution corresponding to yielding of the reinforcement depends on the rotational capacity of the section. In lightly reinforced concrete beams, the reinforcement will yield while the concrete compressive strains are well below the ultimate strain. Therefore, considerable increases in curvature can occur before the concrete fails in compression. The ratio of c/d_e is an indirect measurement of this potential increase. Values of c and d_e for both test bridges are shown

in the nominal moment calculations (Figures 5.40 and 5.41). The maximum redistribution allowed by AASHTO was 17.4% for Bridge #1 and 17.8% for Bridge #2.

Figures 5.68 through 5.71 show the maximum positive and negative moments which occurred during the failure loadings of both bridges, along with the corresponding moments determined by elastic analysis, using both the CTL and PCA methods. The moments calculated by elastic analysis do not reflect the restraint moments due to shrinkage and creep effects, since these do not effect the behavior at ultimate. Therefore, at zero applied load, negative elastic moments are equal to zero and positive dead load moments are calculated assuming a simply supported member. Positive elastic moments calculated by the PCA and CTL methods were nearly identical for the diaphragm and span lengths used in this study.

5.13.1 Moment Redistribution in Bridge #1

Figure 5.68 shows that the maximum negative moments at the east and west sides of the pier were 250 kip-ft. The negative moments determined by elastic analysis were 558 kip-ft using the PCA method and 479 kip-ft using the CTL method. The experimentally determined moments represent a 55% reduction of the moments calculated using the PCA method and a 48% reduction of the moments calculated using the CTL method. Figure 5.69 shows that the maximum positive moments in Bridge #1 were 567 kip-ft, while the elastic moments calculated by the PCA and CTL methods were 423 kip-ft. The experimentally determined positive moments were 34% more than the moments calculated using elastic analysis.

5.13.2 Moment Redistribution in Bridge #2

Figure 5.70 shows that the maximum negative moments for Bridge #2 were 190 kip-ft at the east side of the pier and 200 kip-ft at the west side of the pier. The corresponding moments calculated by elastic analysis were 339 kip-ft using the PCA method and 291 kip-ft using the CTL method. The experimentally determined moment of 200 kip-ft represents a 41% reduction in the PCA moment and a 31% reduction in the CTL moment. Figure 5.71 shows that the maximum positive moment occurring in Bridge #2 was 338 kip-ft, compared with the elastically determined moments of 281 kip-ft. The experimentally determined positive moments correspond to a 20% increase in the elastic moments.

5.13.3 Moment Redistribution Summary

Full redistribution of elastic moments occurred during the failure loading of each bridge. The percentage of moment redistribution exceeded the AASHTO allowable value for both bridges based on elastic analysis using uncracked section properties. Although not explicitly stated, AASHTO section 5.7.3.5 does imply that the elastic analysis be based on uncracked sections properties. Redistribution of moments based on cracked section properties at the negative moment region would be unconservative. The calculated negative moment corresponding to the failure load of Bridge #1, based on a fully cracked diaphragm section, is 245 kip-ft. This is slightly less than the experimental moment of 250 kip-ft. Similarly, the calculated negative moment corresponding to the failure load of

Bridge #2, based on a fully cracked diaphragm section, is 138 kip-ft. This is considerably less than the experimental moment of 190 kip-ft.

5.14 Summary of Failure Loadings

The failure load of each bridge could be determined using the principle of virtual work, with moment capacities at hinges equal to the nominal moment capacities determined by strain compatibility. For both bridges, the experimentally determined positive and negative moments exceeded the nominal design moments calculated using the AASHTO equations. Negative moment capacities were considerably higher than the AASHTO values because of strain hardening of the mild steel reinforcement.

The ultimate load carrying capacity of the bridge was not affected by the initial restraint moments due to time-dependent effects, as these were relieved by yielding of the steel reinforcement and subsequent redistribution of moments. Moment redistribution for both bridges exceeded the maximum percentage allowed by AASHTO for design considerations. For Bridge #1, the experimentally determined negative moments at the maximum sustained load were 48% less than the moments calculated using elastic analysis. For Bridge #2, these moments were 31% less than the elastic moments.

Table 5.1 Nominal Moment Capacities and Estimated Failure Loads of Bridge #1

Method	Negative Moment (M_1)	Positive Moment (M_2)	Calculated Failure Load (kips)
AASHTO Equations	145	547	124
Strain Compatibility	241	557	139

Table 5.2 Nominal Moment Capacities and Estimated Failure Loads of Bridge #2

Method	Negative Moment (M_1)	Positive Moment (M_2)	Calculated Failure Load (kips)
AASHTO Equations	118	290	66
Strain Compatibility	198	312	81

Table 5.3 Crack Widths at Diaphragm During Failure Loading of Bridge #1

	Crack Width in Inches	
Load (Kips)	North Side	South Side
0	.007	.005
10	.008	.005
20	.0100	.007
30	.015	.007
40	.019	.013
50	.020	.015
60	.025	.016
70	.029	.025
80	.032	.027
90	.038	.035
100	.065	.075
110	7/64	8/64
115	8/64	9/64
120	9/64	10/64
125	13/64	15/64
130	16/64	15/64
135	16/64	16/64

*Crack widths less than 0.08 inches were measured using an optical measuring scale with a resolution of 0.001 inch.

*Crack widths greater than 0.08 inches were measured with a machinist's ruler having a resolution of 1/64 inch.

Table 5.4 Strand Slip at West End During Failure Loading of Bridge #1

Load (kips)	Strand #2	Strand #4	Strand #6	Strand #8	Strand #9	Strand #11	Strand #13	Strand #15
80	------	0.003	------	------	------	0.002	------	------
85	------	0.003	------	------	------	0.002	------	------
90	------	0.003	------	------	------	0.002	------	------
95	------	0.003	------	------	------	0.002	------	------
100	------	0.003	------	------	------	0.002	------	------
105	------	0.003	------	------	------	0.002	------	------
110	------	0.003	------	------	------	0.002	------	------
115	------	0.003	------	------	------	0.004	------	------
120	------	0.003	------	0.024	------	0.004	------	------
125	------	0.003	0.002	0.024	------	0.004	------	------
130	0.005	0.045	0.002	0.024	0.023	0.059	0.042	------
135	0.090	0.095	0.002	0.136	0.163	0.099	0.075	0.055
140	0.189	0.205	0.106	0.251	0.305	0.199	0.131	0.143

All values are in inches. Strand slip = 0.000 inches unless noted otherwise.
Strand slip prior to 80 kips was 0.000 inches for all strands.
Strand # corresponds to the strand position (from left to right) when facing panel ends.

Table 5.5 Strand Slip at East End During Failure Loading of Bridge #1

Load (kips)	Strand #2	Strand #4	Strand #6	Strand #8	Strand #9	Strand #11	Strand #13	Strand #15
95	------	0.003	------	------	------	------	------	------
100	------	0.003	------	------	------	------	------	------
105	------	0.003	------	------	------	------	------	------
110	------	0.003	------	------	------	------	------	------
115	------	0.003	------	------	------	0.004	0.002	------
120	------	0.003	------	------	------	0.004	0.002	------
125	------	0.003	------	------	------	0.004	0.002	------
130	------	0.003	0.062	0.083	------	0.004	0.002	------
135	------	0.003	0.102	0.129	------	0.004	0.052	0.039

All values are in inches. Strand slip = 0.000 inches unless noted otherwise.
Strand slip prior to 95 kips was 0.000 inches for all strands.
Strand # corresponds to the strand position (from left to right) when facing panel ends.

Table 5.6 Crack Widths at Diaphragm During Failure Loading of Bridge #2

	Crack Width in Inches	
Load (Kips)	North Side	South Side
0	.020	.018
10	.021	.030
20	.025	.035
25	.032	.035
30	.035	.038
35	.030	.035
40	.040	.038
45	.045	.038
50	.045	.038
55	.048	.038
60	0.061	.046
65	0.077	.048
70	7/64	.063
75	10/64	6/64
80	14/64	10/64

*Crack widths less than 0.08 inches were measured using an optical measuring scale with a resolution of 0.001 inch.

*Crack widths greater than 0.08 inches were measured with a machinist's ruler having a resolution of 1/64 inch.

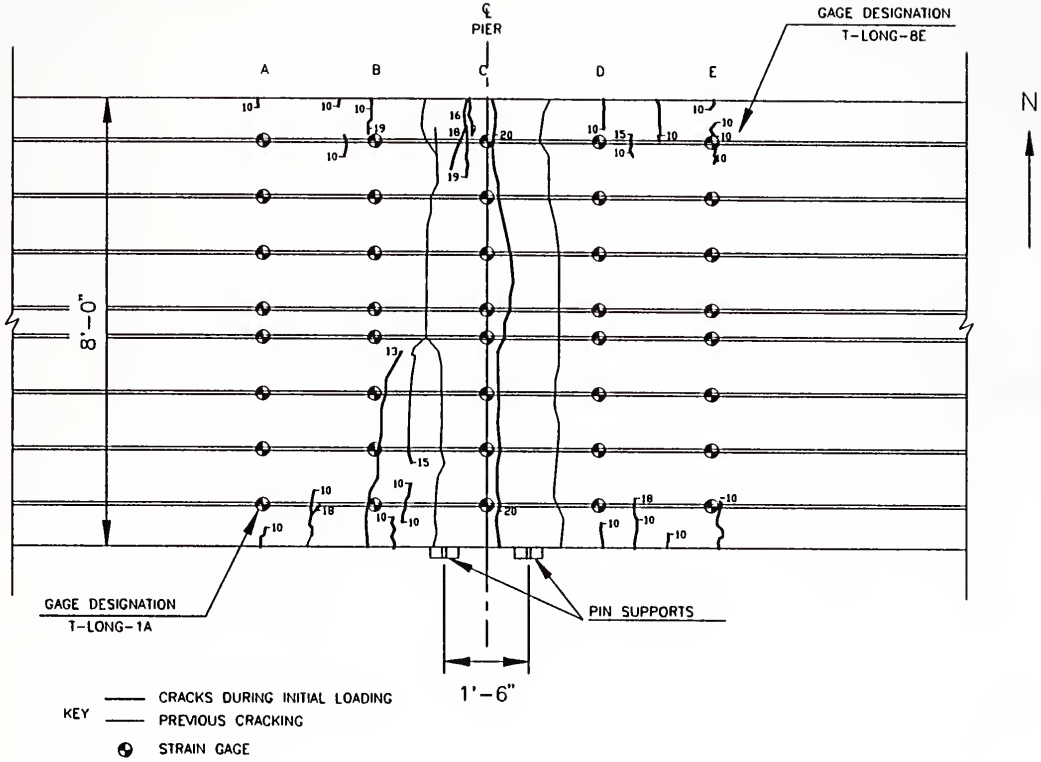

Figure 5.1 Cracks Occurring During the Initial Loading of Bridge #1 (Plan View)

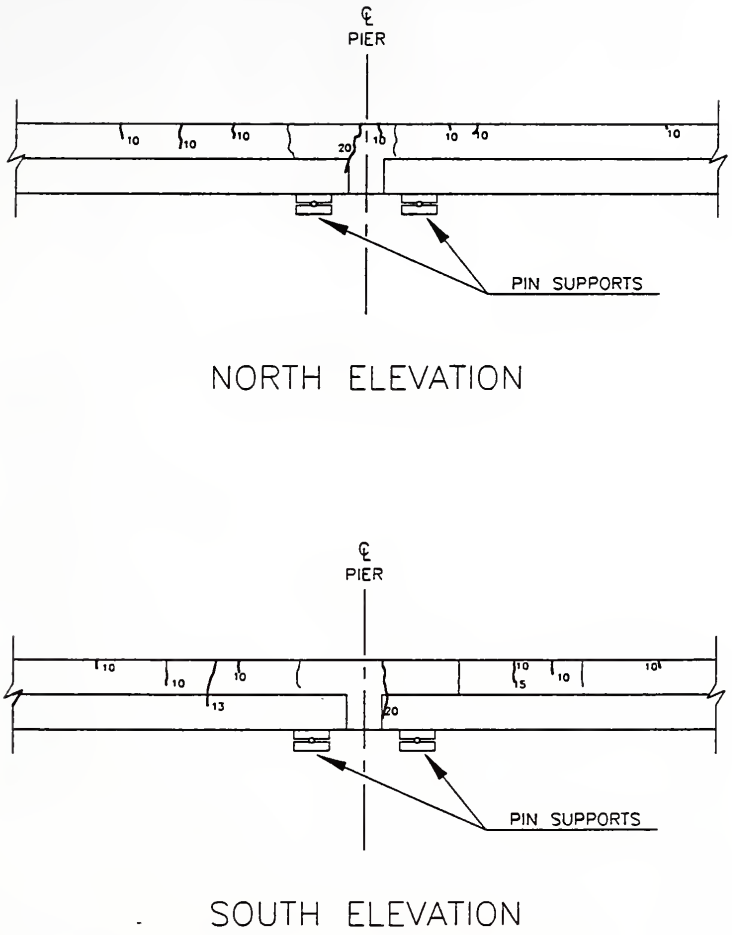

Figure 5.2 Cracks Occurring During the Initial Loading of Bridge #1 (Elevations at Pier)

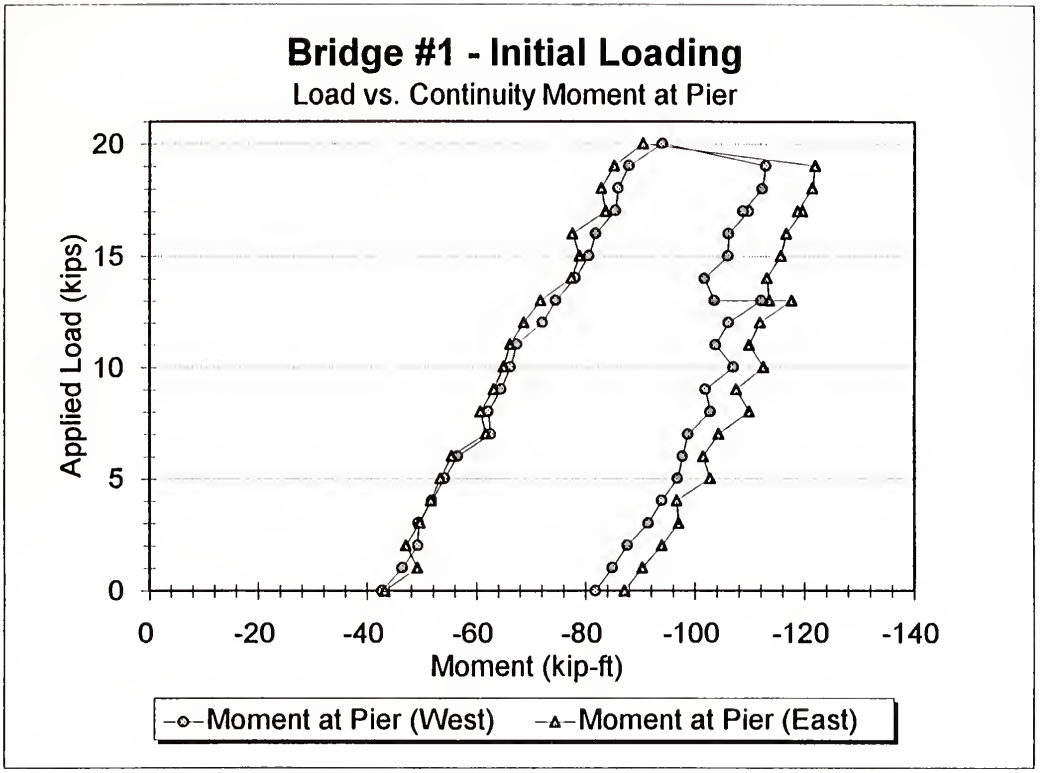

Figure 5.3 Continuity Moments During the Initial Loading of Bridge #1

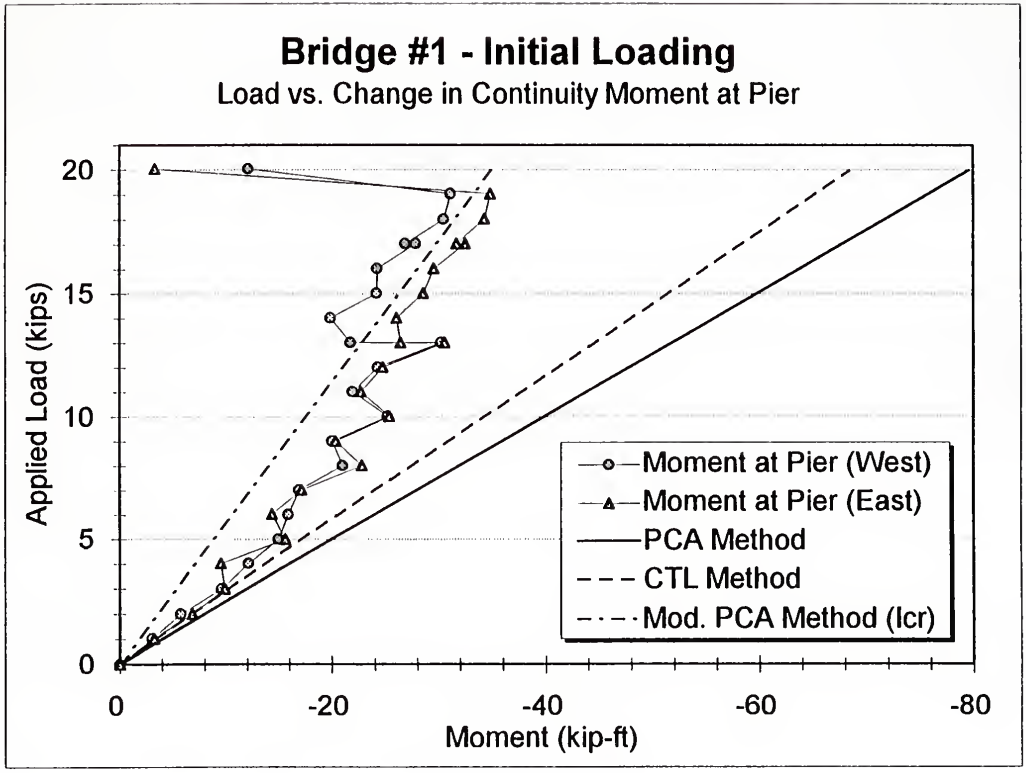

Figure 5.4 Change in Continuity Moments During the Initial Loading of Bridge #1

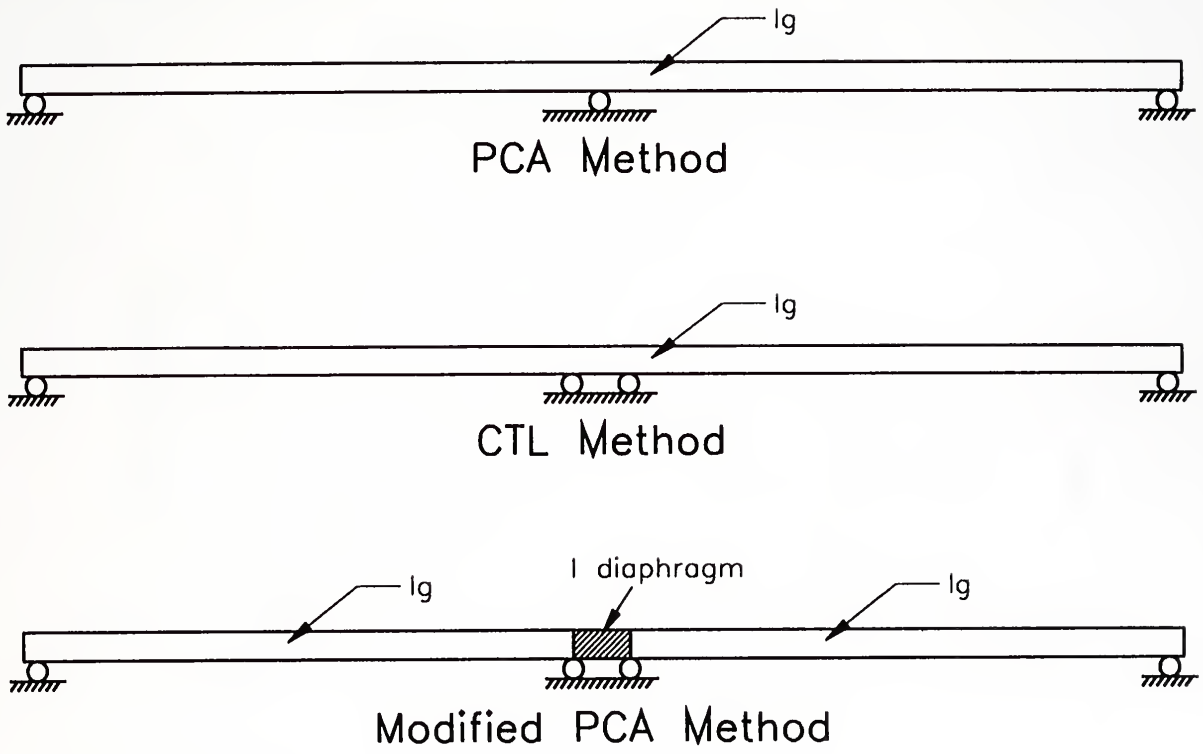

Figure 5.5 Models Used to Calculate Moments and Deflections Due to Superimposed Loading

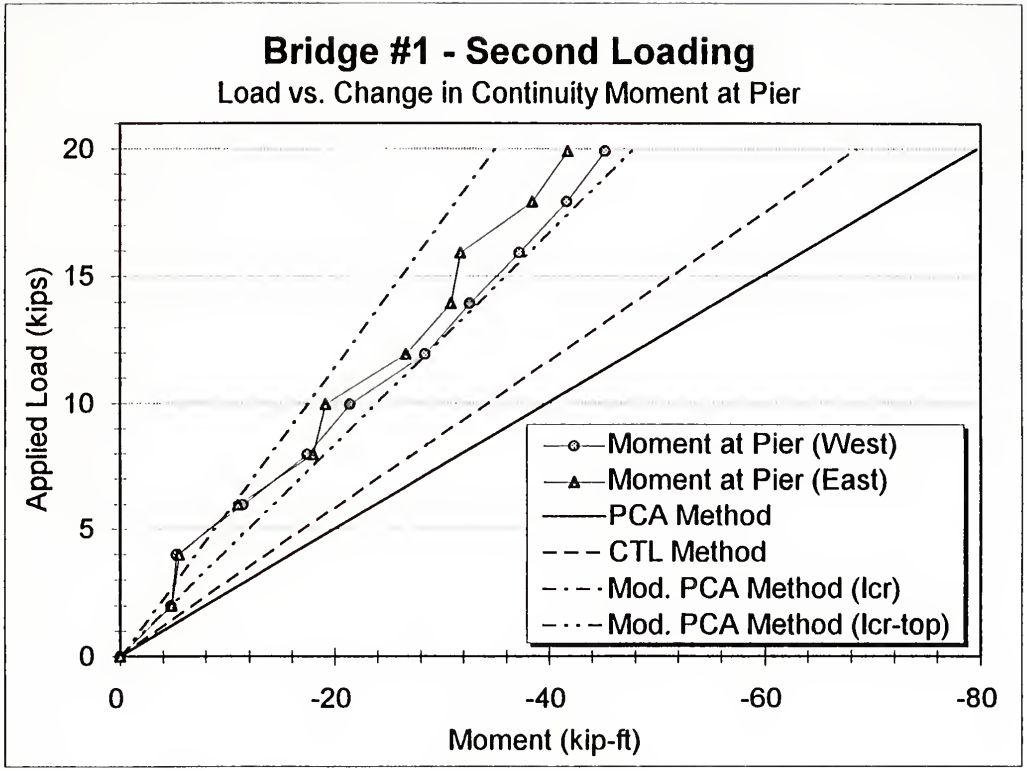

Figure 5.6 Changes in Continuity Moments During Second Loading of Bridge #1

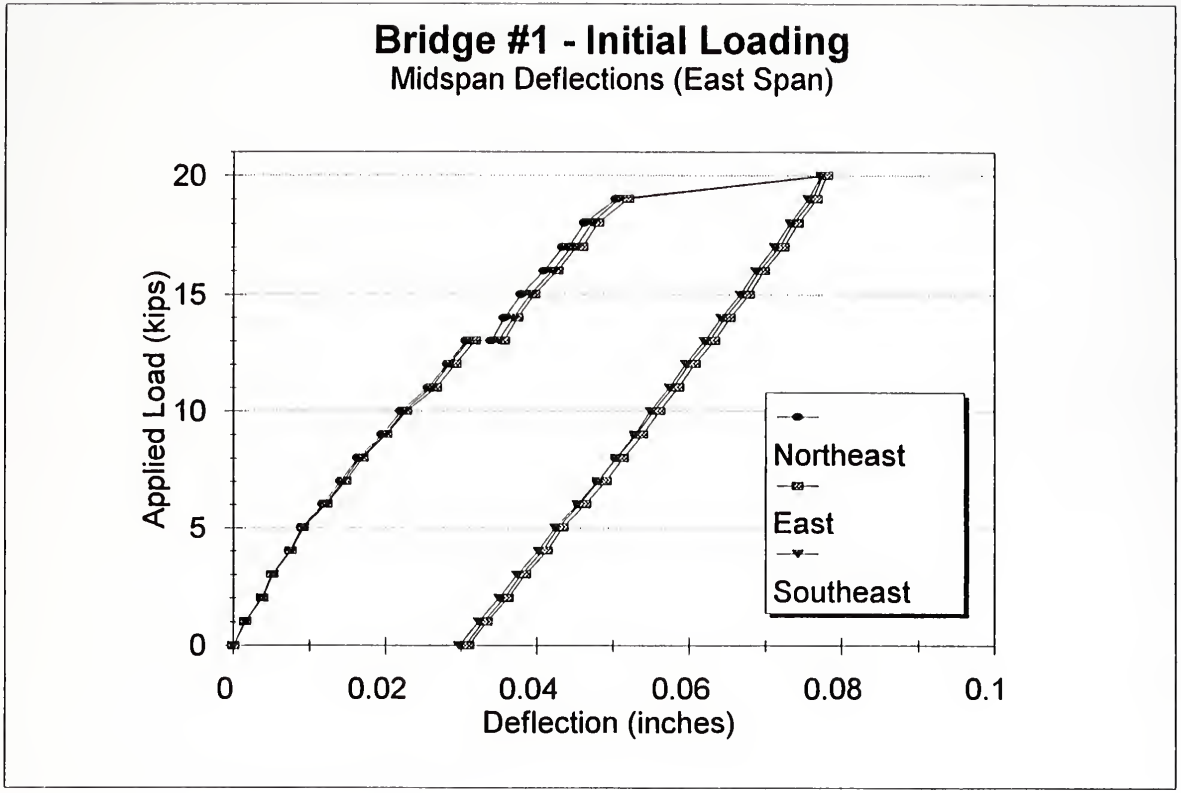

Figure 5.7 Midspan Deflections During the Initial Loading of Bridge #1 (East Span)

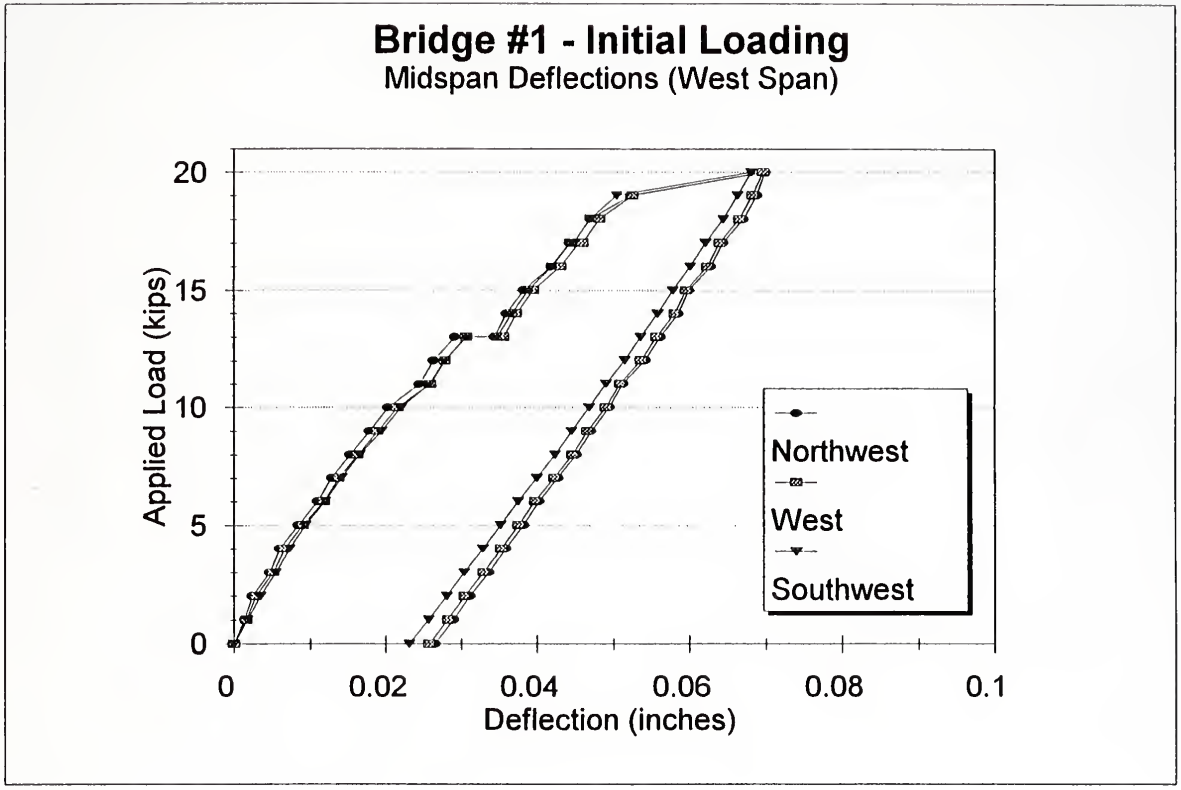

Figure 5.8 Midspan Deflections During the Initial Loading of Bridge #2 (West Span)

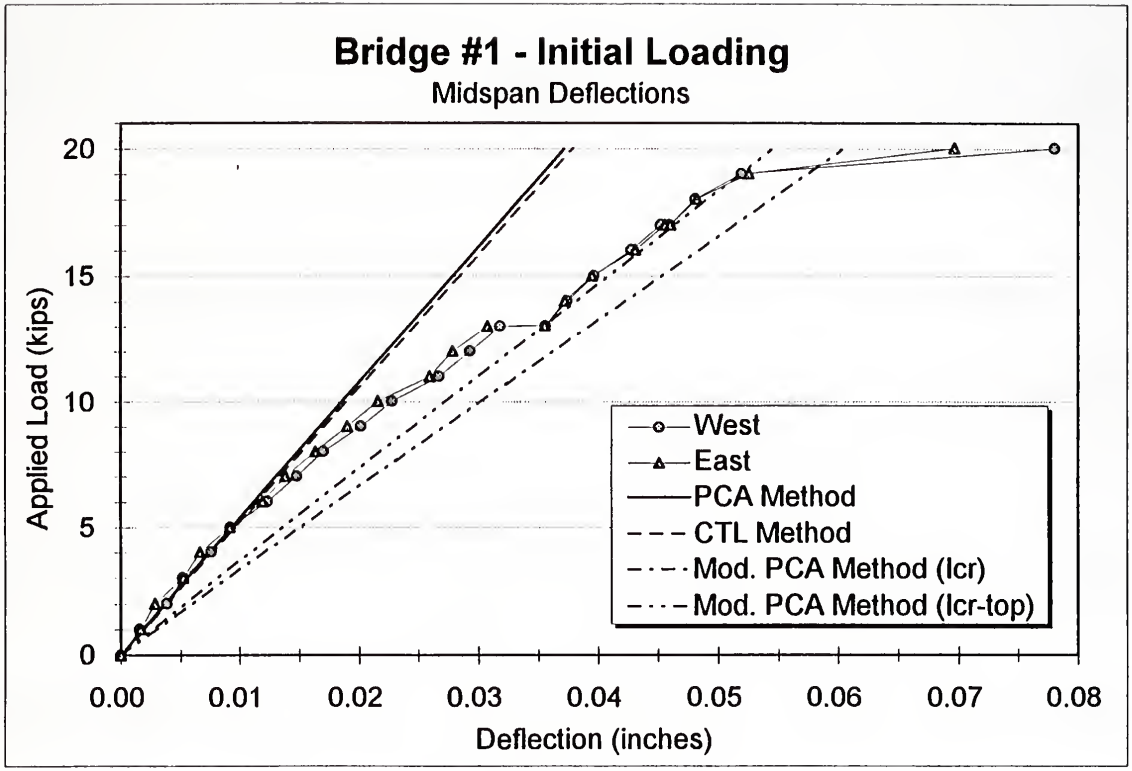

Figure 5.9 Comparison of Measured Deflections with Values Calculated Using Analytical Models (Bridge #1)

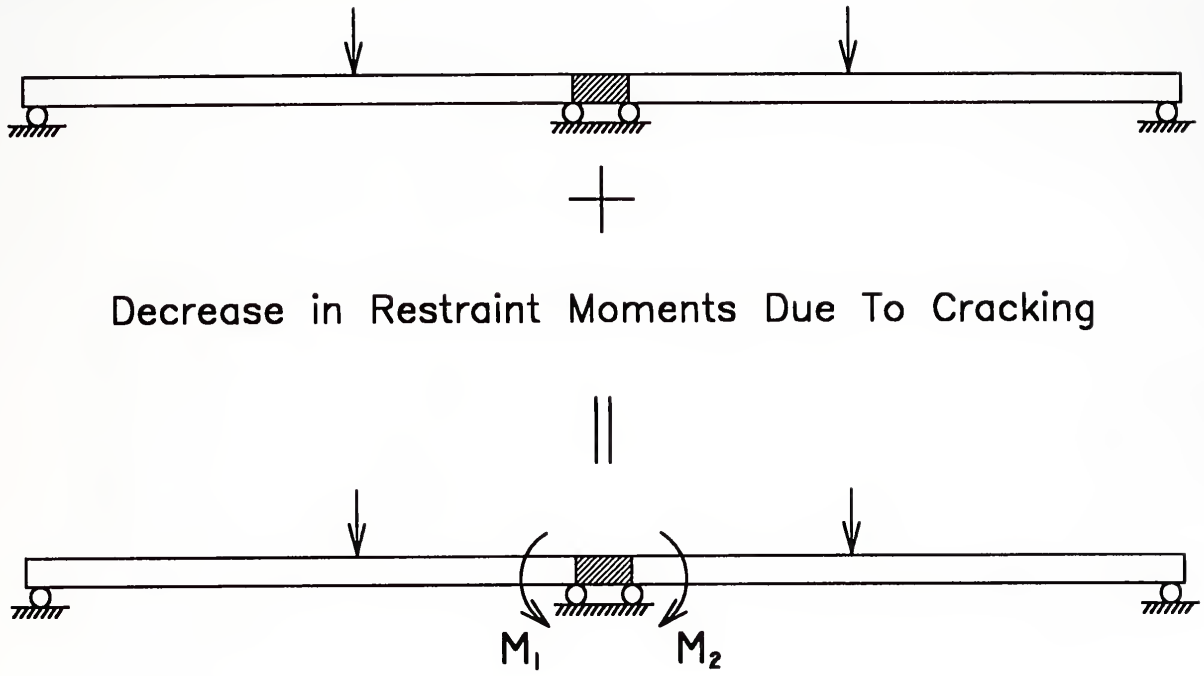

Figure 5.10 Illustration of Method Used to Calculate Deflections Occurring Simultaneously with Decreasing Restraint Moments

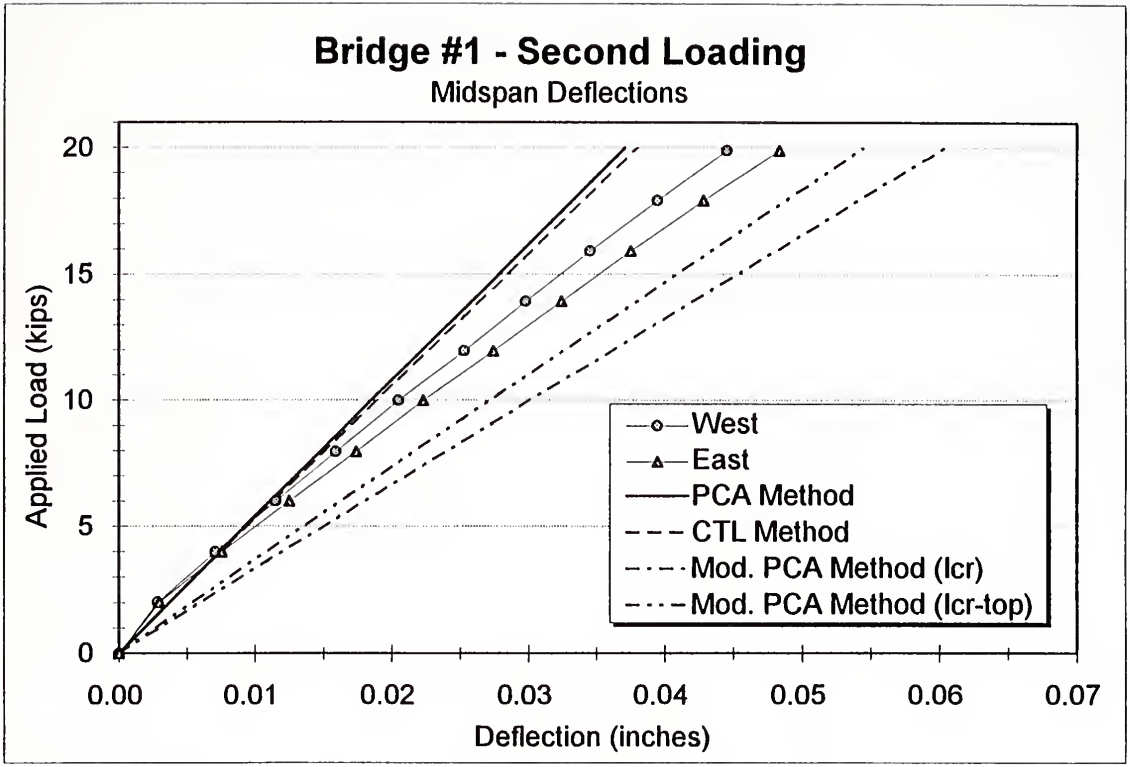

Figure 5.11 Incremental Deflections During the Second Loading of Bridge #1

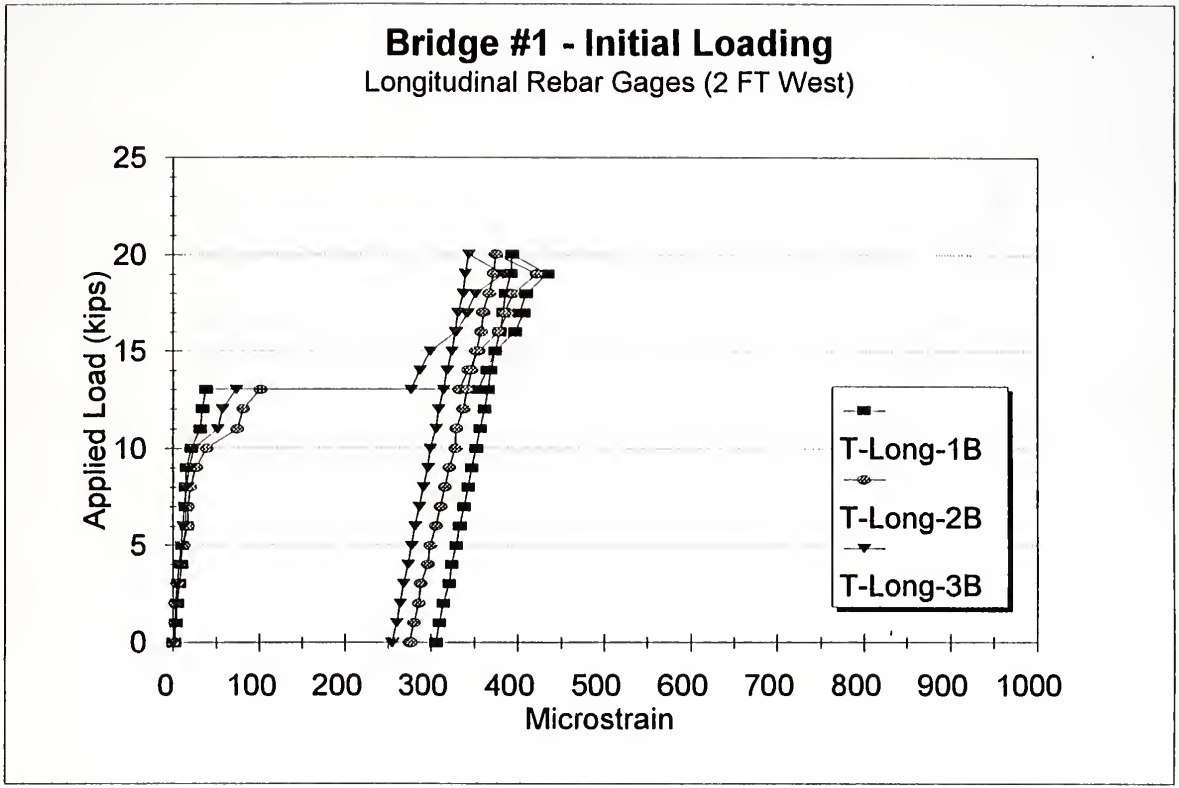

Figure 5.12 Incremental Strains in Rebar Gages Located Near the Crack Which Opened at 13 Kips (Bridge #1)

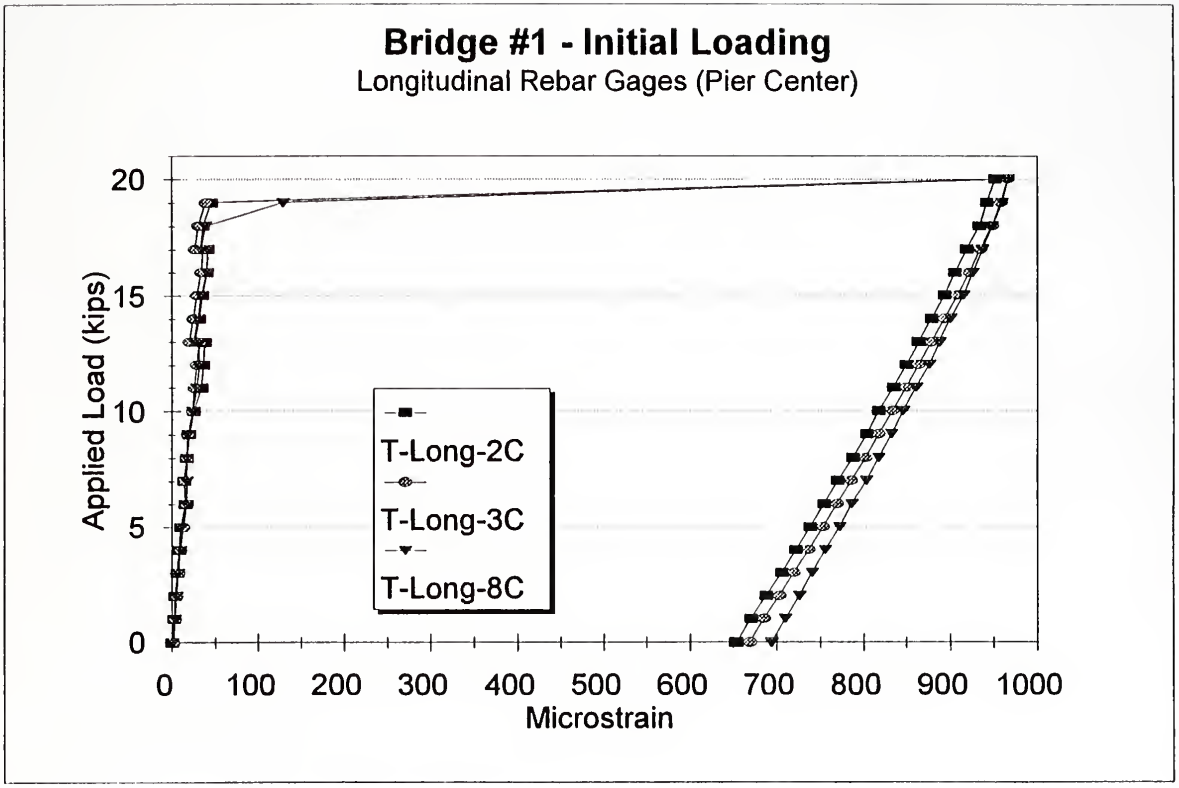

Figure 5.13 Incremental Strains in Rebar Gages Located Near the Crack Which Opened at 19.9 Kips (Bridge #1)

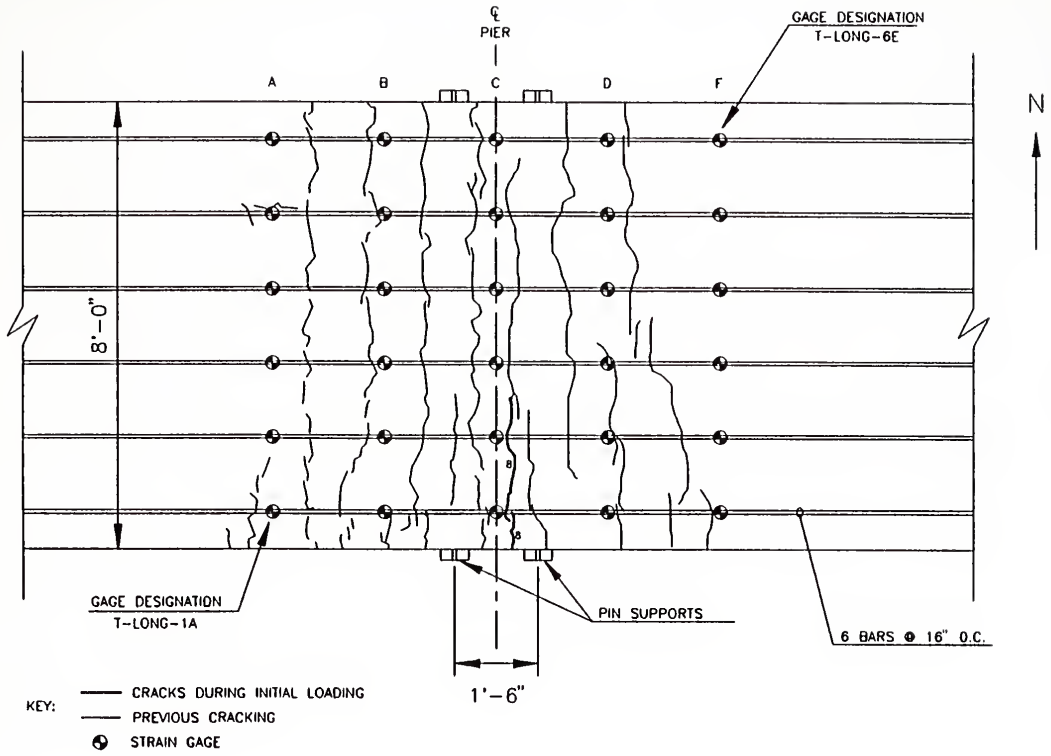

Figure 5.14 Cracks Occurring During the Initial Loading of Bridge #2 (Plan View)

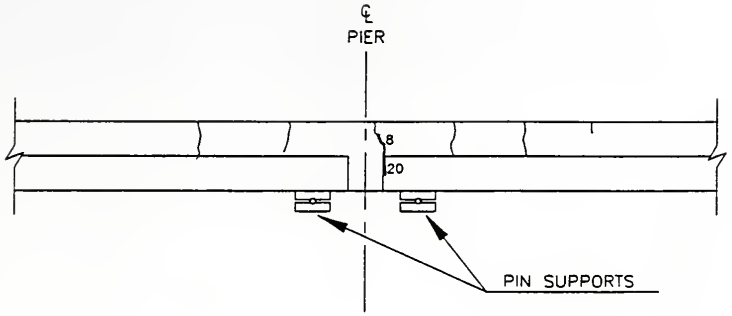

NORTH ELEVATION

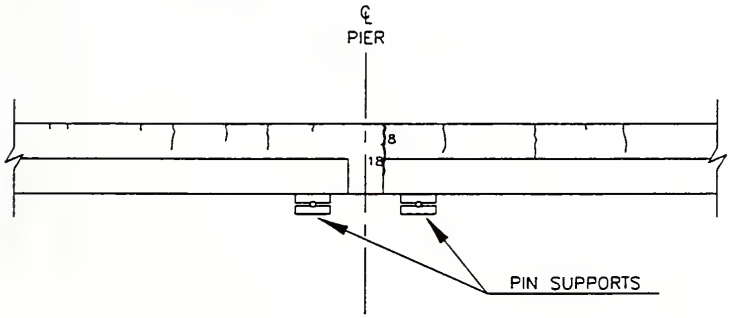

SOUTH ELEVATION

KEY: —— CRACKS DURING INITIAL LOADING
—— PREVIOUS CRACKING

Figure 5.15 Cracks Occurring During the Initial Loading of Bridge #2 (Elevations at Pier)

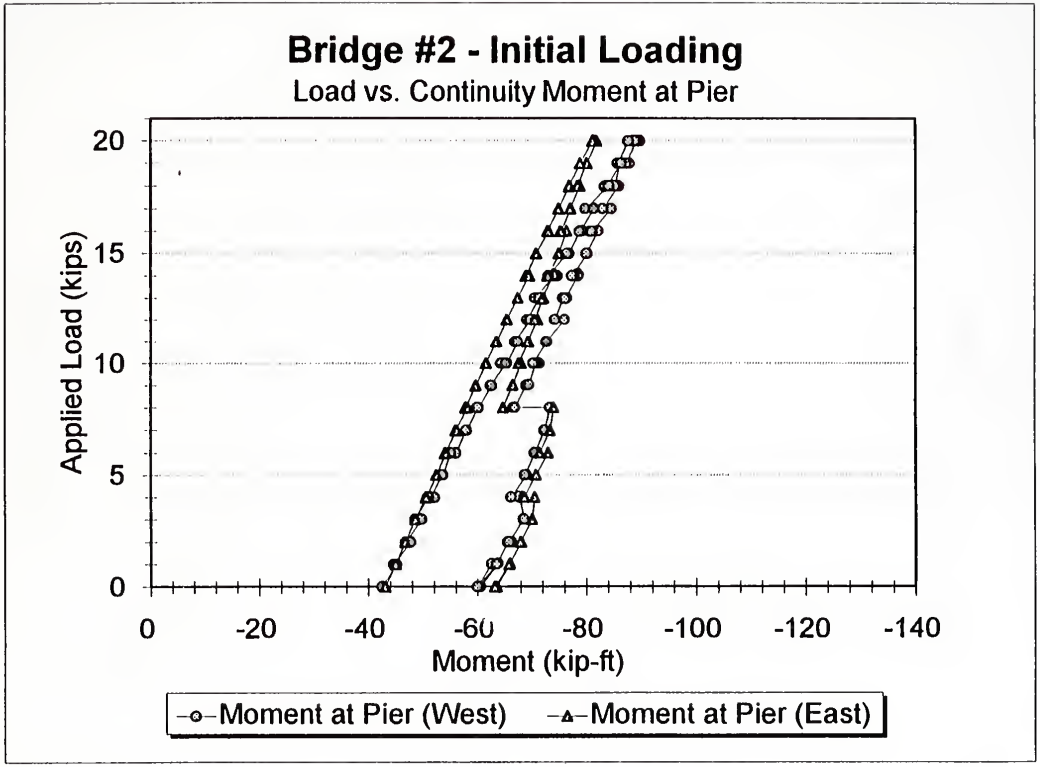

Figure 5.16 Continuity Moments During the Initial Loading of Bridge #2

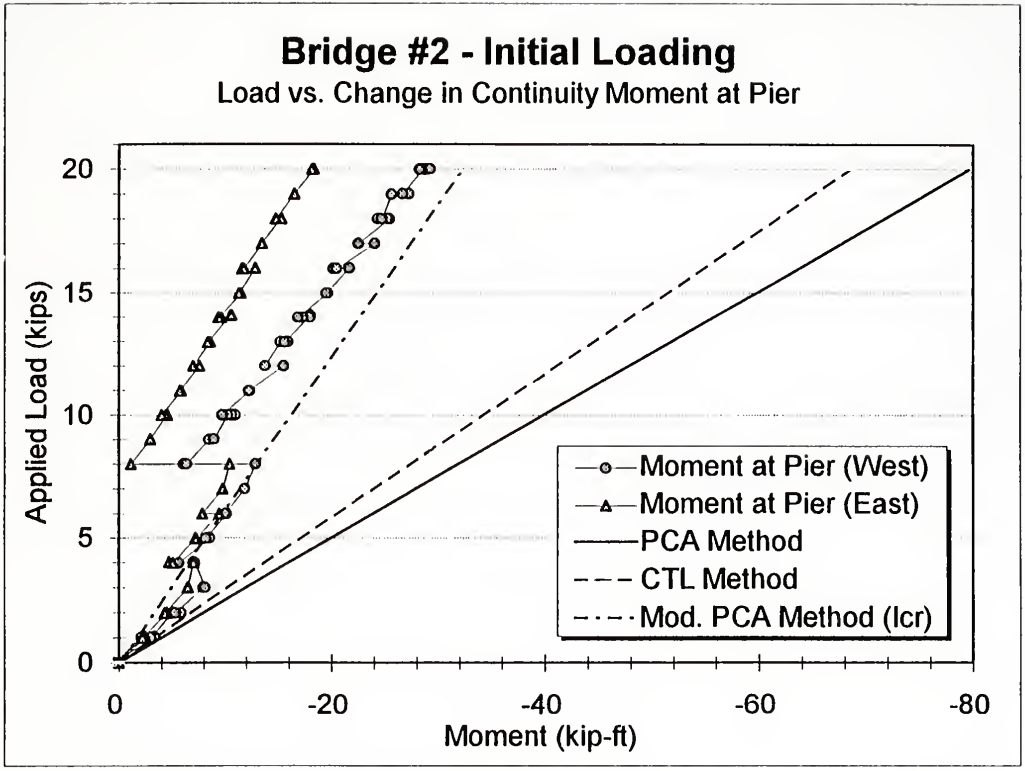

Figure 5.17 Change in Continuity Moments During the Initial Loading of Bridge #2

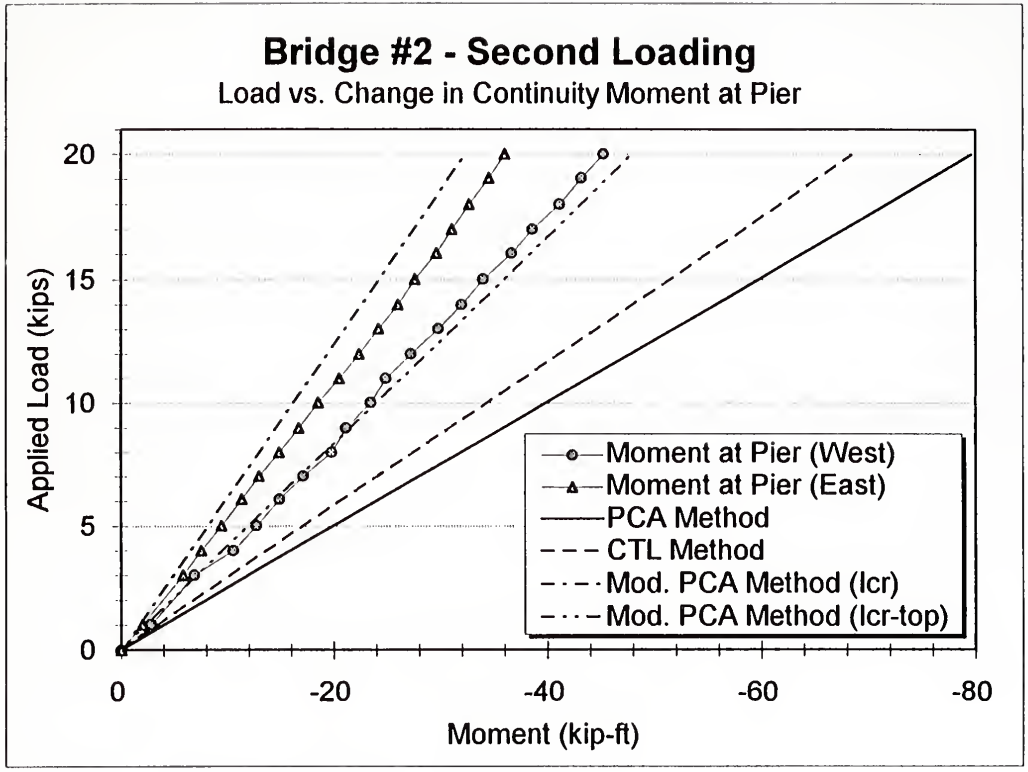

Figure 5.18 Change in Continuity Moments During the Second Loading of Bridge #2

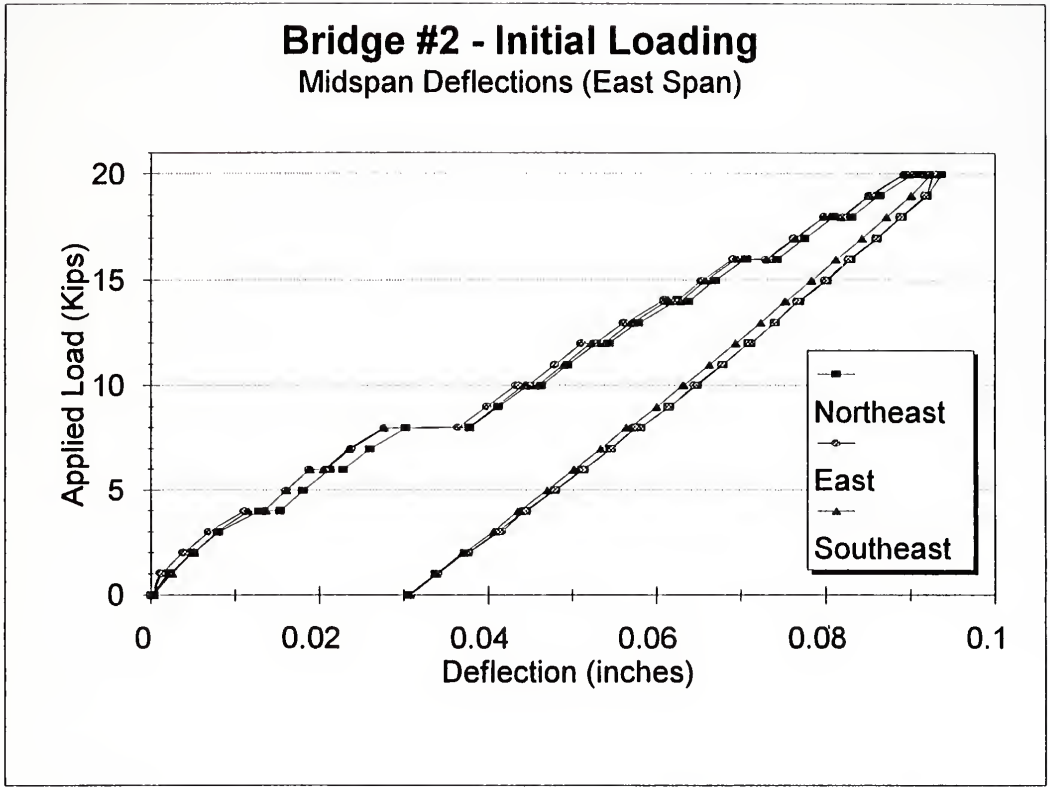

Figure 5.19 Midspan Deflections During the Initial Loading of Bridge #2 (East Span)

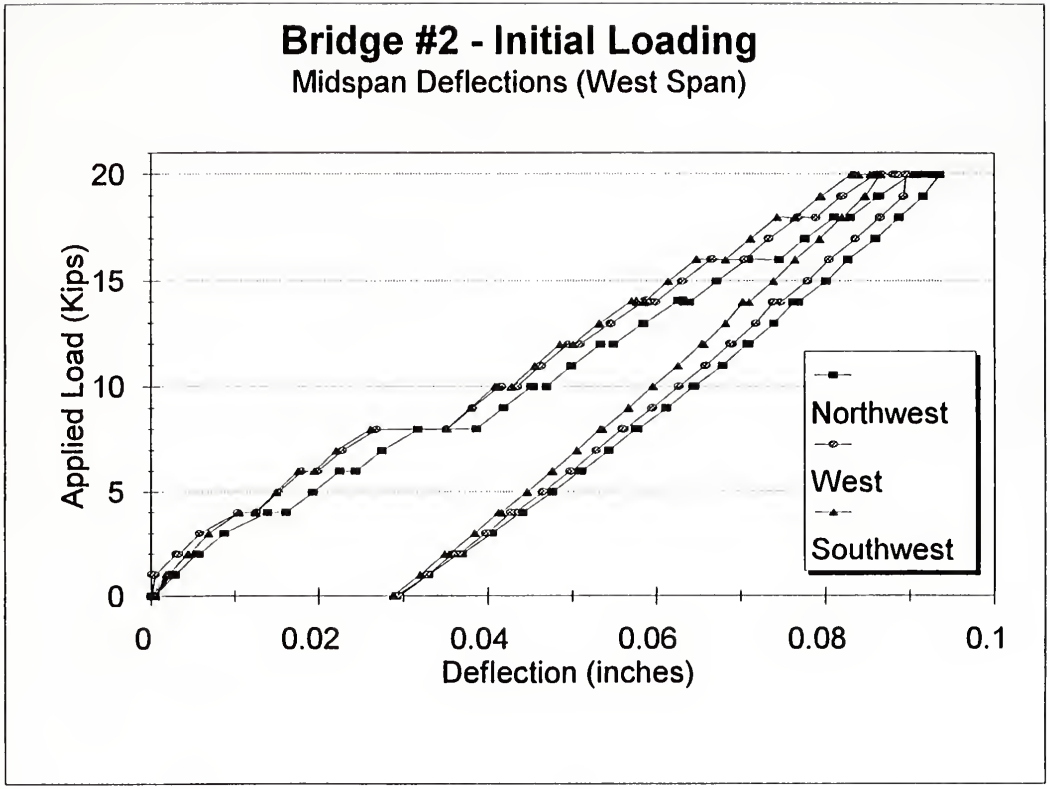

Figure 5.20 Midspan Deflections During the Initial Loading of Bridge #2 (West Span)

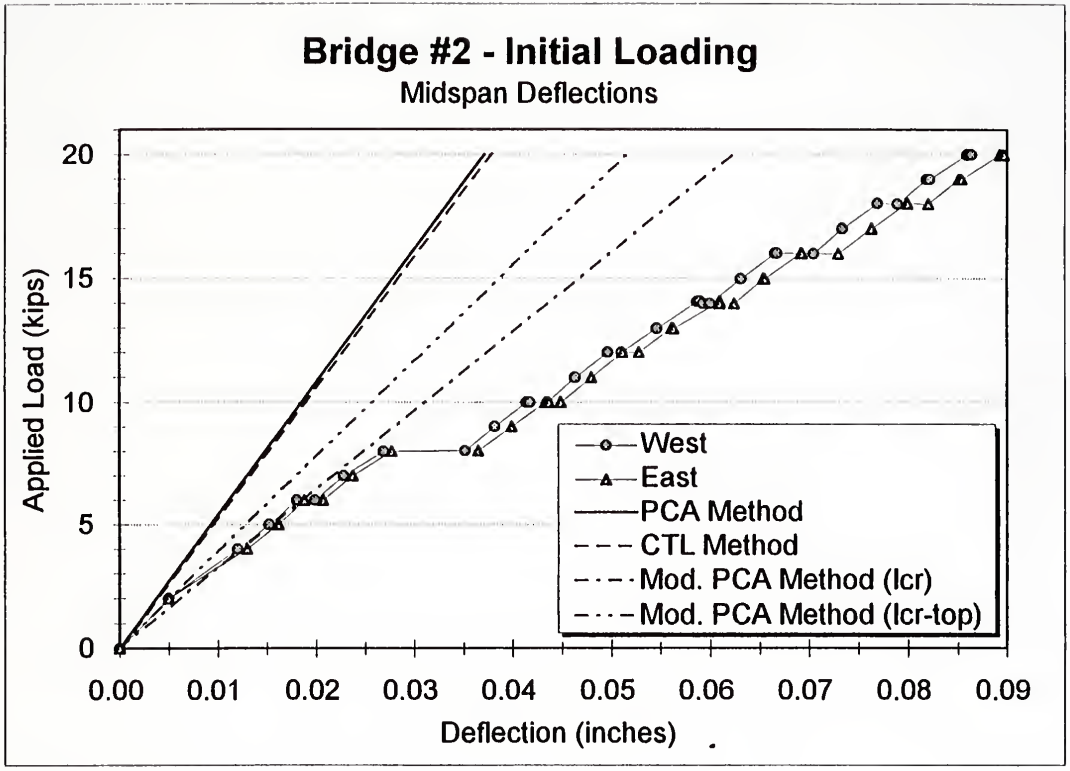

Figure 5.21 Comparison of Measured Deflections with Values Calculated Using Analytical Models (Bridge #2)

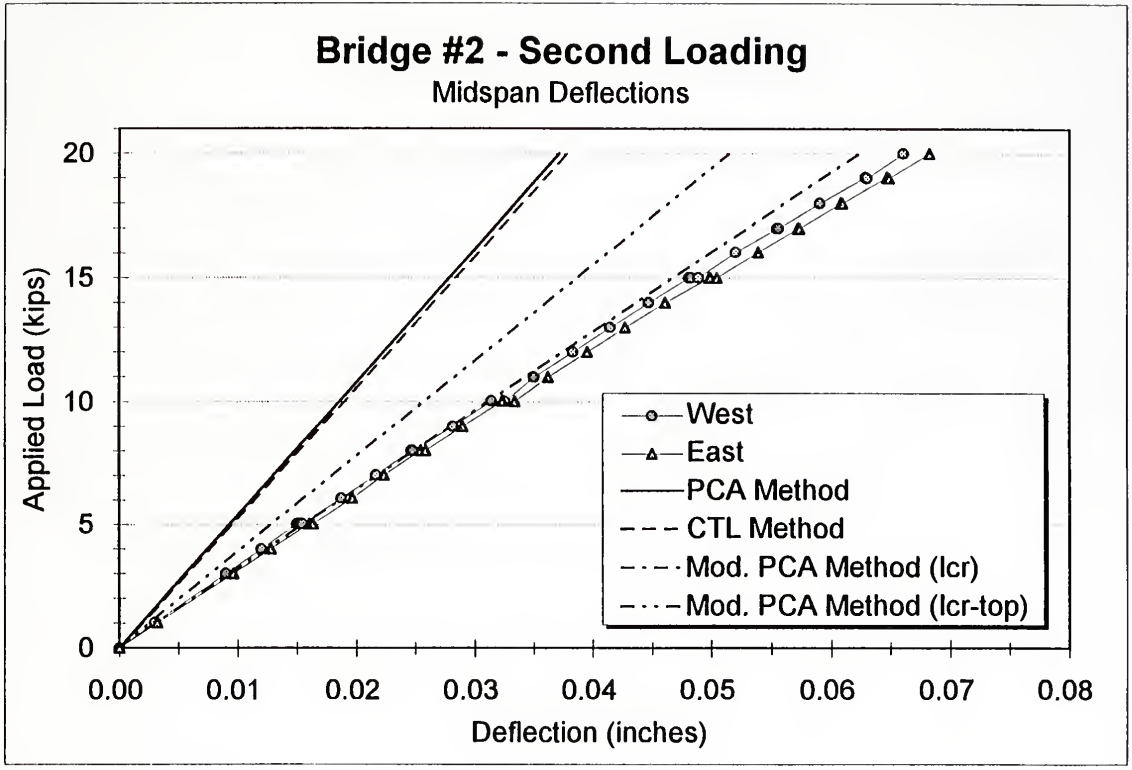

Figure 5.22 Incremental Deflections During the Second Loading of Bridge #2

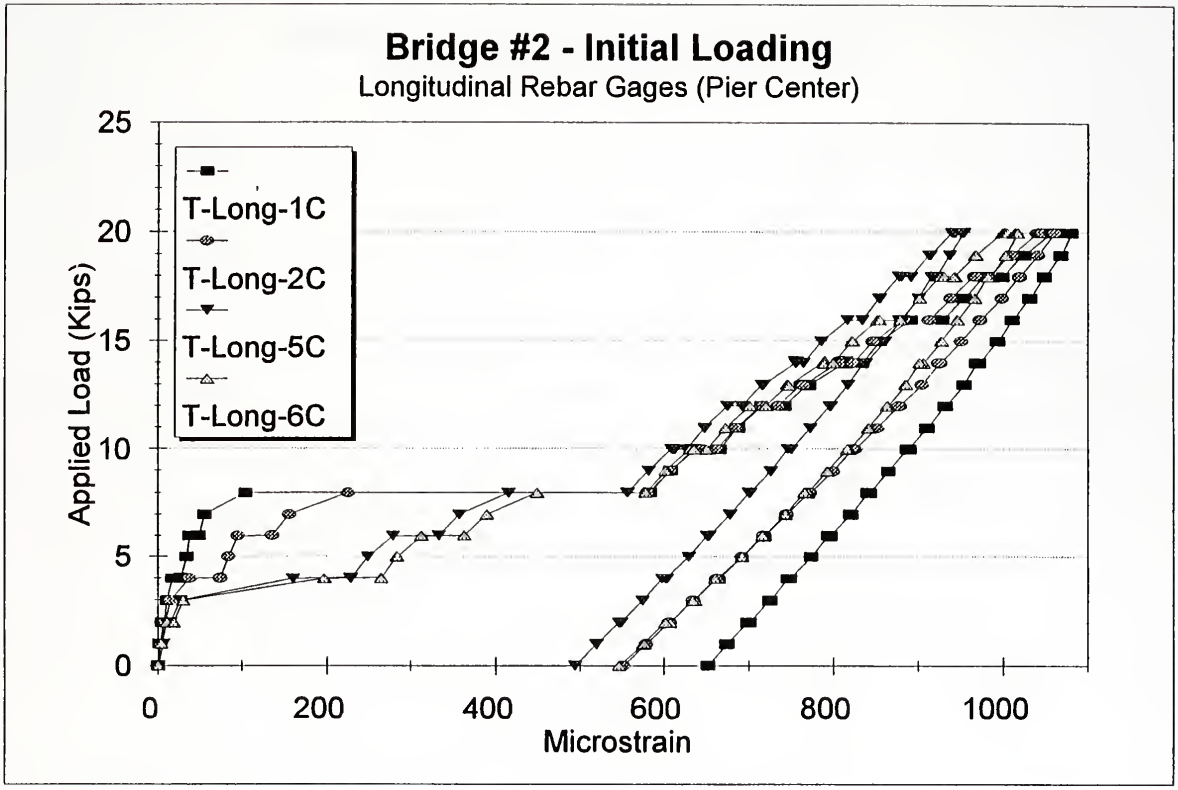

Figure 5.23 Incremental Strains in Rebar Gages Located at the Center of the Pier (Bridge #2)

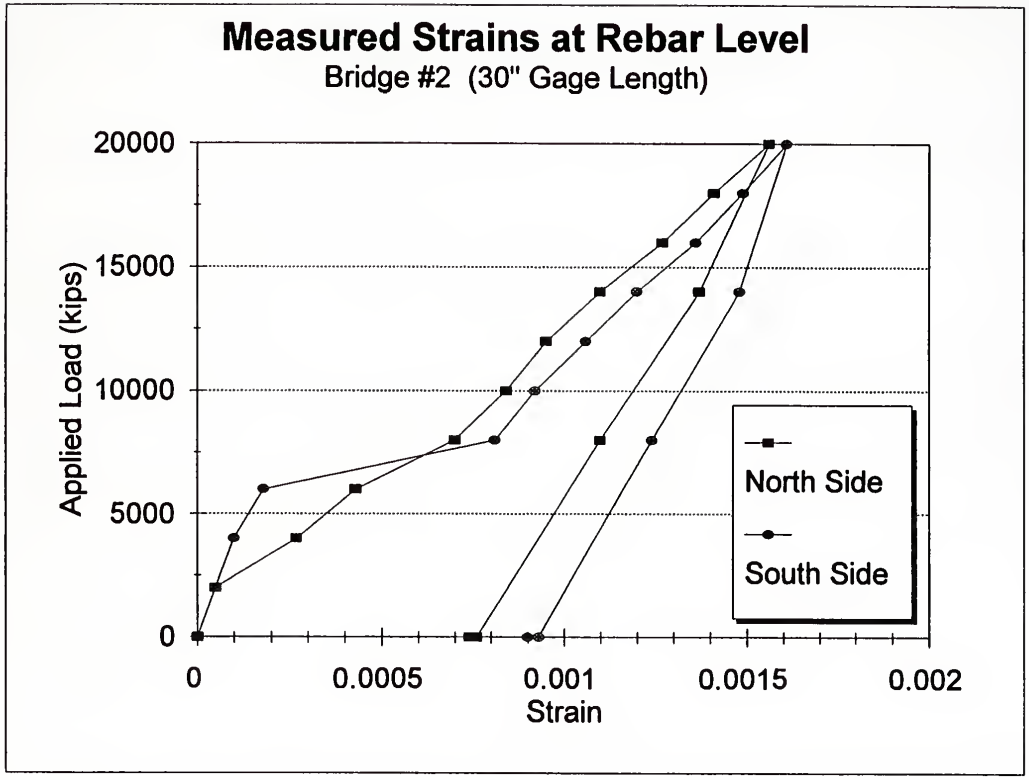

Figure 5.24 Strains Measured During the Initial Loading of Bridge #2 Using a Whittemore Gage

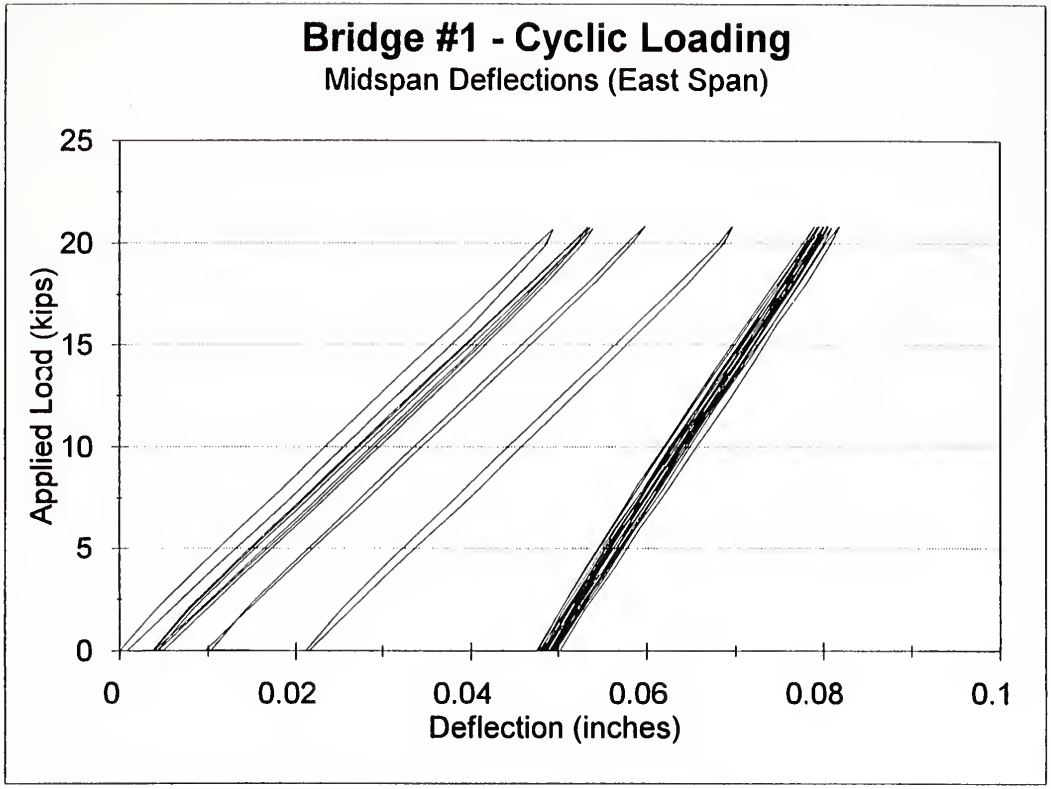

Figure 5.25 Load Versus Deflection Curves During the Cyclic Loading of Bridge #1 (East Span)

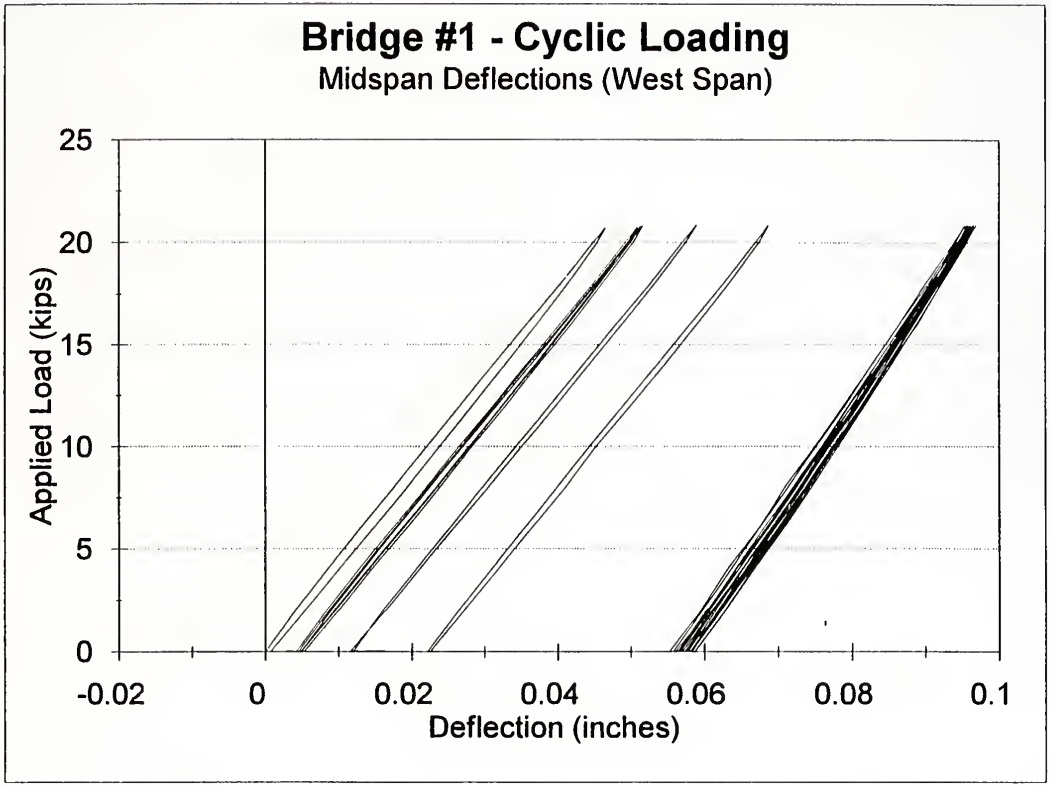

Figure 5.26 Load Versus Deflection Curves During the Cyclic Loading of Bridge #1 (West Span)

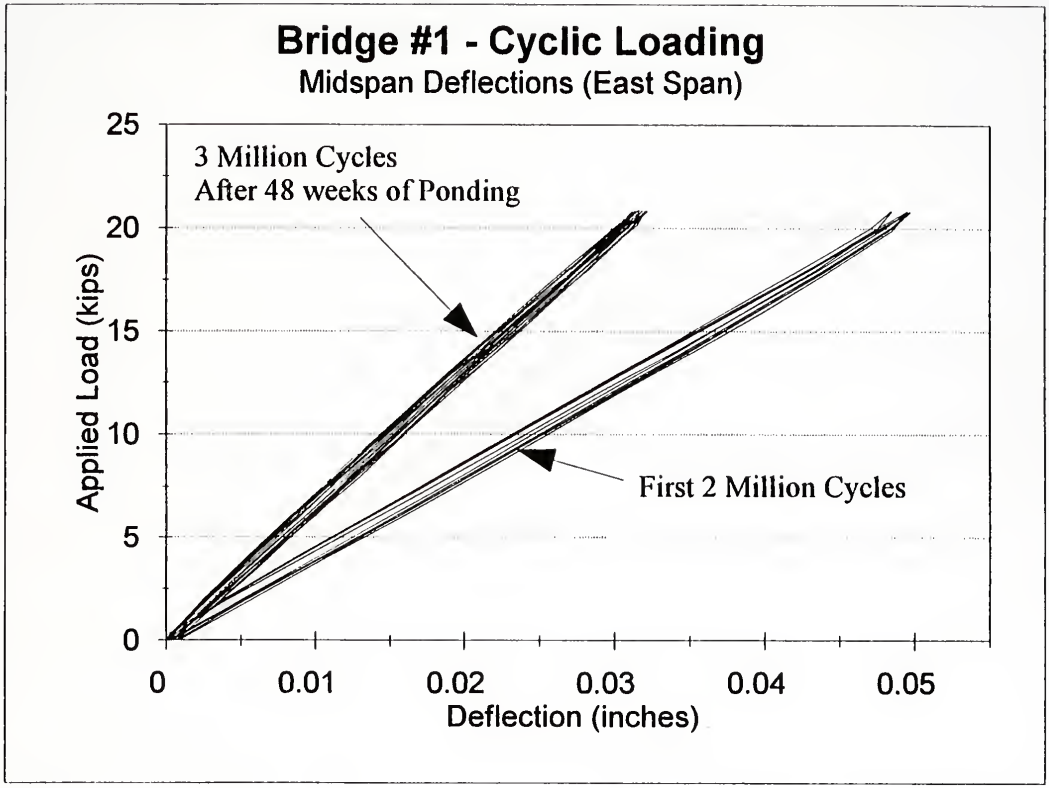

Figure 5.27 Comparison of Instantaneous Deflections During the Cyclic Loading of Bridge #1 (East Span)

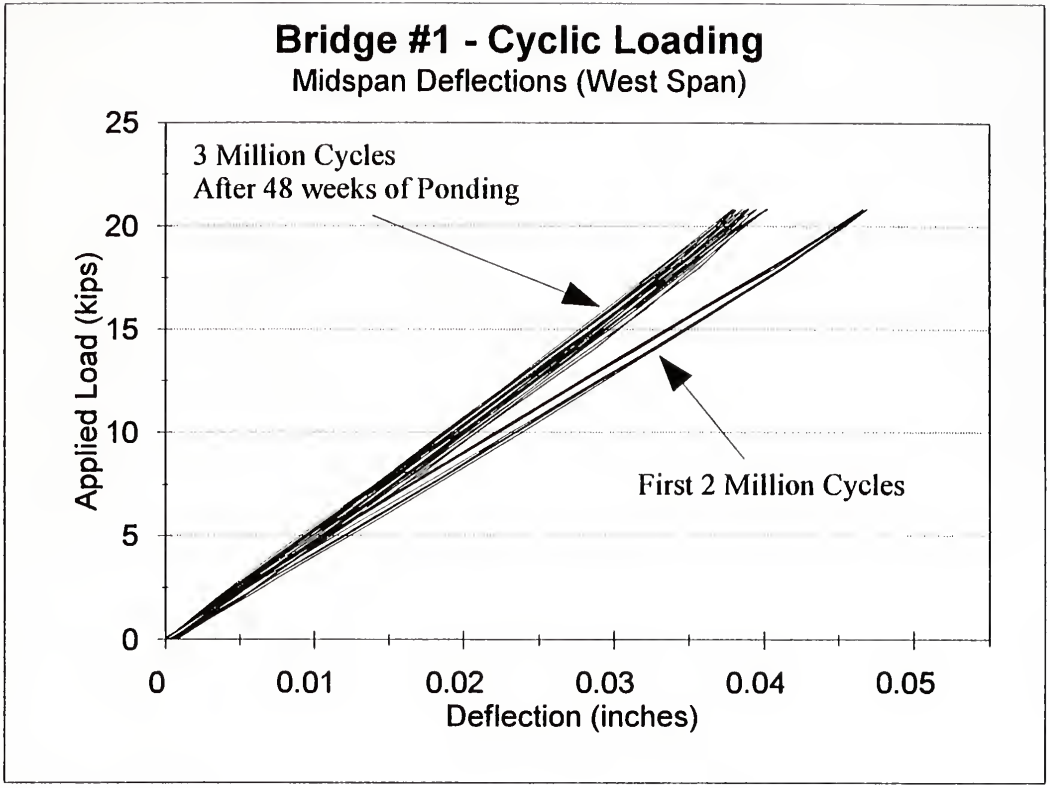

Figure 5.28 Comparison of Instantaneous Deflections During the Cyclic Loading of Bridge #1 (West Span)

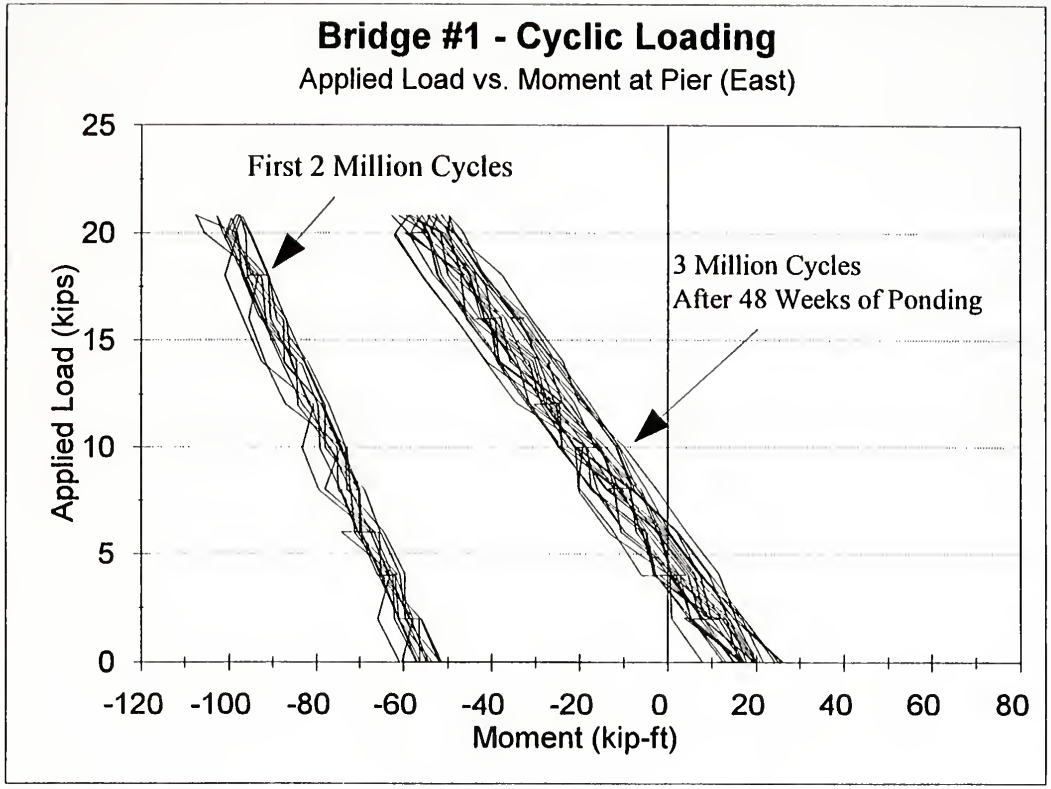

Figure 5.29 Continuity Moments at East Side of Pier During the Cyclic Loading of Bridge # 1

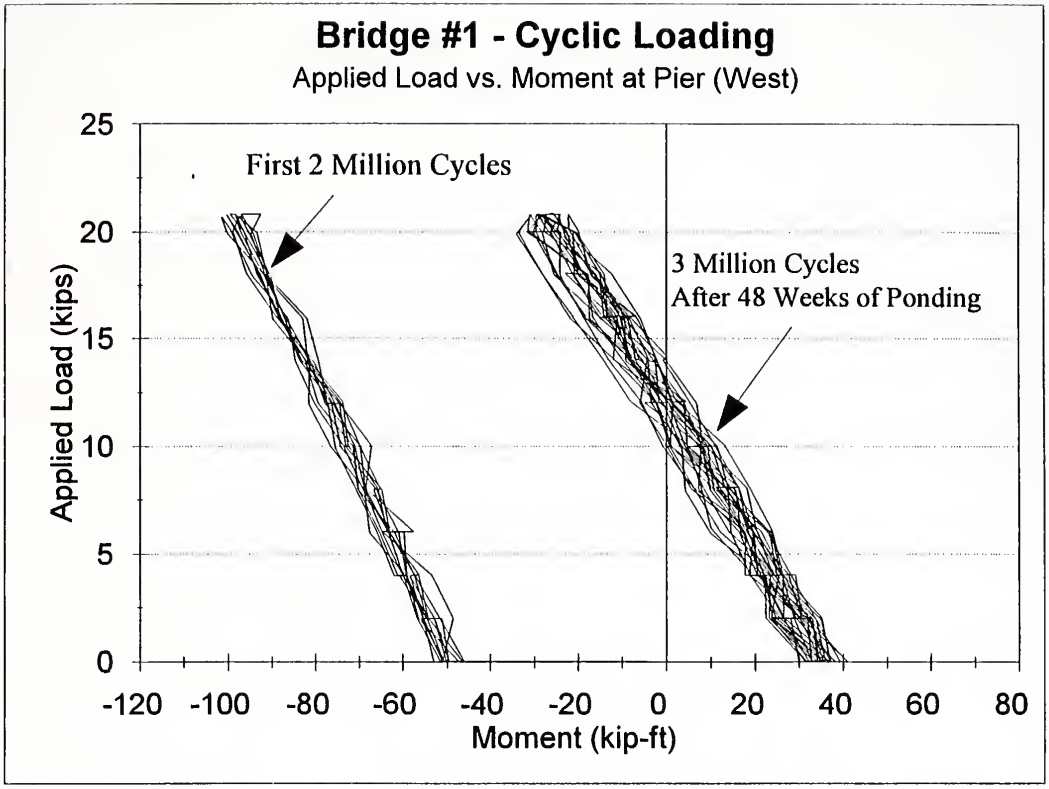

Figure 5.30 Continuity Moments at West Side of Pier During the Cyclic Loading of Bridge # 1

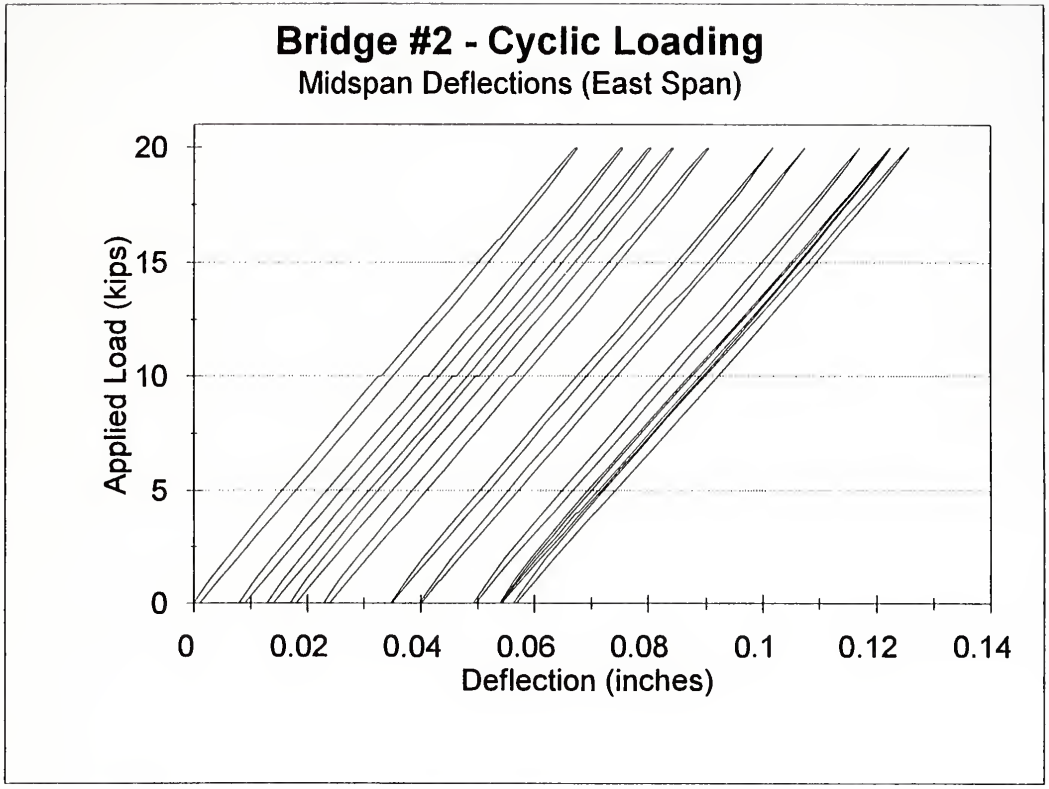

Figure 5.31 Load Versus Deflection Curves During the Cyclic Loading of Bridge #2 (East Span)

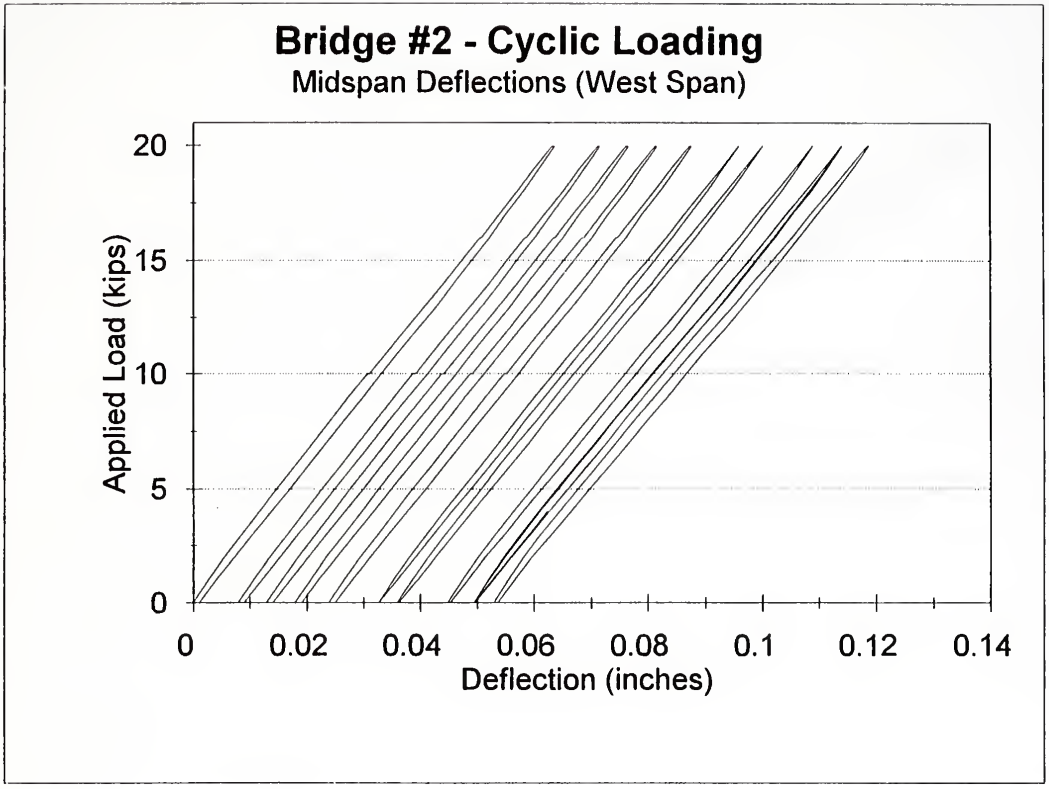

Figure 5.32 Load Versus Deflection Curves During the Cyclic Loading of Bridge #2 (West Span)

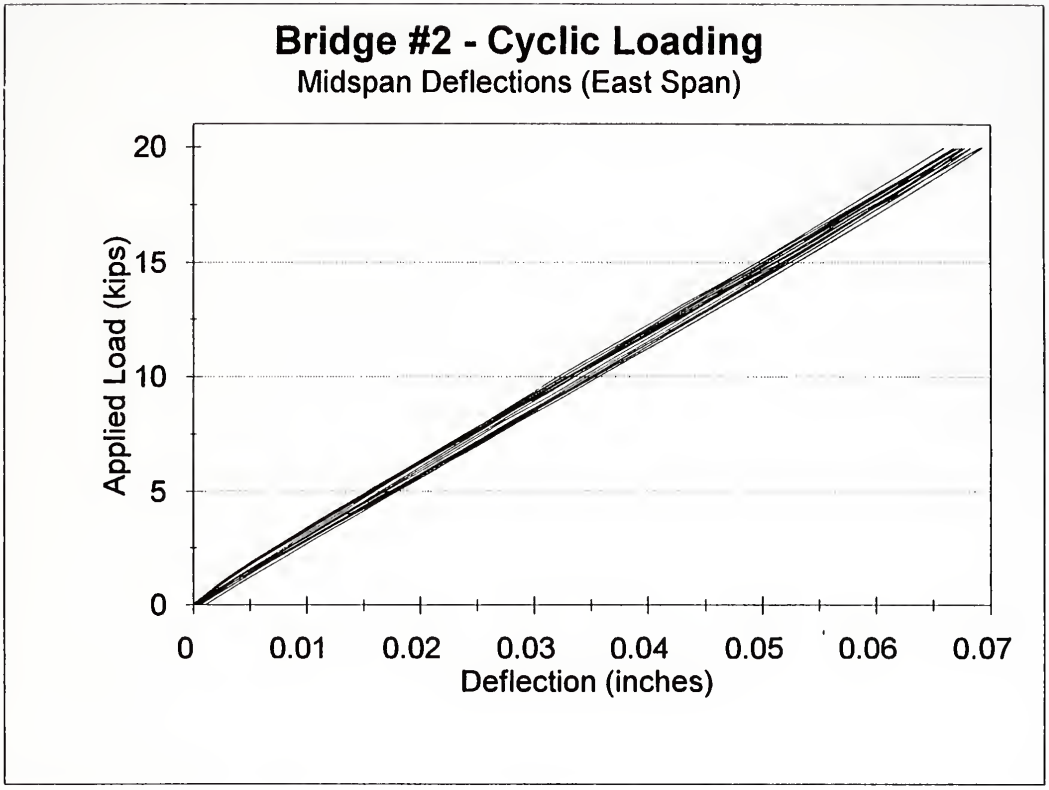

Figure 5.33 Comparison of Instantaneous Deflections During the Cyclic Loading of Bridge #2 (East Span)

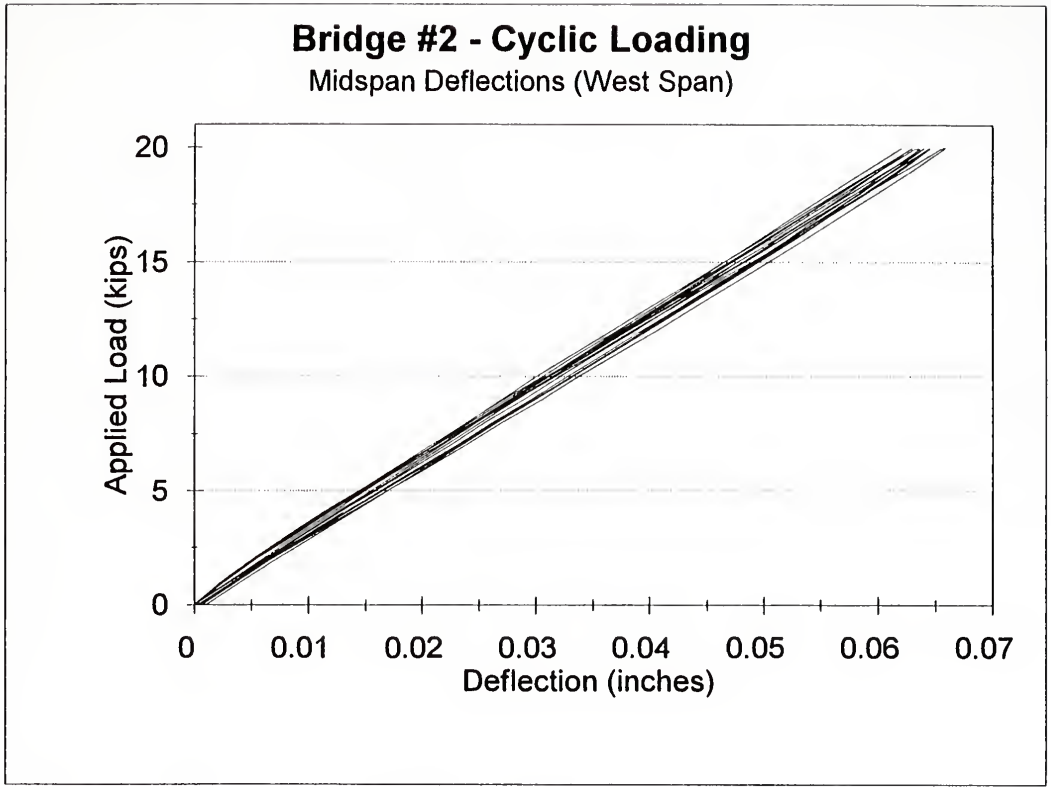

Figure 5.34 Comparison of Instantaneous Deflections During the Cyclic Loading of Bridge #2 (West Span)

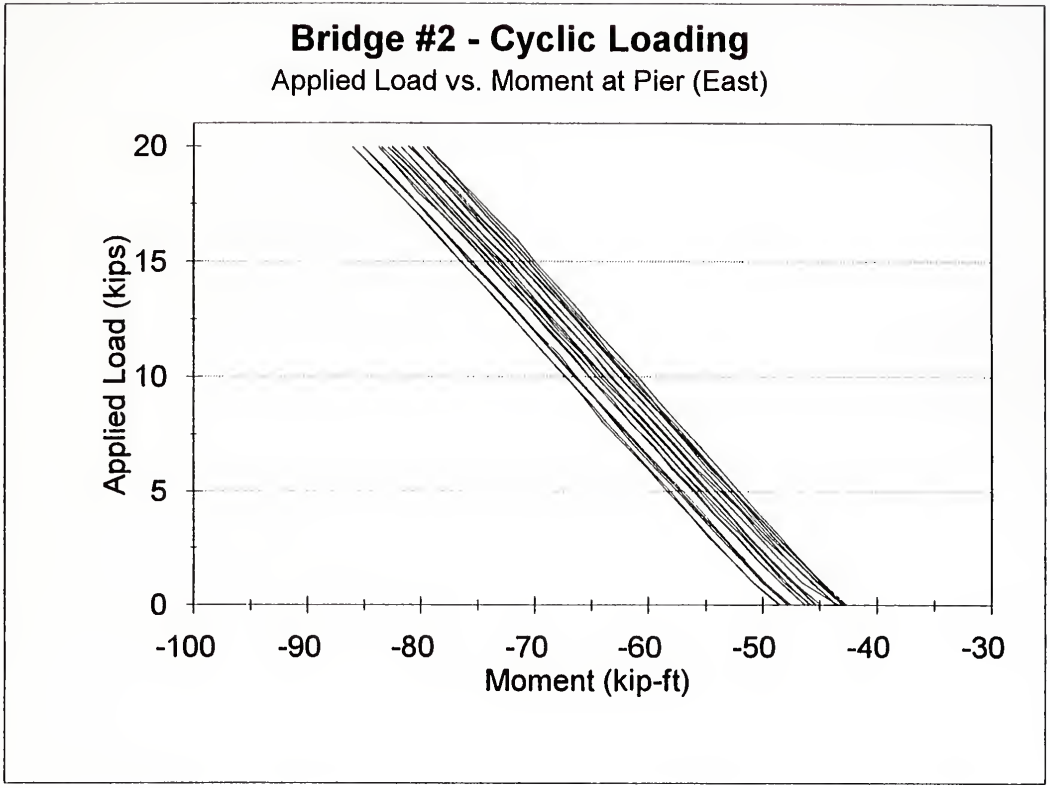

Figure 5.35 Continuity Moments at East Side of Pier During the Cyclic Loading of Bridge # 2

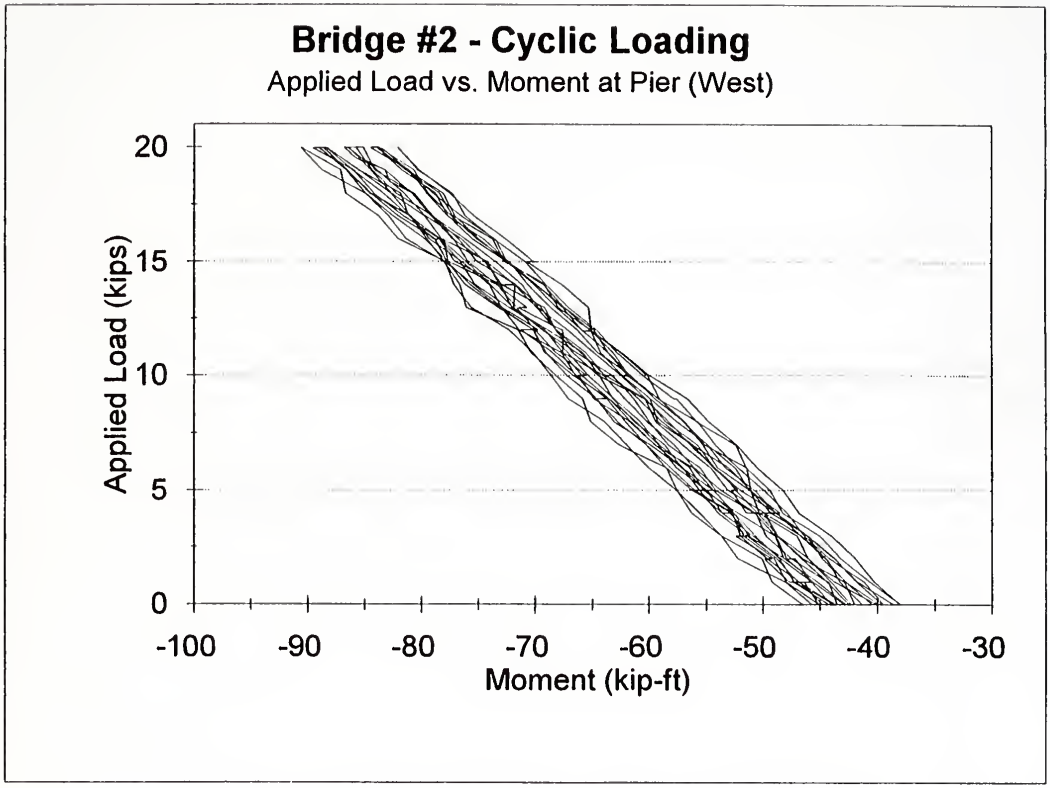

Figure 5.36 Continuity Moments at West Side of Pier During the Cyclic Loading of Bridge # 2

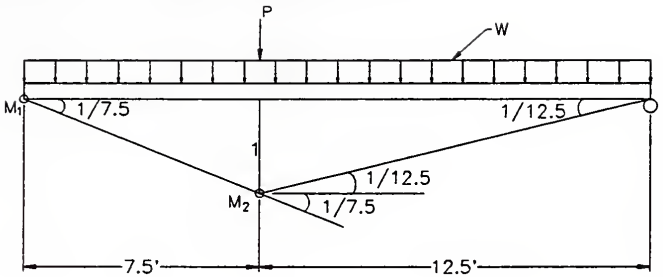

Internal Work = External Work

$$M_1\left(\frac{1}{7.5}\right)+M_2\left(\frac{1}{7.5}+\frac{1}{12.5}\right)=P(1)+w\left(\frac{1}{2}\right)(20)(1) \tag{1}$$

$$0.133M_1+0.213M_2=P+10w \tag{2}$$

$$P=0.133M_1+0.213M_2-10w \tag{3}$$

Figure 5.37 Calculation of Failure Loads By Virtual Work

AASHTO Nominal Prestressed Moments for Bridge #1

$$f_{ps} = f_{pu}\left(1 - k\frac{c}{d_p}\right) \qquad (5.7.3.1.1\text{-}1)$$

f_{pu} = 70 ksi
k = .28 for low-relaxation strand

$$c = \frac{A_{ps}f_{pu}}{.85f'_c\beta_1 b + kA_{ps}\dfrac{f_{pu}}{d_p}} \qquad (5.7.3.1.1\text{-}4)$$

$f'_c \approx 6.2$ ksi for both bridges
β_1 = 0.74
b = 96 in.
A_{ps} = 2.672 in^2 for Bridge #1
= 1.336 in^2 for Bridge #2
d_p = 12 in. - 1.75 in. = 10.25 in.

$$c = \frac{(2.672\ in^2)(270\ ksi)}{.85(6.2)(0.74)(96)+.28(2.672)\dfrac{270}{10.25}} = 1.831\ in.$$

$$f_{ps} = 270\left(1-.28\left(\frac{1.831}{10.25}\right)\right) = 256.5\ ksi$$

$$M_n = A_{ps}f_{ps}\left(d_p - \frac{a}{2}\right) \qquad (5.7.3.2.2\text{-}1)$$

$$a = \beta_1 c = 0.74(1.831) = 1.355\ in.$$

$$M_n = 2.672(256.5\ ksi)\left(10.25 - \frac{1.355}{2}\right) = 6561\ k\text{-}in = 547\ k\text{-}ft$$

Figure 5.38 Calculation of AASHTO Moment at Prestressed Section (Bridge #1)

AASHTO Nominal Prestressed Moments for Bridge #2

$$f_{ps} = f_{pu}\left(1 - k\frac{c}{d_p}\right) \qquad (5.7.3.1.1\text{-}1)$$

f_{pu} = 70 ksi
k = .28 for low-relaxation strand

$$c = \frac{A_{ps}f_{pu}}{.85f'_c\beta_1 b + kA_{ps}\frac{f_{pu}}{d_p}} \qquad (5.7.3.1.1\text{-}4)$$

$f'_c \approx 6.2$ ksi for both bridges
β_1 = 0.74
b = 96 in.
A_{ps} = 2.672 in^2 for Bridge #1
= 1.336 in^2 for Bridge #2
d_p = 12 in. - 1.75 in. = 10.25 in.

$$c = \frac{(1.336\ in^2)(270\ ksi)}{.85(6.2)(0.74)(96)+.28(1.336)\frac{270}{10.25}} = 0.939\ in.$$

$$f_{ps} = 270\left(1-.28\left(\frac{0.939}{10.25}\right)\right) = 263.1\ ksi$$

$$M_n = A_{ps}f_{ps}\left(d_p - \frac{a}{2}\right) \qquad (5.7.3.2.2\text{-}1)$$

$$a = \beta_1 c = 0.74(0.939) = 0.695\ in.$$

$$M_n = 1.336(263.1\ ksi)\left(10.25 - \frac{0.695}{2}\right) = 3481\ k\text{-}in = 290\ k\text{-}ft$$

Figure 5.39 Calculation of AASHTO Moment at Prestressed Section (Bridge #2)

AASHTO Nominal Moments at Pier for Bridge #1

16-#4 bars

$A_s = 16(.2) = 3.20\ in^2$ $\qquad$ $d_s = 12\ in. - 2.5\ in. - .25\ in = 9.25\ in.$

$f_y = 60\ ksi$ $\qquad$ $f_c = 6.2\ ksi$

$\beta_1 = 0.74$ $\qquad$ $b = 96\ in.$

$$c = \frac{A\ f_y}{.85 f'_c\ \beta_1 b} = \frac{3.2(60)}{.85(6.2)(0.74)(96)} = .513\ in. \qquad (5.7.3.1.1\text{-}4)$$

$$a = \beta_1 c = 0.380$$

$$M_n = A_s f_y \left(d_s - \frac{a}{2}\right) = 3.2(60)\left(9.25 - \frac{.380}{2}\right) = 1740\ k\text{-}in. = 145\ k\text{-}ft$$

Figure 5.40 Calculation of AASHTO Moment at Pier (Bridge #1)

AASHTO Nominal Moments at Pier for Bridge #2

6-#6 bars

$A_s = 6(.44) = 2.64 \text{ in}^2$ $\quad$ $d_s = 12 \text{ in.} - 2.5 \text{ in.} - .325 \text{ in} = 9.125 \text{ in.}$

$f_y = 60 \text{ ksi}$ $\quad$ $f_c = 6.2 \text{ ksi}$

$\beta_1 = 0.74$ $\quad$ $b = 96 \text{ in.}$

$$c = \frac{A\, f_y}{.85 f'_c \beta_1 b} = \frac{2.64(60)}{.85(6.2)(0.74)(96)} = .423 \text{ in.} \qquad (5.7.3.1.1\text{-}4)$$

$$a = \beta_1 c = 0.313$$

$$M_n = A_s f_y \left(d_s - \frac{a}{2} \right) = 2.64(60)\left(9.125 - \frac{.313}{2} \right) = 1421 \text{ k-in.} = 118 \text{ k-ft}$$

Figure 5.41 Calculation of AASHTO Moment at Pier (Bridge #2)

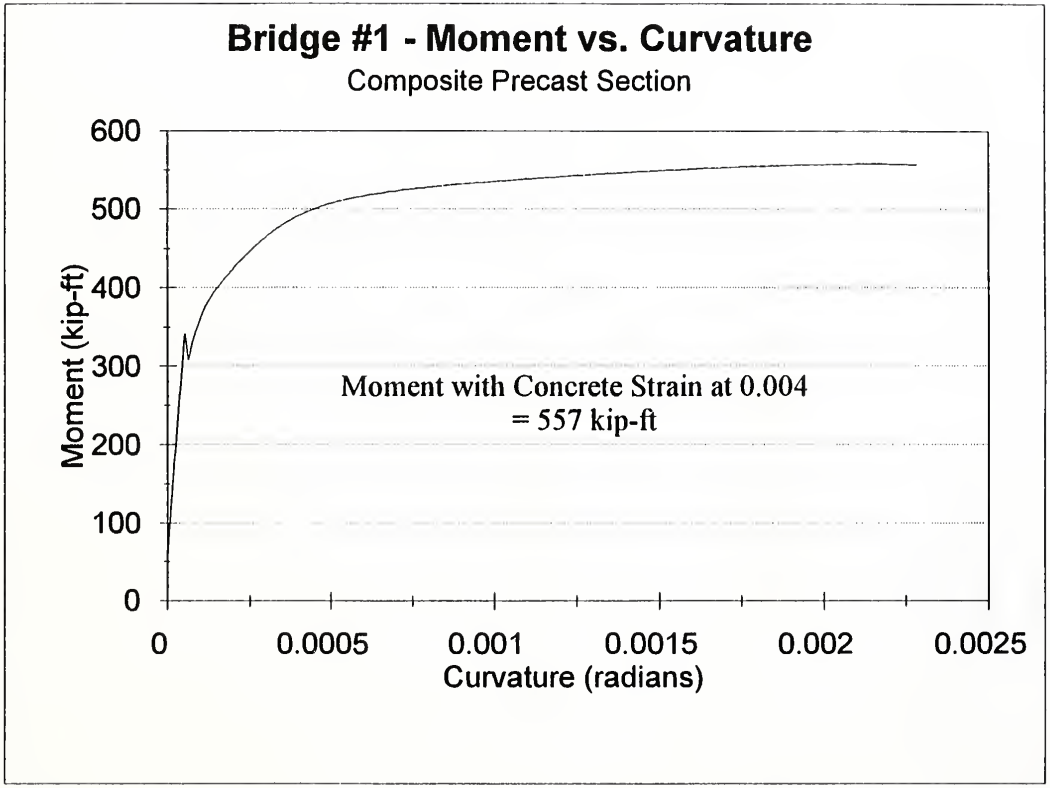

Figure 5.42 Moment-Curvature Relationship of Composite Precast Section (Bridge #1)

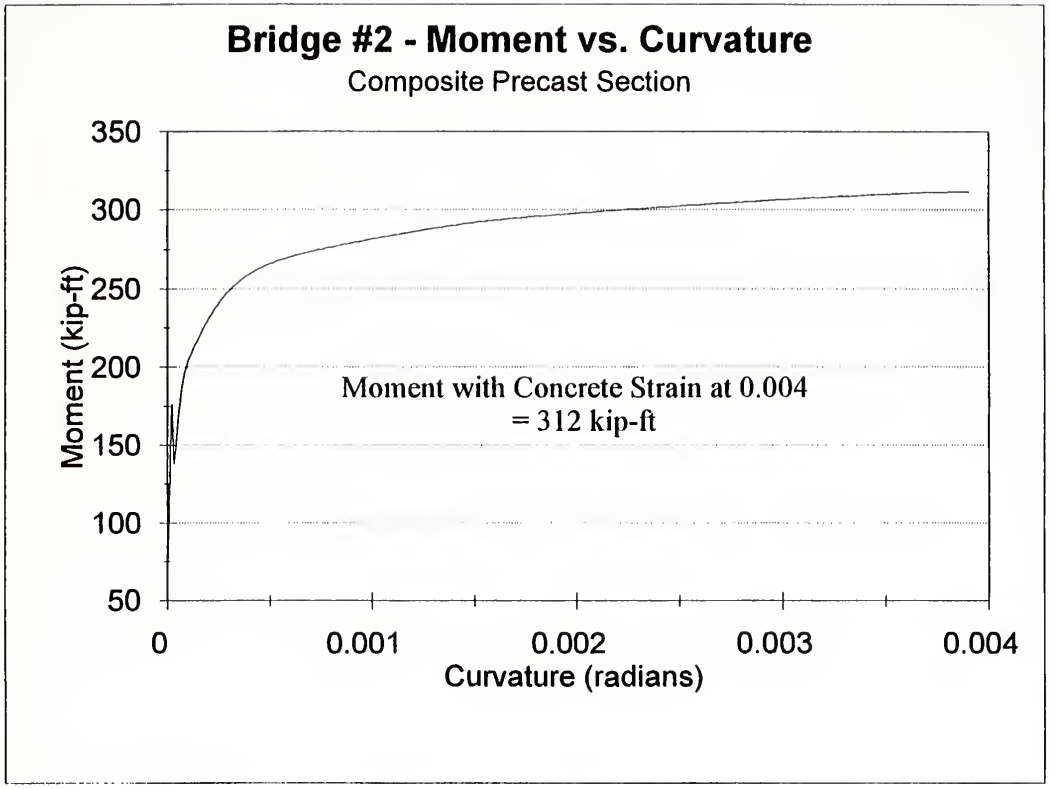

Figure 5.43 Moment-Curvature Relationship of Composite Precast Section (Bridge #2)

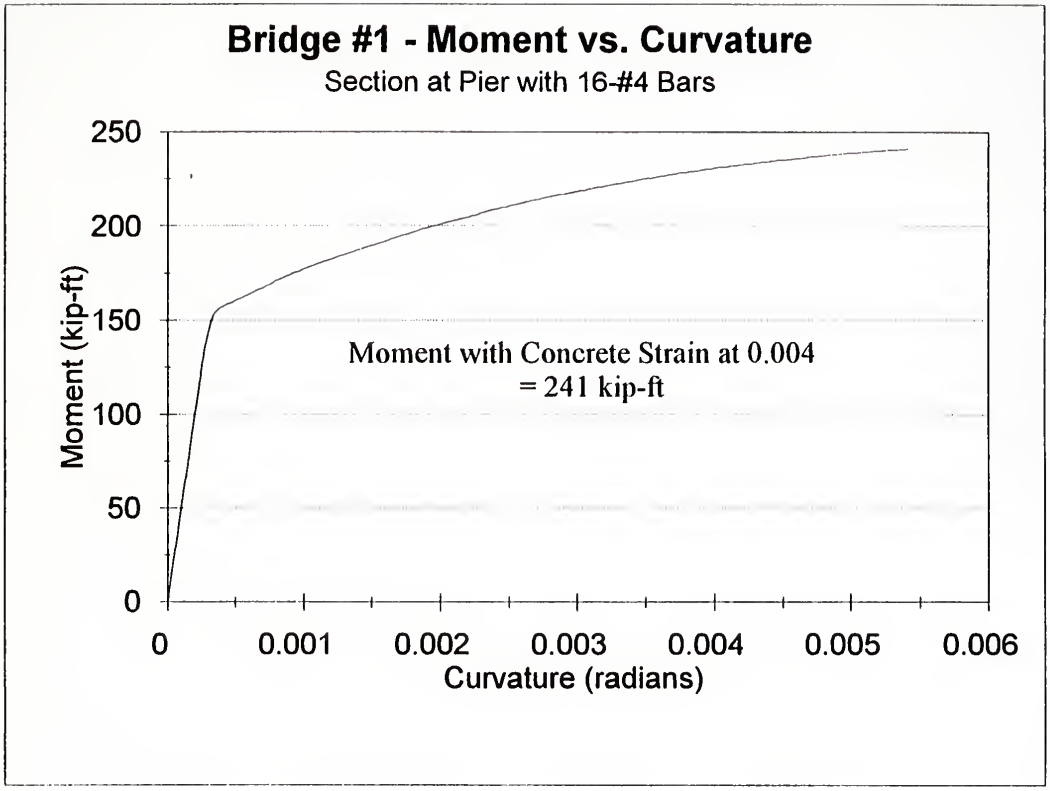

Figure 5.44 Moment-Curvature Relationship of Section at Pier (Bridge #1)

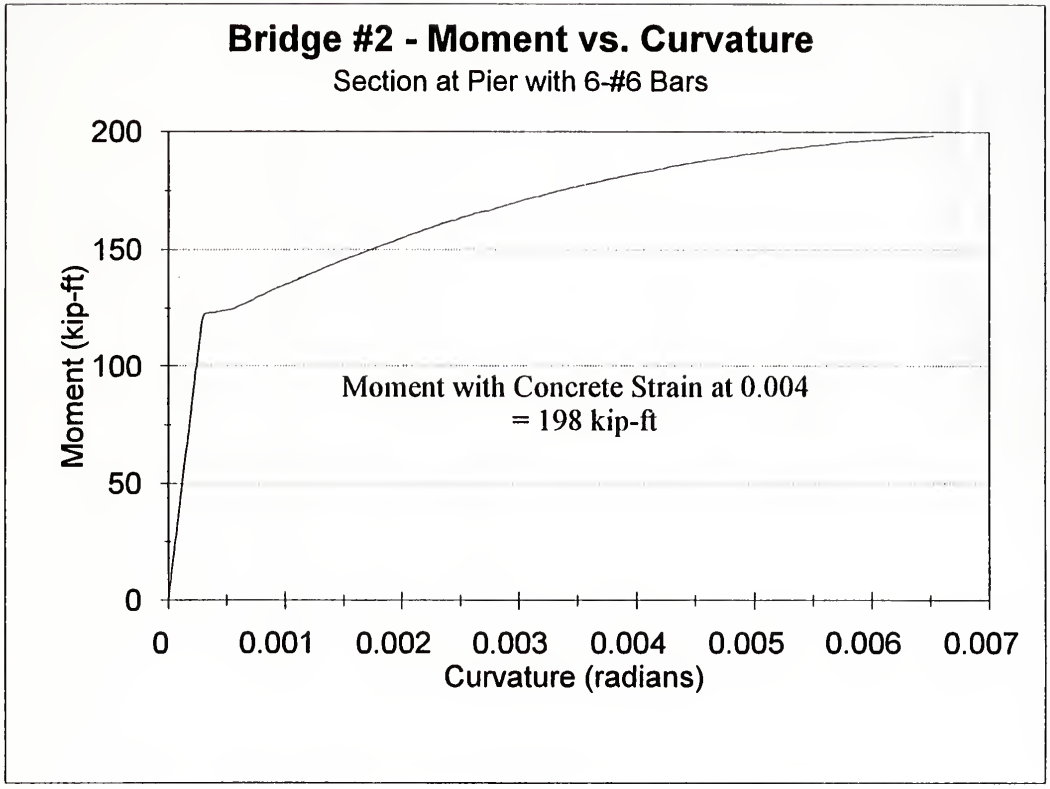

Figure 5.45 Moment-Curvature Relationship of Section at Pier (Bridge #2)

Calculation of Cracking Moment for Bridge #1

Estimated strand stress at start of final loading = 174 ksi

Estimated Modulus of Rupture, f_r = 820 psi
(average of flexure beam tests)

$$\frac{P}{A}+\frac{Pe}{S_{NC}}-\frac{M_{self}}{S_{NC}}-\frac{M_{top}}{S_{NC}}-\frac{M_{LL}}{S_C}=f_r$$

$e = 3$ in.-1.75 in.$= 1.25$ in. $\qquad A = 96(6) = 576$ in^2

$$S_C=\frac{96(12)^2}{6}=2304 \text{ in}^3 \qquad S_{NC}=\frac{96(6)^2}{6}=576 \text{ in}^3$$

$$P = 16(0.167)(174) = 464{,}930 \text{ lb}$$

$$M_{self} = M_{top} = \frac{96(6)}{144}\times 150 \times \frac{20^2}{8} = 30{,}000 \text{ lb - ft} = 360{,}000 \text{ lb - in.}$$

$$\frac{464{,}930}{576}+\frac{464{,}930(1.25)}{576}-\frac{360000}{576}-\frac{360000}{576}-\frac{M_{LL}}{2304}=-820$$

$$M_{LL} = 3{,}194{,}000 \text{ lb - in} = 266 \text{ k - ft}$$

$$M_{cr} = M_{self} + M_{top} + M_{LL} = 266 + 30 + 30 = 326 \text{ k - ft}$$

Figure 5.46 Calculation of Cracking Moment at Prestressed Section (Bridge #1)

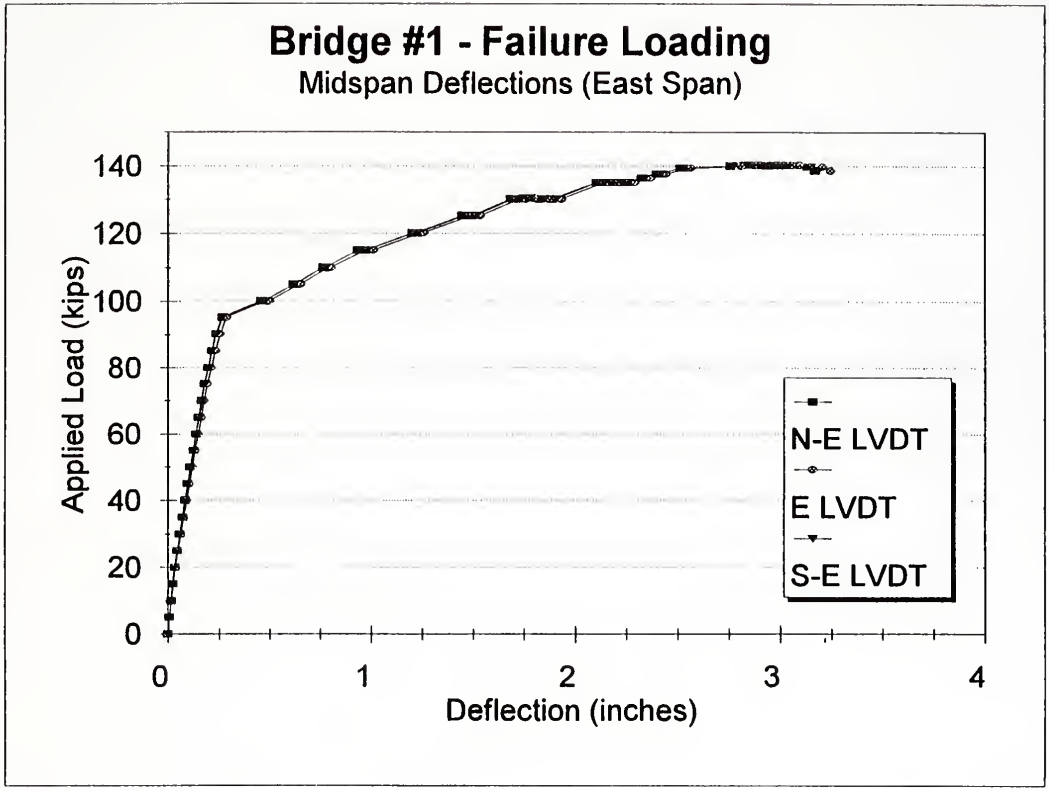

Figure 5.47 Midspan Deflections During the Failure Loading of Bridge #1 (East Span)

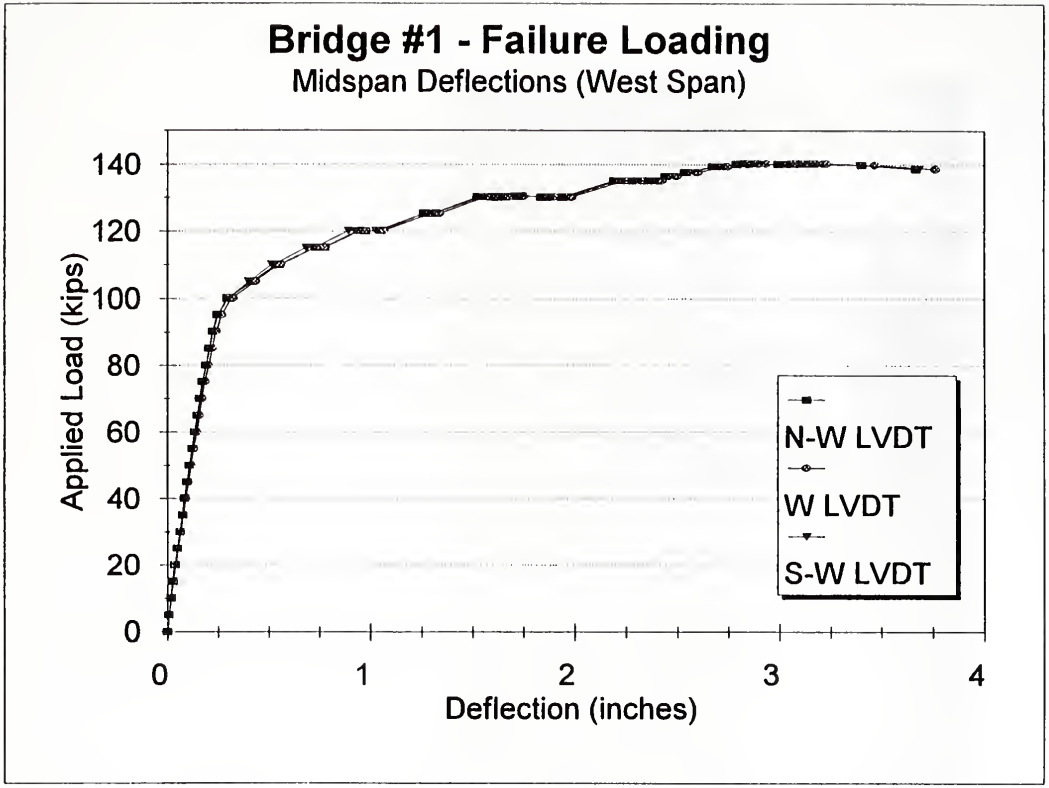

Figure 5.48 Midspan Deflections During the Failure Loading of Bridge #1 (West Span)

Figure 5.49 Failure of Bridge #1 at the Loading Point in the West Span

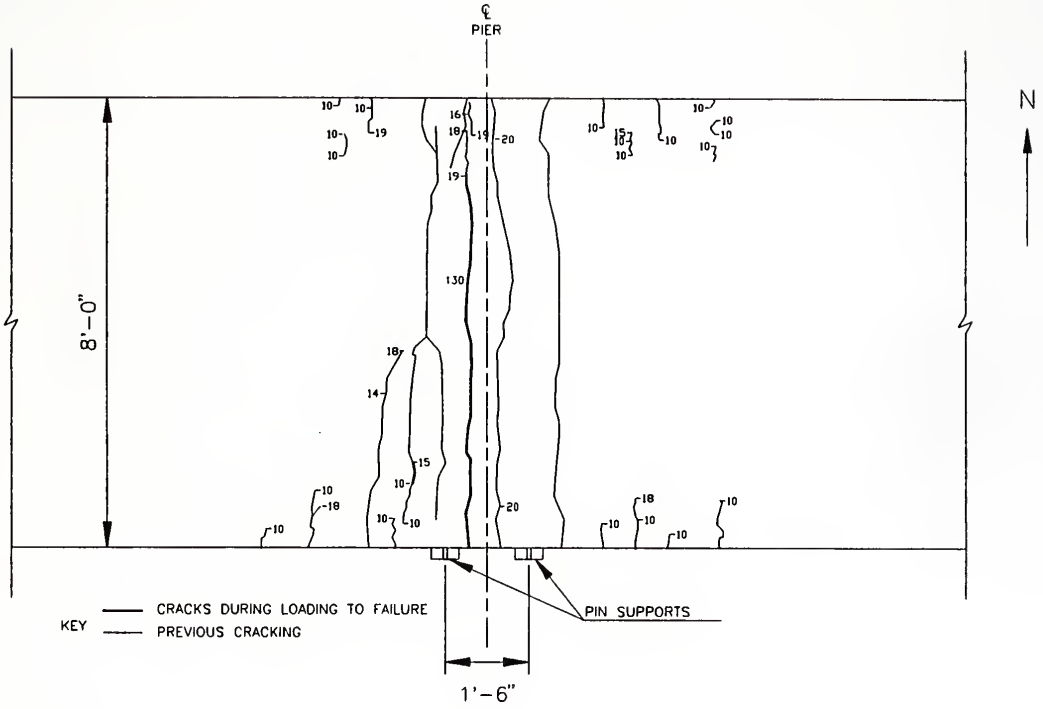

5.50 Cracks Occurring During the Failure Loading of Bridge #1 (Plan View)

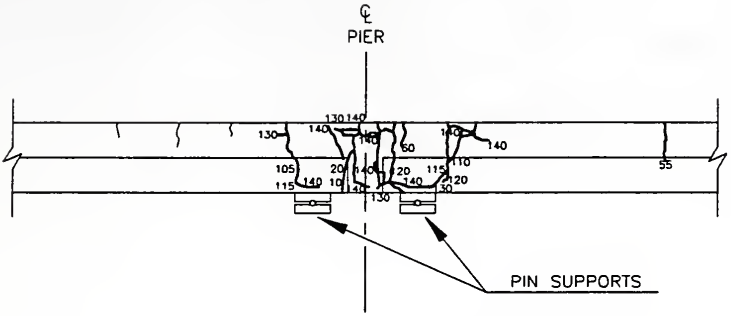

NORTH ELEVATION

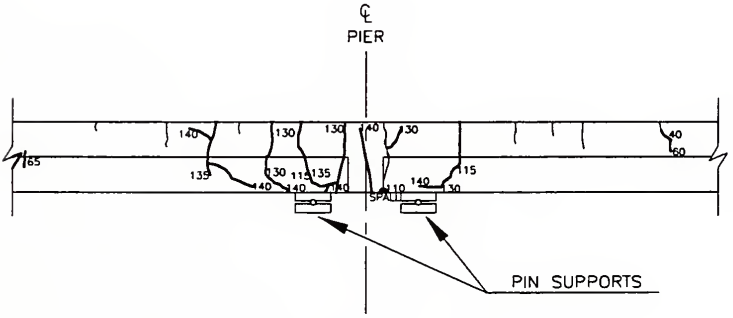

SOUTH ELEVATION

KEY
CRACKS DURING LOADING TO FAILURE
PREVIOUS CRACKING

Figure 5.51 Cracks During the Failure Loading of Bridge #1 (Elevations at Pier)

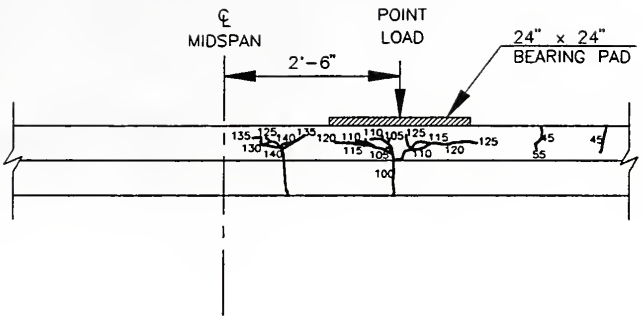

NORTH ELEVATION

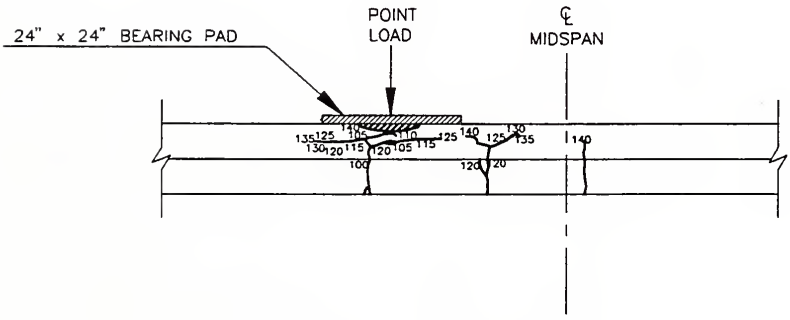

SOUTH ELEVATION

KEY
——— CRACKS DURING LOADING TO FAILURE
——— PREVIOUS CRACKING

Figure 5.52 Cracks During the Failure Loading of Bridge #1 (East Span Elevations)

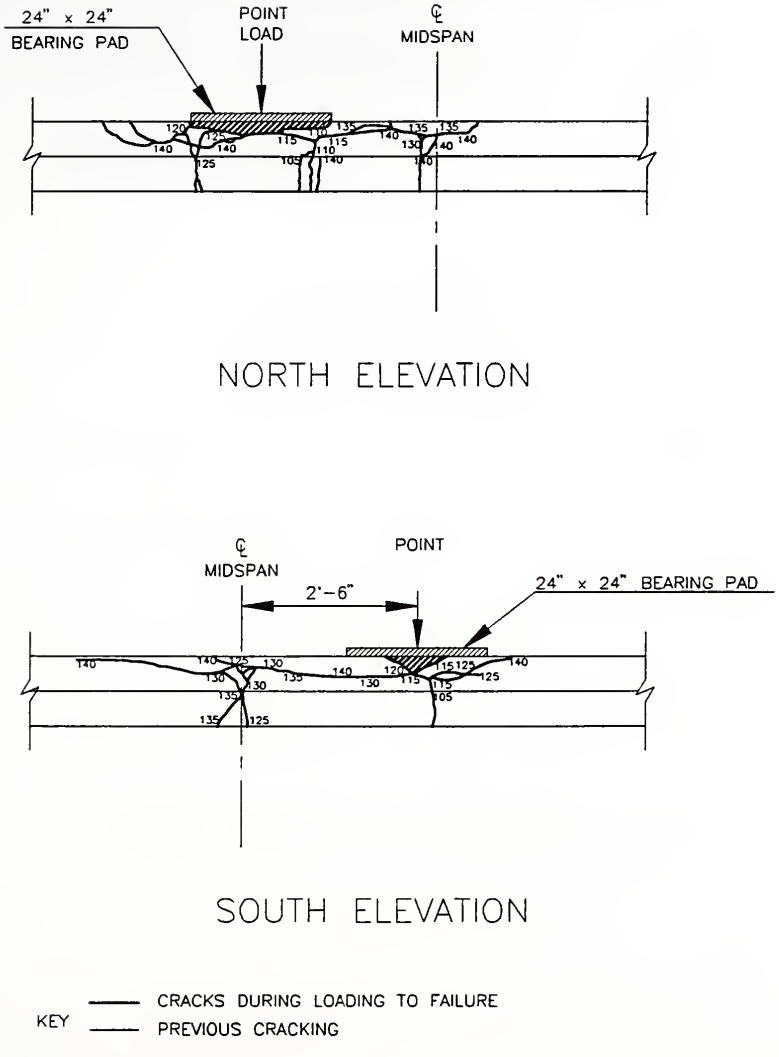

Figure 5.53 Cracks During the Failure Loading of Bridge #1 (West Span Elevations)

Calculation of Cracking Moment for Bridge #2

Estimated strand stress at start of final loading = 182 ksi

Estimated Modulus of Rupture, f_r = 875 psi
(average of flexure beam tests)

$$\frac{P}{A}+\frac{Pe}{S_{NC}}-\frac{M_{self}}{S_{NC}}-\frac{M_{top}}{S_{NC}}-\frac{M_{LL}}{S_C}=f_r^-$$

$e = 3 \text{ in.} - 1.75 \text{ in.} = 1.25 \text{ in.}$ $\qquad A = 96(6) = 576 \text{ in}^2$

$$S_C = \frac{96(12)^2}{6} = 2304 \text{ in}^3 \qquad S_{NC} = \frac{96(6)^2}{6} = 576 \text{ in}^3$$

$$P = 8(0.167)(182) = 182 \text{ lb}$$

$$M_{self} = M_{top} = \frac{96(6)}{144} \times 150 \times \frac{20^2}{8} = 30{,}000 \text{ lb - ft} = 360{,}000 \text{ lb - in.}$$

$$\frac{243{,}150}{576}+\frac{243{,}150(1.25)}{576}-\frac{360000}{576}-\frac{360000}{576}-\frac{M_{LL}}{2304}=-875$$

$$M_{LL} = 1{,}324{,}000 \text{ lb - in} = 110 \text{ k - ft}$$

$$M_{cr} = M_{self} + M_{top} + M_{LL} = 110 + 30 + 30 = 170 \text{ k - ft}$$

Figure 5.54 Calculation of Cracking Moment at Prestressed Section (Bridge #2)

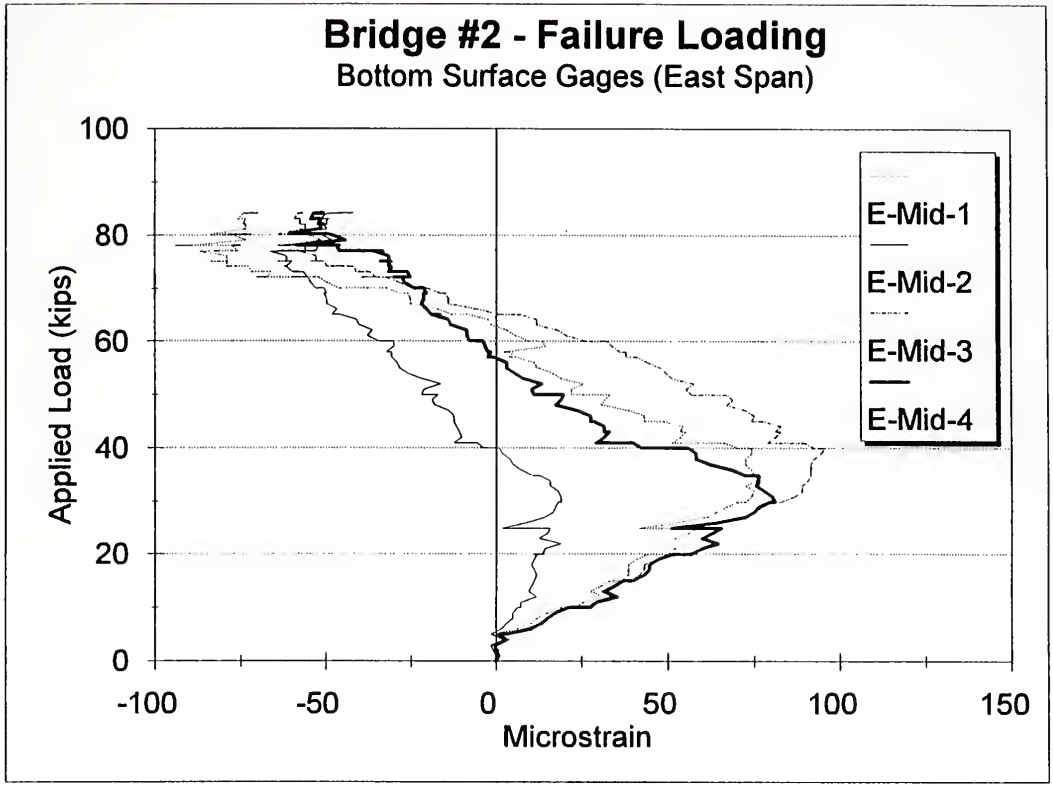

5.55 Incremental Strains in Concrete Surface Gages on Bottom of Precast Panels (Bridge #2 - East Span)

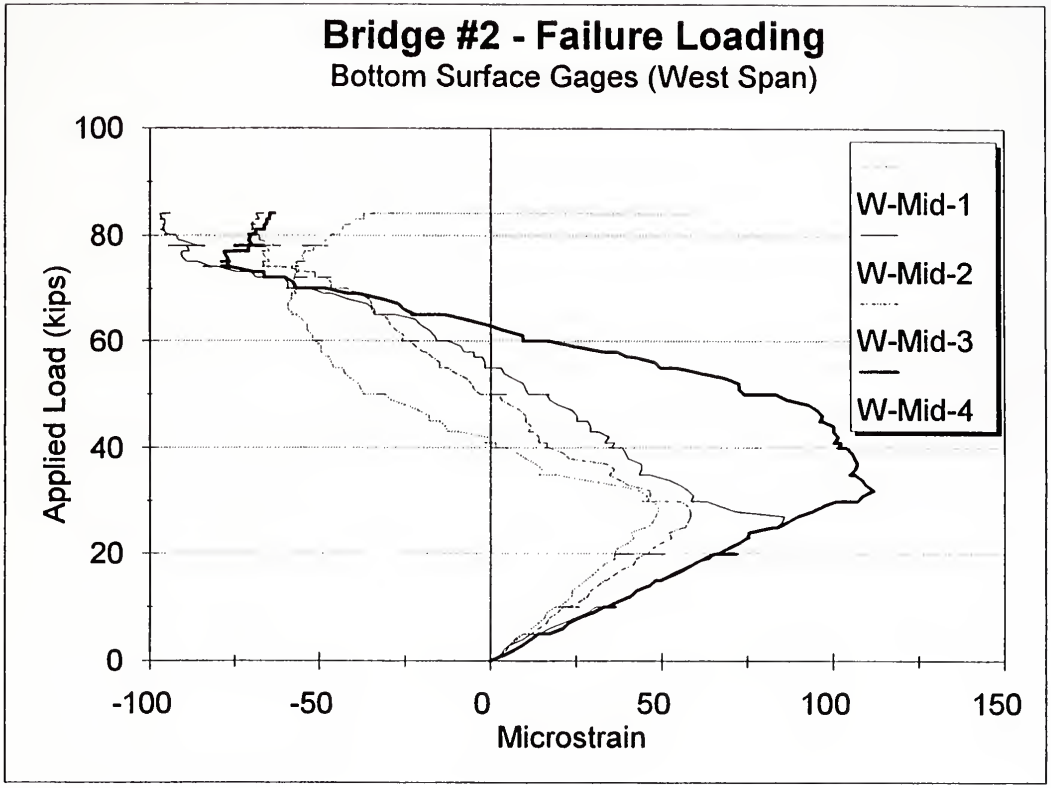

5.56 Incremental Strains in Concrete Surface Gages on Bottom of Precast Panels (Bridge #2 - West Span)

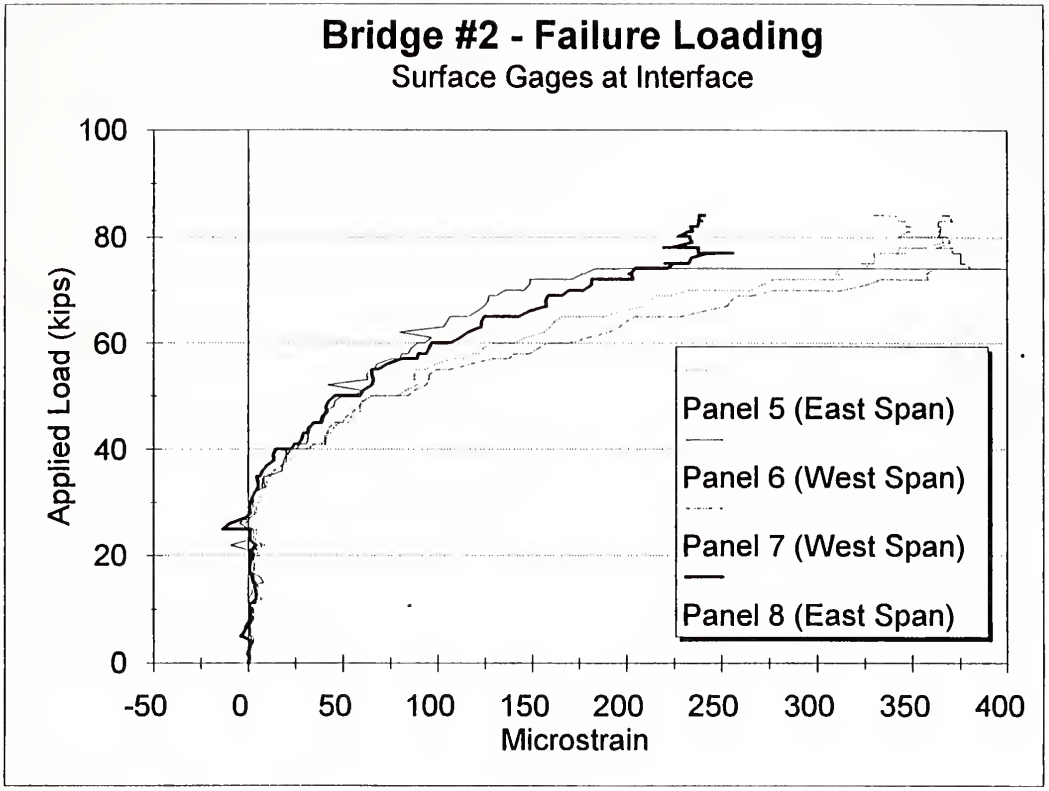

5.57 Incremental Strains in Concrete Surface Gages at Interface (Bridge #2)

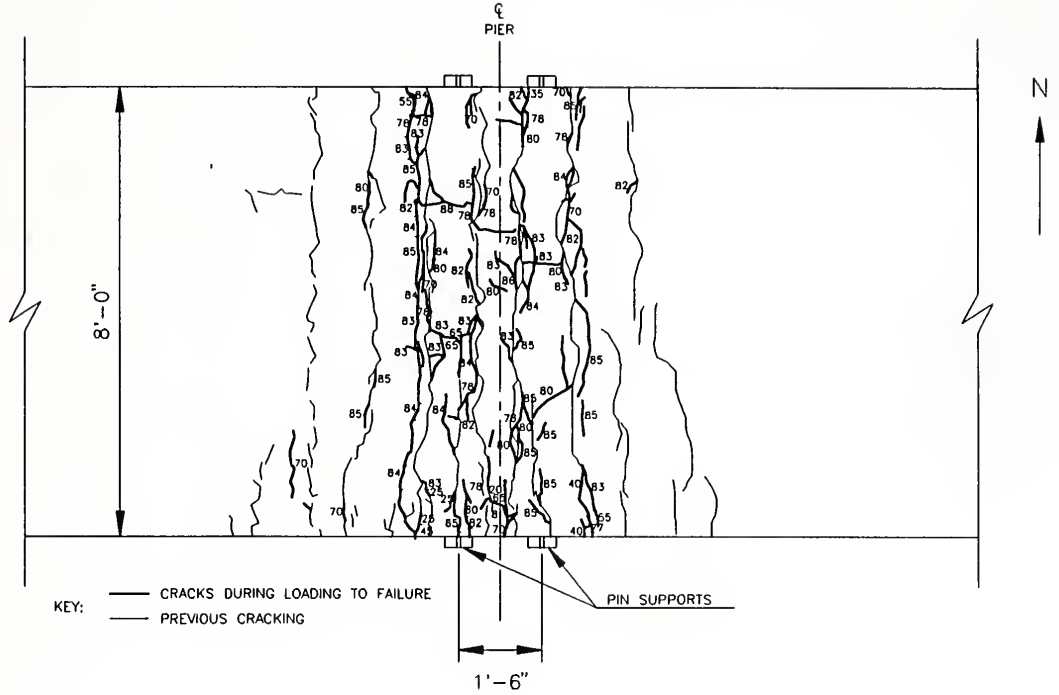

5.58 Cracks Occurring During the Failure Loading of Bridge #2 (Plan View)

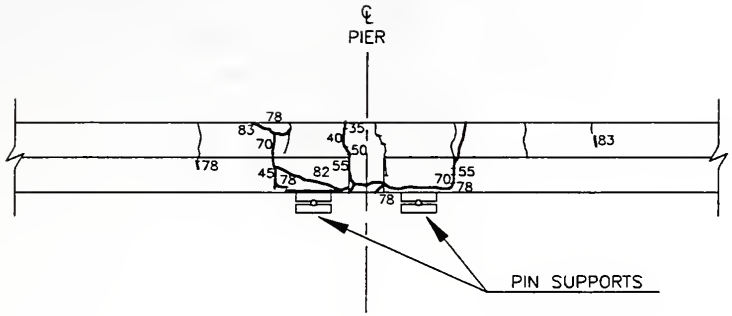

NORTH ELEVATION

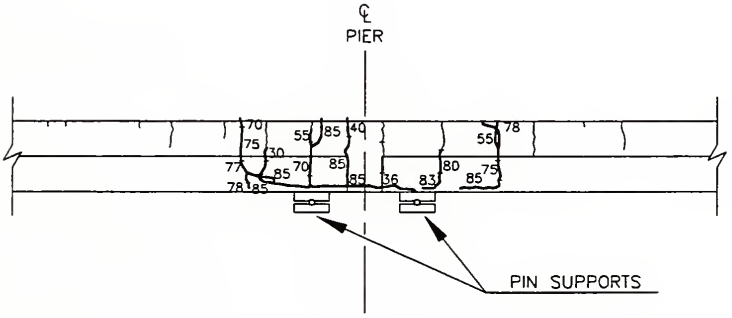

SOUTH ELEVATION

KEY:
CRACKS DURING LOADING TO FAILURE
PREVIOUS CRACKING

Figure 5.59 Cracks During the Failure Loading of Bridge #2 (Elevations at Pier)

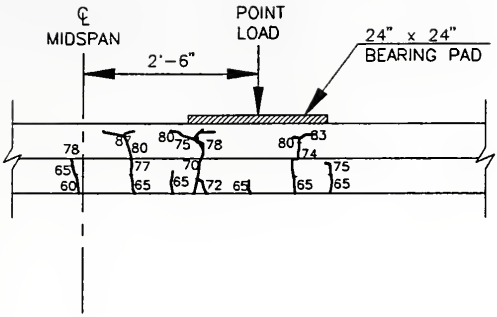

NORTH ELEVATION

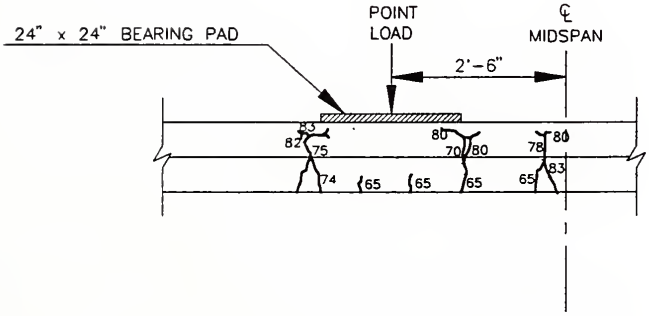

SOUTH ELEVATION

KEY: —— CRACKS DURING LOADING TO FAILURE
—— PREVIOUS CRACKING

Figure 5.60 Cracks During the Failure Loading of Bridge #2 (East Span Elevations)

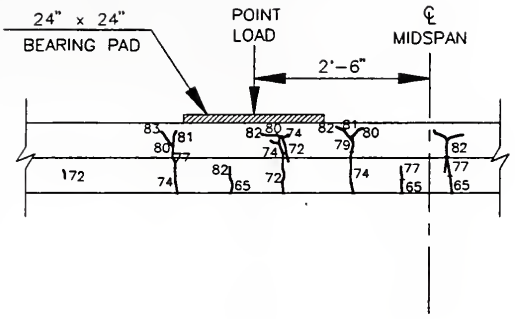

NORTH ELEVATION

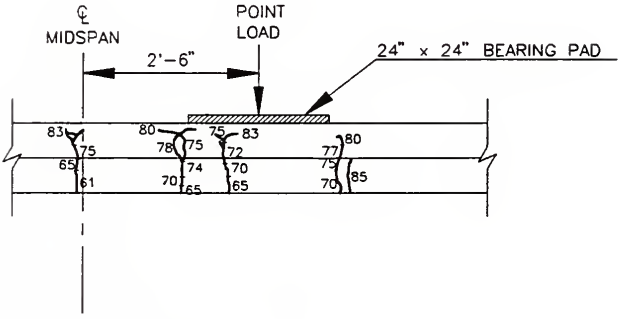

SOUTH ELEVATION

KEY:
—— CRACKS DURING LOADING TO FAILURE
—— PREVIOUS CRACKING

Figure 5.61 Cracks During the Failure Loading of Bridge #2 (West Span Elevations)

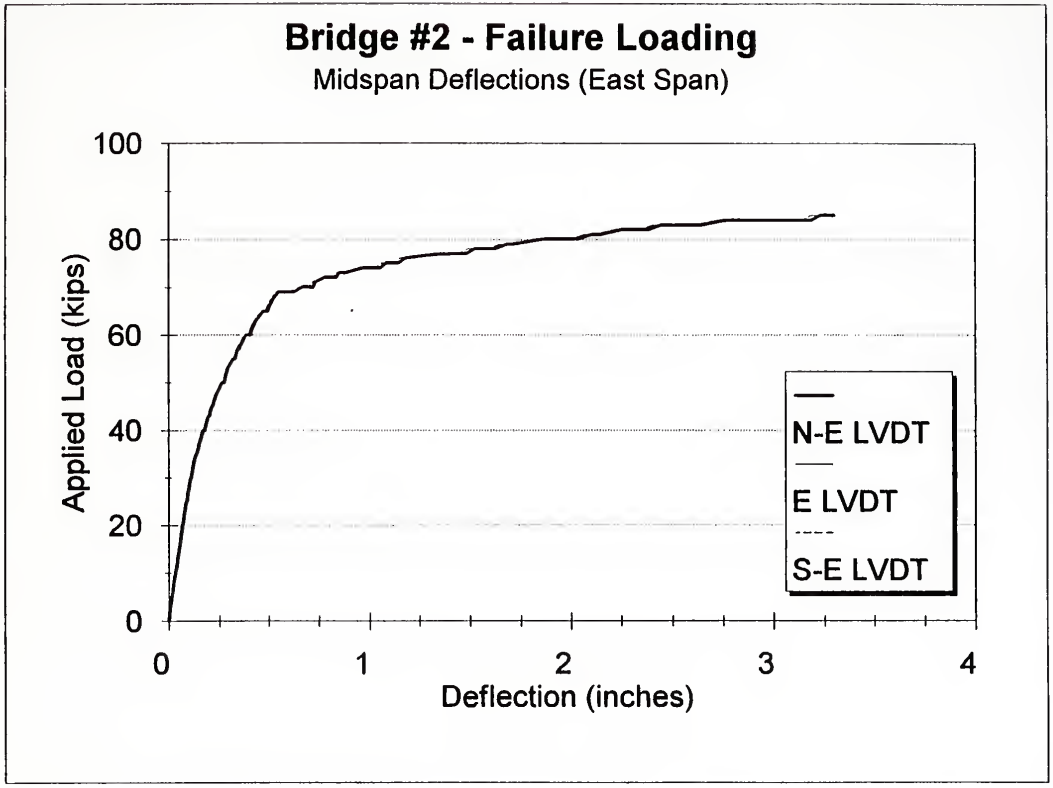

Figure 5.62 Midspan Deflections During the Failure Loading of Bridge #2 (East Span)

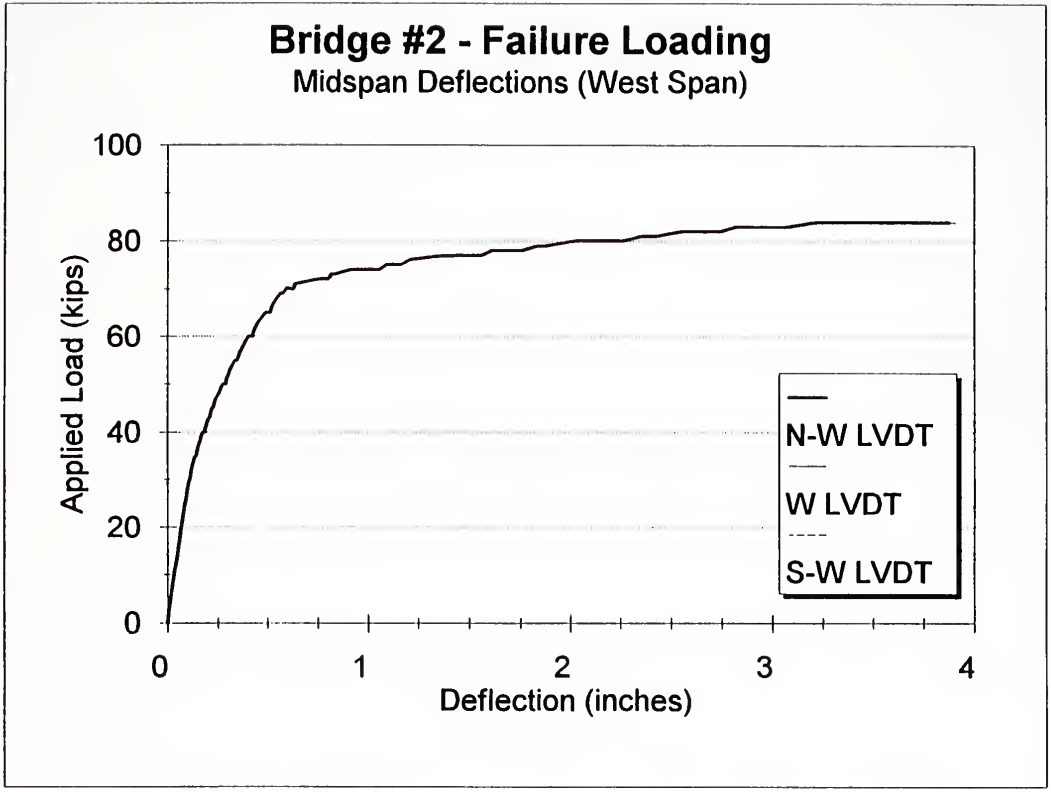

Figure 5.63 Midspan Deflections During the Failure Loading of Bridge #2 (West Span)

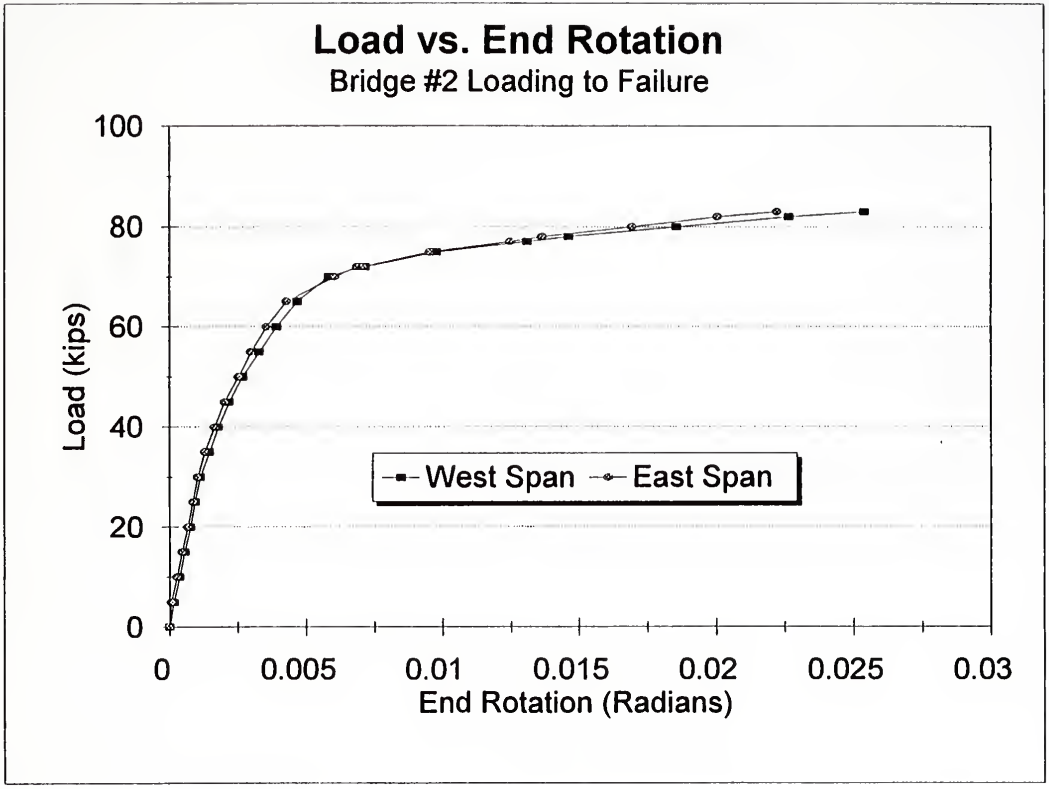

Figure 5.64 End Rotations During the Failure Loading of Bridge #2

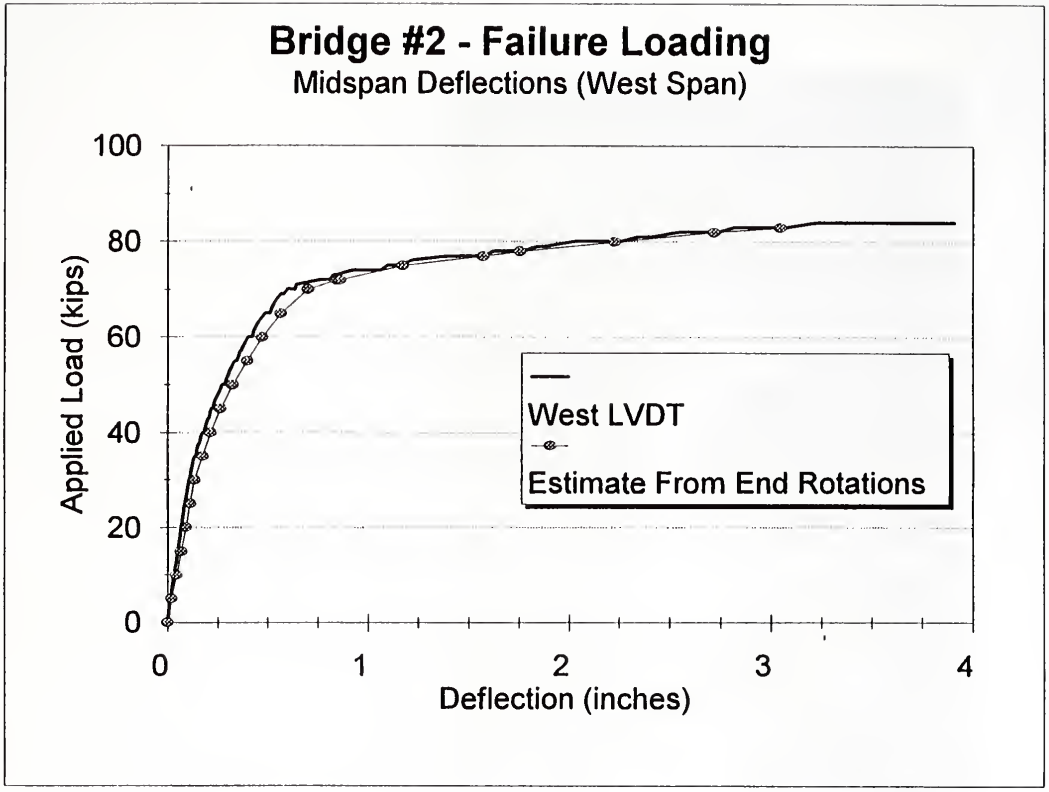

Figure 5.65 Comparison of Midspan Deflections with Values Estimated From End Rotations

Figure 5.66 Failure of Bridge #2 Occurred at the Edge of the Loading Plate

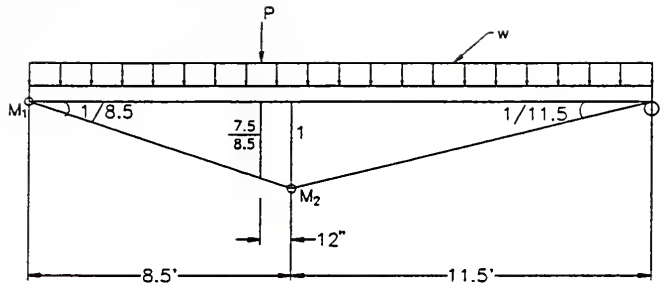

Internal Work = External Work

$$M_1\left(\frac{1}{8.5}\right)+M_2\left(\frac{1}{8.5}+\frac{1}{11.5}\right)=P\left(\frac{7.5}{8.5}\right)+w\left(\frac{1}{2}\right)(20)(1) \tag{1}$$

$$0.118M_1+.205M_2=.882P+10w \tag{2}$$

$$P=0.133M_1+.232M_2-11.333w \tag{3}$$

Figure 5.67 Calculation of Failure Load of Bridge #2 By Virtual Work

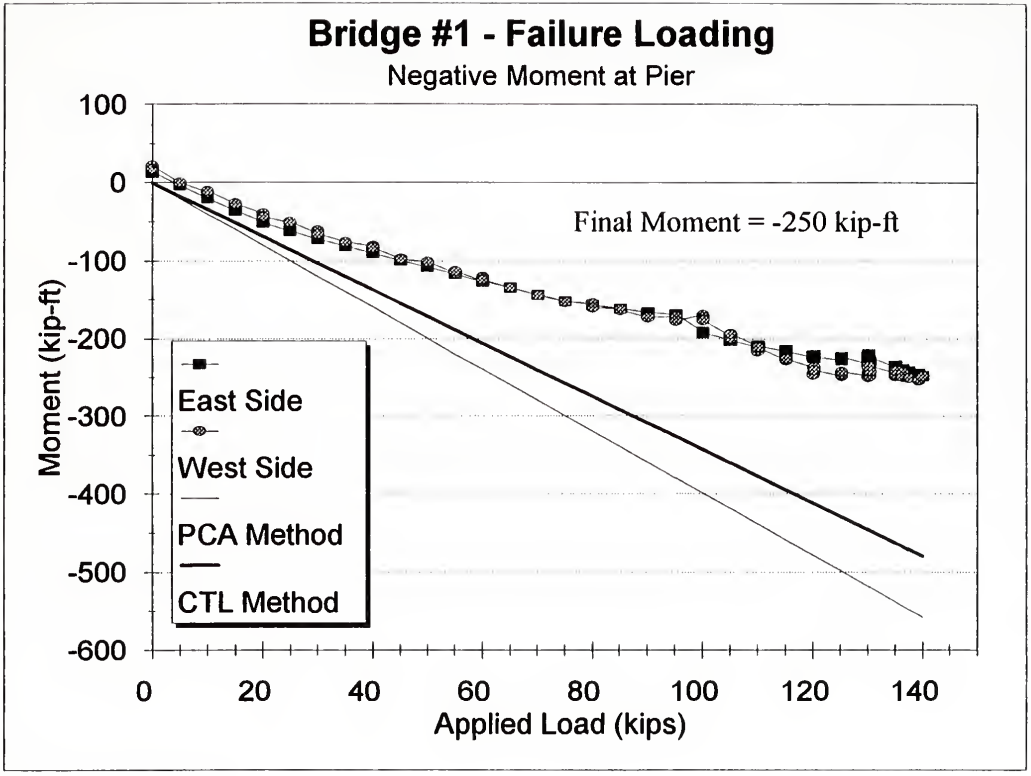

Figure 5.68 Comparison of Negative Moments at Pier with Elastic Moments (Bridge #1)

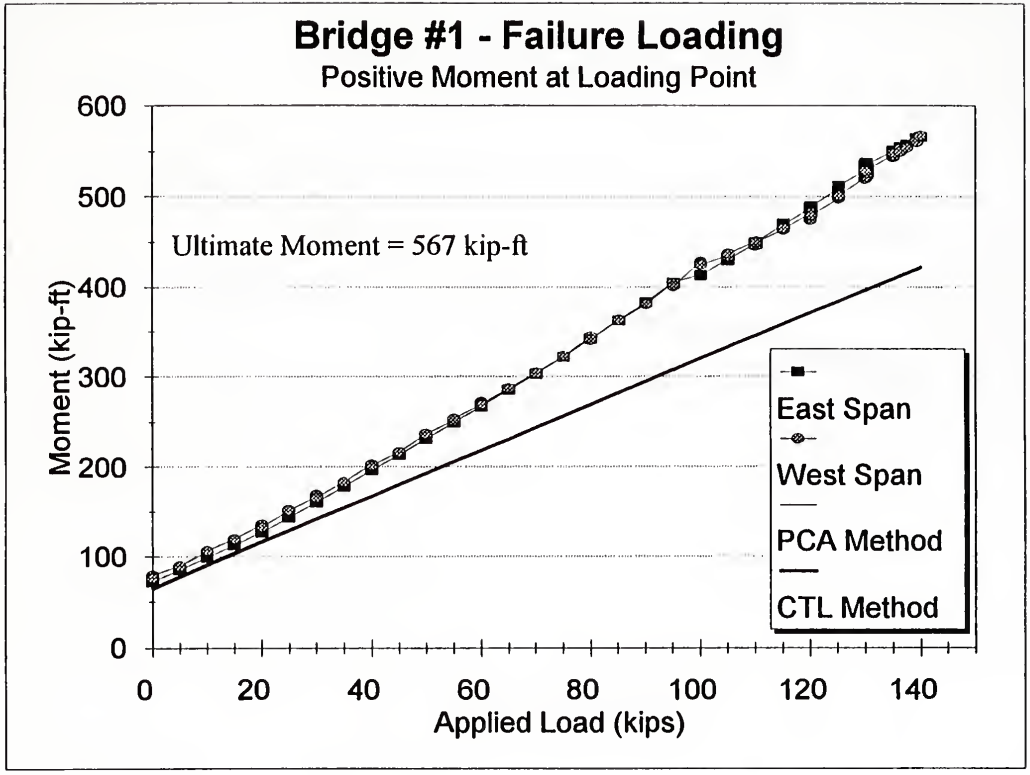

Figure 5.69 Comparison of Positive Moments at Loading Point with Elastic Moments (Bridge #1)

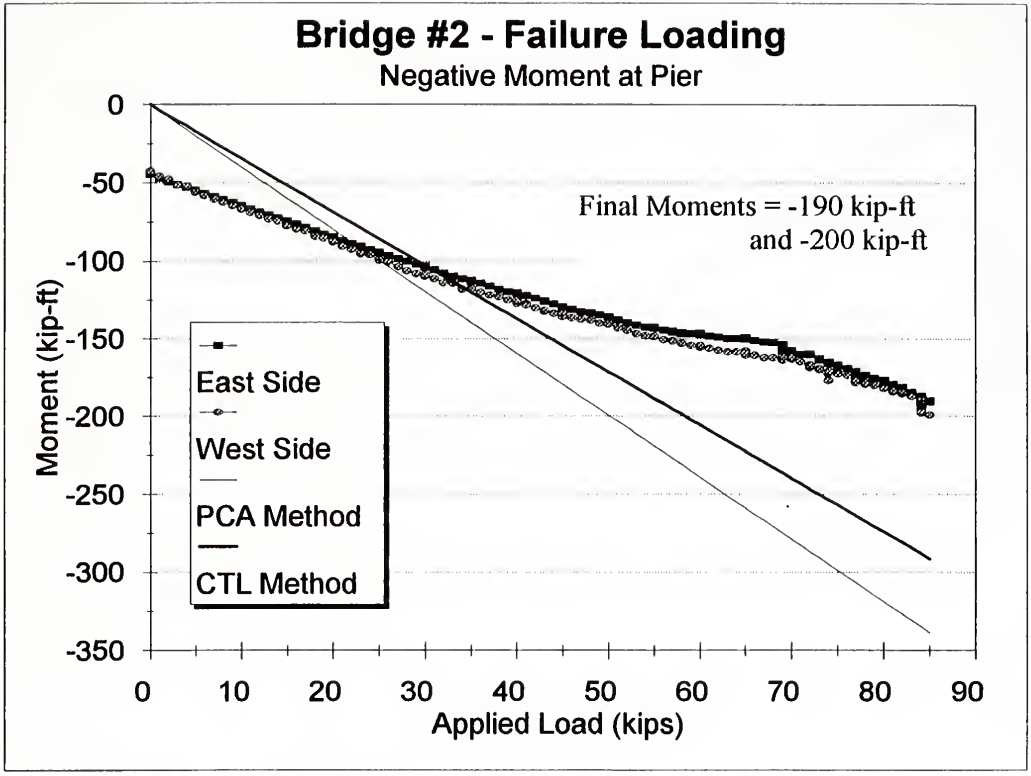

Figure 5.70 Comparison of Negative Moments at Pier with Elastic Moments (Bridge #2)

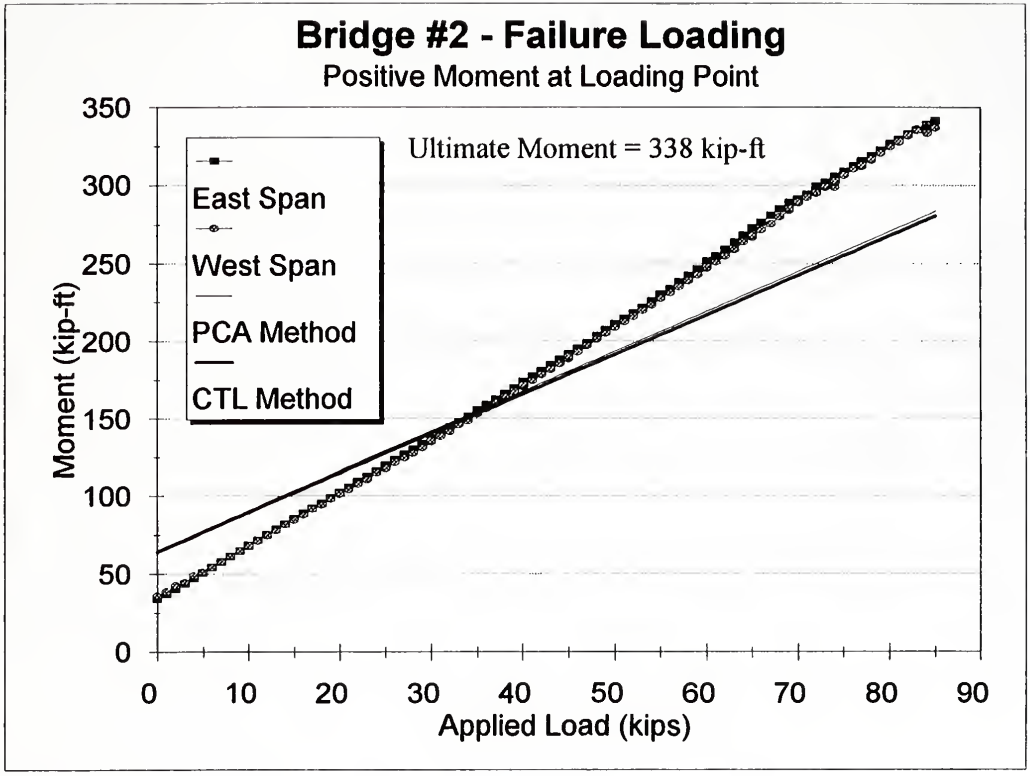

Figure 5.71 Comparison of Positive Moments at Loading Point with Elastic Moments (Bridge #2)

CHAPTER 6 DURABILITY EVALUATION

6.1 Introduction

One objective of this study was to evaluate the durability of multi-span bridges constructed with full-span prestressed concrete form panels. This was done, in part, by assessing the potential for the accumulation of chlorides at the interface between the CIP concrete topping and the prestressed panels. The durability of these bridges was also assessed in regard to the resistance to chloride induced reinforcement corrosion. This chapter contains the findings of this study pertaining to these two concerns. The results from the durability testing of Bridge #1 and the five 3 ft x 3 ft specimens described in Chapter 3 are presented.

6.2 Durability Assessment of Bridge #1

Following 2 million cycles of applied load, a portion of Bridge #1 was subjected to 48 weeks of southern exposure cycling [26] in order to simulate the effects of long-term exposure to chlorides. This weekly cycle consisted of 4 days of exposure to a 15% sodium chloride solution (salt water) followed by 3 days of drying at a minimum of 100° F (38° C). The area subjected was the negative moment region over the center support. After the salt water was applied, the bridge was loaded to 20.8 kips in each span using the hydraulic actuators. The load was held for 10 seconds and then decreased to zero. This

loading was done ten times each week, to hold the cracks open at the pier and facilitate the penetration of chlorides into the bridge deck. The bridge was also subjected to 5 cycles of similar loading during the drying period.

6.2.1 Chloride Ion Powder Samples Taken From Bridge #1

Chloride ion powder samples were extracted from the ponded region of Bridge #1 after every 12 weeks of exposure cycling. These samples were obtained during the drying period using a hammer drill. Holes were drilled at one-half inch increments to a depth of at least seven inches (through the CIP topping and into the precast panels). The concrete powder was then tested at INDOT's Materials and Testing Facility to determine the total chloride ion content using the AASHTO Standard Test T 260 procedure [29].

These powder samples were the primary means of evaluating the potential for chloride accumulation at the interface of the CIP topping and precast panels. An accumulation of chlorides at the interface, if existing, would be manifested in higher total chloride ion concentrations in powder samples taken at that level. Powder samples were extracted from the ponded region near cracks in the CIP topping, and at locations away from all cracking. The locations of the powder sample holes drilled after 12, 24, 36, and 48 weeks of ponding are shown in Figures 6.1 through 6.4, respectively. These figures also list the depth of each hole as well as the thickness of the CIP topping at the hole location. The thickness of the CIP topping varied due to camber of the panels, and was approximately 7 inches at the panel ends and 6 inches at midspan. The total measured

chloride ion concentrations corresponding to these holes are shown in Tables 6.1 through 6.4. In these tables the location of the interface is indicated by a heavy line.

Figure 6.1 shows that two holes (holes G and H) were drilled at locations outside of the ponded region. The chloride concentrations corresponding to these holes are base values for the concrete. The average (mean) base value for these two holes was 2.61 pounds per cubic yard. These base chloride ion concentrations are extremely high for concrete. Typical chloride base values for concrete are less than 1.00 pounds per cubic yard. In order to confirm the high values of base chlorides, powder samples were also tested at two depths from hole FF (see Figure 6.3) at the INDOT laboratory and at The Erlin Company (TEC) laboratory in Latrobe, PA. The total chloride ion contents (in pounds per cubic yard) were reported as 3.02 and 2.39 by the INDOT lab and 2.42 and 2.02 by the Erlin lab. These high base values are believed to be due to high chloride concentrations in the concrete aggregates. In addition, 25 random powder samples were taken from the CIP concrete at areas outside of the ponded region. The locations of these random samples were determined by generating random numbers for the quadrant of the bridge, transverse and longitudinal distances, and the sampling depth using a spreadsheet. The locations of these samples, as well as the corresponding chloride ion concentrations, are shown in Table 6.5. These 25 samples had an average (mean) of 2.13 lb/yd^3 and a standard deviation of 0.44 lb/yd^3. If the samples are normally distributed, then there is a 95% probability that chloride ion concentrations higher than 3.01 (mean + 2 standard deviations) are due to chlorides induced by the exposure cycling. Therefore, when viewing powder sample data, the depth of chloride penetration into the bridge deck is

approximately equal to the location of the deepest sample where chloride concentrations exceed 3.01 (say 3) pounds per cubic yard. Following this rationale, the chloride penetration, by diffusion, after 12 weeks of exposure cycling was approximately 2 1/2 inches (see Table 6.1 - holes A, B, C, and D which are not near cracks). After 24 weeks, the chloride penetration is approximately 3 1/2 inches (see Table 6.2 - holes N, O, P, and Q). After 36 weeks, the depth of chloride penetration was approximately 4 inches (see Table 6.3 - holes BB, CC, DD, and EE). At 48 weeks, the depth of chloride penetration was approximately 4 1/2 to 5 inches (see Table 6.4 - holes MM, NN, OO, and PP). Thus, after 48 weeks of ponding, the chloride penetration had not reached the depth of the interface (between 6 3/8 inches and 7 inches in the ponded region). Since chlorides due to exposure cycling were not found below a depth of 5 inches at holes located away from all cracking, a build-up of chlorides, if existing, must be located near the cracks in the CIP topping.

Figures 6.3 shows that holes V, W, and X (drilled after 36 weeks of exposure cycling) were located at distances of 3, 6, and 9 inches, respectively, from a transverse crack. Figure 6.3 also indicates that the topping thickness at these holes was approximately 6 3/4 inches. The corresponding chloride concentrations for these 3 holes are shown in Figure 6.5. This figure shows that the chloride concentrations at the hole located 3 inches from the crack were approximately 9 lb/yd^3 at a depth of 6 3/4 inches (the location of the interface). Figure 6.5 does not show chloride contents to be higher at the level of the interface than at levels above and below this point, as would be expected if chlorides were accumulating at the interface. At the holes located at distances of 6 inches

and 9 inches from the crack the total chloride ion concentrations at a depth of 6 3/4 inches were approximately equal to 2 1/2 lb/yd^3 (base values for the concrete). Therefore, any accumulation of chlorides at the interface of the CIP concrete topping and precast panels, if occurring, remained within 6 inches of the crack location during the 36 weeks of exposure cycling.

Figure 6.6 shows the results from powder samples taken at 3 additional holes near transverse cracks after 36 weeks of exposure cycling. The depth of the CIP topping was approximately 7 inches at these hole locations. Figure 6.6 shows that powder samples taken from hole Z, which was directly on a crack, had a considerably higher chloride ion content at the level of the interface than at adjacent levels, indicating an accumulation of chloride had occurred at the crack location. Hole Y, which was located only 6 1/2 inches from hole Z, does not show a similar increase. This indicates that the build-up of chlorides that occurred at the crack location remained isolated at the crack location during the 36 weeks of exposure. The chloride concentrations at hole AA were similar to those at hole Y, revealing that an accumulation of chlorides had not occurred at this location.

Similarly, Figures 6.4 shows that holes HH, II, JJ, KK, and LL (drilled after 48 weeks of exposure cycling) were located at distances of 0, 3, 6, 9, and 12 inches, respectively, from a transverse crack. Figure 6.4 also indicates that the topping thickness at these hole locations was approximately 6 3/4 inches. The corresponding chloride ion contents for these holes are shown in Figure 6.7. Figure 6.7 shows that chloride ion contents at the crack location and 3 inches away were 26 lb/yd^3 and 14 lb/yd^3, respectively, at the depth of the interface. While these values are higher than the base

values of the concrete, they are not significantly higher than the chloride ion contents from the same hole at depths immediately above and below the interface, as would be expected if there was an accumulation of chlorides at this level. At holes located 6, 9, and 12 inches from the same crack the chloride ion contents at the interface were between one 1 and 3 lb/yd^3 (base values for the concrete). Therefore, any accumulation of chlorides due to the exposure cycling, if existing, was confined within 6 inches of this crack location during the 48 weeks of exposure cycling.

Figure 6.8 shows the results from powder samples taken at 3 additional holes near transverse cracks after 48 weeks of exposure cycling. Each of these holes were located between two transverse cracks, and the corresponding distances to the cracks are indicated in Figure 6.8. The depth of the CIP topping was between 6 3/4 inches and 7 inches at these hole locations. This figure shows a very small increase in the chloride ion concentration at depth of 6 3/4 inches for hole GG, which was only 5 inches from a transverse crack. This increase (from 9.1 lb/yd^3 at a depth of 6 1/4 inches to 10.4 lb/yd^3 at a depth of 6 3/4 inches) might indicate an accumulation of chlorides at the interface. However, since the increase is so small, it may be due to differences in base values of the two locations. Table 6.5 shows that the base chloride values measured for the 25 random samples varied from 1.1lb/yd^3 to 3.4 lb/yd^3. Figure 6.8 shows that no build-up of chlorides was observed for holes QQ and RR, which were at least 7 inches from a crack.

6.2.2 Summary of Chloride Ion Powder Samples

The data obtained from the chloride ion powder samples taken throughout the 48 weeks of exposure cycling showed that chloride penetration did not reach the level of the interface at locations which were at least 12 inches from observed cracks. The depth of chloride penetration was approximately 5 inches after 48 weeks of ponding, while the depth of the interface was between 6 3/8 inches and 7 inches in the exposed region. An accumulation of chlorides at the level of the interface was detected from powder samples taken at a hole drilled directly on a crack. However, a build-up of chlorides was not indicated from numerous powder samples taken at holes that were 6 inches or more from observed cracks. Therefore, any accumulation of chlorides that occurred at the interface of the CIP topping and precast panels remained isolated at the crack locations during the 48 weeks of the exposure cycling.

6.2.3 Comparison of Chloride Data With Data From Bridges In Service

While the powder sample data showed that a widespread build-up of chlorides did not occur during the 48 weeks of exposure cycling, the actual time simulated by this cycling remained uncertain. In order to estimate the amount of time represented by the 48 weeks of southern exposure cycling, the chloride powder sample data obtained from Bridge #1 was compared with similar data from bridges located throughout the state of Indiana. This data was obtained from INDOT and from reference [27]. Only data from bridges which still had their original concrete decks, without overlays, was used in this

comparison. Also, the powder sample data from Bridge #1 used for comparison with other bridges corresponded to holes located at least 12 inches from observed cracks.

Figures 6.9 through 6.14 show the chloride ion concentrations obtained from Bridge #1 compared with similar data from six bridges that had been in service over 10 years, but had not been previously overlaid. These figures each show 2 curves intersecting vertical lines. The curves represent the average (mean) chloride concentrations for each bridge, while the vertical lines depict the range of values obtained from powder samples at the indicated depth. The numerical values of the chloride concentrations for these six bridges are shown in Figures 6.15 through 6.17.

Figures 6.9 compares the chloride concentrations of Bridge #1 with concentrations from a bridge in Gary, IN that was tested after being in service for 13 years. This bridge was located in the northwest region of Indiana, where deicing salt usage is the highest in the state. This figure shows that the chloride ion concentrations from Bridge #1 are considerably higher than those from the 13-year-old deck at all depths tested. This was the case for all other bridges compared. Figure 6.10 shows the results from a 13-year-old Bridge near South Bend, Indiana (also in the northwest corner of the state where deicing salt usage is highest). Figure 6.11 shows the results from a 17-year-old Bridge in Jennings County, Indiana (in the southeast corner of the state). Figures 6.12 and 6.13 shows the results from a 20-year-old bridge and a 24-year-old bridge, both on interstate I-70 near Indianapolis, Indians (at the center of the state). Figure 6.14 shows the results from a 35-year-old Bridge in Carroll County, Indiana (in the north-central part of the state).

Since the chloride ion concentrations from Bridge #1 exceeded the concentrations of all bridges in Indiana from which data was available, additional field sampling was required. A database search was made by INDOT personnel to identify the oldest concrete deck in the central part of the state which had not been previously overlaid. The bridge identified was a 37-year-old, four-span reinforced concrete bridge on State Road 144 near Mooresville, IN (see Figure 6.18). This bridge deck was badly deteriorated, having large areas of delamination and cracking over the transverse rebars. The deck appeared to have been in need of repair for a long time, as numerous asphalt patches had been used to fill holes in the concrete (over 120 patches were counted). Most of these patches were in the eastbound lane. This was believed to be due to heavier deicing salt applications in this lane, since a traffic signal was located only a few hundred feet to the east of the bridge. Therefore, all powder samples were taken from the eastbound lane, at locations away from delaminations and cracking. Figure 6.19 shows the location of powder samples and cores taken from this bridge, as well as the number of patches counted in each span (and lane) of the bridge. The cores were tested for both compressive strength and chloride permeability. The measured concrete compressive strengths were 3670 psi and 3970 psi. Rapid Chloride Ion Permeability testing yielded values of 1561 and 1359 coulombs, indicating the concrete had a low permeability. Figure 6.20 shows the comparison of the chloride concentrations from Bridge #1 with those from the 37-year-old bridge near Mooresville, IN. At every depth sampled, the chloride concentrations in Bridge #1 exceeded the chloride concentrations in the 37-year-old Bridge. Thus, the

chloride concentrations in Bridge #1 after 48 weeks of ponding exceeded the level of chlorides in all Indiana bridges from which data was available.

The actual time represented by the 48 weeks of ponding can be estimated using the data from the 7 bridges previously discussed, by assuming a linear variation of chlorides (induced by diffusion through the concrete) with time. This assumption yields a lower-bound estimate of time due to the nature of diffusion through a porous medium as discussed below.

The diffusion of chlorides into concrete can be represented using Fick's diffusion equation [28] as follows:

$$C_{(x,t)} = C_o\left\{1 - \text{erf}\left[\frac{x}{2\sqrt{D_c t}}\right]\right\} \tag{6.1}$$

where

$C_{(x,t)}$ = chloride concentration at depth x after time t

C_o = surface chloride concentration

D_c = Chloride diffusion constant for the concrete

erf = the error function (from standard mathematical tables)

x = depth of interest

t = elapsed time

Equation 6.1 indicates the chloride concentration at a given depth is a function of the chloride concentration at the surface, the diffusion characteristics of the concrete, and the elapsed time. Figure 6.21 shows the variation of chloride concentrations with time, calculated using Equation 6.1, at depths of 1, 2, 3, and 4 inches. In this graph, the

chloride concentrations ($C_{(x,t)}$)have been normalized with respect to the surface concentration (C_o). The value of the chloride diffusion constant (D_c) used to generate Figure 6.18 was 0.09 in^2/yr, the value recommended for bridges in Indiana by reference [28]. This figure shows that at shallow depths, a two-fold increase in time will result in chloride concentrations that are less than doubled. Therefore, when estimating the time represented by the southern exposure cycling, a linear extrapolation of the chloride concentration data taken from bridges in service will yield upper-bound values for the chloride concentrations, and therefore lower-bound (conservative) estimates of time. For example, the average chloride concentration at a depth of 3/4 inches for the 37-year-old bridge near Mooresville, IN was 15.5 lb/yd^3. If this bridge were in service for an additional 37 years, an estimated upper-bound value for the average chloride concentration at the same depth (assuming no additional cracking or delaminations occur) would be 31.0 lb/yd^3.

The time represented by the 48 weeks of exposure cycling, in terms of chloride penetration, was estimated by this linear extrapolation technique using data from the 7 bridges previously discussed. The results of these estimations are shown in Table 6.6. This table includes 2 estimates of time from each bridge. The first estimate is an average time based on chloride data from the top three inches of concrete. The second estimate uses the average of chloride data within depths of one to three inches. This estimate was also calculated since levels of chlorides at the surface of bridges are sometimes less than those below the surface because some surface chlorides are dissolved and washed away by precipitation. However, all times calculated without the data from the top inch of

concrete were higher than those including the top inch of concrete. Therefore, the following discussion will focus on the values obtained using chloride concentration data from depths zero to three inches.

Table 6.6 shows that the minimum time represented by the exposure cycling was calculated as 45 years. This was extrapolated from the chloride data from the 13-year-old bridge near Gary, IN. This bridge was located in the northwest corner of the state, where snow fall is heaviest and deicing salt usage is most severe. The estimated time from the other bridge in this part of the state, the 13-year-old bridge in South Bend, IN, was 72 years. The maximum calculated time represented by the exposure cycling (187 years) was obtained using data from the 37-year-old structure near Mooresville, IN. This was the oldest bridge from which data was available, and was located in the central part of the state. Table 6.6 shows that calculations based on older structures yielded higher time estimates than those based on younger structures. The author believes this is due to the linear extrapolation method, which is more conservative for younger structures. For example, if a 5 year old structure had a chloride concentration of 10 lb/yd^3 at a depth of 1 inch, the value at the same depth after 15 years would be extrapolated as 30 lb/yd^3. Due to the nature of diffusion, however, this estimated value would be excessive. On the other hand, if data were available for the same bridge after 10 years, the chloride concentration at the same depth might be 15 lb/yd^3. If this data were extrapolated to 15 years it would only be 22.5 lb/yd^3.

It is also important to note the values of the chloride concentrations near the surface of Bridge #1 after 48 weeks of exposure cycling. The average chloride

concentration within the top 1/2 inch of concrete was 60 lb/yd^3 and the average for the top inch of concrete was 49 lb/yd^3. These values were approximately twice as high as the maximum chloride concentrations recorded for bridges in the state of Indiana. Previous research has shown that the chloride concentrations near the top surface of bridge decks tend to equilibrate at some relatively constant value [6]. At the surface and for some very shallow depth, the chloride concentrations will vary seasonally, being higher in the winter and lower in the summer. These fluctuations result in chloride concentrations which approach an upper limit with time. Therefore, the chloride concentrations obtained during the exposure cycling of Bridge #1 may represent values which exceed the maximum possible values for a bridge subjected to seasonal changes, irrespective of time.

6.2.4 Summary of Comparisons With Other Bridges

The chloride concentrations in Bridge #1, resulting from the 48 weeks of exposure cycling, were higher than available chloride concentration data from all bridges in Indiana. The available data was from bridges tested between the ages of 13 and 37 years, the latter representing the oldest bridge in the central part of the state which had not been previously overlaid or resurfaced. Conservative (lower-bound) estimates of the time represented by the exposure cycling, in terms of chloride penetration into the deck, were made by linearly extrapolating the available chloride data from these bridges. These estimates show the laboratory ponding represented a minimum of 45 years of exposure to chlorides in the northwest portion of the state, where deicing salt usage is heaviest. Estimates of the represented time of exposure in other parts of the state were higher. Therefore, the

chloride penetration resulting from the 48 weeks of exposure cycling is believed to have surpassed the chloride penetration which could be expected during the life of concrete bridge decks in the field.

6.2.5 Concrete Permeability

Rapid Chloride Ion Permeability testing of the CIP concrete and precast concrete used in Bridge #1 was performed both during and after the southern exposure cycling. The results of this testing, as well as the results from permeability testing of the concrete used in Bridge #2 and the 3 ft x 3 ft durability specimens, are shown in Figure 6.22. AASHTO classifies chloride permeability as "very low" if the charge passed is less than 1000 coulombs. Additional classifications are "low" if the charge passed is between 1000 and 2000 coulombs, "moderate" if the charge passed is between 2000 and 4000 coulombs, and "high" if the charge passed is above 4000 coulombs. Figure 6.22 shows that precast concrete in Bridge #1 had a low-moderate permeability, while the "Class A" CIP concrete had a high permeability. This represented the most severe condition in terms of a potential build-up of chlorides at the interface between the CIP concrete and the precast concrete, as chloride permeability in the horizontal direction at the interface was likely higher than the chloride permeability in the vertical direction.

As expected, the "Class C" CIP concrete in the 3 ft x 3 ft durability specimens performed better (in the rapid chloride ion permeability tests) than the "Class A" CIP concrete in Bridge #1. The "Class C" concrete had a higher cement content than the "Class A" concrete, and is the current mix used for INDOT Bridge Decks. Rapid chloride

ion permeability testing of the 5-month-old "modified Class C" CIP concrete in Bridge #2 yielded unusually high coulomb results. These values may not accurately reflect the concrete's ability to resist chloride penetration. Fly ash was used as a mineral admixture and may have changed the electrical properties of the concrete pore solution [49]. Strict interpretation of the coulomb results according to the AASHTO T277 Test Method [14] is not accurate for all mixes.

6.2.6 Results From Impact-Echo Testing

Impact-echo testing was conducted at various places within the ponded region of Bridge #1 following the 5 million cycles of applied service loading and the 48 weeks of southern exposure cycling, but prior to the final loading to failure. These results were compared with results from readings taken outside of the ponded region, revealing that there had not been any delamination at the level of the interface or the level of the top mat of steel. In addition, impact-echo testing was conducted during the final loading at load increments of 55, 100, and 120 kips, respectively, and also after flexural failure had occurred at the point of loading. The results from this testing clearly indicated that there had been no significant separation between the topping concrete and the precast panels due to the final loading. Figure 6.23 shows the amplitude spectrums corresponding to impact-echo tests conducted prior to, and after loading to failure. This figure shows that the dominant frequency before and after loading to failure was essentially the same (about 6.5 kHz), indicating that there had not been any delamination or reduction in composite

action. This is consistent with the results discussed in Chapter 5, where it was noted that the full composite nominal moment capacity was attained.

6.2.7 Measured Corrosion Current in Bridge #1

Corrosion currents flowing between the epoxy coated steel in the CIP topping and the uncoated mat of steel in the precast panels were monitored weekly during the southern exposure cycling of Bridge #1, at the end of the drying phase. These currents are, by nature, proportional to the rate of corrosion occurring at the time of measurement. Since measurements were taken using the voltmeter "common" lead attached to the bottom bars, negative currents reflect positive galvanic action, where the top bar acts as the anode. The corrosion currents corresponding to epoxy-coated reinforcement within the ponded region are shown in Figure 6.24, while corrosion currents corresponding to epoxy coated reinforcement outside of the ponded region are shown in Figure 6.25. Figure 6.24 shows that corrosion current within the ponded area of the deck increased after only one week of exposure, indicating corrosion of the epoxy-coated bars had begun. The corrosion current continued to increase until about week 8, when it reached about 150 μA (micro-amps), then began slowly decreasing until week 28. At week 28 there is a large increase in the corrosion currents, with additional increases until week 35, when the corrosion current was approximately 760 μA. After week 35, there is considerable fluctuation in the corrosion current but it remains above 550 μA.

The currents measured after only one week of exposure must have been caused by corrosion at the crack locations, since powder sample data revealed that chloride ions did

not reach the level of reinforcement (by diffusion) until the bridge had been subjected to approximately 22 more weeks of exposure. The decrease in corrosion currents between weeks 13 and 28 may have been the result of lower relative humidities in the laboratory, as this period corresponded to the period between September and January, when the laboratory heating system was being used. The increase in corrosion currents beginning at week 28 is believed to have been due to the onset of widescale corrosion of the epoxy coated bars at locations away from cracks. Figure 6.26 shows the average chloride ion concentrations at the depth of the epoxy-coated steel reinforcement obtained from powder samples taken after 12, 24, 36, and 48 weeks of exposure cycling. The minimum chloride concentration shown is 3 lb/yd^3. This corresponds to the mean base chloride value plus 2 standard deviations (refer to section 6.2.1). Concentrations above this value likely correspond to chlorides induced by salt-water ponding of the bridge. Figure 6.26 indicates that chlorides reached the level of the epoxy-coated reinforcement after about 24 weeks of ponding. This was only 4 weeks prior to the large increase in corrosion current, which occurred after 28 weeks of exposure cycling. Figure 6.25 shows the measured corrosion currents for the epoxy-coated reinforcement which was outside of the ponded region. This figure shows that corrosion currents were essentially zero until week 39 for the west end of the bridge and week 44 for the east end, at which time corrosion began. This indicated corrosion is believed to have occurred at the ends of the epoxy coated bars which extended about 6 inches into the ponded area.

Figure 6.27 shows the typical variation of corrosion current within the ponded region during the weekly cycle. The data for this figure was obtained by monitoring the

corrosion current at 30 minute intervals using a data acquisition system. This was done during several weeks of ponding, the results of which all exhibited the same trend. In Figure 6.27, day zero corresponded to the application of the 15% sodium chloride solution. The application of salt water resulted in an immediate decrease in the corrosion current. The current continued to decrease with time, but at a reduced rate. After about 3 1/2 days, at the time the salt water was removed and the drying phase began, the corrosion current increased suddenly. This current then increased throughout the remainder of the week. The author believes this phenomenon was caused by the availability of oxygen. At day zero, the application of salt water meant that the entire surface was covered and the oxygen required for the corrosion reactions would decrease, causing a decrease in the corrosion rate. When the salt water was removed, however, the moist environment coupled with an oxygen rich environment would cause an increase in the rate of corrosion. Since all weekly corrosion readings were taken at the end of day six (just before applying the sodium chloride solution), these should reflect the highest level of corrosion activity occurring during that week.

6.2.8 Half-Cell Potentials (Bridge #1)

Copper-copper sulfate half-cell potentials were measured weekly during the drying phase of the exposure cycling. These weekly measurements were taken at the locations shown in Figure 3.13. Electrical connections were made to the epoxy-coated bars at the places shown in Figure 3.14. Figures 6.28 and 6.29 show the half-cell potentials recorded inside and outside of the ponded region, respectively during the 48 weeks of exposure

cycling. The half-cell potentials shown in Figure 6.28 were taken at the center pier, directly over the diaphragm. This figure shows a sharp decrease in the half-cell potentials during the first two weeks of exposure cycling. The half-cell potentials then stabilized and increased slightly until week 28, when another decrease occurred. These changes agree well with the two noted changes observed in the corrosion current readings (during the first week and at week 28). Corrosion currents indicated that corrosion of the epoxy coated reinforcement began during the first week of exposure cycling. Figure 6.28 shows that the half-cell potentials at the diaphragm after one week of exposure were about -0.42 volts. This value is more negative than -0.35 volts, the empirical number corresponding to the 95% confidence interval for corrosion activity in uncoated bars. The decrease in half-cell potentials at week 28 corresponds to a substantial increase in the rate of corrosion, as indicated by the measured corrosion currents.

The half-cell potentials shown in Figure 6.29 were taken outside of the ponded region, near the discontinuous ends of the bridge (refer to Figure 3.13). This figure shows that during the first 39 weeks of exposure cycling, the half-cell potentials were higher (more positive) than -0.20 volts, the number corresponding to the 95% confidence interval for no corrosion activity in black bars. After week 39, however, the half-cell potentials decrease below -0.20 volts yet remain more positive than -0.35 volts. Half-cell potentials for uncoated bars within this range indicate the corrosion activity is uncertain. The change in half-cell potentials during the last 8 weeks of exposure cycling corresponds to the onset of corrosion in the epoxy-coated bars outside of the ponded region, as indicated by the measurements of corrosion current.

Figure 6.30 compares the recorded half-cell potentials at points located within the ponded region (at the diaphragm) with those located outside of this exposed area. In this figure, the empirical limits for uncoated bars of -0.20 volts and -0.35 volts are shown as horizontal lines. As discussed in section 3.4.4, these empirical limits were established from testing on structures with uncoated reinforcement, where there is electrical interconnectivity between the bars and the steel is in direct contact with the concrete at all locations. Therefore, the application of these limits to structures containing epoxy-coated reinforcement cannot be justified. As discussed in the preceding paragraphs, however, the measured corrosion currents during the first week of ponding did correspond to half-cell potentials which would indicate corrosion for uncoated bars. In addition, the half-cell potentials recorded outside of the ponded region during the first 39 weeks of exposure would indicate that corrosion activity was not occurring. After week 39, these half-cell potentials were within range of uncertainty for black bars (-0.20 to -0.35 volts). This data suggests that the empirical limits developed for black bars were also relevant for the bridge tested in this study, which utilized epoxy-coated bars.

One of the most useful applications of the half-cell measurements is to compare potentials at many points on the surface of the structure to determine areas of relative corrosion activity. This can be easily done using equi-potential contour maps (maps of the surface potentials in which lines are drawn between points having equal potentials). Figure 6.31 shows an equi-potential contour map of the ponded region of Bridge #1, created from half-cell potentials recorded after 7 weeks of ponding. This figure shows that the potential variations were essentially symmetric with respect to the center of the

pond. At the center of the ponded region, which is at diaphragm, the half-cell potentials are the most negative, indicating that corrosion activity was greatest in this part of the bridge deck. This area corresponded to the location of transverse cracking due to time-dependent effects and superimposed loading (see Figure 5.1). Corrosion of the epoxy-coated steel is believed to have initiated at these crack locations. Also, the uncoated prestressing strands comprising the positive moment connection were located in the diaphragm. These strands were bent upwards for anchorage and extended to within 2 1/2 inches of the surface. Since a crack was located directly at the diaphragm, corrosion of these uncoated strands probably began during the first few weeks of exposure cycling. Figure 6.32 shows an equi-potential contour map of the same area, created from half-cell measurements taken after 48 weeks of exposure cycling. While half-cell potentials in Figure 6.32 are more negative throughout the entire ponded region than those in Figure 6.31, the contours indicate that corrosion activity was still highest at the diaphragm.

6.2.9 AC-Resistance

The electrical resistance between the epoxy-coated mat of steel in the CIP topping and the uncoated mat of steel in the precast panels was measured using a Nilsson soil resistance meter. This was done once per week during the exposure cycling of Bridge #1, at the same time the corrosion currents and half-cell potentials were monitored. Figure 6.33 shows the mat-to-mat resistances measured inside and outside of the ponded region during the 48 weeks of cycling. This figure shows that the resistance between the bars located within the ponded region decreased with time, presumably due to the presence of

chloride ions and possibly deterioration of the epoxy coating due to corrosion. During this same time the resistance between the two mats of steel outside of the exposed area increased, as the concrete became dryer due to the evaporation of moisture.

6.2.10 Visual Inspection of Reinforcement

After Bridge #1 was loaded to failure, the reinforcement was extracted from a portion of the bridge deck for visual inspection. The area of the deck examined was a 5 foot long x 4 foot wide portion at the center pier, where half-cell potentials indicated corrosion activity was highest. This included the southern half of the diaphragm, which was parallel to the 4 foot dimension. The steel reinforcement was exposed by carefully removing the concrete with a small air powered chisel. This inspection revealed widespread corrosion on every longitudinal epoxy-coated #4 bar, accompanied by staining of the surrounding concrete. Corrosion of the transverse epoxy-coated #4 bars was also observed at several locations, but had not progressed as extensively. These transverse bars were located below the longitudinal bars, thereby having a larger concrete cover. The following paragraph pertains to the condition of the longitudinal bars.

Longitudinal splitting and staining of the epoxy-coating was observed at many locations (see Figures 6.34 and 6.35). This was presumably due to the formation of an expansive corrosion product below the surface of the epoxy coating. In addition, transverse splitting was observed along the bar ribs, as shown in Figure 6.36. Staining of the concrete surrounding the epoxy-coated reinforcement was most severe at the diaphragm. Although splitting of the epoxy coating and staining of the surrounding

concrete was prevalent for all longitudinal bars, a significant loss of cross-sectional area was not observed. This was confirmed by tensile tests performed on the extracted bars. The average tensile strength was within 4% of the initial strength measured for these bars. The minimum tensile strength of the extracted bars was 91% of the initial strength.

In addition to the examination of the epoxy-coated reinforcement, visual inspection of the prestressing strands that were anchored in the diaphragm was also performed. These strands were severely corroded, having areas of deep pitting and significant area loss (see Figure 6.34). This corrosion was isolated at the diaphragm, as additional inspection showed these strands had not corroded inside of the precast panels.

6.2.11 Summary of Corrosion Assessment of Bridge #1

Measured corrosion currents and half-cell potentials indicated that corrosion of the epoxy-coated reinforcement began during the first week of southern exposure cycling. The half-cell potentials also indicated that the corrosion activity was most severe at the pier location, where transverse cracking was located. After 28 weeks of ponding there was an increase in the corrosion rate of the epoxy-coated steel. Chloride ion powder samples showed this corresponded to about 4 weeks after chlorides had reached the mat of epoxy-coated steel by diffusion. Visual inspection of the steel reinforcement at the conclusion of the testing revealed extensive corrosion of the epoxy-coated reinforcement, which was most severe for the longitudinal bars. This corrosion was accompanied by longitudinal and transverse splitting of the epoxy coating and staining of the surrounding concrete. Significant area loss of the epoxy-coated reinforcement due to corrosion was

not observed. Additional inspection of the diaphragm region showed the uncoated bent prestressing strands had experienced severe corrosion, exemplified by deep pitting and area loss. Strand corrosion was only observed at the diaphragm and did not extend into the precast panels.

6.3 Durability Assessment of 3 ft x 3 ft Specimens

In addition to the durability testing of Bridge #1, (5) 3 ft x 3 ft composite specimens were also fabricated and subjected to southern exposure cycling. These specimens were used to obtain additional data regarding the build-up of chlorides at the interface on the CIP topping and precast panels, as well as the effects of coating defects on the corrosion resistance of epoxy coated reinforcement. The exposure cycling of these specimens will continue beyond the conclusion of this study, thus only preliminary findings will be reported in this section. The composite durability specimens are described, in detail, in section 3.4.9.

6.3.1 Chloride Ion Powder Samples

Figure 6.38 shows the location of powder samples taken after 12 weeks of exposure cycling. The five durability specimens are labeled alphabetically from A to E. The notations used to identify the powder sample holes consist of the specimen letter followed by the hole number for that specimen. One hole, which was 4 inches deep and located 13 inches away from the crack, was drilled in each specimen after 12 weeks of exposure. Three additional holes (7 inches deep) were drilled in Specimen B near the

crack location to obtain chloride data at the interface. Table 6.7 shows the chloride concentrations corresponding to these locations. The chloride concentrations at the holes located away from the crack are graphed in Figure 6.39. This figure shows that chlorides had penetrated to a depth of about 1 3/4 inches in all specimens after the 12 weeks of exposure cycling. Figure 6.40 shows the chloride concentrations near the crack location of Specimen B after 12 weeks of exposure cycling. This figure shows that the chloride concentrations were very high (above 30 lb/yd^3) at the crack location for all depths sampled. In addition, there is an increase in the chloride concentration near the depth of the interface (approximately 6 inches) at the crack location. However, chloride concentrations at holes located 3 and 6 inches away from the crack show that only base chloride values were found at depths below 2 1/4 inches. This data is consistent with the data obtained from Bridge #1, which revealed that a build-up of chlorides at the interface would remain isolated at the crack locations.

Figure 6.41 shows the location of powder samples taken after 24 weeks of exposure cycling. One hole, which was 7 inches deep and located 12 inches away from the crack, was drilled in each specimen. In addition, powder samples were obtained from 7-inch-deep holes drilled in Specimen C at distances of 0, 3, 6, and 9 inches from the crack. The numerical values of the chloride concentrations corresponding to these holes are listed in Table 6.8.

Figure 6.42 shows the chloride concentrations, after 24 weeks of exposure, at the holes located 12 inches from the crack. This figure shows that chlorides induced by the 24 weeks of ponding had penetrated to a depth of approximately 2 inches in all five

specimens. Chloride contents below this level are base values. Figure 6.43 shows the chloride concentrations from samples taken near the crack in Specimen C. This graph indicates that the crack did not have a noticeable effect on the chloride concentrations at these locations, as the profiles shown for these powder sample holes are essentially identical. Chloride concentrations at depths below approximately 2 3/4 inches corresponded to base values for the concrete. Thus, an increase in chlorides was not detected at the level of the interface.

6.3.2 Summary of Chloride Ion Powder Samples

Chloride ion powder samples extracted from the 3 ft x 3 ft durability specimens showed that chloride penetration, by diffusion, had reached depths of approximately 2 inches after 12 weeks of exposure cycling and 2 1/2 inches after 24 weeks of exposure cycling. Holes drilled near crack locations after 12 and 24 weeks of exposure showed the crack did not significantly influence the chloride concentrations at distances of only 3 inches away. Increased chloride concentrations at the level of the interface were detected from powder samples taken at a hole drilled directly on the crack. This increase was shown to be isolated at the crack location, as chloride contents only 3 inches away (and at the same depth) were equal to base values for the concrete.

6.3.3 Measured Corrosion Currents

Macrocell corrosion currents were measured between the epoxy-coated bars in the CIP topping and the mat of uncoated steel reinforcement in the precast portion of the

durability specimens. As described in Chapter 3, each of the 5 specimens had seven #4 bars in the CIP topping, each with varying degrees of initial damage to the epoxy coating. One of the bars was not intentionally damaged prior to casting, and was from the same bundle of #4 bars used in both full-scale specimens. The coating on five of the epoxy-coated bars was intentionally removed, in varying degrees, at rib locations to simulate damage which might occur during shipping and handling of the bars. In addition, one black bar was cast in the CIP topping of each specimen.

At the time of this report, corrosion current data was available for the first 36 weeks of exposure cycling. This data is presented in Figures 6.44 through 6.50. The measured corrosion currents for the epoxy-coated bars which were not intentionally damaged were essentially zero for all 5 specimens tested (Specimens A through E), indicating that corrosion of these bars had not occurred (see Figure 6.44). Corrosion currents corresponding to the epoxy-coated bars with initial damages of 1/2%, 1%, 2%, 4%, and 8% indicated that corrosion of all these bars initiated within the first 32 weeks of testing. The macrocell currents measured for these bars vary widely from specimen to specimen , and the effects due to the amount of initial damage on corrosion cannot be determined from the data obtained during the first 36 weeks of exposure cycling. Figures 6.45 through 6.49 graph the corrosion currents corresponding to these bars. Figure 6.50 shows the measured corrosion currents corresponding to the black bar located in each specimen. This figure shows that macrocell corrosion initiated during the first week of exposure cycling and has continued. The magnitude of these currents is considerably higher than those measured for the epoxy-coated bars. Average corrosion currents for the

black bars were in excess of 1000 μA, while the average corrosion currents measured for the epoxy-coated bars were under 300 μA.

6.3.4 Half-Cell Potentials

Half-cell potentials measured for the durability specimens were also widely scattered during the first 36 weeks of exposure cycling. Due to the small size and close rebar spacing of these specimens, variations in the half-cell potentials across the surface of the specimens were minimal. Therefore, the use of half-cell potentials to identify areas of probable corrosion was not possible. The value of the half-cell potentials were primarily a function of the corrosion state of the bar to which electrical connection was made. Surface potentials recorded while connecting the lead wire to a bar which had measurable corrosion currents were usually more negative than -0.4 volts. Potentials measured at the same surface location, but using an electrical connection to a rebar which was not corroding (i.e. when macrocell currents were equal to zero) were more positive than -0.35 volts.

6.3.5 Visual Inspection of Rebars

The exposure cycling of Specimen C was discontinued after 24 weeks of exposure cycling in order to remove the rebars for visual inspection. As with Bridge #1, the rebar were exposed by carefully removing the concrete with a small air chisel. This inspection revealed that the black bar had experienced severe pitting at the crack location (see Figure

6.51). This pitting resulted in an estimated cross-section area loss of 50%. Except for the deep pitting at the crack location, the surface of the black bar was mostly uncorroded.

The visual examination also showed that epoxy-coated bars containing initial defects had each experienced corrosion, as indicated by the measured corrosion currents. The bars with 1/2%, 1%, and 4% defects each contained small areas where the epoxy coating had blistered and pitting of the bars was observed. This pitting did not result in a significant loss of bar area. In addition, surface corrosion was observed at the initial defects of these three bars. Staining of the epoxy coating and surface rusting at one initial defect was observed for the bar with 2% initial damage. The bar with 8% initial damage did not have any blistering or staining. Only surface corrosion at one initial defect was observed on this bar. No corrosion was observed on the epoxy coated bar that did not have initial damage.

6.3.6 Summary of Corrosion Assessment of Durability Specimens

All epoxy-coated bars having initial defects began corroding during the first 32 weeks of the exposure cycling. Epoxy-coated bars without initial defects did not experience corrosion during this time period. The quantity of initial defects did not appear to influence the corrosion of the bars during the first 36 weeks ponding, as bars with small percentages of defects had similar corrosion currents and half-cell potentials as bars with larger areas of defects. The corrosion currents measured for the black bars were considerably higher than currents corresponding to the epoxy-coated bars containing defects. Visual inspection of the reinforcement in Specimen C after 24 weeks of exposure

revealed severe pitting and loss of cross-section area had occurred for the black bar at the crack location. Corrosion damage to the epoxy-coated bars with initial defects consisted of surface rusting and minor pitting at the initial defects, and small areas of blistering of the epoxy coating. Corrosion of the epoxy-coated bars was not accompanied by a significant loss of area during the first 24 weeks of exposure cycling.

6.3.7 Comparison of Durability Specimens With Bridge #1

In Section 6.2.1 the authors noted that the depth of chloride penetration after 24 weeks of ponding was approximately 3 1/2 inches (90 mm) for Bridge #1, which contained "Class A" concrete in the CIP portion of the deck. In Section 6.3.1, however, it was noted that the chloride penetration in the 3 ft x 3 ft durability specimens (which contained "Class C" concrete), after a similar exposure period, had reached only 2 inches (50 mm). The difference in chloride permeability of the two concrete mixes can also be seen when comparing chloride concentrations in Figures 6.26 and 6.42. Figure 6.42 shows that the chloride concentrations in the 3 ft x 3 ft durability specimens after 24 weeks of exposure were still at base levels at a depth of 2 - 2 1/2 inches. Figure 6.26 shows the chloride concentrations in Bridge #1 for the corresponding depth and exposure period were about 18 pounds per cubic yard (approximately 6 times the base level measured for the concrete).

Rapid chloride ion permeability tests taken from the "Class A" concrete used in Bridge #1 and the "Class C" concrete in the 3 ft x 3 t durability specimens also indicate the lower permeability of the "Class C" concrete. Permeability tests taken when the concrete

specimens were approximately one year old showed the "Class C" concrete allowed (on average) the passage of 33% fewer coulombs than the "Class A" concrete. The average coulomb values were 5900 for the "Class A" concrete in Bridge #1 and 3950 for the "Class C" concrete in the 3 ft x 3 ft durability specimens.

Therefore, the results from both chloride-ion powder sample testing and rapid chloride ion permeability testing indicate the superior performance of the "Class C" concrete in terms of chloride permeability. The "Class C" concrete is currently INDOT's standard mix used in the construction of new bridge decks.

Table 6.1 Chloride Ion Concentrations After 12 Weeks of Exposure Cycling (Bridge #1)

Chloride Ion Concentrations

* Values Are Total Chloride Concentrations In Pounds Per Cubic Yard
* Heavy Line Indicates Location of Interface

Powder Samples at 12 Weeks

	A	B	C	D	E	F	G	H
0-.5"	36.41	44.59	46.12	50.76	71.59	44.24	2.81	2.64
.5"-1"	22.54	24.18	33.11	25.46	46.23	29.86	2.42	2.65
1"-1.5"	18.15	19.12	20.91	18.87	48.23	14.10	2.75	1.82
1.5"-2"	9.96	10.69	13.44	10.64	38.93	11.05	3.43	3.18
2"-2.5"	3.58	4.69	4.67	4.98	38.82	6.63	1.81	3.31
2.5"-3"	2.22	1.81	1.89	2.58	40.17	3.75	2.03	2.20
3"-3.5"	1.89	1.41	2.06	1.88	31.57	2.38	2.10	2.74
3.5"-4"	2.10	1.62	2.69	2.18	35.95	2.69	2.05	2.49
4"-4.5"	2.29	2.92	2.12	2.51	32.95	3.24	2.47	1.83
4.5"-5"	1.88	2.27	1.87	1.56	32.38	1.96	2.06	2.27
5"-5.5"	1.77	2.23	2.33	1.82	36.37	3.00	4.04	2.89
5.5"-6"	1.59	1.49	2.48	2.11	24.94	3.89	2.38	3.13
6"-6.5"	2.29	0.82	2.39	2.00	30.79	3.58	3.38	3.08
6.5"-7"	1.03	1.09	1.46	0.98	23.88	2.41	1.49	1.45
7"-7.5"	*****	*****	*****	*****	16.78	3.95	0.73	1.01

Table 6.2 Chloride Ion Concentrations After 24 Weeks of Exposure Cycling (Bridge #1)

Chloride Ion Concentrations

* Values Are Total Chloride Concentrations In Pounds Per Cubic Yard
* Heavy Line Indicates Location of Interface

Powder Samples at 24 Weeks

	L	M	N	O	P	Q
0-.5"	50.91	58.54	53.16	54.55	59.56	62.57
.5"-1"	36.51	32.77	24.10	41.90	51.04	39.70
1"-1.5"	30.19	25.08	29.10	25.78	33.64	25.79
1.5"-2"	21.85	17.41	20.40	18.17	27.99	23.44
2"-2.5"	15.39	13.72	10.60	14.80	15.53	15.50
2.5"-3"	16.67	10.26	5.92	8.23	7.50	9.67
3"-3.5"	11.47	11.06	3.23	3.66	4.62	4.49
3.5"-4"	10.06	11.14	2.07	2.39	3.10	2.34
4"-4.5"	9.32	9.67	2.08	2.61	2.11	2.31
4.5"-5"	8.38	8.00	2.49	2.15	2.19	3.61
5"-5.5"	6.27	7.01	2.24	2.21	2.36	2.34
5.5"-6"	4.75	5.63	1.81	2.74	2.28	3.01
6"-6.5"	3.66	5.03	2.73	1.46	2.11	1.20
6.5"-7"	3.73	4.76	1.79	0.93	1.38	0.95
7"-7.5"	2.65	1.79	0.78	0.81	1.16	0.74

Table 6.3 Chloride Ion Concentrations After 36 Weeks of Exposure Cycling (Bridge #1)

Chloride Ion Concentrations

* Values Are Total Chloride Concentrations In Pounds Per Cubic Yard
* Heavy Line Indicates Location of Interface

Powder Samples at 36 Weeks

	V	W	X	Y	Z	AA	BB	CC	DD	EE	FF
0-.5"	43.59	52.21	47.57	50.91	74.70	63.77	57.05	42.22	46.87	56.08	3.02
.5"-1"	38.23	33.65	28.45	33.72	47.11	35.16	37.66	32.06		42.39	
1"-1.5"	32.97	30.74	23.73	30.16	50.14	33.18	30.16	23.34	29.44	36.78	2.36
1.5"-2"	37.56	23.11	28.37	30.27	62.44	25.23	26.18	16.97		27.21	
2"-2.5"	23.68	18.10	20.43	24.48	46.39	20.68	22.43	12.42	13.43	19.85	2.39
2.5"-3"	24.98	13.61	15.31	21.89	47.38	19.40	12.90	7.77		16.07	
3"-3.5"	23.66	11.62	10.43	20.23	47.87	21.51	*	4.71	6.40	8.87	
3.5"-4"	18.99	9.54	7.74	15.78	44.04	18.87	*	3.00		5.31	
4"-4.5"	20.66	6.81	5.50	15.69	34.86	17.34	2.75	2.61	2.76	2.54	
4.5"-5"	16.83	5.08	3.61	12.40	29.15	12.38	2.57	2.49		2.70	
5"-5.5"	*	*	2.06	10.03	30.76	8.59	1.81	2.39	2.70	2.35	
5.5"-6"	12.38	3.64	2.84	11.43	25.58	6.68	1.83	2.38		2.28	
6"-6.5"	10.60	2.96	2.24	10.59	25.03	6.62	2.58	1.74	1.04	1.47	
6.5"-7"	9.01	2.25	2.68	10.24	36.15	4.08	2.13	0.82		1.16	
7"-7.5"	6.56	1.98	2.25	5.05	15.69	1.01	0.79	1.68		0.70	

* The values reported by the lab for these locations appear to be incorrect. It is believed that the values for hole V (5"-5 1/2") and hole W (5"-5 1/2") have been switched. The values reported for these holes are 3.77 and 14.99 respectively. Also, values for hole BB (3"-3 1/2") and hole BB (3 1/2"-4") are believed to be switched. The values reported for these holes are

Table 6.4 Chloride Ion Concentrations After 48 Weeks of Exposure Cycling (Bridge #1)

Chloride Ion Concentrations

* Note, Values Are Total Chloride Concentrations In Pounds Per Cubic Yard

Powder Samples at 48 Weeks

	GG	HH	II	JJ	KK	LL	MM	NN	OO	PP	QQ	RR
0-.5"	43.98	61.51	57.44	56.95	60.97	59.24	60.88	65.48	53.09	62.00	63.12	62.35
.5"-1"	45.12	56.79	42.91	52.95	50.82	47.53	39.77	32.67	30.07	47.78	27.27	42.56
1"-1.5"	28.74	48.47	46.23	48.28	36.91	29.52	38.75	29.34	31.96	46.72	25.79	26.88
1.5"-2"	30.50	54.25	36.57	48.30	32.69	29.46	30.49	25.47	33.54	32.46	19.64	33.42
2"-2.5"	27.85	45.32	44.19	23.53	24.16	29.05	19.96	15.80	24.60	25.63	14.19	22.63
2.5"-3"	22.93	44.63	30.84	21.60	21.89	23.87	15.41	12.77	16.29	19.94	12.30	20.69
3"-3.5"	19.98	44.78	34.00	21.42	17.08	16.11	10.48	6.70	14.80	16.57	8.05	17.86
3.5"-4"	11.98	34.75	24.18	16.30	13.88	14.75	5.88	4.39	11.83	10.03	8.08	16.00
4"-4.5"	14.49	34.54	19.56	11.41	11.68	8.71	3.26	3.60	6.21	6.74	5.36	13.39
4.5"-5"	*	26.85	18.57	11.72	6.54	6.37	2.18	2.03	3.51	3.68	4.10	9.36
5"-5.5"	9.21	26.80	17.90	8.60	6.00	4.22	2.72	1.88	1.82	2.26	*	10.43
5.5"-6"	9.95	25.30	18.96	5.98	4.32	2.99	2.16	1.54	2.13	1.40	2.99	7.24
6"-6.5"	9.14	28.79	14.24	5.72	2.95	2.10	1.20	1.34	2.02	1.98	2.14	5.27
6.5"-7"	10.40	25.84	14.21	3.05	1.77	1.09	1.00	1.10	0.86	0.93	1.82	3.61
7"-7.5"	3.64	19.90	6.30	0.89	2.09	2.55	0.84	1.24	0.58	0.66	0.71	0.93

* The values reported by the lab for these locations appear to be incorrect. The value for hole GG (4 1/2"-5") was reported as 99.94. It appears that this should be 9.94 instead. Also, the value for hole QQ(5"- 5 1/2") was reported as 20.56. It appears that the correct value for this hole would be 2.56.

Table 6.5 Random Sampling of Base Chlorides in the CIP Concrete of Bridge #1

Random Sampling of Chloride Base Values (Bridge #1)					
Sample	Panel	Transverse Distance	Longitudinal Distance	Depth	Chloride Content (lbs/yd^3)
1	1	1'-8 7/8"	1'-0 5/8"	0 3/4" - 1 1/4"	2.47
2	1	0'-5 3/8"	6'-4"	3 1/4" - 3 3/4"	1.93
3	2	1'-2"	7'-5 7/8"	4" - 4 1/2"	2.14
4	2	2'-5"	8'-8 1/8"	1 3/4" - 2 1/4"	2.30
5	2	3'-4 1/8"	11'-11 1/8"	1" - 1 1/2"	2.22
6	2	2'-2 7/8"	2'-1 5/8"	5 1/2" - 6"	3.38
7	2	0'-3 1/2"	3'-7"	5" - 5 1/2"	1.67
8	2	1'-5 1/4"	1'-5"	5" - 5 1/2"	2.14
9	2	0'-5"	7'-11 3/4"	1" - 1 1/2"	1.55
10	3	0'-6 1/2"	8'-10 3/8"	1" - 1 1/2"	1.77
11	3	1'-9"	1'-9 1/4"	5 1/4" - 5 3/4"	2.02
12	3	1'-6"	8'-7 3/4"	1" - 1 1/2"	1.14
13	3	0'-3 3/8"	2'-5"	3 1/2" - 4"	2.32
14	3	0'-8 5/8"	6'-11 3/4"	4 1/2" - 5"	2.42
15	3	1'-3 3/4"	1'-11"	4 3/4" - 5 1/4"	2.71
16	3	3'-6 3/8"	7'-4 1/8"	0 1/4" - 0 3/4"	1.78
17	3	2'-2 5/8"	2'-11 3/8"	1" - 1 1/2"	2.02
18	3	2'-2 3/8"	2'-8 5/8"	2 1/2" - 3"	1.78
19	4	2'-8 1/2"	8'-9 5/8"	2 1/4" - 2 3/4"	2.54
20	4	0'-8 1/8"	5'-6 1/2"	3 3/4" - 4 1/4"	1.93
21	4	2'-9 1/4"	8'-11 1/2"	4 1/4" - 4 3/4"	1.87
22	4	2'-2 1/8"	4'-5"	4 1/4" - 4 3/4"	2.10
23	4	2'-5 5/8"	0'-2 3/4"	2 3/4" - 3 1/4"	2.22
24	3	3'-7"	10'-2 1/8"	1/2" - 1"	2.34
25	4	1'-5 5/8"	1'-11 5/8"	4 1/2" - 5"	2.52

* Transverse distance was measured from the outside edges of the bridge.
* Longitudinal Distance was measured from the discontinuous ends of the bridge.
* The sample mean was 2.13 lbs/yd^3. The standard deviation was 0.44 lbs/yd^3.

Table 6.6 Estimated Time Represented by Exposure Cycling (By Linear Extrapolation)

Bridge	Estimated Time (Years) Using Data From Depths (0-3")	Estimated Time (Years) Using Data From Depths (1"-3")
S.R 912 (Gary, IN) (13-years-old)	72	82
US-31 (South Bend, IN) (13-years-old)	45	53
SR. 7 (Jennings Co., IN) (17-years-old)	63	69
I-70 (Indianapolis, IN) (20-years-old)	74	82
I-70 (Indianapolis, IN) (24-years-old)	119	139
SR. 29 (Carroll Co., IN) (35-years-old)	131	157
SR 144 (Mooresville, IN) (37-years-old)	187	232

Table 6.7 Chloride Ion Concentrations in Durability Specimens After 12 Weeks of Exposure

Chloride Ion Concentrations in 3ft x 3ft Specimens

* Values Are Total Chloride Concentrations In Pounds Per Cubic Yard

Powder Samples Taken After 12 wks of Exposure Cycling

	A1	B1	B2	B3	B4	C1	D1	E1
0-.5"	44.70	79.21	47.48	53.60	44.84	52.14	48.23	39.88
.5"-1"	23.56	50.66	22.35	28.27	23.70	35.96	22.81	26.39
1"-1.5"	4.20	36.18	11.10	14.55	5.68	12.24	7.89	11.59
1.5"-2"	1.01	41.41	13.03	5.03	1.04	1.35	1.45	1.61
2"-2.5"	0.77	41.93	1.23	1.01	1.95	1.06	1.04	0.86
2.5"-3"	0.98	36.61	0.99	0.96	1.08	0.94	0.67	0.74
3"-3.5"	0.61	32.43	0.84	0.98	0.81	1.04	0.84	0.64
3.5"-4"	0.62	37.56	0.67	0.72	1.13	0.67	0.67	1.45
4"-4.5"	-------	40.08	0.98	0.56	-------	-------	-------	-------
4.4"-5"	-------	32.78	0.82	0.74	-------	-------	-------	-------
5"-5.5"	-------	37.74	0.67	0.74	-------	-------	-------	-------
5.5"-6"	-------	39.99	0.77	0.71	-------	-------	-------	-------
6"-6.5"	-------	49.46	0.67	0.67	-------	-------	-------	-------
6.5"-7"	-------	36.51	1.19	0.69	-------	-------	-------	-------

Table 6.8 Chloride Ion Concentrations in Durability Specimens After 24 Weeks of Exposure

Chloride Ion Concentrations in 3ft x 3ft Specimens

* Values Are Total Chloride Concentrations in Pounds Per Cubic Yard

Powder Samples Taken After 24 wks of Exposure Cycling

	A2	B5	C2	C3	C4	C5	C6	D2	E2
0-.5"	42.57	64.18	?	56.83	56.19	56.59	60.34	46.32	45.31
.5"-1"	23.61	34.19	?	35.42	33.06	30.04	33.72	25.51	23.83
1"-1.5"	11.57	22.74	?	22.57	21.88	16.99	18.33	16.62	13.17
1.5"-2"	2.64	7.37	?	13.59	11.66	12.09	11.60	6.91	5.95
2"-2.5"	1.56	1.18	?	4.12	2.14	2.57	1.51	1.23	0.99
2.5"-3"	0.91	0.74	?	0.86	1.03	0.94	1.60	0.93	0.76
3"-3.5"	1.55	0.66	?	1.93	0.94	0.69	0.77	0.79	0.52
3.5"-4"	0.82	0.84	?	0.94	0.84	1.14	1.26	0.77	0.62
4"-4.5"	0.77	0.57	?	0.76	0.86	0.74	0.96	0.64	0.74
4.4"-5"	0.71	0.57	?	1.50	0.74	1.46	1.23	1.35	0.96
5"-5.5"	0.96	0.57	?	0.74	1.21	0.64	1.11	0.56	1.33
5.5"-6"	0.69	0.61	?	1.04	0.81	1.67	0.96	0.84	0.81
6"-6.5"	0.52	0.64	?	0.81	0.62	0.67	0.62	0.74	0.59
6.5"-7"	0.89	0.94	?	0.59	0.57	0.99	0.61	1.24	1.23

* Chloride Concentrations At Hole C2 Were Too High To Determine Using Available Testing Equipment

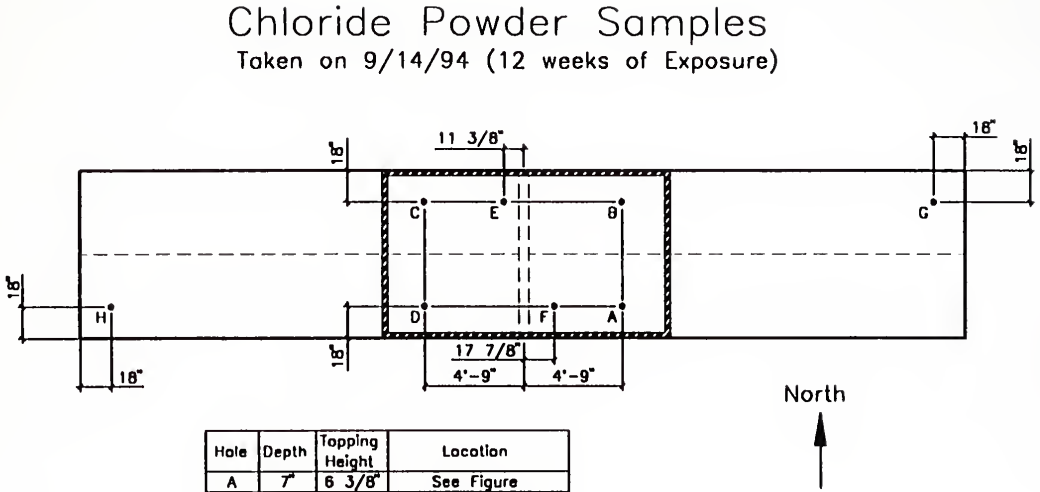

Hole	Depth	Topping Height	Location
A	7"	6 3/8"	See Figure
B	7"	6 3/8"	See Figure
C	7"	6 1/2"	See Figure
D	7"	6 3/8"	See Figure
E	7 1/2"	7"	Directly on Crack
F	7 1/2"	6 7/8"	3" from Crack
G	7 1/2"	7"	See Figure
H	7 1/2"	6 7/8"	See Figure
J	2"	N/A	Sample "A"
K	2"	N/A	Sample "B"

Figure 6.1 Location of Powder Samples Taken After 12 Weeks of Exposure (Bridge #1)

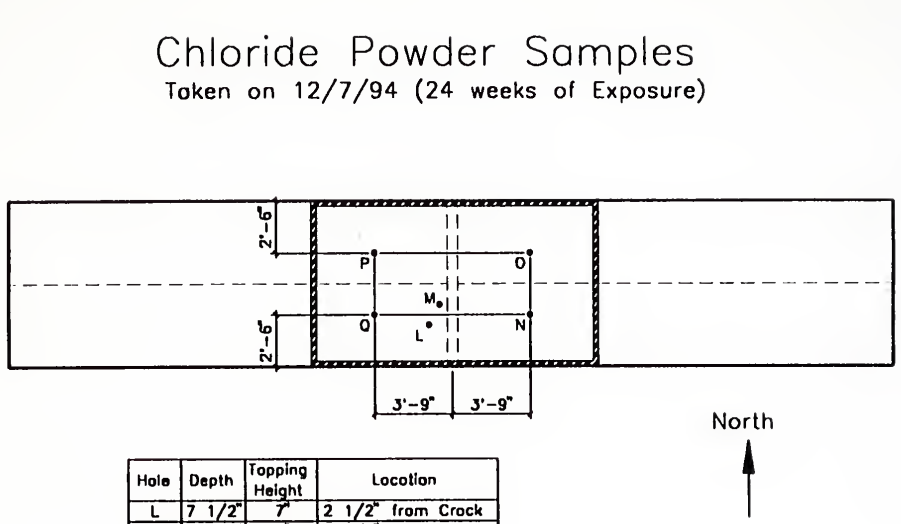

Hole	Depth	Topping Height	Location
L	7 1/2"	7"	2 1/2" from Crack
M	7 1/2"	7"	3 1/2" from Crack
N	7 1/2"	6 1/2"	See Figure
O	7 1/2"	6 1/2"	See Figure
P	7 1/2"	6 5/8"	See Figure
Q	7 1/2"	6 1/2"	See Figure

Figure 6.2 Location of Powder Samples Taken After 24 Weeks of Exposure (Bridge #1)

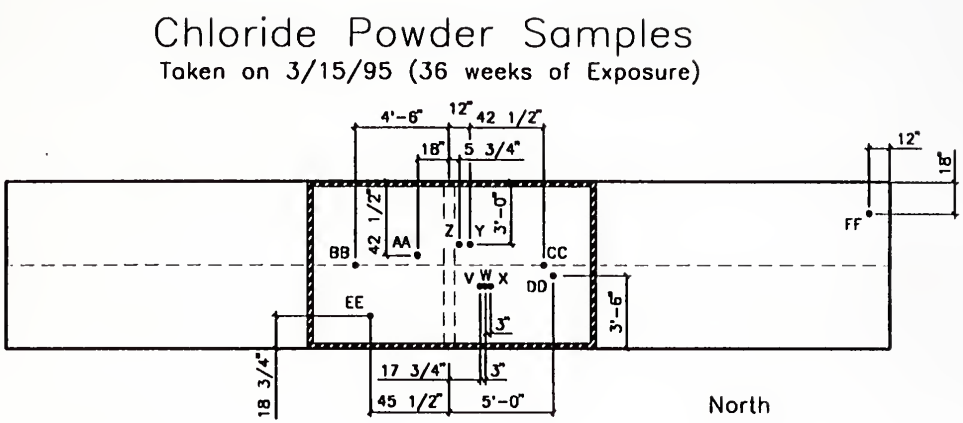

Hole	Depth	Topping Height	Location
V	7 1/2"	6 7/8"	3" from Crack
W	7 1/2"	6 7/8"	6" from Crack
X	7 1/2"	6 3/4"	9" from Crack
Y	7 1/2"	7"	6 1/2" from Crack
Z	7 1/2"	7"	Directly on Crack
AA	7 1/2"	6 7/8"	5 1/4" from Crack
BB	7 1/2"	6 1/2"	See Figure
CC	7 1/2"	6 1/2"	See Figure
DD	7"	6 3/8"	See Figure
EE	7 1/2"	6 1/2"	See Figure
FF	3"	7"	See Figure

Figure 6.3 Location of Powder Samples Taken After 36 Weeks of Exposure (Bridge #1)

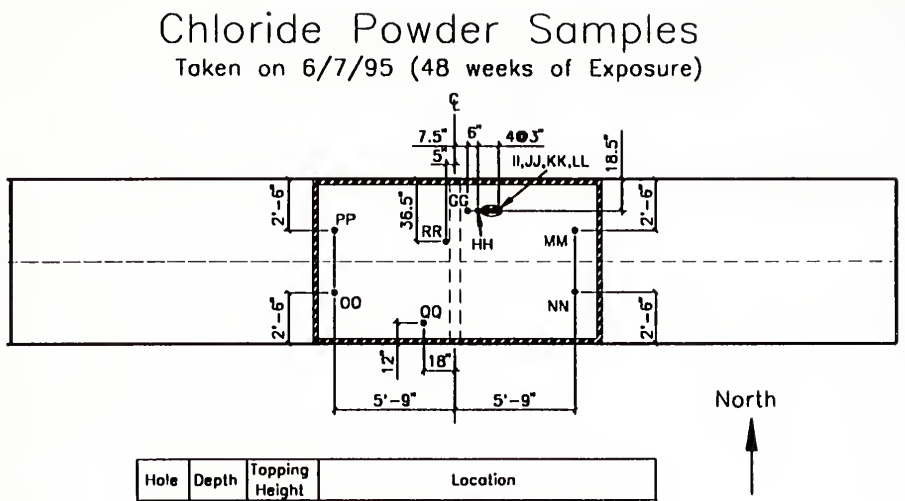

Hole	Depth	Topping Height	Location
GG	7 1/2"	6 7/8"	Between Cracks (5" & 6" Away)
HH	7 1/2"	6 7/8"	Directly on Crack
II	7 1/2"	6 7/8"	3" from Crack
JJ	7 1/2"	6 3/4"	6" from Crack
KK	7 1/2"	6 3/4"	9" from Crack
LL	7 1/2"	6 3/4"	12" from Crack
MM	7 1/2"	6 3/8"	See Figure
NN	7 1/2"	6 3/8"	See Figure
OO	7 1/2"	6 3/8"	See Figure
PP	7 1/2"	6 3/8"	See Figure
QQ	7 1/2"	6 3/4"	Between Cracks (7" & 7 1/2" Away)
RR	7 1/2"	7"	Between Cracks (8" & 11" Away)

Figure 6.4 Location of Powder Samples Taken After 48 Weeks of Exposure (Bridge #1)

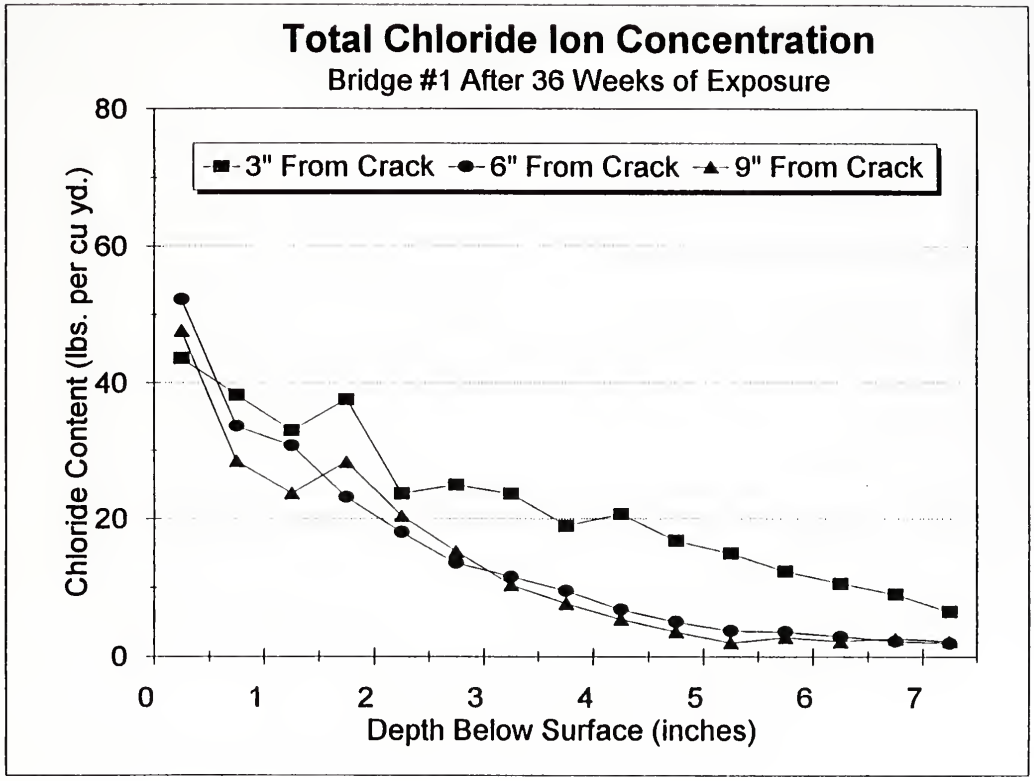

Figure 6.5 Chloride Concentrations Near Transverse Cracks After 36 Weeks of Exposure (Bridge #1)

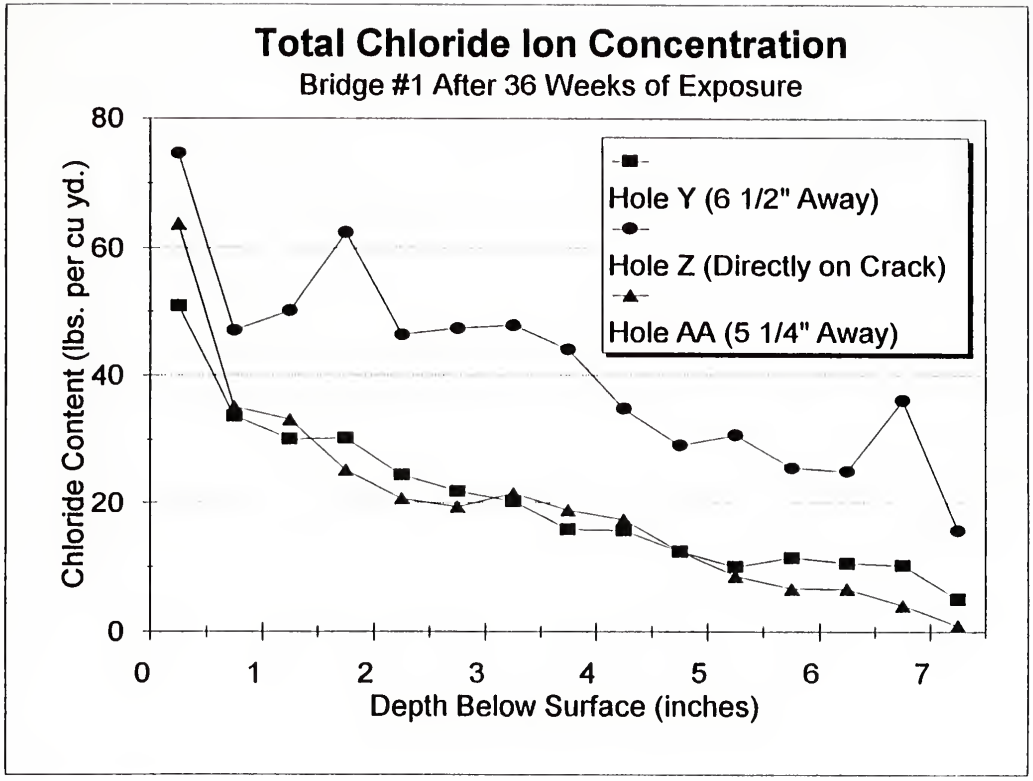

Figure 6.6 Additional Data from Powder Samples Taken Near Transverse Cracks After 36 Weeks of Exposure (Bridge #1)

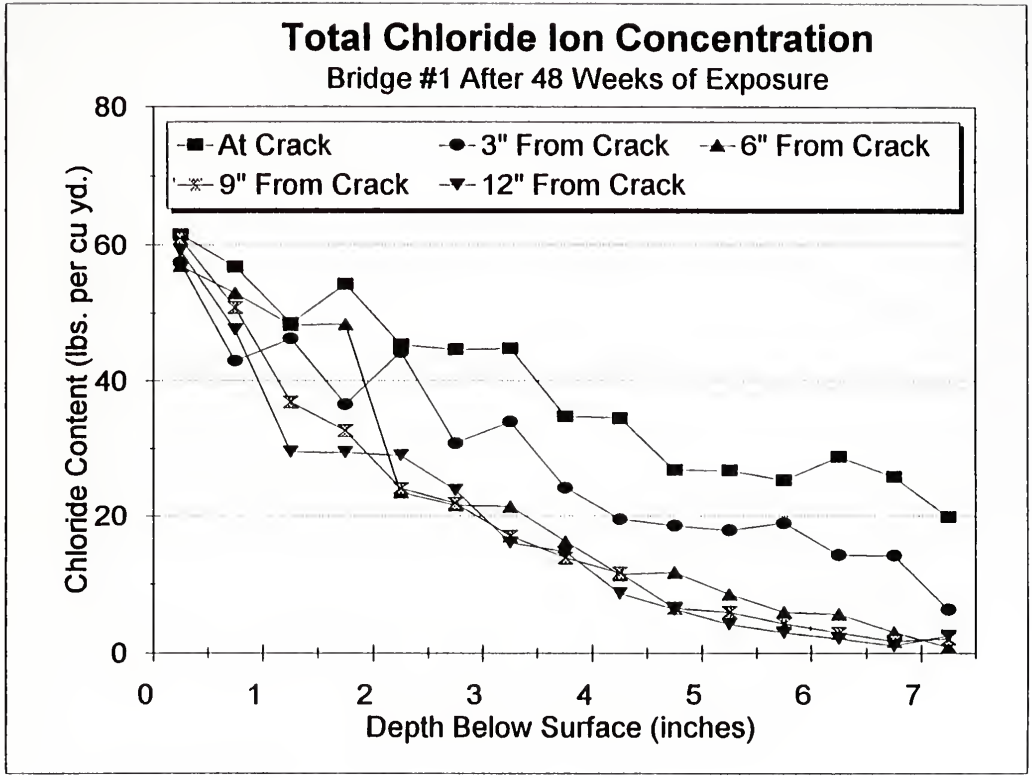

Figure 6.7 Chloride Concentrations Near Transverse Cracks After 48 Weeks of Exposure (Bridge #1)

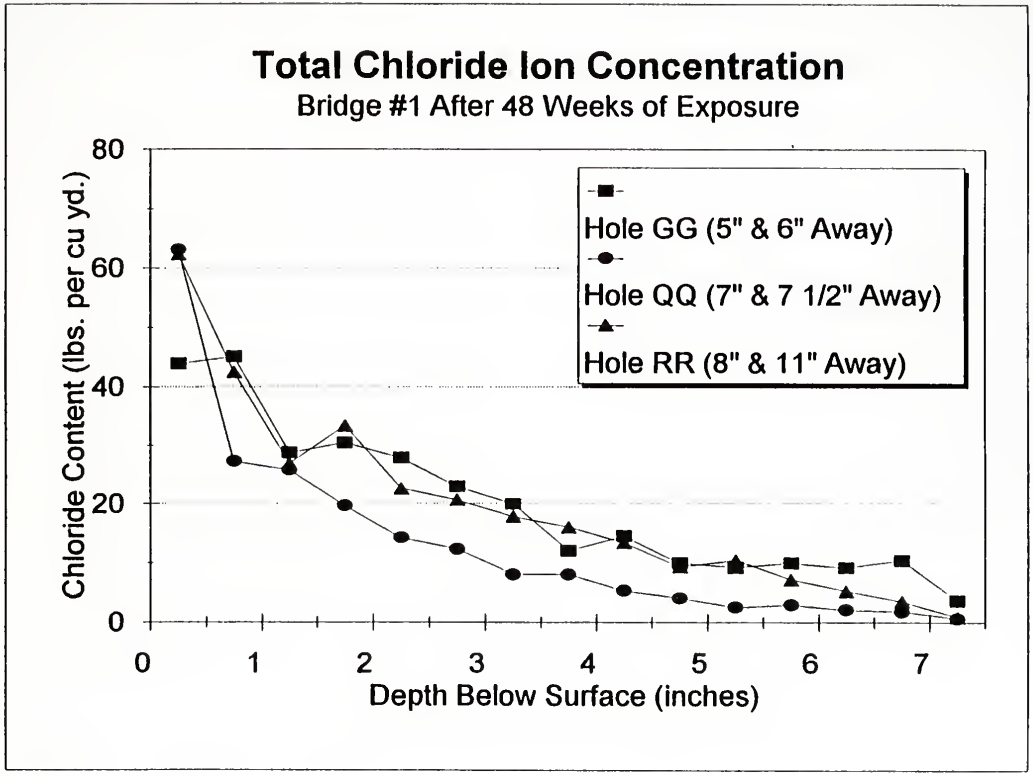

Figure 6.8 Additional Data from Powder Samples Taken Near Transverse Cracks After 48 Weeks of Exposure (Bridge #1)

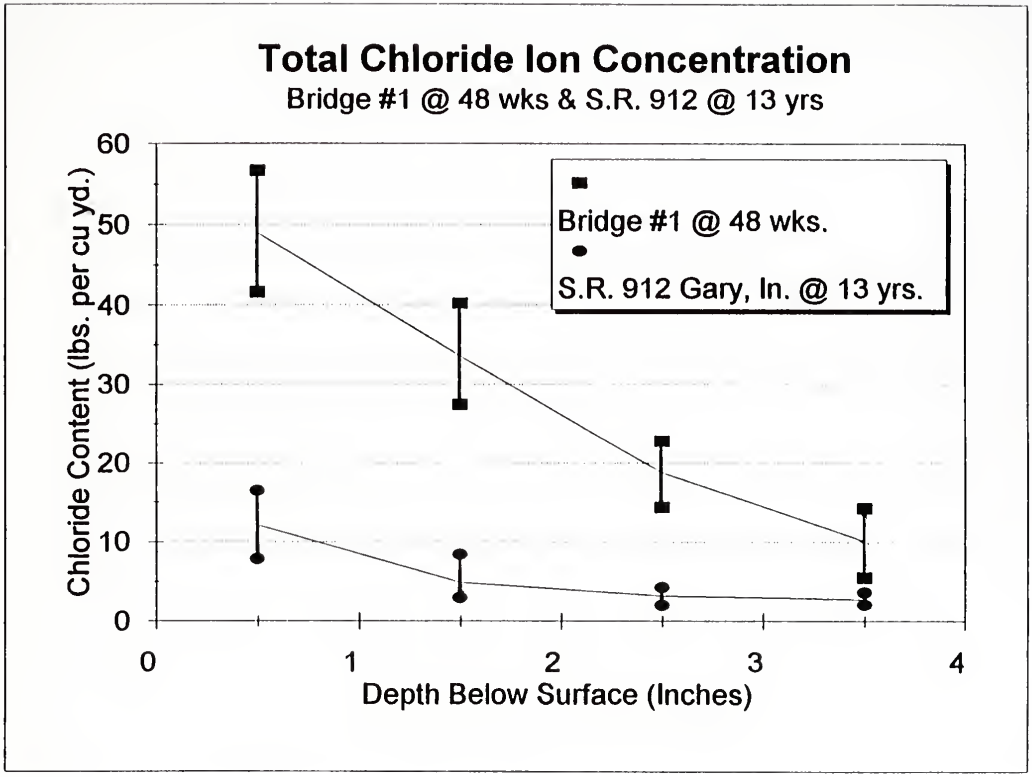

Figure 6.9 Comparison of Chlorides in Bridge #1 With Data from S.R. 912 Near Gary, IN

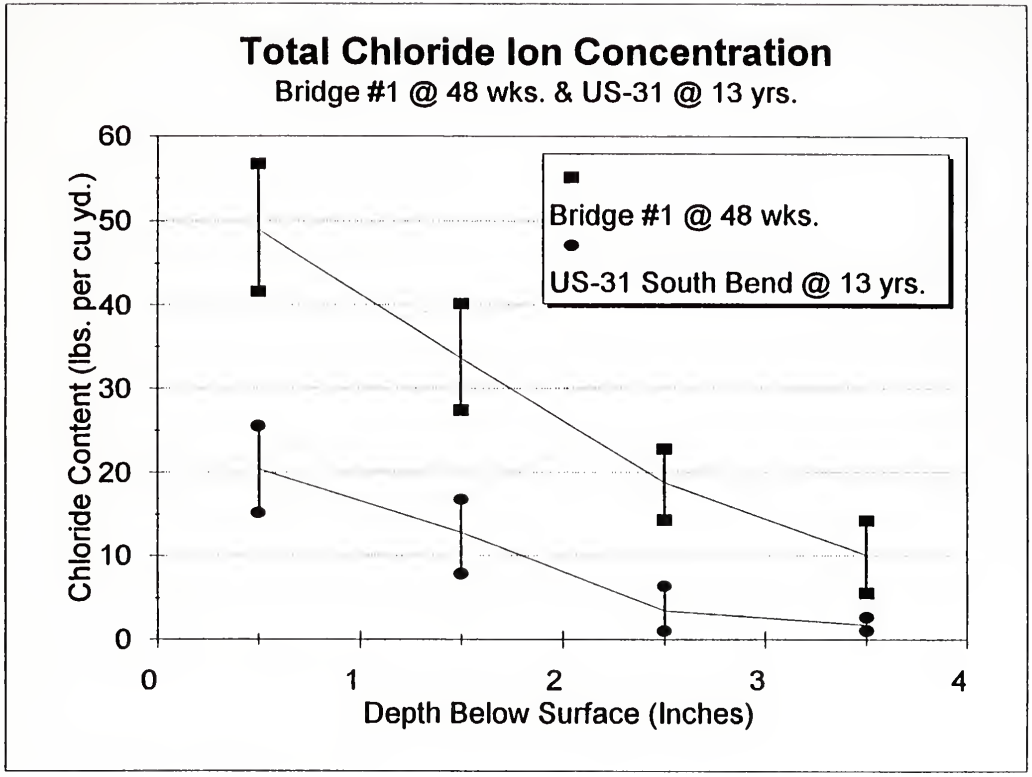

Figure 6.10 Comparison of Chlorides in Bridge #1 With Data from U.S. 31 in South Bend, IN

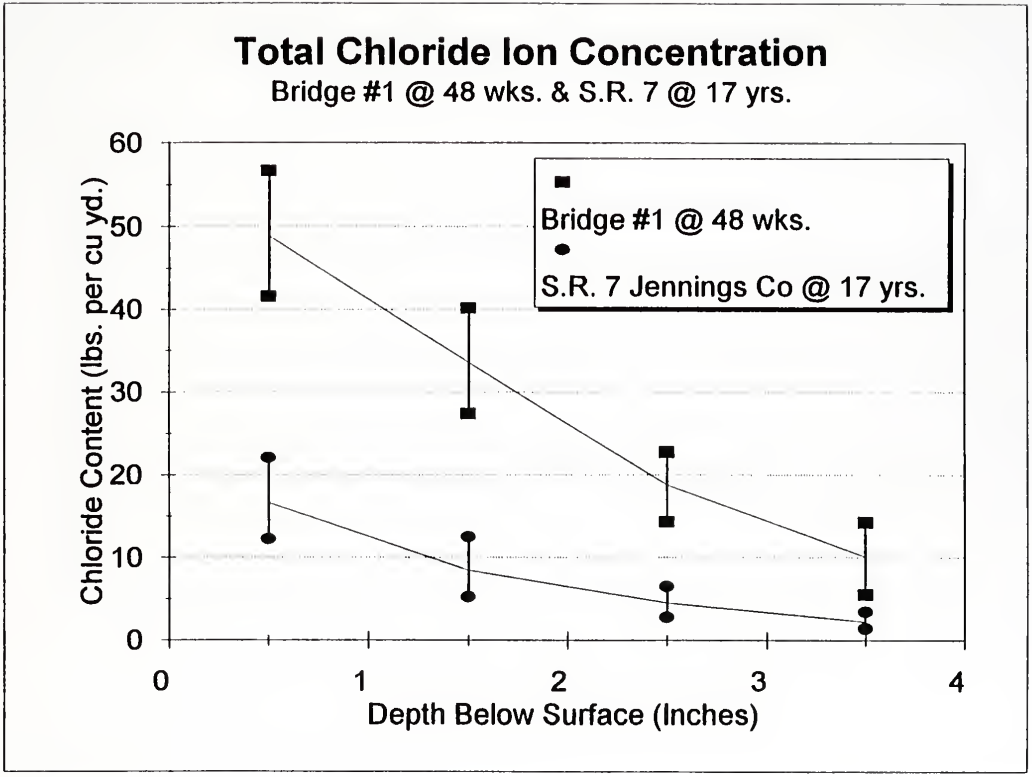

Figure 6.11 Comparison of Chlorides in Bridge #1 With Data from S.R. 7 in Jennings County, IN

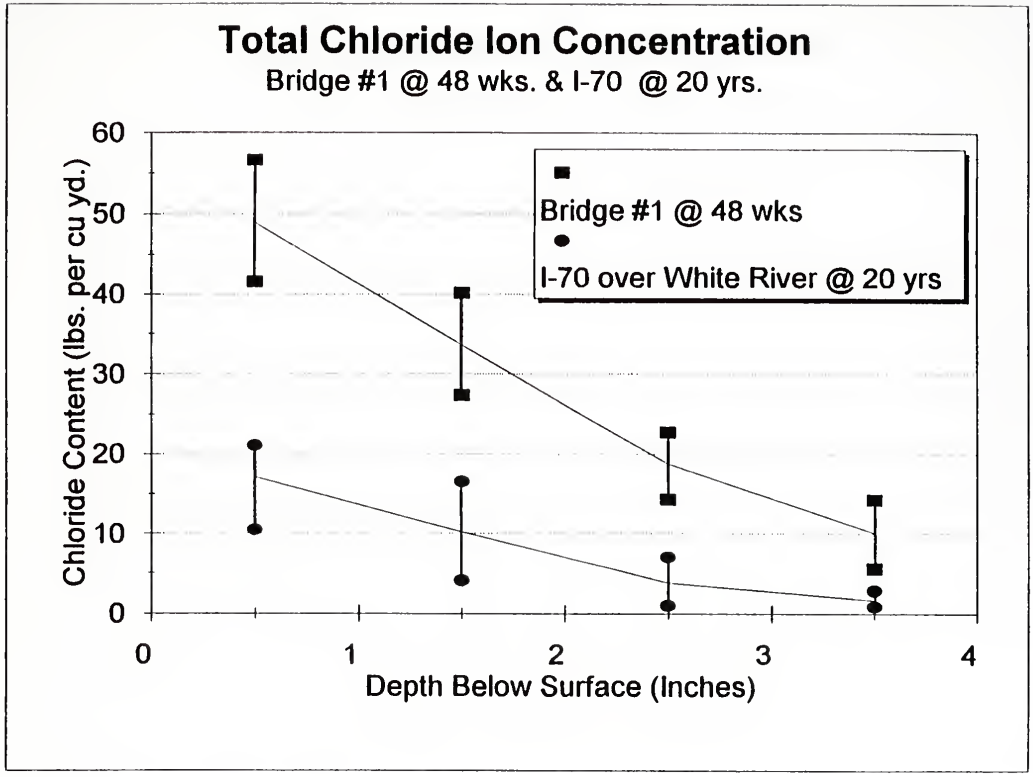

Figure 6.12 Comparison of Chlorides in Bridge #1 With Data from I-70 Over White River in Indianapolis, IN

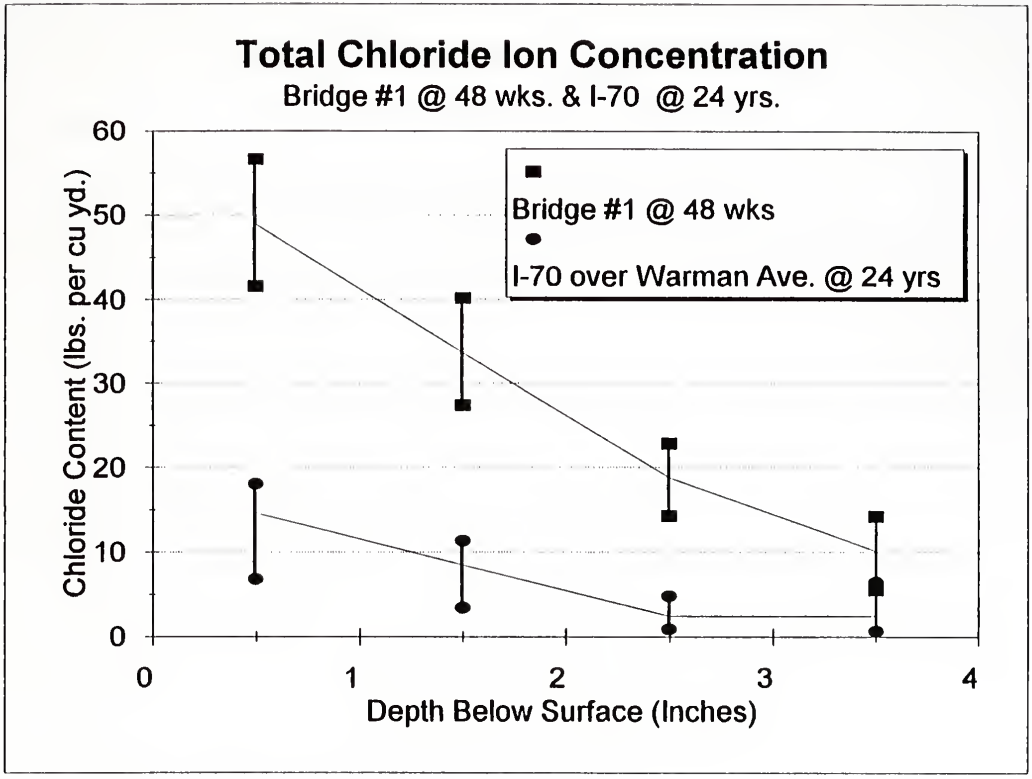

Figure 6.13 Comparison of Chlorides in Bridge #1 With Data from I-70 Over Warman Ave in Indianapolis, IN

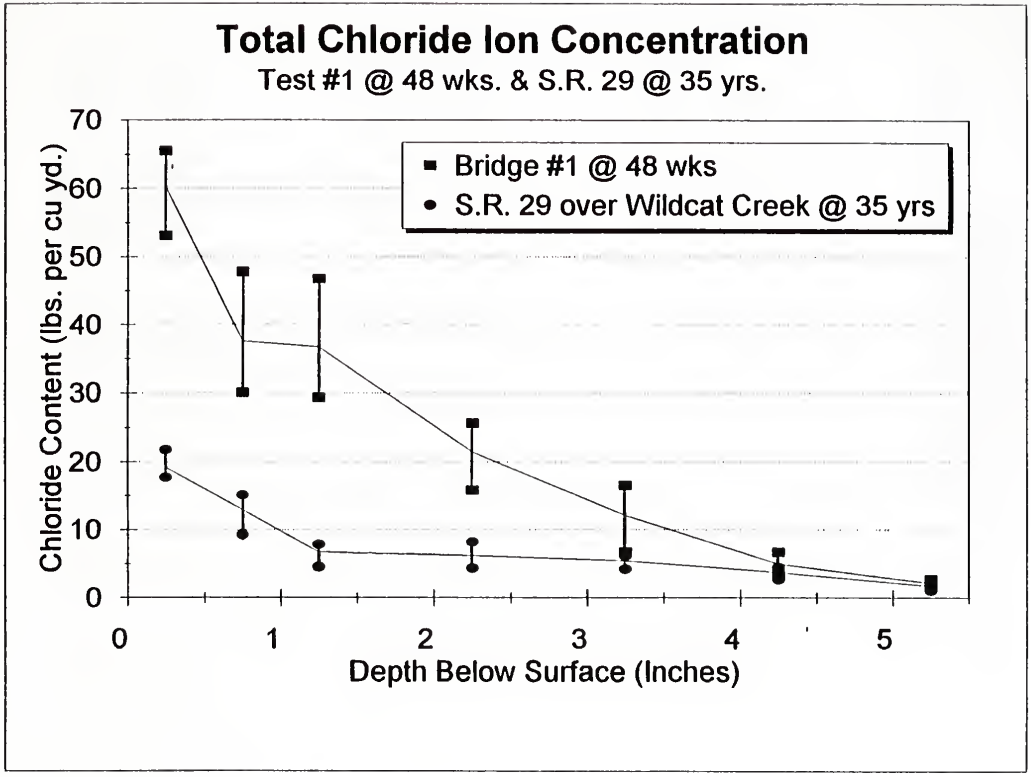

Figure 6.14 Comparison of Chlorides in Bridge #1 With Data from S.R. 29 in Carroll County, IN

Chloride Ion Concentrations

* Values Are Total Chloride Concentrations In Pounds Per Cubic Yard

S.R. 912 Gary, In. (13 yrs old)

Depth	Hole #1	Hole #2	Hole #3	Hole #4	Hole #5	Hole #6
0-1"	16.41	15.91	9.85	11.01	11.62	7.84
1"-2"	6.32	8.39	4.06	4.17	3.39	2.97
2"-3"	4.08	3.94	2.01	2.89	4.27	2.42
3"-4"	3.65	2.57	2.11	3.1	2.53	2.83

US-31 South of South Bend (13 yrs old)

Depth	Hole #1	Hole #2	Hole #3	Hole #4	Hole #5	Hole #6
0-1"	19.27	23.12	25.56	15.15	18.71	20.60
1"-2"	16.77	12.00	14.66	15.12	7.84	10.61
2"-3"	5.63	1.71	6.36	0.99	1.85	4.04
3"-4"	1.82	1.26	2.63	1.03	1.32	2.17

S.R. 7 Jennings County (17 yrs old)

Depth	Hole #1	Hole #2	Hole #3	Hole #4	Hole #5	Hole #6
0-1"	12.89	21.51	22.07	15.31	12.21	16.05
1"-2"	12.47	7.38	6.93	8.81	5.18	10.19
2"-3"	6.47	4.55	3.46	4.62	2.76	5.13
3"-4"	3.03	2.06	1.8	3.39	1.72	1.43

Figure 6.15 Chloride Concentrations for Bridges on S.R. 912, U.S. 31, and S.R. 7

Chloride Ion Concentrations

* Values Are Total Chloride Concentrations In Pounds Per Cubic Yard

I-70 over White River, Eastbound & Westbound (20 yrs old)

Depth	Hole #1	Hole #2	Hole #3	Hole #4	Hole #5	Hole #6
0-1"	20.5	13.9	18.4	14.3	19.5	19.4
1"-2"	11.8	6.4	16.5	11.2	9.7	11.2
2"-3"	4.0	1.0	6.1	5.8	3.2	3.3
3"-4"	1.1	1.0	1.6	2.1	2.9	2.9

Depth	Hole #7	Hole #8	Hole #9	Hole #10	Hole #11	Hole #12
0-1"	19.3	12.0	21.1	18.3	10.5	18.4
1"-2"	9.7	4.1	12.8	13.6	5.0	10.6
2"-3"	7.0	2.4	5.2	3.6	1.2	2.9
3"-4"	1.7	0.9	1.7	1.4	1.0	1.2

I-70 over Warman Avenue, Eastbound & Westbound (24 yrs old)

Depth	Hole #1	Hole #2	Hole #3	Hole #4	Hole #5	Hole #6	Hole #7	Hole #8	Hole #9	Hole #10
0-1"	6.77	17.35	14.77	13.84	14.58	9.53	17.59	17.42	16.34	18.08
1"-2"	3.48	10.61	9.28	6.92	8.92	4.08	11.32	10.26	9.69	10.14
2"-3"	0.93	4.78	3.03	2.3	2.59	1.31	3.39	2.51	2.78	1.12
3"-4"	0.7	0.94	1.48	0.81	0.87	2.31	3.32	6.16	6.46	1.66

Figure 6.16 Chloride Concentrations for I-70 Over White River and I-70 Over Warman Avenue

Chloride Ion Concentrations

* Values Are Total Chloride Concentrations In Pounds Per Cubic

SR 29 over Wildcat Creek (35 yrs old)

Depth	Hole #1	Hole #2	Hole #3	Hole #4	Hole #5
0-.5"	18.59	17.73	21.76	19.69	18.40
.5"-1"	15.09	9.26	------	------	14.47
1"-1.5"	------	7.71	4.52	7.83	------
1.5"-2"	10.07	------	------	------	14.40
2"-2.5"	------	8.17	4.34	6.13	------
2.5"-3"	11.12	------	------	------	7.88
3"-3.5"	------	6.17	4.20	5.90	------
3.5"-4"	7.49	------	------	------	4.51
4"-4.5"	------	2.68	4.02	4.47	------
4.5"-5"	5.07	------	------	------	------
5"-5.5"	------	1.23	1.12	2.73	------
5.5"-6"	4.45	------	------	------	------
6"-6.5"	------	------	------	2.37	------

S.R. 144 Near Mooresville (37 yrs old)

Depth	Hole #1	Hole #2	Hole #3	Hole #4
0-.5"	19.19	20.93	31.04	14.11
.5"-1"	11.07	10.35	27.22	13.43
1"-1.5"	1.59	2.79	18.34	11.16
1.5"-2"	0.48	1.50	7.60	10.70
2"-2.5"	0.84	1.34	2.69	7.56
2.5"-3"	0.83	1.83	0.74	4.84
3"-3.5"	1.37	0.76	0.93	2.60
3.5"-4"	1.43	1.47	1.09	2.07
4"-4.5"	1.33	0.91	0.69	3.54
4.5"-5"	0.72	0.61	0.84	2.46

Figure 6.17 Chloride Concentrations for Bridges on S.R. 29 and S.R. 144

Figure 6.18 37-Year-Old Bridge on S.R. 144 Near Mooresville, IN

Bridge on SR 144 Over Little White Lick Creek

Number of Repair Patches

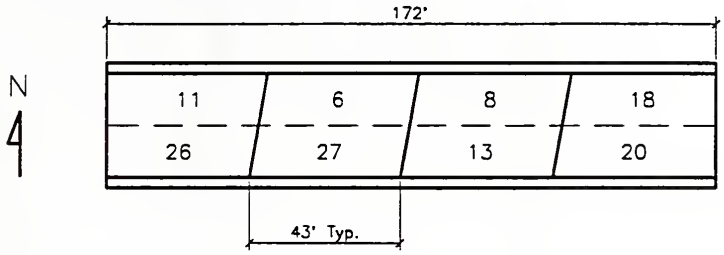

Bridge on SR 144 Over Little White Lick Creek

Field Sample Locations

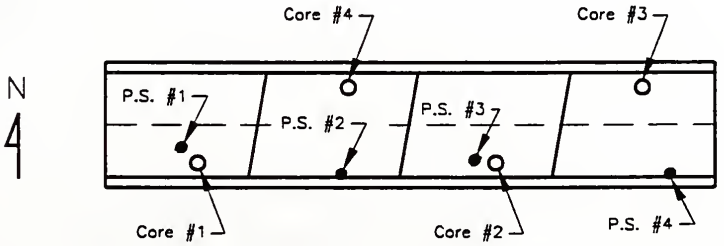

* P.S. Denotes Powder Sample Hole

Figure 6.19 Field Data Collected from S.R. 144 Near Moorseville, IN

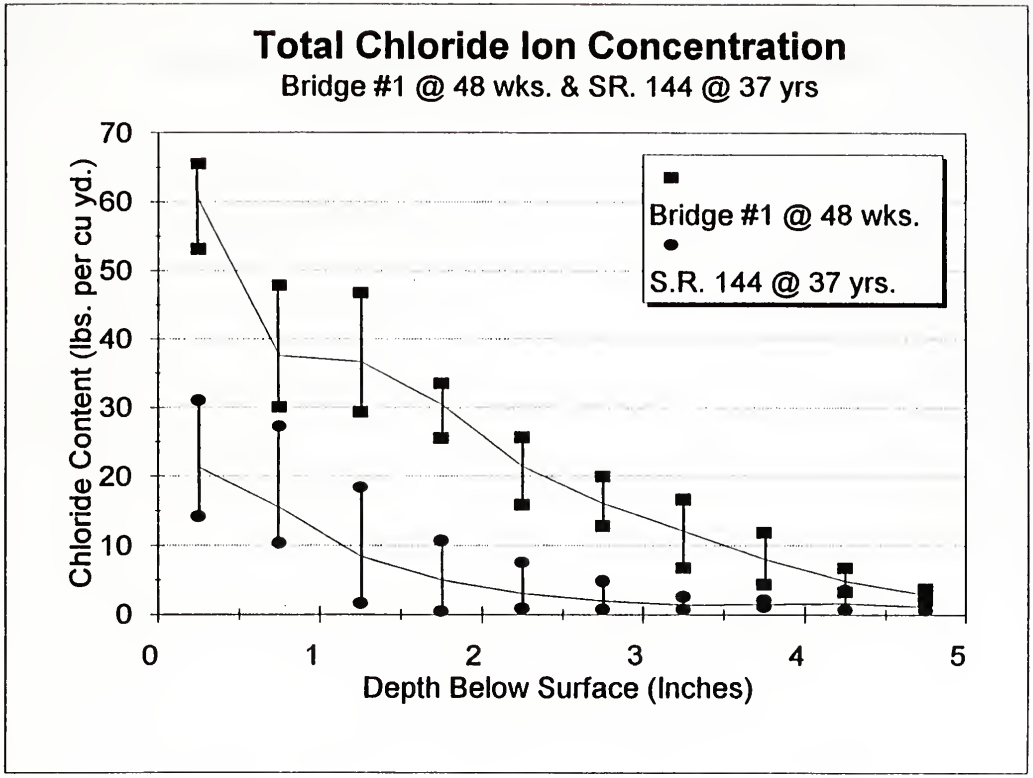

Figure 6.20 Comparison of Chlorides in Bridge #1 With Data from S.R. 144 Near Mooresville, IN

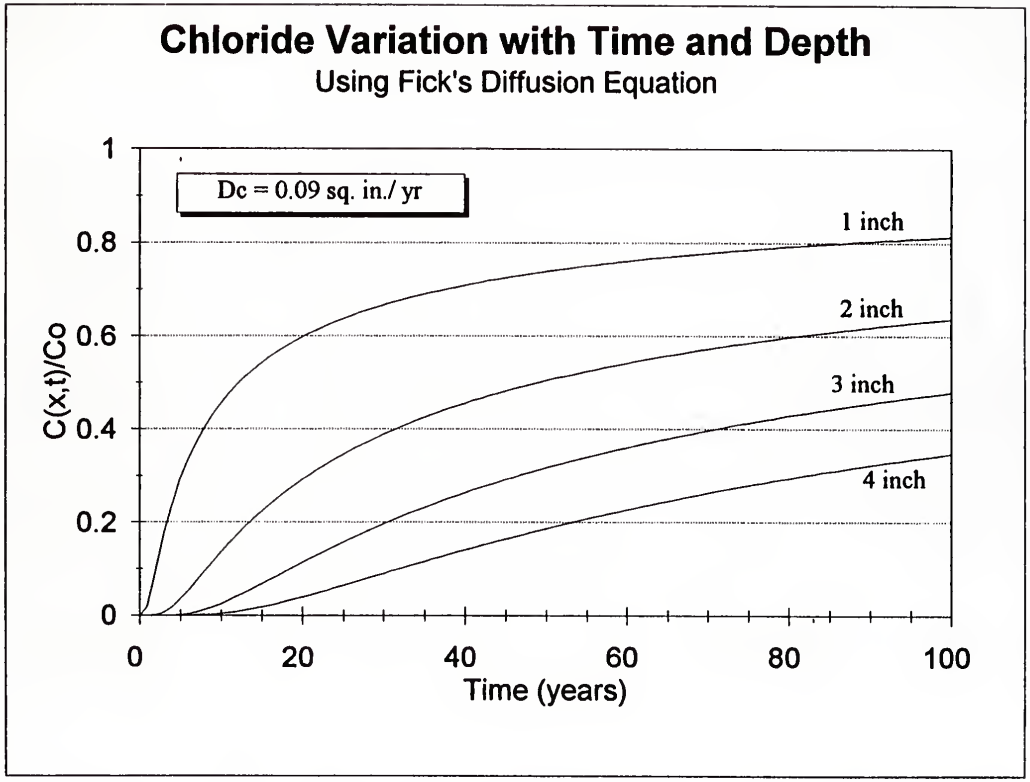

Figure 6.21 Chloride Concentrations Calculated Using Fick's Diffusion Equation

Bridge #1

Material	Date Tested	Test Lab	Coulombs Passed
CIP Concrete	March '95	INDOT	5430
	March '95	INDOT	6401
	April '96	Purdue	4386
	April '96	Purdue	3999
	April '96	Purdue	4157
	April '96	Purdue	4543
Precast Concrete	March '95	INDOT	2634
	March '95	INDOT	2916
	April '96	Purdue	2059
	April '96	Purdue	2165
	April '96	Purdue	2090
	April '96	Purdue	1595

Bridge #2

Material	Date Tested	Test Location	Coulombs Passed
CIP Concrete	May '96	Purdue	7460
	May '96	Purdue	5794
	May '96	INDOT	*
	May '96	INDOT	4647
Precast Concrete	May '96	Purdue	1425
	May '96	Purdue	1094

* The high value of 9334 coulombs recorded was due to a void which extended to the top surface specimen.

3 ft x 3 ft Durability Specimens

Material	Date Tested	Test Location	Coulombs Passed
CIP Concrete	May '96	Purdue	3839
	May '96	Purdue	4062
Precast Concrete	May '96	Purdue	1425
	May '96	Purdue	1094

Figure 6.22 Results from Rapid Chloride Ion Permeability Testing

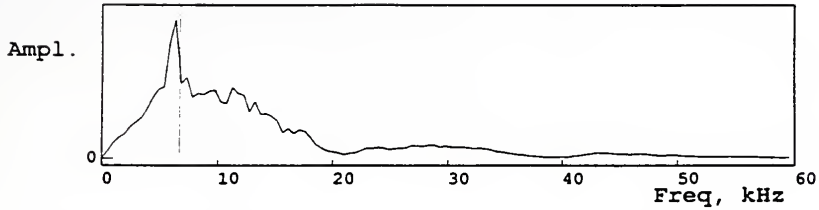

Amplitude Spectrum from Impact-Echo Testing Prior to Failure (PT. C5)

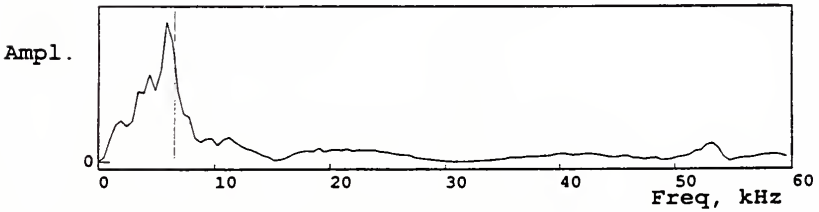

Amplitude Spectrum from Impact-Echo Testing After Failure (PT. C5)

Figure 6.23 Amplitude Spectrums from Impact-Echo Testing of Bridge #1

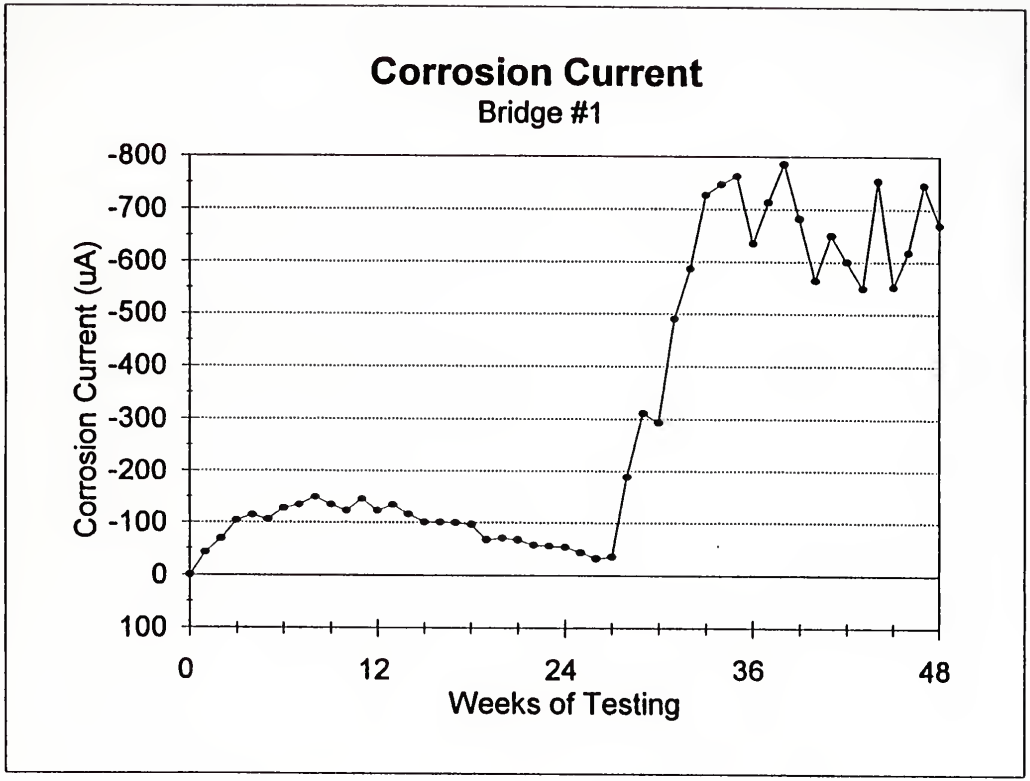

Figure 6.24 Corrosion Currents Within the Ponded Region of Bridge #1

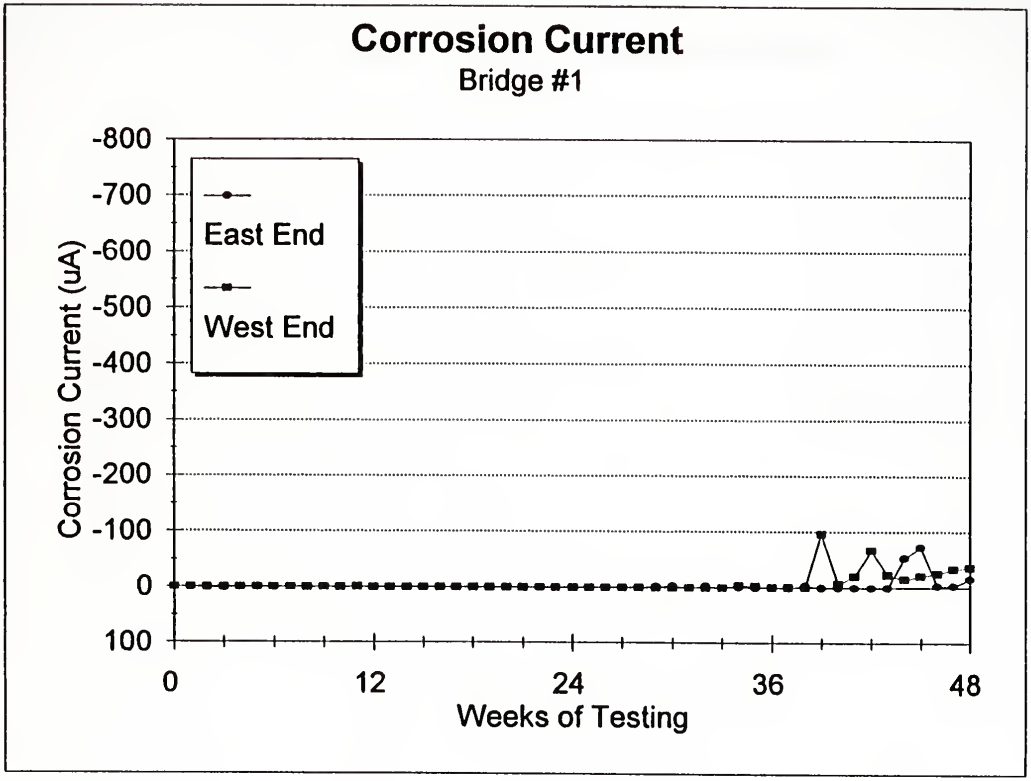

Figure 6.25 Corrosion Currents Outside of the Ponded Region of Bridge #1

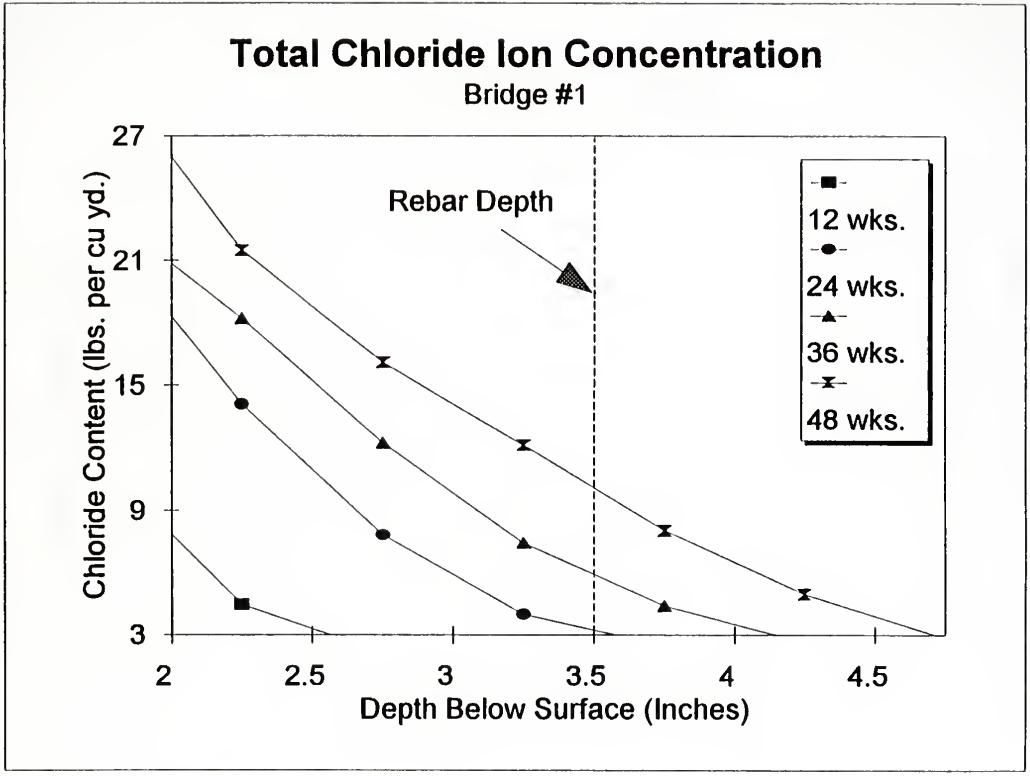

Figure 6.26 Average Chloride Concentrations Taken After 12, 24, 36, and 48 Weeks of Exposure

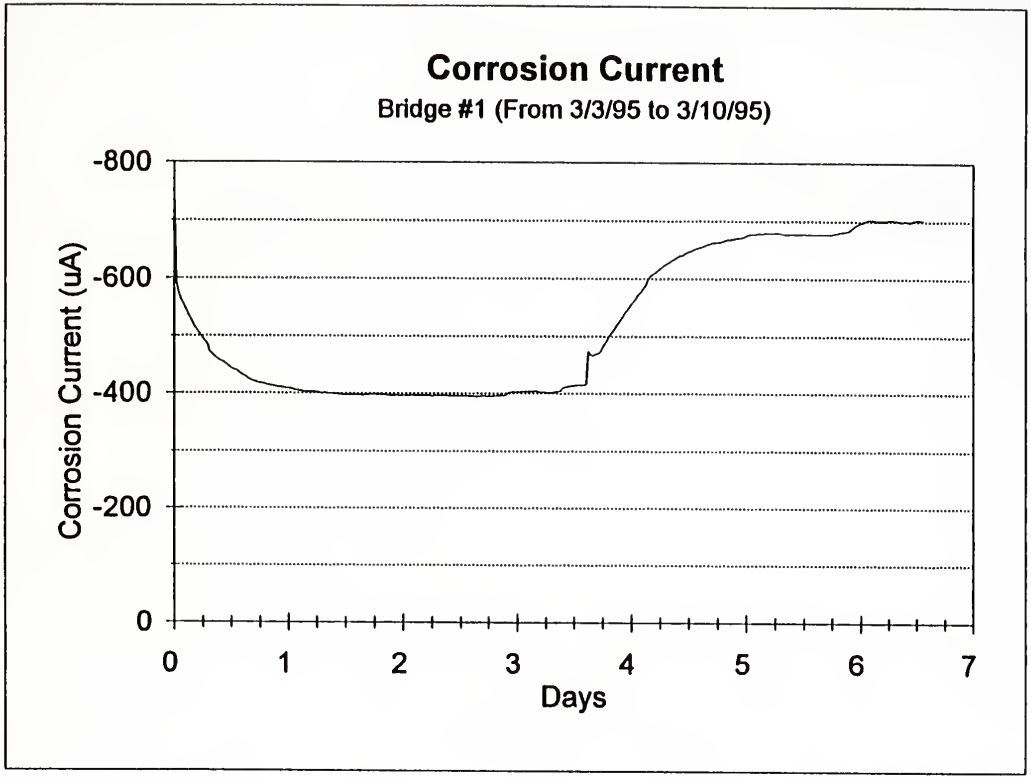

Figure 6.27 Variation of Corrosion Currents During the Weekly Exposure Cycle

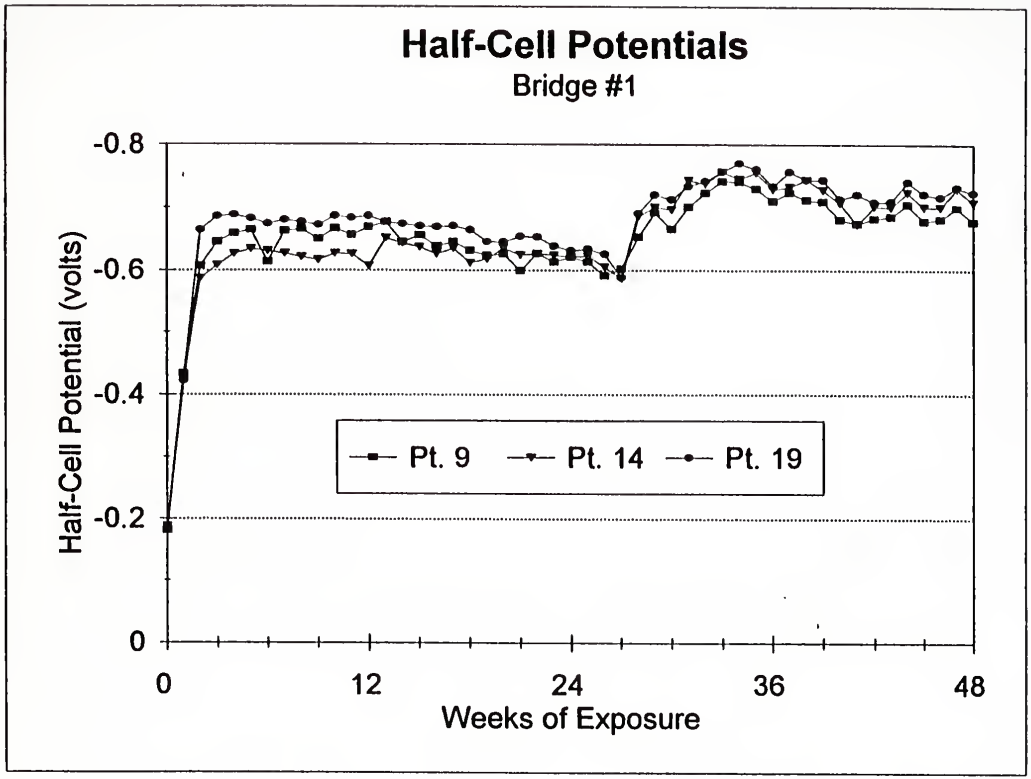

Figure 6.28 Half-Cell Potentials Measured Inside of the Ponded Region of Bridge #1

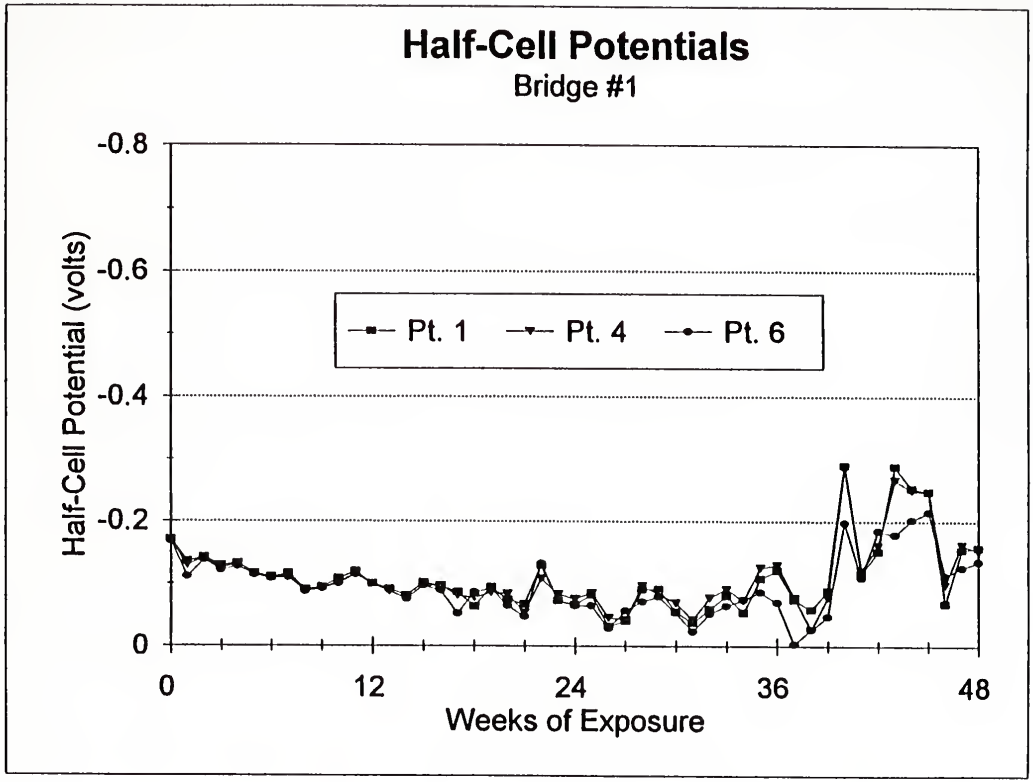

Figure 6.29 Half-Cell Potentials Measured Outside of the Ponded Region of Bridge #1

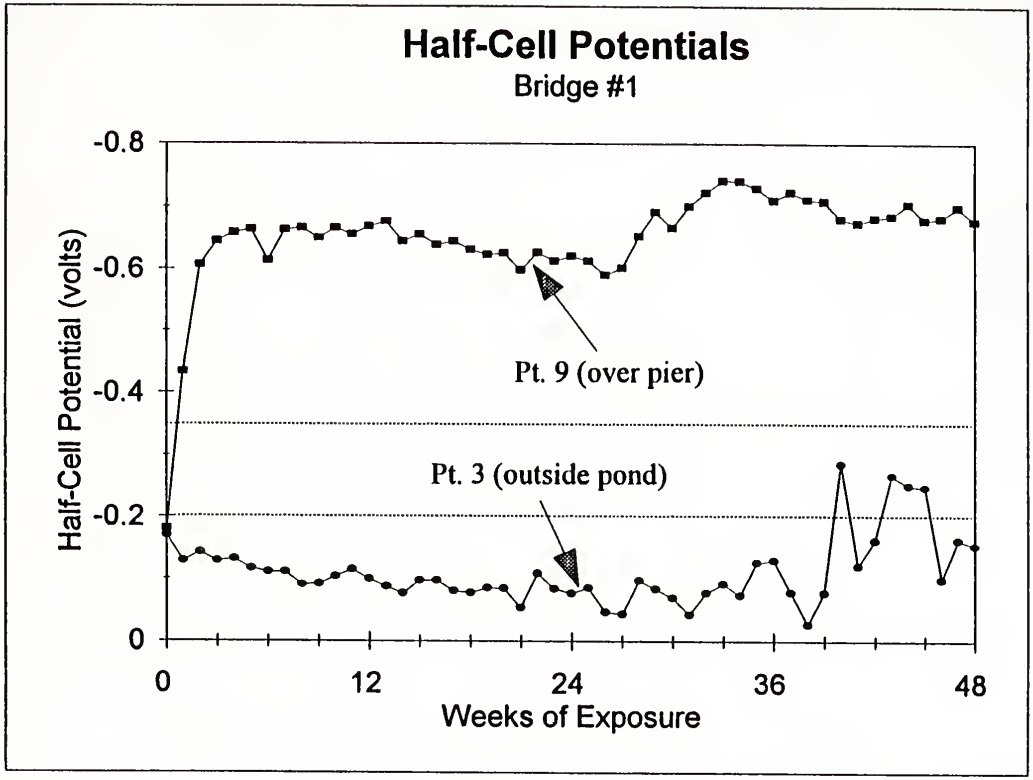

Figure 6.30 Comparison of Measured Half-Cell Potentials of Bridge #1

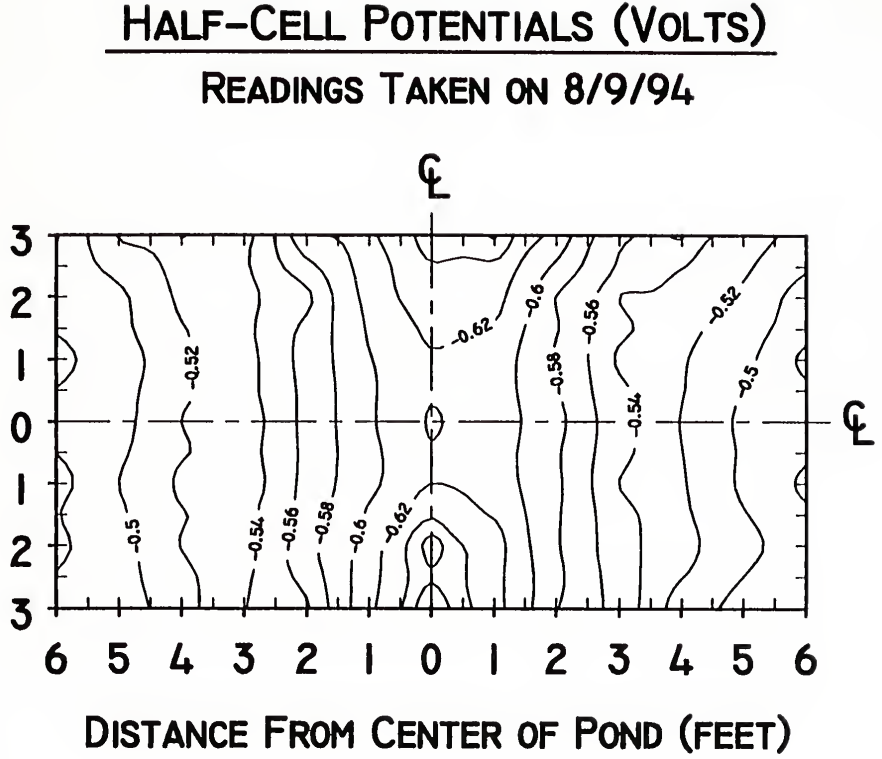

Figure 6.31 Equi-potential Contour Map of the Ponded Region of Bridge #1 After 7 Weeks of Exposure

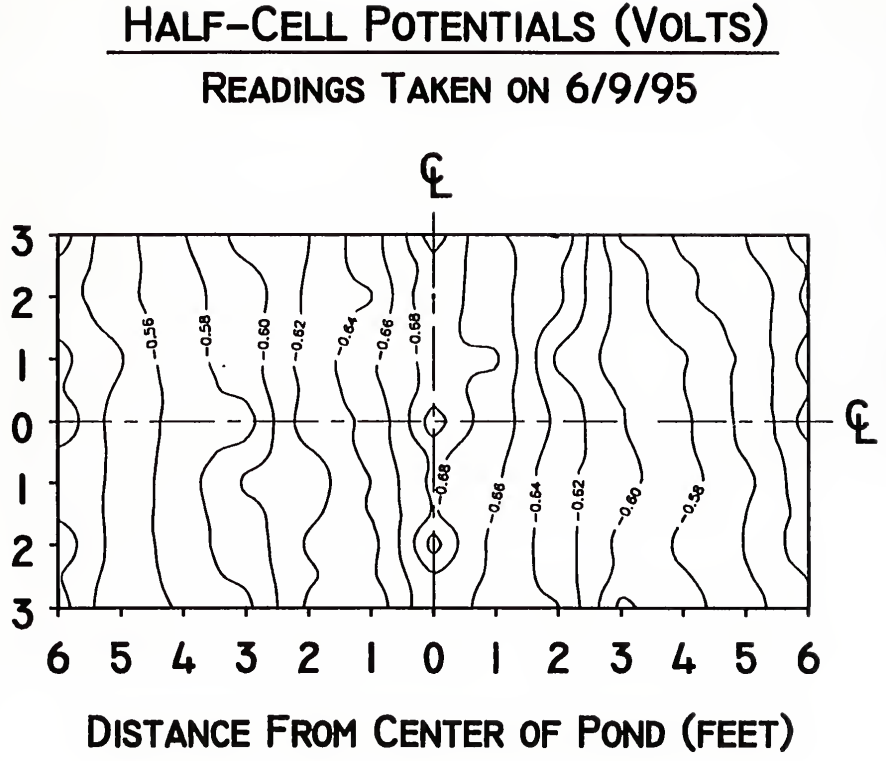

Figure 6.32 Equi-potential Contour Map of the Ponded Region of Bridge #1 After 48 Weeks of Exposure

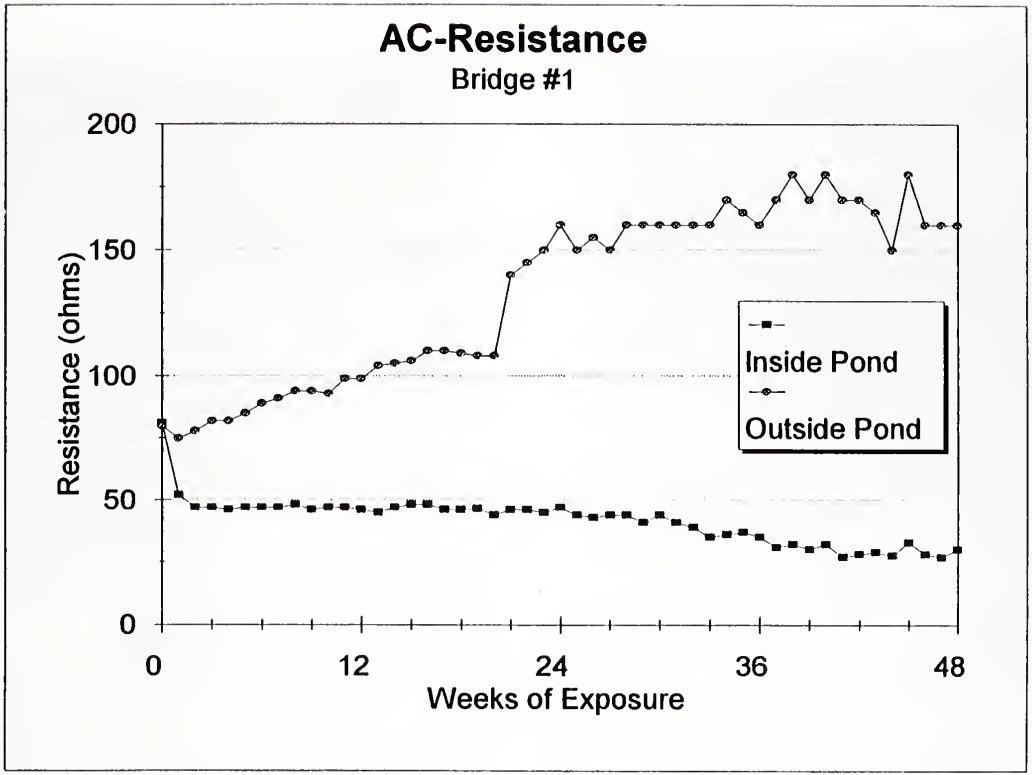

Figure 6.33 AC-Resistances Measured During the 48 Weeks of Exposure Cycling (Bridge #1)

Figure 6.34 Longitudinal Splitting of Epoxy-Coating Due to Corrosion (A)

Figure 6.35 Longitudinal Splitting of Epoxy-Coating Due to Corrosion (B)

Figure 6.36 Corrosion of Epoxy-Coated Bar at Rib Locations

Figure 6.37 Severe Corrosion and Pitting of Prestressing Strand in Diaphragm

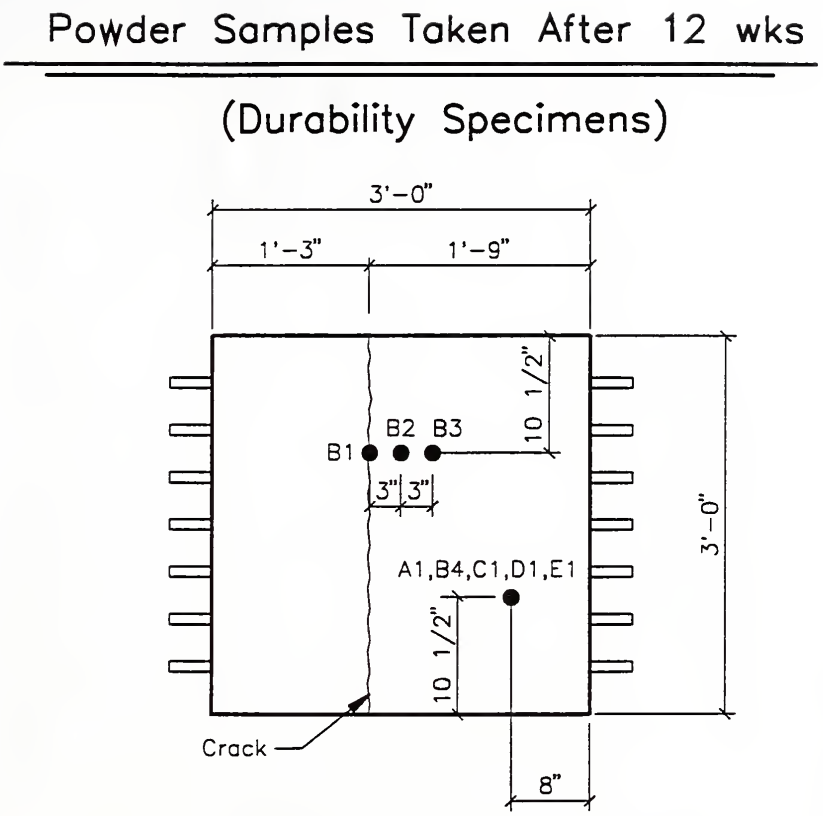

Figure 6.38 Location of Powder Samples Taken After 12 Weeks (Durability Specimens)

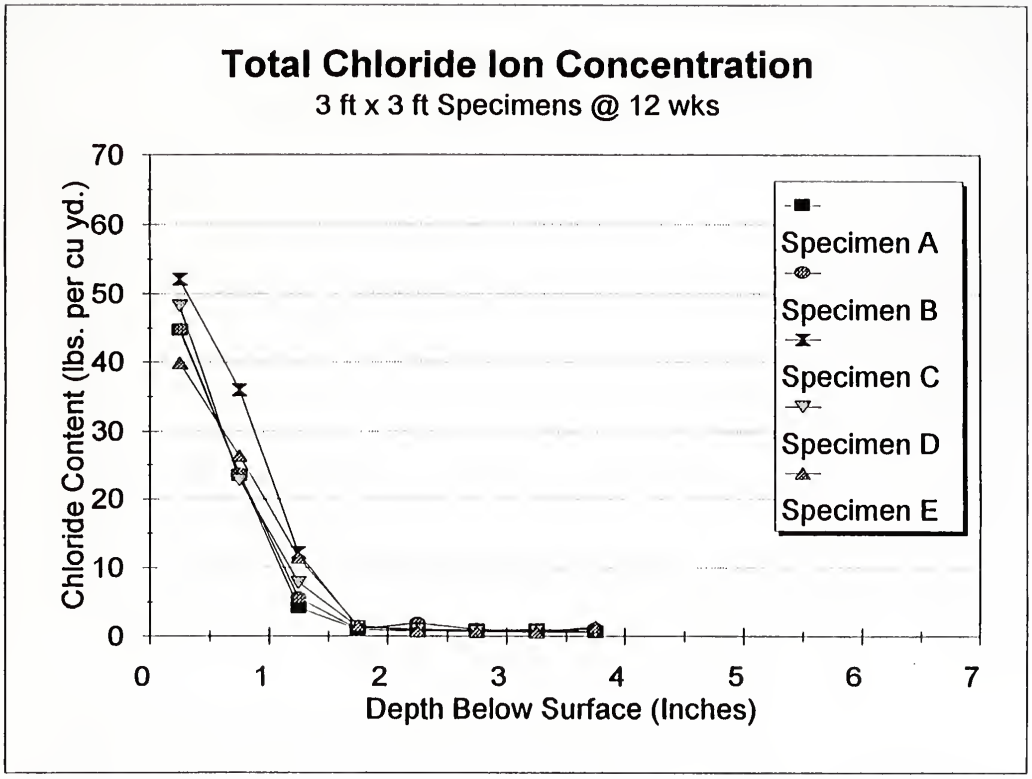

Figure 6.39 Chloride Concentrations at Holes Located Away from Crack after 12 Weeks of Exposure (Durability Specimens)

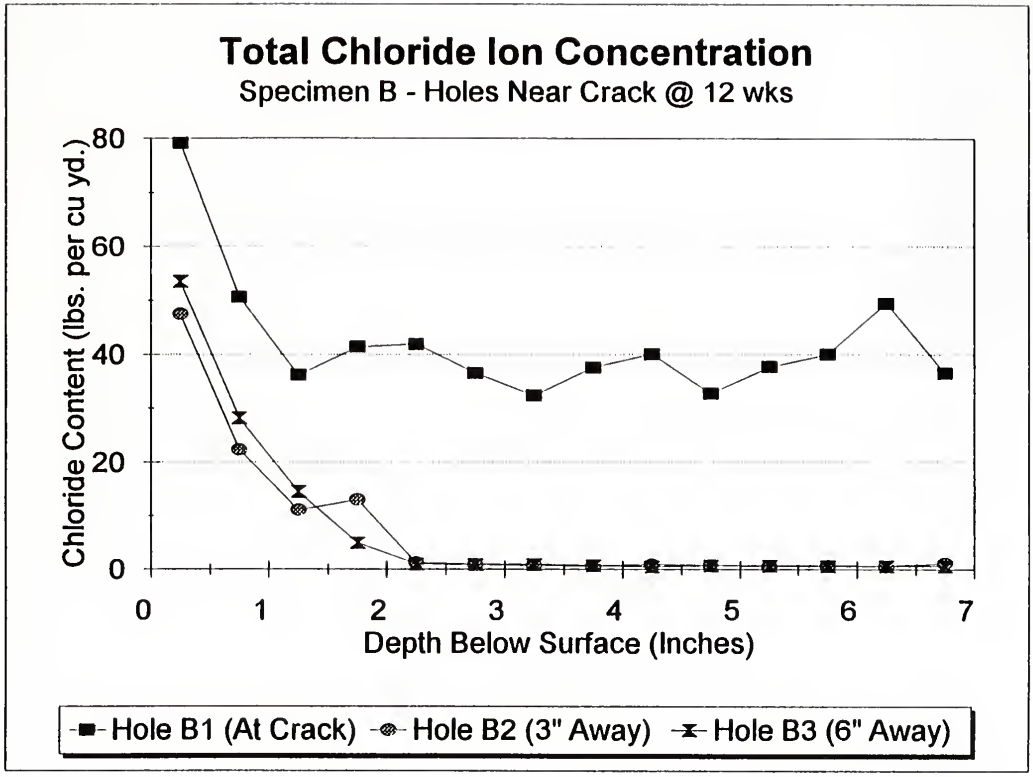

Figure 6.40 Chloride Concentrations at Holes Located Near the Crack after 12 Weeks of Exposure (Durability Specimens)

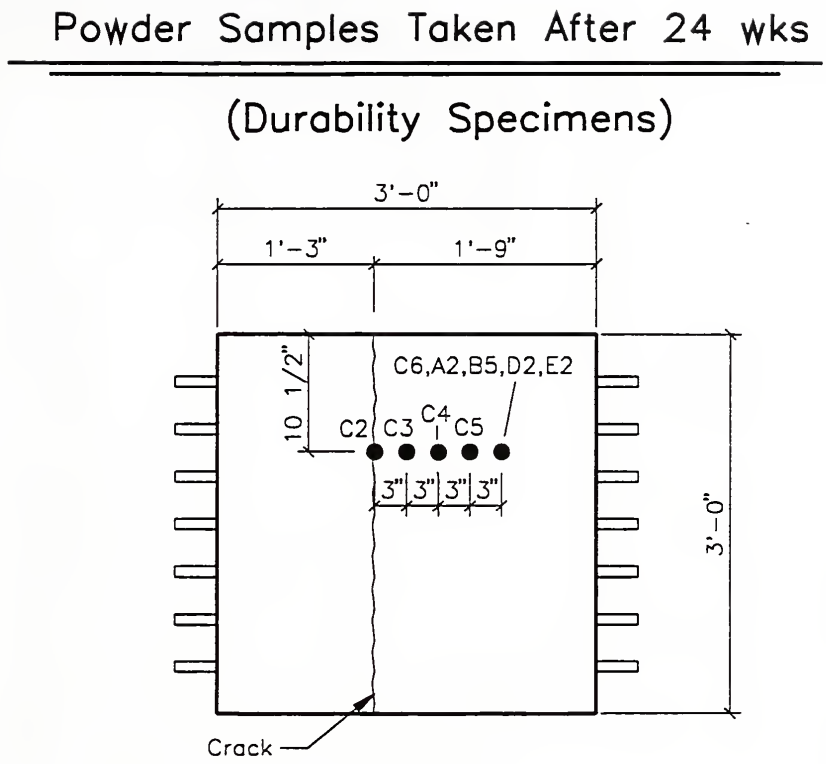

Figure 6.41 Location of Powder Samples Taken After 24 Weeks (Durability Specimens)

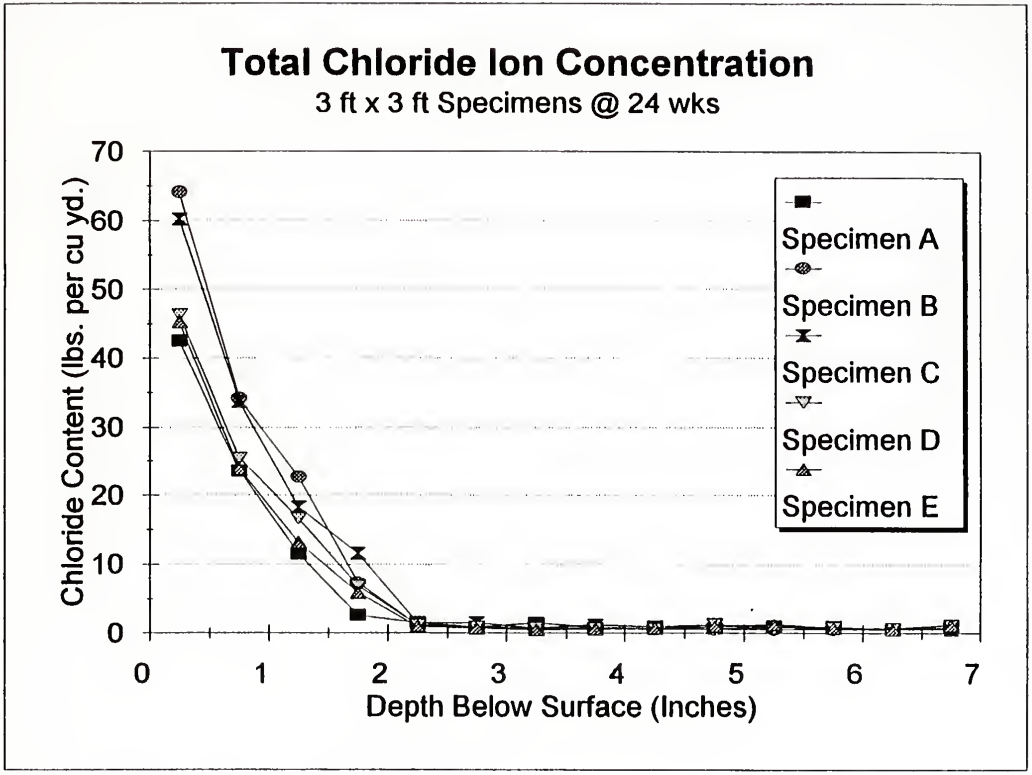

Figure 6.42 Chloride Concentrations at Holes Located Away from Crack after 24 Weeks of Exposure (Durability Specimens)

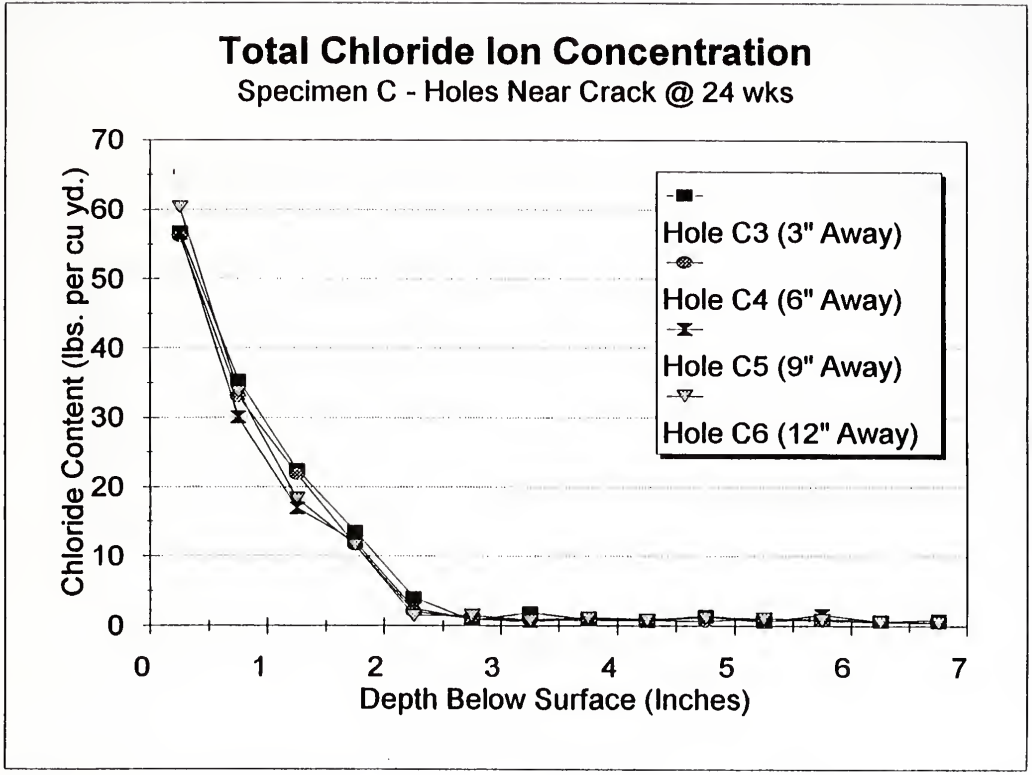

Figure 6.43 Chloride Concentrations at Holes Located Near the Crack after 24 Weeks of Exposure (Durability Specimens)

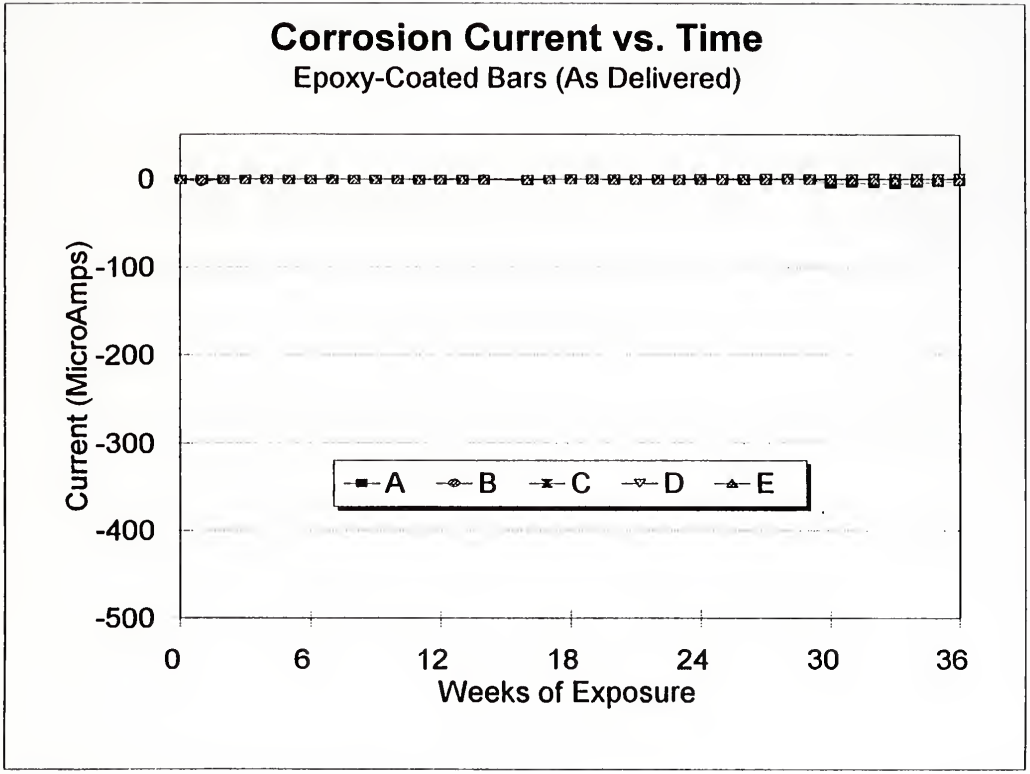

Figure 6.44 Measured Corrosion Currents of Undamaged Epoxy-Coated Bars

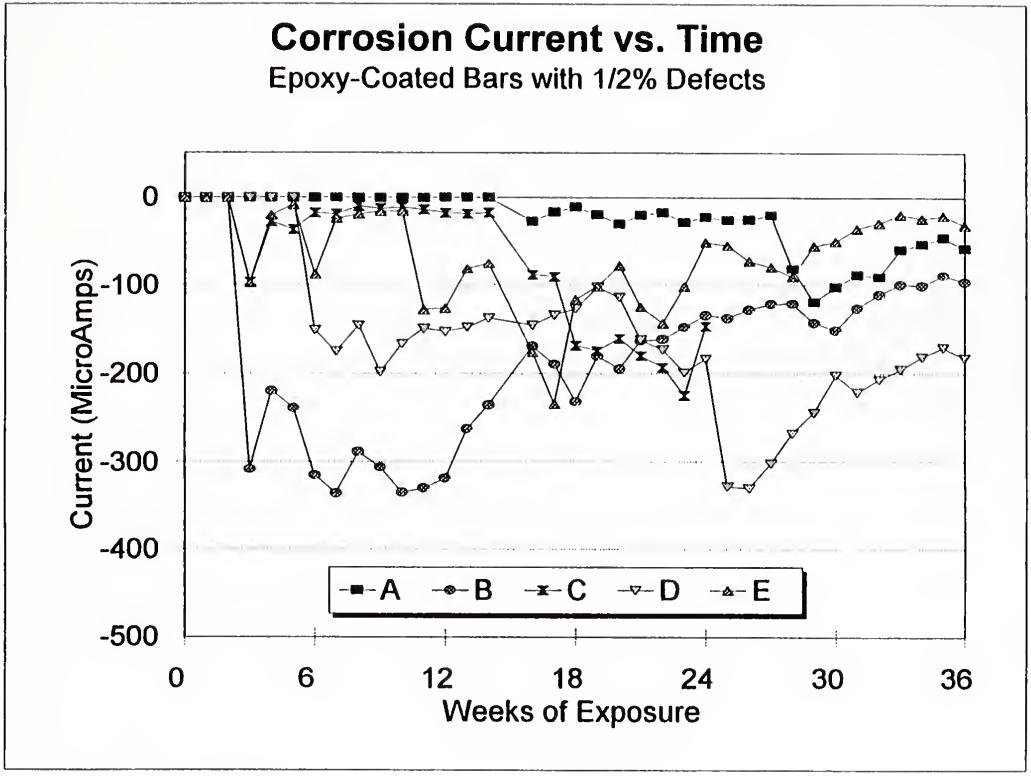

Figure 6.45 Measured Corrosion Currents of Epoxy-Coated Bars With 1/2% Defects

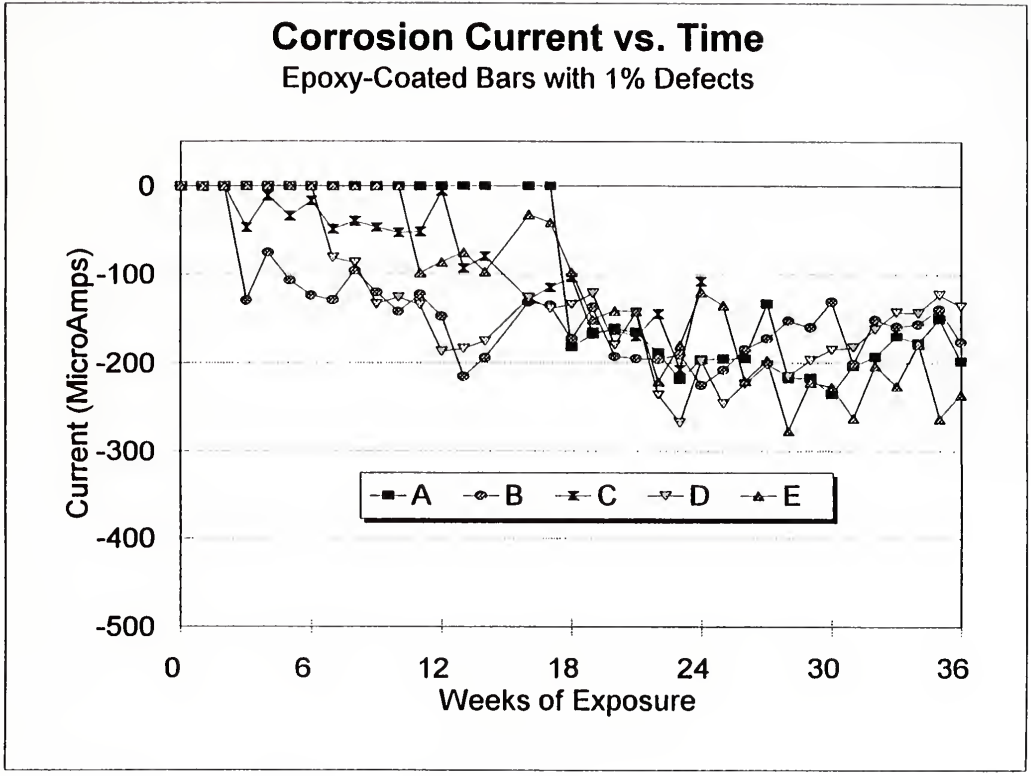

Figure 6.46 Measured Corrosion Currents of Epoxy-Coated Bars With 1% Defects

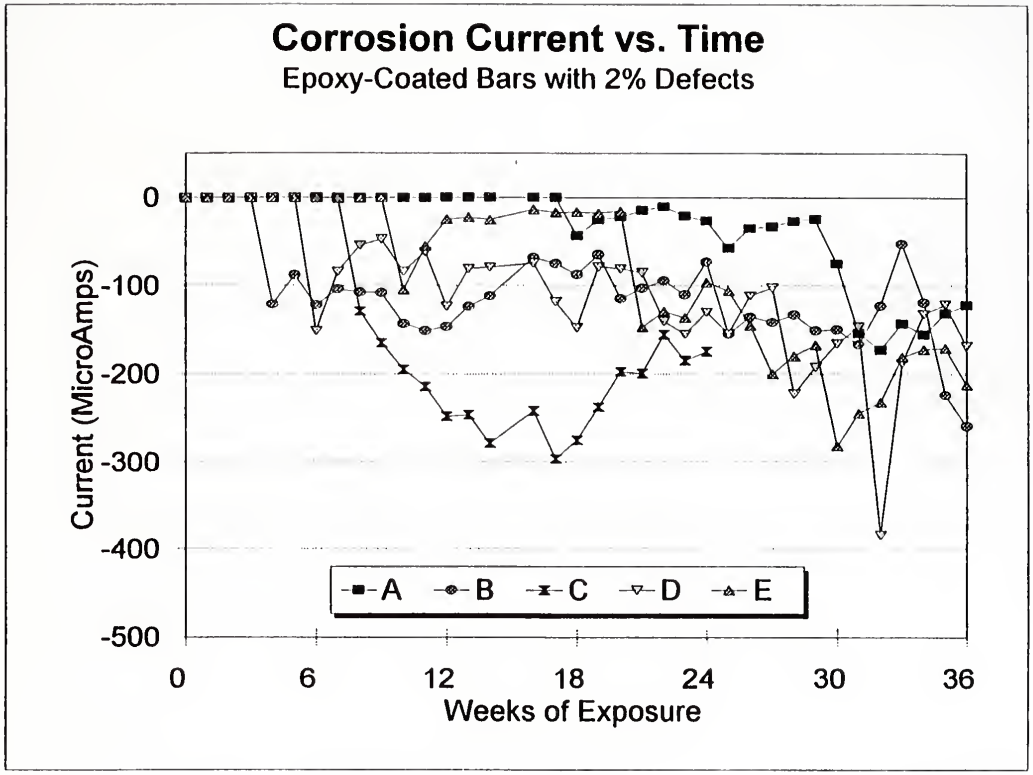

Figure 6.47 Measured Corrosion Currents of Epoxy-Coated Bars With 2% Defects

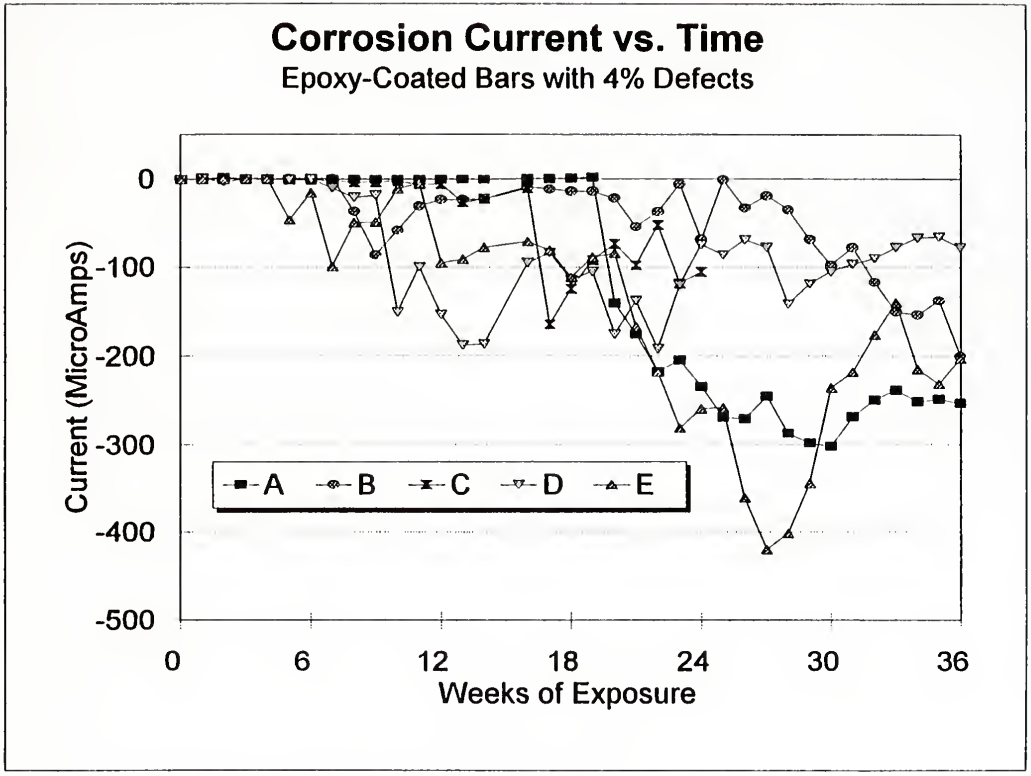

Figure 6.48 Measured Corrosion Currents of Epoxy-Coated Bars With 4% Defects

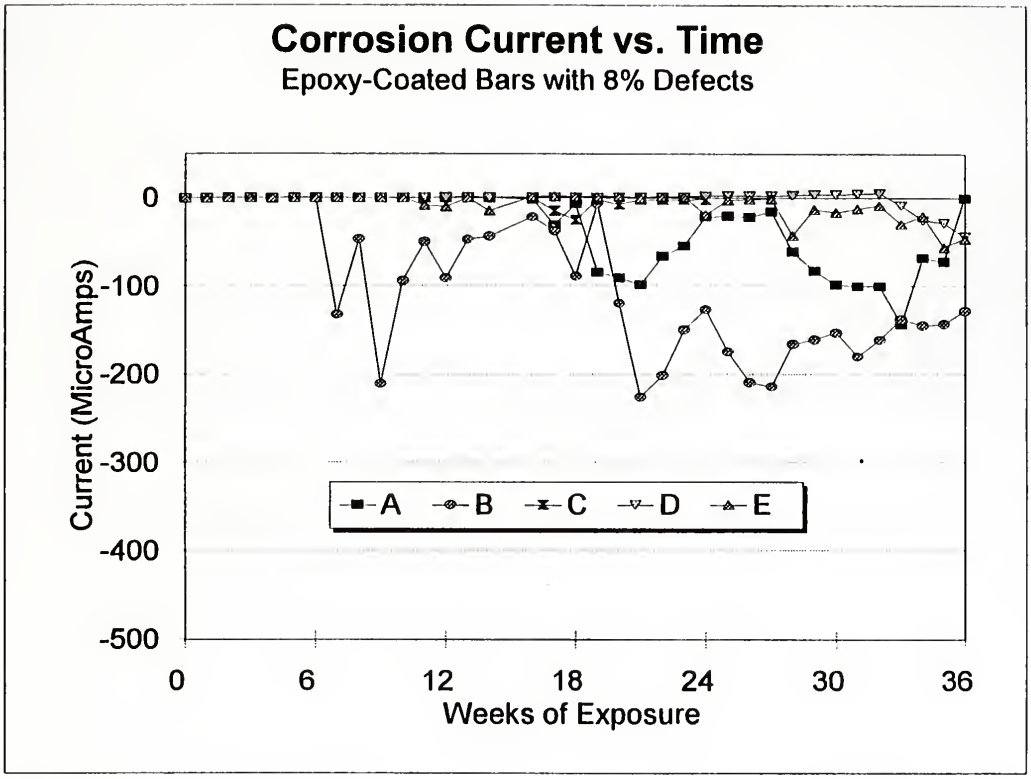

Figure 6.49 Measured Corrosion Currents of Epoxy-Coated Bars With 8% Defects

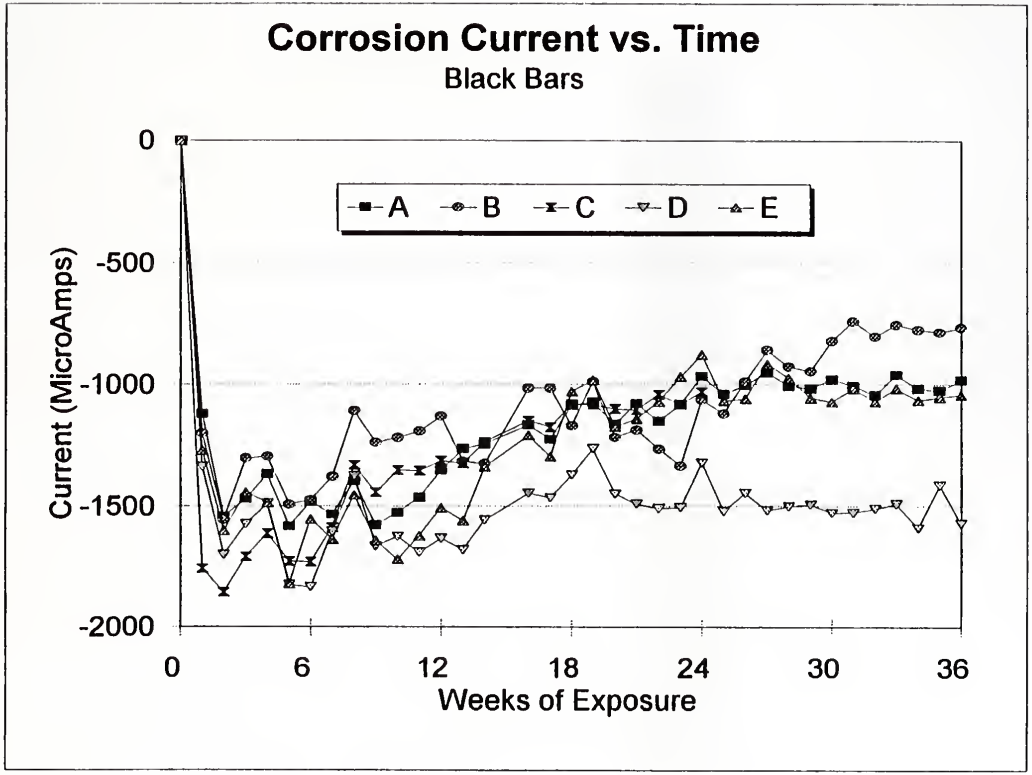

Figure 6.50 Measured Corrosion Currents of Black Bars

Figure 6.51 Severe Pitting of Black Bar After 24 Weeks of Exposure (Specimen C)

CHAPTER 7 SUMMARY, CONCLUSIONS AND RECOMMENDATIONS

7.1 Summary of Results

7.1.1 Introduction

This experimental program consisted of testing two composite bridges, utilizing precast prestressed concrete panels, in the laboratory. During the cast-in-place (CIP) concrete cure period of these two-span continuous structures the moments at the center pier, induced by the restraint of creep and shrinkage, were determined from measurements of discontinuous-end reactions. These bridges were then exposed to 5 million cycles of service load prior to the final monotonic failure loading. Possible degradation of these bridges due to repeated loading was assessed by monitoring the discontinuous-end reactions, midspan deflections, and strains in the steel reinforcement. The long-term performance of this type of structure was determined by subjecting one bridge (Bridge #1) to 48 weeks of southern exposure cycling, consisting of exposure to salt water and heat lamps. During this time, half-cell potentials, corrosion currents, and AC-resistances were measured weekly. Additional information about the durability of these structures was obtained from the southern exposure cycling of 5 smaller composite specimens, each containing reinforcement with varying degrees of defects in the epoxy-coating.

7.1.2 Restraint Moments

The experimentally determined restraint moments were compared with calculated restraint moments using the PCA and CTL methods (described in Sections 4.2 and 4.3), both of which overestimated the negative restraint moments due to differential shrinkage and creep under dead load. The failure of the PCA method to account for restraint of shrinkage due to the precast elements and steel reinforcement led to an overestimation of early shrinkage moments. Also, neither the PCA nor the CTL method accounts for cracking. Cracking reduces the magnitude of the restraint moments and the rate at which additional restraint moments develop. A modified PCA method was developed by the author (refer to Section 4.5.1) which accounts for the restrained shrinkage of the CIP concrete and the length of the diaphragm. The modified PCA method was more accurate than the PCA and CTL approaches in the calculation of restraint moment magnitudes for both test bridges. While this method improved the calculation of the restraint moment magnitudes, it overestimated the change in moments due to cracking and the ability of the moments to increase after cracking. For both specimens tested, negative restraint moments due to differential shrinkage and creep due to dead load were largest prior to cracking. A reasonable model of the restraint moments during the CIP concrete cure period of the two test bridges was obtained using the modified PCA method before cracking, and then assuming moments due to differential shrinkage remain unchanged after cracking.

7.1.3 Response to Superimposed Loading

7.1.3.1 Initial Loading

The restraint moments (induced by creep and shrinkage) decreased during the initial loading of each bridge due to additional transverse cracking at the pier. There was a 49% decrease in the restraint moments for Bridge #1, which had higher initial restraint moments and fewer initial cracks than Bridge #2, and a 30% decrease for Bridge #2. Because of cracking, the PCA, CTL, and modified PCA methods overestimated the increase in continuity moments for each bridge during this initial loading. For subsequent loadings which did not produce additional cracking, the modified PCA method (which assumed a diaphragm stiffness based on a section having a crack depth equal to the thickness of the CIP topping) gave a reasonable estimate of the change in continuity moments. Both the PCA and CTL methods, which are based on gross section properties, considerably overestimated the additional continuity moments.

Similarly, due to the additional cracking and corresponding decrease in restraint moments, all three methods underestimated the midspan deflections caused by the initial loadings of each bridge. Values equal to the observed deflections could be obtained using the modified PCA method, assuming a fully cracked diaphragm region, with applied positive moments at the pier that were equal in magnitude to the measured decrease in restraint moments. Midspan deflections due to subsequent loadings could be reasonably estimated by using the modified PCA method, assuming a fully cracked diaphragm.

7.1.3.2 Cyclic Loading

Each bridge was subjected to 5 million cycles of service loading, in which the calculated maximum reinforcement stress range at the pier (26 ksi to 44 ksi) exceeded the AASHTO allowable design stress range by 20 percent. The continuity between adjacent spans was evaluated by monitoring the instantaneous midspan deflections and discontinuous-end reactions during static loadings which were conducted periodically throughout the 5 million cycles. These measurements showed that the repeated loadings did not cause an appreciable change in the continuity between adjacent spans.

7.1.3.3 Failure Loading

The failure load of each bridge could be determined using the principle of virtual work, with moment capacities at hinges equal to the nominal moment capacities determined by strain compatibility. For both bridges, the experimentally determined positive and negative moments exceeded the nominal design moments calculated using the AASHTO equations (refer to Figures 5.38 through 5.41). Negative moment capacities were considerably higher than the AASHTO values because of strain hardening of the mild steel reinforcement.

The ultimate load carrying capacity of the bridge was not affected by the initial restraint moments due to time-dependent effects, as these were relieved by additional cracking of the concrete and yielding of the steel reinforcement. Moment redistribution for both bridges exceeded the limit allowed by AASHTO (see Equation 5.3) for design

considerations. For Bridge #1, the experimentally determined negative moments at the maximum sustained load were 48% less than the moments calculated using linear-elastic analysis. For Bridge #2, these moments were 31% less than the elastic moments.

7.1.4 Durability

7.1.4.1 Chloride Penetration in Bridge #1

The data obtained from the chloride ion powder samples taken from Bridge #1 throughout the 48 weeks of exposure cycling showed that chloride penetration did not reach the level of the interface at locations which were at least 12 inches from observed cracks. The depth of chloride penetration was approximately 5 inches after 48 weeks of ponding, while the depth of the interface was between 6 3/8 inches and 7 inches in the exposed region. An accumulation of chlorides at the level of the interface was detected from powder samples taken at a hole drilled directly on a crack. However, a build-up of chlorides was not indicated from numerous powder samples taken at holes that were 6 inches or more from observed cracks. Therefore, it was concluded that any accumulation of chlorides that occurred at the interface of the CIP topping and precast panels remained isolated at the crack locations during the 48 weeks of the exposure cycling.

The chloride concentrations in Bridge #1, resulting from the 48 weeks of exposure cycling, were higher than all chloride concentration data from bridges in Indiana. The available data was from bridges tested between the ages of 13 and 37 years, the latter representing the oldest bridge in the central part of the state which had not been previously overlaid or resurfaced. Conservative (lower-bound) estimates of the time represented by

the exposure cycling, in terms of chloride penetration, were made by linearly extrapolating the available chloride data from these bridges. These estimates show the laboratory ponding represented a minimum of 45 years of exposure to chlorides in the northwest portion of the state, where deicing salt usage is heaviest. Estimates of the represented time of exposure in other parts of the state were higher. Therefore, the chloride penetration resulting from the 48 weeks of exposure cycling is believed to have surpassed the chloride penetration which could be expected during the life of concrete bridge decks in the field.

7.1.4.2 Chloride Penetration in the 3 ft x 3 ft Durability Specimens

Chloride ion powder samples extracted from the five additional durability specimens showed that chloride penetration, by diffusion, had reached depths of approximately 2 inches after 12 weeks of exposure cycling and 2 1/2 inches after 24 weeks of exposure cycling. Holes drilled near crack locations after 12 and 24 weeks of exposure showed the crack did not significantly influence the chloride concentrations at distances of only 3 inches away. Increased chloride concentrations at the level of the interface were detected from powder samples taken at a hole drilled directly on the crack. This increase was shown to be isolated at the crack location, as chloride contents only 3 inches away (and at the same depth) were equal to base values for the concrete.

7.1.4.3 Reinforcement Corrosion in Bridge #1

Measured corrosion currents and half-cell potentials indicated that corrosion of the epoxy-coated reinforcement in Bridge #1 began during the first week of southern exposure cycling. The half-cell potentials indicated that the corrosion activity was most severe at the pier location, where transverse cracking occurred. This was also the location of the uncoated strands comprising the positive moment connection in the diaphragm. After 28 weeks of ponding there was an increase in the corrosion rate of the epoxy-coated steel. Chloride ion powder samples showed this corresponded to about 4 weeks after chlorides had reached the entire mat of epoxy-coated steel by diffusion. Visual inspection of the steel reinforcement at the conclusion of the testing revealed extensive corrosion of the epoxy-coated reinforcement, which was most severe for the longitudinal bars. This corrosion was accompanied by longitudinal and transverse splitting of the epoxy coating and staining of the surrounding concrete. Significant area loss of the epoxy-coated reinforcement due to corrosion was not observed. Tensile tests performed on the extracted epoxy-coated bars revealed the average breaking strength was within 4% of the initial tensile strength measured for the bars. Additional inspection of the diaphragm region showed the uncoated bent prestressing strands had experienced severe corrosion, exemplified by deep pitting and area loss. Strand corrosion was only observed at the diaphragm and did not extend into the precast panels.

7.1.4.4 Reinforcement Corrosion in the 3 ft x 3 ft Durability Specimens

Testing of the five additional durability specimens, each having a one-inch reinforcement cover, revealed that all epoxy-coated bars having initial defects began corroding during the first 32 weeks of the exposure cycling. Epoxy-coated bars without initial defects did not experience corrosion during this time period. The quantity of initial defects did not appear to influence the corrosion of the bars during the first 36 weeks ponding, as bars with small percentages of defects had similar corrosion currents and half-cell potentials as bars with larger areas of defects. The corrosion currents measured for the black bars were considerably higher than currents corresponding to the epoxy-coated bars containing defects. Visual inspection of the reinforcement in Specimen C after 24 weeks of exposure revealed severe pitting and loss of cross-sectional area had occurred for the black bar at the crack location. Corrosion damage to the epoxy-coated bars with initial defects consisted of surface rusting and minor pitting at the initial defects, and small areas of blistering of the epoxy coating. Corrosion of the epoxy-coated bars was not accompanied by a significant loss of area during the first 24 weeks of exposure cycling.

7.2 Conclusions

Based of the test results from this study, the following conclusions can be drawn:

1. Both the PCA and CTL methods considerably overestimated the negative moments due to the restraint of time-dependent deformations in bridges with full-span prestressed concrete panels. The two-bridge average ratio of calculated to experimentally determined restraint moments was 4.65 for the PCA method and 2.35

for the CTL method. A modified version of the PCA method, presented in this report, was more accurate in estimating these restraint moments. This average ratio of calculated to experimental restraint moments using this method was 1.38.

2. The restraint moments in each test bridge decreased during the initial loading due to additional cracking at the diaphragm. There was a 49% decrease in the restraint moments of Bridge #1, and a 30% decrease in the restraint moments of Bridge #2 during their corresponding first loadings. The restraint moments remaining after the initial loading were approximately equal to 32% and 38% of the calculated cracking moments at the center pier for Bridges #1 and #2, respectively, based on a modulus of rupture equal to $7.5\sqrt{f'c}$.
3. Instantaneous deflections due to applied loadings could be reasonably estimated (within 8% for Bridge #1 and 26% for Bridge #2) using the modified PCA method, assuming a fully cracked section at the diaphragm. The deflections corresponding to the initial loading of the bridge could be calculated using this method by superimposing moments at the center pier. These moments were equal in magnitude to the decrease in restraint moments caused by additional cracking. The PCA and CTL methods underestimated the deflections due to live load.
4. The continuity between adjacent spans was not affected by 5 million cycles of repeated service loading, in which calculated reinforcement stress range at the pier exceeded the AASHTO allowable design stress range by 20 percent.
5. The experimentally determined positive and negative moments in both bridges at failure exceeded the AASHTO design nominal moment capacities for the composite

sections. Full composite action was attained by applying a raked finish to the surface of the precast panels. The experimentally determined negative moments greatly exceeded the AASHTO design negative moments, primarily due to strain hardening of the mild steel reinforcement. These experimental moments were approximately 1.7 and 1.6 times the AASHTO moments for Bridge #1 and #2, respectively.

6. The ultimate load-carrying capacity of the test bridges was not affected by time-dependent effects.
7. Moment redistribution for both bridges exceeded the maximum percentages allowed by AASHTO for design considerations.
8. Chloride powder sample data taken from Bridge #1 and from five additional durability specimens revealed that a build up of chlorides at the interface of the CIP concrete and precast panels, if existing, will remain isolated at crack locations during the life of the structure.
9. Visual inspection of the reinforcement, after the 48 weeks of exposure cycling of Bridge #1, revealed widespread corrosion of the epoxy-coated bars had occurred. This was accompanied by splitting of epoxy coating and staining of the surrounding concrete. However, corrosion did not lead to a noticeable reduction in cross-sectional area of the epoxy-coated bars during this time period, which is believed to have represented more than 45 years of exposure to deicing salt in the field. Inspection of the uncoated steel in the diaphragm revealed severe pitting and loss of cross-sectional area had occurred during this same time period.

10. Visual inspection of the reinforcement after 24 weeks of southern exposure cycling of Specimen C, which had a 1-inch clear cover, showed that the epoxy-coated bar without initial defects had not corroded. All five epoxy-coated bars containing defects had experienced mild corrosion. This was evidenced by blistering of the epoxy at a few places and mild pitting. Loss of cross-sectional area of the epoxy-coated bars due to corrosion was negligible. During this same 24-week exposure period, the uncoated bar in Specimen C had experienced severe corrosion at the crack location. Pitting of this bar resulted in a loss of cross-sectional area of approximately 50 percent.

7.3 Implementation

Based on the findings of this experimental program the following recommendations are made pertaining to the design of multi-span bridges using full-span precast concrete form panels.

1. The calculation of restraint moments at interior piers due to time-dependent effects should include provisions for possible cracking of the CIP concrete and the restraint of CIP concrete shrinkage due to the precast panels and steel reinforcement. This can be done using the modified PCA method proposed in this report.
2. The design moments at service load should include the calculated moments due to the restraint of time-dependent effects. However, since superimposed loading will likely cause a decrease in negative restraint moments due to cracking, the reduction of positive midspan moments due to negative restraint moments should be based on a decreased value of the calculated restraint moment. Based on the two bridges tested

in this study, the value of the negative restraint moment used to decrease positive moments should not exceed about 30% of the calculated cracking moment at the pier.

3. Design service load moments due to superimposed loading should be calculated using cracked section properties at the diaphragm if calculation of restraint moments indicates cracking is likely.
4. Calculation of instantaneous deflections due to superimposed loading should be based of a fully-cracked section at the diaphragm section.
5. The design moments at ultimate should not include moments due to the restraint of time-dependent effects, since these will be relieved by additional cracking and yielding of the reinforcement.
6. Moment redistribution in accordance with AASHTO section 5.7.3.5 should be allowed. Redistribution should be based on ultimate moments calculated by linear-elastic analysis using uncracked section properties.
7. Full composite action between the precast panels and CIP topping should be insured by applying a raked finish on the top surface of the panels.
8. Design for shear should be done according to AASHTO Section 5.8.
9. The positive moment connection at interior piers (which currently consists of extending uncoated prestressing strands out of the precast panel ends and anchoring them in the CIP concrete diaphragm) should be modified to provide a more durable structure. These strands experienced severe corrosion during the durability testing of this study.

10. Since widespread corrosion of the epoxy-coated reinforcement in Bridge #1 initiated within a few weeks after the arrival of chlorides, the concrete was the primary corrosion inhibitor. Results from the 3 ft x 3 ft durability specimens indicate that INDOT's current practice of using "Class C" concrete and a minimum reinforcement cover of 2 1/2 inches is superior to the chloride penetration protection afforded by the "Class A" concrete in Bridge #1 of this study. Corrosion of the epoxy-coated steel in Bridge #1 did not result in a significant loss of cross-sectional area, even when subjected to chloride concentrations representing more than 40 years of exposure in the field.

7.4 Suggestions for Phase 2

Phase 1 of this research study provided the much needed information about the behavior and durability of bridges constructed with full-span precast prestressed concrete panels. Phase 2 will involve the construction and monitoring of a continuous bridge with full-span precast panels in Indiana. It is the recommendation of the authors that Phase 2 should proceed at this time, provided the following concerns are addressed.

1. Cracking due to differential shrinkage between the precast panels and CIP concrete allowed for immediate penetration of chlorides to the level of reinforcement, resulting in premature corrosion at these areas. Attempts to reduce this cracking should be incorporated in Phase 2. Some possible areas of investigation include:
    - The use of longitudinal and transverse post-tensioning in the CIP topping.

- The use of special low-shrinkage concrete mixes.
- The addition of control joints.

2. The exposure cycling of Bridge #1 showed that the current positive moment connection at the diaphragm was deficient in terms of long-term resistance to corrosion. The bridge constructed in Phase 2 should utilize a different reinforcement detail at the diaphragm. Two alternate details are shown in Figure 7.1.

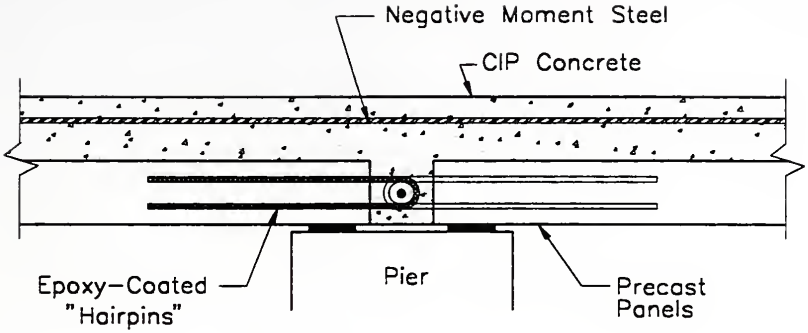

Detail A

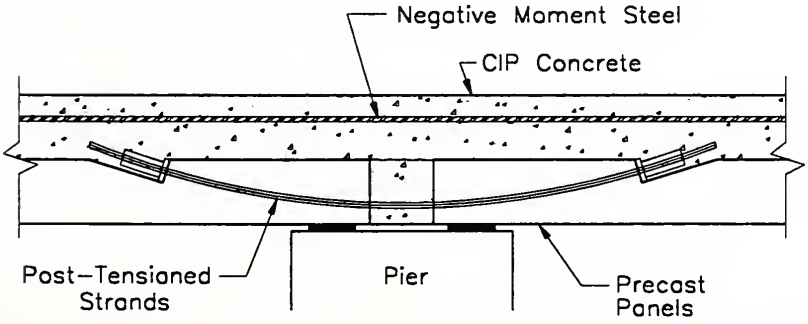

Detail B

Figure 7.1 Alternate Pier Details

LIST OF REFERENCES

LIST OF REFERENCES

1. C. O. Hays, Jr., R. L. Cox, Jr., and G. O. Obranic, Jr. "Full Span Form Panels for Short Span Highway Bridges." Department of Civil Engineering, University of Florida, Gainesville, Final Report U17F, 1980.

2. C. D. Buckner and H. T. Turner. "Performance Tests of Full Span Panel Form Bridges." Research and Development Section, Louisiana Department of Transportation and Development, Baton Rouge, Final Report 80-1c, 1981.

3. AASHTO. LRFD Bridge Design Specifications. Customary U.S. Units First Edition. American Association of State Highway and Transportation Officials, Washington, D.C., 1994.

4. H. Woods. Durability of Concrete Construction. ACI and The Iowa State University Press, 1968, Chapters 2, 6.

5. F. B. Coggins and C. W. French. "Chloride Ion Distribution in Twenty-Year-Old Prestressed Bridge Girders." ACI Materials Journal, September-October 1990.

6. P. D. Cady and R. E. Weyers. "Chloride Penetration and the Deterioration of Concrete Bridge Decks." Cement, Concrete, and Aggregates, CCAGDP, Vol. 5, No. 2, Winter 1983, pp 81-87.

7. K. C. Clear "Reinforcing Bar Corrosion in Concrete: Effect of Special Treatments," Special Publication SP-49, American Concrete Institute, Detroit, MI, 1975, pp. 71-82.

8. K. C. Clear "Time-to-Corrosion of Reinforcing Steel in Concrete Slabs." Report No. FHWA-RD-76-70, Federal Highway Administration, Washington, D.C., April 1976.

9. J. R. Van Daveer, "Techniques for Evaluating Reinforced Concrete Bridge Decks." ACI Journal, December 1975, pp. 697-704.

10. ASTM. "Standard Test Method for Half-Cell Potentials of Uncoated Reinforcing Steel in Concrete." (ASTM Designation: C 876-91), 1993, pp. 440-445.

11. Department of Transportation Federal Highway Administration User Manual. "Corrosion Detection in Reinforced Concrete Bridge Structures." Demonstration Project No. 84, Washington, D.C., March 1992.

12. ASTM. "Standard Test Method for Determining the Effects of Chemical Admixtures on the Corrosion of Embedded Steel Reinforcement in Concrete Exposed to Chloride Environments." (ASTM Designation: G 109 - 92) 1993, pp. 466-469.

13. AASHTO Specifications for Materials, "Standard Specification for Epoxy-Coated Reinforcing Bars." (AASHTO Designation M 284), 1991.

14. AASHTO Methods of Sampling and Testing. "Standard Method of Test for Electrical Indication of Concrete's Ability to Resist Chloride." (AASHTO Designation: T277-93), pp. 876-881.

15. Department of Transportation Federal Highway Administration. "Improved Method for Measuring the Chloride Permeability of Concrete." TR News, May-June 1987, pp. 18-19.

16. J. M. Lin and M. Sansalone. "Impact-Echo Studies of Interfacial Bond Quality in Concrete: Part I--Effects of Unbonded Fraction Area." ACI Materials Journal, May-June 1996, pp. 223-232.

17. R. Park and T. Paulay. Reinforced Concrete Structures. John Wiley and Sons, New York, 1975.

18. A. H. Mattock, "Precast-Prestressed Concrete Bridges 5. Creep and Shrinkage Studies." Journal of the PCA Research, May 1961, pp. 32-66.

19. C. L. Freyermuth, "Design of Continuous Highway Bridges with Precast, Prestressed Concrete Girders." PCI Journal, April 1969, pp. 14-39.

20. R. G. Oesterle, J. D. Glikin, and S.C. Larson. "Design of Simple-Span Precast Prestressed Bridge Girders Made Continuous Final Report." By Construction Technology Laboratories, Inc. for National Cooperative Highway Research Program, Transporation Research Board. (NCHRP Project 12-29), May 1989.

21. F. Dischinger, "Investigations on Resistance to Buckling, Elastic Deformation, and Creep of Concrete in Arch Bridges (Untersuchungen Uber die Knicksicherheit, die Elastiche Verformung und das Kriechen des Betons bei Bogenbruecken)." Der Bauingenieur (Berlin), V. 18, No. 39/40, Oct. 1937, pp. 595-621, and V. 20, No. 47/48, Dec. 1939.

22. W. G. Corley, and M. A. Sozen, "Time Dependent Deflections of Reinforced Concrete Beams." Journal of the American Concrete Institute, Proceedings V. 63, No. 3, March 1966, pp. 373-386.

23. ACI Committee 209, "Prediction of Creep, Shrinkage, and Temperature Effects in Concrete Structures." American Concrete Institute, Special Publication SP-76, Detroit, Michigan 1982, pp. 193-300.

24. "Recommendations for Estimating Prestress Losses." reported by PCI Committee on Prestress Losses, J. PCI, Vol. 20, No. 4, July-August 1975, pp 43-75.

25. M. P. Collins and D. Mitchell. Prestressed Concrete Structures. Prentice-Hall, Inc., Englewood Cliffs, N.J., 1991.

26. A. B. Zoob, P. J. LeClaire, D. W. Pfeifer. "Corrosion Protection Tests on Reinforced Concrete Treated with SIL-ACT Silane Sealer For Advanced Chemical Technologies Company." Wiss, Janney, Elstner Associates, Inc., 1995

27. H. O. Hasan, "Structural Performance of Concrete Bridge Decks Reinforced with Epoxy-Coated Steel Under Fatigue Loading." Ph.D. Dissertation, Purdue University, 1994.

28. "Participant's Workbook for Workshop of Strategic Highway Research Program." Wilbur Smith Associates, Falls Church, VA (Prepared for U. S. Dept. of Transportation, Federal Highway Administration), April 1996.

29. AASHTO Methods of Sampling and Testing. "Standard Method of Sampling and Testing for Total Chloride Ion in Concrete and Concrete Raw Materials." (AASHTO Designation: T 260-84), pp. 771-84.

30. J. Flis, S. Sabol, H. W. Pickering, A. Sehgal, K. Osseo-Asare, and P.D. Cady. "Electrochemical Measurements on Concrete Bridges for Evaluation of Reinforcement Corrosion Rates." Corrosion, Vol 49, No. 7 (Corrosion Engineering Section), NACE International, 1993, pp. 601-613.

31. N. S. Berke, M. P. Dallaire, M.C. Hicks, and R.J. Hoopes. "Corrosion of Steel in Cracked Concrete." Corrosion, Vol. 49, No. 11, NACE International, pp. 934-943.

32. R.W. Poston and K. E. Kesner. "Impact Echo Strikes Home." Civil Engineering, June 1995, pp. 60-62.

33. B. J. Jaeger, M. J. Sansalone, and R.W. Poston. "Detecting Voids in Grouted Tendon Ducts of Post-Tensioned Concrete Structures Using the Impact-Echo Method." ACI Structures Journal, (forthcoming in July-August 1996 issue).

34. D. Pfeifer, R. Landgren, and P. Krauss. "Performance of Epoxy-Coated Rebars: A Review of CRSI Research Studies." Transportation Research Board/ National Research Council, Transportation Research Circular, Number 403, March 1993, pp. 57-65.

35. Department of Transportation. "Protective Systems for New Prestressed and Substructure Concrete." Federal Highway Administration Final Report, Report No. FHWA-RD-86/193, April 1987.

36. D. L. Spellman and R. F. Stratfull. "Chlorides and Bridge Deck Deterioration." Materials and Research Department of California Division of Highways. Sponsored by Committee on Effect of Ice Control. Highway Research Record No. 328, 1970, pp 38-49.

37. J. Bungey. "Non-Destructive Testing for Reinforcement Corrosion." Concrete. January/February 1993, pp. 16-18.

38. K. McLaughlin. "The Detection of Corroding Reinforcement in Concrete Structures." British Journal of Non-Destructive Testing. Vol. 31, No. 12, December 1989, 683 pp.

39. A. K. Suryavanshi, S. Syam Sunder, and B. U. Nayak. "A Comparison of Surface Potentials of R. C. Structures Using Reference Electrodes--Part 1." Corrosion Prevention and Control, August 1991, pp. 105-131.

40. M. G. Ali and K. Fahd. "Reference Half Cells for Monitoring Corrosion Condition of Steel in Reinforced Concrete Structures." Anti-Corrosion. June 1990, pp. 10-11.

41. Gruner and G. A. Plain. "Type K Shrinkage-Compensating Cement in Bridge Deck Concrete." Concrete International, October 1993, pp. 44-47.

42. AASHTO Methods of Sampling and Testing. "Standard Method of Test for Rapid Determination of the Chloride Permeability of Concrete." (AASHTO Designation: T 277-83), pp. 1229-1236.

43. B. Ost and G. E. Monfore. "Penetration of Chloride into Concrete." Materials Performance, June 1974, pp. 21-24.

44. P. K. Mehta, P. Monteiro. Concrete Structure, Properties, and Materials. Second Edition. Prentice Hall, Inc., Englewood Cliffs, N.J., 1993.

45. C. Wang and C. G. Salmon, Reinforced Concrete Design (fourth edition). Harper and Row, Publishers, Inc., New York, 1985.

46. D. R. Jackson, W. T. Scannell, A. Sohanghpurwala, and M. Islam. "Methodology to Evaluate the Corrosion Condition of Bridge Decks Containing Epoxy Coated Reinforcing Steel." Federal Highway Administration and CONCORR, Inc., June 1995.

47. J. M. Lin, M. Sansalone, and R. Poston. "Impact-Echo Studies of Interfacial Bond Quality in Concrete: Part II--Effects of Bond Tensile Strength." ACI Materials Journal, July-August 1996, pp. 318-326.

48. H. Tokuda, M. Shoya, M. Kawakami, M. Kagaya. "Application of Superplasticizer to reduce Drying Shrinkage and Thermal Cracking of Concrete." American Concrete Institute, Special Publication SP-68, Detroit, Michigan, pp. 101-120.

49. J. M. Scanlon, M. R. Sherman "Fly Ash Concrete: An Evaluation of Chloride Penetration Testing Methods" Concrete International, June 1996, pp. 57-62.

COVER DESIGN BY ALDO GIORGINI